University of Stavanger

Faculty of Science and Technology

MASTER'S THESIS

Study program/ Specialization: Offshore Technology Marine and Subsea	Spring semester, 2016 Open / ~~Restricted access~~
Writer: Sølve Nilsen	..... (Writer's signature)
Faculty supervisor: Professor Arnfinn Nergaard External supervisor(s):	
Thesis title: A study of principal hull parameters for a Spar buoy foundation for a vertical axis wind turbine in the MW-class	
Credits (ECTS): 30	
Key words: Spar buoy Vertical Axis Wind Turbine Parametric study Hydrodynamic modelling Dynamic simulations Renewable energy	Pages: .....169..... + enclosure: .....8 + CD..... Stavanger, ...14.06.2016..... Date/year

Front page for master thesis
Faculty of Science and Technology
Decision made by the Dean October 30th 2009

Abstract

This thesis analyses a vertical axis wind turbine (VAWT) in the MW-class used in relation with a floating Spar buoy. The objective was to study the effect of varying principal hull parameters including diameter and draft on the overall system's hydrostatic and hydrodynamic performance. First, a spreadsheet was constructed, containing certain engineering simplifications to evaluate a number of floating geometries with varying drafts and diameters in an effective manner. These results formed the basis for selecting three potential floaters to be evaluated in comprehensive hydrodynamic simulations. However, frequency dependent added mass and damping matrices, displacement RAOs and load RAOs in the six degrees of freedom (DOFs) had to be established prior to running the simulations. The software HydroD was used for this purpose, which utilizes three-dimensional potential theory to calculate the aforementioned parameters.

The parameters metacentric height, natural periods and static inclination angles were evaluated in the spreadsheet calculations to analyze the effect of varying principal hull parameters on the system's hydrostatic performance. The evaluated floater geometries were established by varying the draft in increments of 25 meters and calculate the needed diameter to gain a displacement of 5300 tons.

A new vessel was generated in OrcaFlex using the output gained from the HydroD analysis, where a total of two environmental conditions were evaluated. The first, referred to as EC 1, represented an operational condition at rated power output, while the second, referred to as EC 2, represented a full storm scenario. The sea state was modelled an irregular wave train generated form a JONSWAP wave spectrum with peakadness factor of 3.3, while the wind was modelled as a point load acting at the center of the rotor blades. The simplified wind environment is a rather coarse approximation, but necessary nonetheless, as time was rather spent on obtaining an accurate hydrodynamic model. Performance parameters such as motions in the six DOFs, minimum freeboard and air-gap, effective tension in the mooring lines and arc-length to touchdown point were evaluated to analyze the effect of varying principal hull parameters on the system's hydrodynamic performance.

The results from the spreadsheet calculations revealed that a floater comprising of a higher draft and lower diameter features a higher metacentric height due to an overall greater rise in $\overline{KB}$ compared to the rise in $\overline{KG}$ associated with such a geometry. Since the studied floaters featured similar displacements, i.e. similar buoyancy force, the high draft and low diameter floaters also illustrated more favorable static inclination angles, as the increased $\overline{GM}$ led to a greater arm in the up-righting moment. Furthermore, all studied geometries featured suitable natural periods to avoid resonance motions with first-order wave effects.

The dynamic simulation indicated that a floater comprising of a higher draft and lower diameter floater obtains the most favorable motion characteristic in surge, sway, heave, roll and pitch. The reduced surge, sway and heave translations were related to a reduced total force, i.e. force that gives net motions, in these DOF caused by the reduced diameter. The reduced roll and pitch motions were related to the increased up-righting moment due to the greater metacentric height associated with a long and slender floater. However, some cost considerations based on intuitive relations revealed that a higher draft would most probably lead to a more expensive floating system. Furthermore, a high draft may limit the number of operation sites suitable in accommodating the turbine system, as the site needs to feature sufficient depth to facilitate the draft and the mooring lines used for station keeping purposes. It is therefore believed that the optimum principal hull parameters combination will be a compromise of sufficient stability, cost and depth at location the turbine shall operate.

Acknowledgements

I would like to express my gratitude to my supervisor, Prof. Arnfinn Nergaard for suggesting the topic for this thesis, which has been both a challenging and interesting process. He willingly spent time on guidance and discussion, even though I sometimes showed up unannounced. Prof. Muk Chen Ong also deserves recognition for acquiring the HydroD license and for checking some preliminary results.

I would also like to thank family and friends. Their support has been essential through this labor-intensive semester.

Sølve Nilsen

University of Stavanger, June 2016
Norway

Table of content

Abbreviations

Abbreviation	Explanation
AP	Aft perpendicular
BEM	Boundary element method
CAPEX	Capital expenditure
CoB	Center of buoyancy
COE	Cost of energy
CoG	Center of gravity
DDF	Deep draught floater
DNV	Det norske veritas
DOE	Department of energy
DOF	Degree of freedom
DP	Dynamic positioning
EC	Environmental condition
FEM	Finite element method
FE-model	Finite element model
FP	Forwards perpendicular
GBS	Gravity based structures
GRE	Glass reinforced epoxy resin composite
HAWT	Horizontal axis wind turbine
HF	High-frequency
IPCC SRREN	Intergovernmental panel on climate change special report on renewable energy sources and climate change mitigation
JONSWAP	Joint North Sea Wave Observation Project
KC-number	Keulegan Carpenter number
LF	Low-frequency
NACA	National Advisory Committee for Aeronautics
NREL	National Renewable Energy Laboratory
OC3	Offshore Code Comparison Collaborative
OWT	Offshore wind turbine
Postresp	Postprocessor for Statistical Response Calculations
QTF	Quadratic transfer function
RAO	Response amplitude operator
SAT	Standard ACIS text
SWL	Still water level
TDP	Touch-down point
TLP	Tension leg platform
ULS	Ultimate limit state
VAWT	Vertical axis wind turbine
VIV	Vortex induced vibrations
WADAM	Wave analysis by diffraction theory
WF	Wave-frequency

Nomenclatures

Symbol	Explanation
$U(z)$	Mean wind component
I	Turbulence intensity
C_A	Shape coefficient
A_{swept}	Swept area
U_W	Undisturbed free air velocity
C_P	Power coefficient
ρ	Density
ν	Kinematic viscosity
Φ	Tip-speed ratio
U_ω	Tangential velocity of the rotor blade
d	Draft
F_B	Buoyancy force
F_G	Gravity force
M_I	Inclination moment
M_R	Up-righting moment
ϕ	Inclination angle
$\overline{GM}$	Metacentric height
$\overline{KB}$	Distance from keel to center of buoyancy
$\overline{BM}$	Metacentric radius
$\overline{KG}$	Distance from keel to center of gravity
∇	Submerged volume
ω	Angular frequency
A	Wave amplitude
k	Wave number
ε	Phase angle
$S_\xi(\omega)$	Wave spectrum
ξ	Sea surface elevation process
H_s	Significant wave height
T_p	Spectral peak period
η_i	Motion in i^{th} DOF
A_{ij}	Added mass coefficients
B_{ij}	Damping coefficients
C_{ij}	Hydrostatic stiffness coefficients
M_{ij}	Mass coefficients
K_{ij}	Mooring line stiffness coefficients
λ	Wave length
T_z	Zero up-crossing period
$H^{(2-)}$	Quadratic drag function
T_j	Natural period in j^{th} direction
S	Water plane area
S_η	Response spectrum
D_0	Diameter of bottom section of floater
D_1	Diameter of top section of floater
L_0	Length of bottom section of floater
L_1	Length of top section of floater
L_2	Length of freeboard

1 Introduction

The ever-increasing energy consumption along with an increased attention in global warming has led to a greater interest in renewable energy. Wind energy is one of the fastest growing renewable energy sources, which has been in steady development the recent years. Figure 1-1 presents the global cumulative installed wind energy capacity from 1997 to 2014, illustrating a total capacity of 369.6 GW by the end of 2014. The average annual growth rate of installed wind power from 2005 to 2014 was almost 23%, with a record setting annual installed capacity of over 51 GW in 2014 [1].

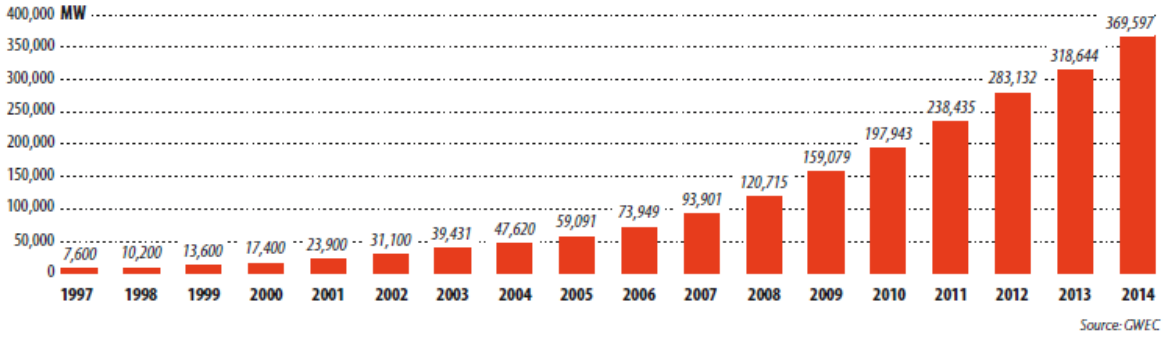

Figure 1-1: Annual cumulative installed wind energy capacity from 1997-2014, retrieved from [1]

Offshore wind is believed to unlock a huge potential in meeting the increased energy demands in a sustainable manner [2]. This is closely related to the amount of offshore areas suitable to accommodate large wind farms, and the fact that offshore wind also blows more consistent and at higher wind speeds. IPCC SRREN special report on renewable energy sources and climate change mitigation from 2011 concluded that the technological energy potential in offshore wind is several times the worldwide electrical production. Hence, exploiting offshore winds for power production has been subjected to accelerated interest and growth the recent years, as illustrated by Figure 1-2 showing the annual cumulative installed offshore wind capacity from 2011 to 2014.

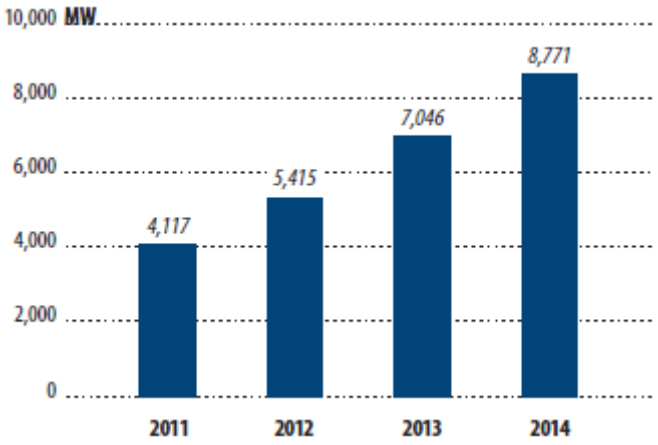

Figure 1-2: Annual cumulative installed offshore wind energy capacity from 2011-2014, retrieved from [1]

However, by comparing the information in Figure 1-2 to Figure 1-1 reveals that only 2.3% of the global wind capacity is installed at offshore locations at the end of 2014. Furthermore, most of the installations are adaptions of onshore wind turbines, which relies on bottom fixed support structures that are limited to shallow water depths [3]. These support structures include monopile, gravity based structures and space frames as illustrated in Figure 1-3. The monopile and gravity based structure are applicable in water depths up to 20 meters, and the space frames are applicable for water depths up to 50-60 meters [3].

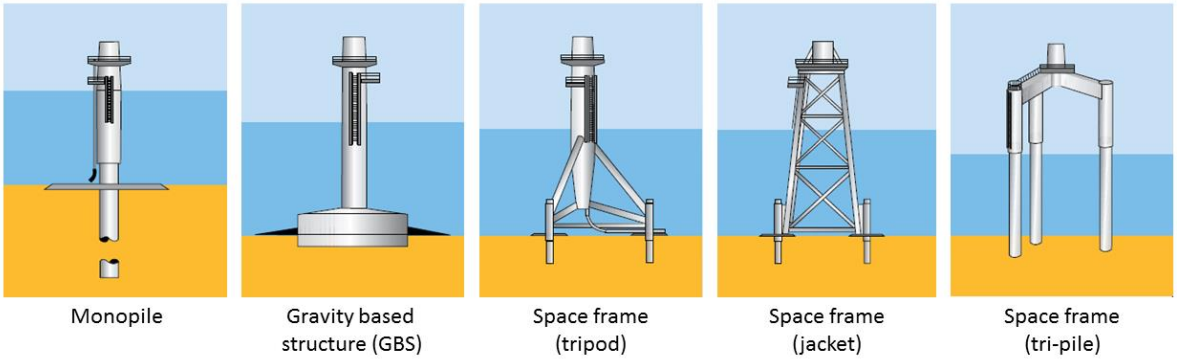

Figure 1-3: Illustration for bottom fixed support structures used for offshore wind turbines, retrieved from [3]

Even though the adoption of onshore wind turbines on bottom fixed structures have matured the offshore wind industry significantly in a relative short period of time, there exist few offshore locations with shallow waters and associated winds that makes such an solution economically viable. This is especially true for the Atlantic, Mediterranean and deeper parts of the North Sea, where the majority of the sea areas have a water depth above 60 meters [3]. Offshore wind turbines therefore needs to operate in deeper waters to exploit more of the available offshore wind energy, for which a floating support structure seems to be the most viable option. Another advantage of utilizing floating support structures is the simplified installation process. The wind turbines can be installed in sheltered waters and successively be transported to location by tugboats, where it is connected to pre laid mooring lines. The only offshore work needed is consequently hooking up the mooring lines. This will reduce the installation cost significantly compared to fixed-to-bottom offshore windmills, which needs to be installed on site by suitable offshore lifting vessels.

The floating support structures most applicable for an offshore wind turbine application includes [4]:

- Spar buoy
- Tension leg platform (TLP)
- Semi-submersible

The possible foundations, from fixed-to-bottom to floating structures, and their appropriate water depth and turbine size is summarized in Figure 1-4.

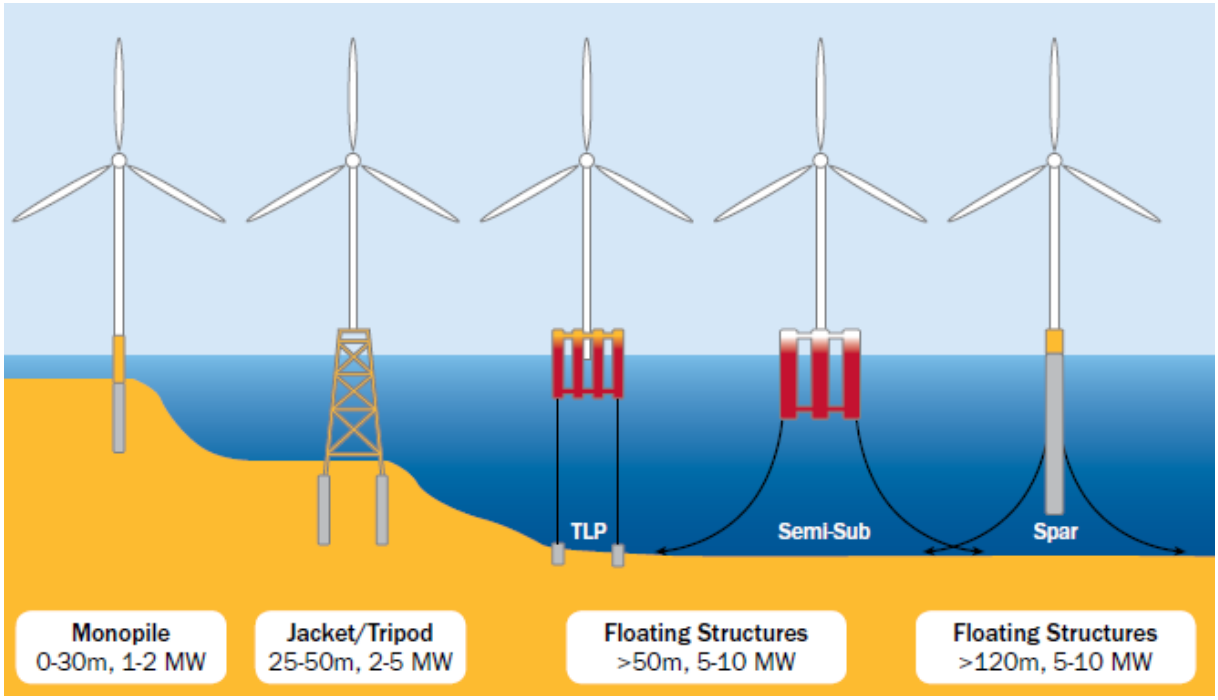

Figure 1-4: Illustration of possible foundations for OWTs, retrieved from [3]

At the date of writing, floating offshore wind turbines represents a relative young technology in its infancy. At the end of 2012, there were seven experimental floating structures in testing phase and two full scale floating pilot project, worldwide. All of these utilizes a horizontal axis wind turbine (HAWT), implying that the turbine's axis of rotation is in line with the incoming wind direction. This is the "normal" type of wind turbine often observed onshore, and is depicted in Figure 1-4. Several of these projects have verified the technical feasibility of using a HAWT on a floating foundation in an offshore environment. Despite these achievements, high cost of energy (COE) remain the biggest challenge for offshore wind energy, and cost reduction is one of the main concerns for the industry [1]. Wind energy is capital intensive, where the production and installation of substructures represents up to 20% of the capital expenditure (CAPEX) [3]. The cost of energy can therefore be considerably reduced if cost of substructure is reduced, which may be achieved by demonstration of new designs and through innovation. Even though the HAWT have proven its technical feasibility when used with a floating support structure, there exist another configuration believed to have certain merits over the HAWT configuration; namely the vertical axis wind turbine (VAWT). The VAWT is characterized by having the axis of rotation transverse (vertical) to the direction of the wind. This makes it possible to place critical and heavy equipment, such as the generator and gearbox assembly, at the base of the turbine, which reduces the center of gravity (CoG) and increases the stability. This implies that a smaller floating support structure may be utilized in combination with a VAWT to achieve the same stability characteristics as a HAWT with the same payload, consequently reducing the associated cost of floater and the turbine system as a whole. A 5-year project founded by the Department of Energy (DOE) was initiated in 2011 at Sandia National Laboratories to study the feasibility of floating VAWT. The study shows thus far a potential reduction in cost of energy (COE) of 20% [5]. Furthermore, the down-to-base placement of the drivetrain increases the maintainability of this equipment, as it is easily accessible [6]. The symmetry around the vertical rotation axis also makes the VAWT omni-directional, i.e. they rotate and produces power independently of the direction of the incoming wind. This excludes the need for complex yaw and pitching systems often needed on HAWT, leading to a simpler and possibly more robust design with less components.

2 Objectives

The presented work studies a floating turbine system comprising of a Spar buoy foundation and a VAWT in the MW-class. The aim is to evaluate the effect of varying principal hull parameters, i.e. diameter and draft, on the system's hydrostatic and hydrodynamic performance.

In order to isolate the effect of varying the principal hull parameters on the system's hydrostatic and hydrodynamic performance, each floater must feature a similar displacement. An estimate for the needed displacement to give sufficient metacentric height and static inclination angles will therefore be evaluated first. A number of floater geometries with varying drafts and diameters will then be constructed based on the identified displacement. These shall be evaluated through a series of spreadsheet calculations to estimate hydrostatic performance parameters such as metacentric height, natural period and static inclination angle. The results will also form the basis for selecting three floaters comprising of different drafts and diameters, which shall be studied further in a comprehensive dynamic simulation. However, frequency dependent added mass and damping matrices, displacement RAOs and load RAOs must be obtained prior to running the simulations. The software HydroD shall be used for this purpose, which utilizes three-dimensional potential theory to calculate the aforementioned parameters. The hydrodynamic simulations will be performed in OrcaFlex, where first-order wave responses from an irregular sea state shall be evaluated for each studied geometry to assess the effect of varying the Spar's draft and diameter on the system's dynamic performance.

3 Report structure

The first chapter of this report presents some promising floating VAWT concepts, which are being evaluated for commercialization at the time of writing. The essential theoretical background relevant for the featured topic is presented next. The evaluated turbine concept is then introduced, before the studied environmental conditions are specified. The next chapter explains the analysis procedures for the spreadsheet calculations, the hydrodynamic modelling in HydroD and the hydrodynamic simulations in OrcaFlex. The results are presented in chapter 9 through 11 followed by a discussion of these results. Lastly, the thesis conclusion is stated along with proposal for further work.

4 State of the art

The following section presents some of the promising floating VAWT. Statoil's Hywind Demo project is also presented in detail, even though the concept features a HAWT. This is done as some of the parameters evaluated in the presented work is based in this project.

4.1 Hywind

Statoil's Hywind pilot project was the world's first full-scale prototype floating wind turbine. It was installed 10 km west of the Norwegian island Karmøy in 200 meter water depth in 2009 [7]. The pilot featured a standard offshore wind turbine of the type Simens SWT-2.3-82 VS placed on ballasted Spar buoy fastened to the seabed by three mooring lines. Each of these mooring lines were connected in a crowfoot configuration to increase the yaw stiffness, which is generally low for Spar buoys [4]. The term crowfoot implies that each mooring line has two connection points on the Spar hull, as illustrated in Figure 4-1.

Figure 4-1: Illustrative picture of the Hywind concept, retrieved from [7].

Table 4-1 and Table 4-2 presents some of the key data for the turbine and floater used on the Hywind project.

Table 4-1: Data for the turbine used in relation with Statoil's Hywind Pilot project, retrieved from [8]

Turbine type	Simens SWT-2.3-82 VS
Turbine size	2.3 MW
Weight rotor	54 tons
Weight nacelle	82 tons
Height of nacelle above SWL	65 m
Rotor diameter	82.4 m
Blade length	40 m
Max. height of rotor blade	65 m + 82.4/2 m = 106.2 m
Min. height of rotor blade	65 m – 82.4/2 m = 23.8 m
Wind speed, nominal power	13-14 m/s
Cut-in wind speed	3-5 m/s
Cut-out wind speed	25 m/s
Rotor speed	6-18 RPM

Table 4-2: Data for floater used in relation with Statoil's Hywind Pilot project, retrieved from [9]

Floater type	Spar buoy
Tower diameter	Tapered; 6 m at sea level, 2 m at top
Diameter of submerged body	8.3 m
Draft	100 m
Displacement	5300 tons

The main purpose of the Hywind pilot turbine was to obtain measurements of the wind and wave imposed responses on the structure in order validate the concept and to optimize the design. In 2011, after two years of testing, the concept was verified showing performance beyond expectation [9]. This gave Statoil the confidence to develop the Hywind Scotland Pilot Park, which has a planned final commissioning at the fourth quarter of 2017, thus being the first floating wind farm in existence. The current base case is to install five units equipped with a 6 MW generator, with an associated lifetime of 20 years. The farm will be located near Buchan Deep in 95-120 m water depths, approximately 25-30 km off the coast of Peterhead in Aberdeenshire [7]. The main goal is to test multiple units in a park-configuration and verify the up-scaled design from 2.3 MW to 6 MW.

4.2 DeepWind

The DeepWind project was a four-year research study launched in 2010 with the aim to explore the feasibility of a new and simple offshore floating VAWT concept, suitable to operate in deep-water sites. The concept features a VAWT with a two bladed Darrieus rotor placed on a Spar buoy, which is kept in place by a mooring system connected to a torque absorption system at the bottom of the support structure [10]. What makes this concept unique is that the entire floating support structure rotates with the rotor, which excludes the need for large mechanical bearings used in most VAWT concepts. The torque is delivered through the rotating floater a generator placed at the bottom of the structure [10]. The first design comprised of a 2 MW rotor with a total height of 75 m and a diameter at equator of 67 m. This turbine was later altered to feature a power capability of 5 MW, which is the first baseline of this concept [10].

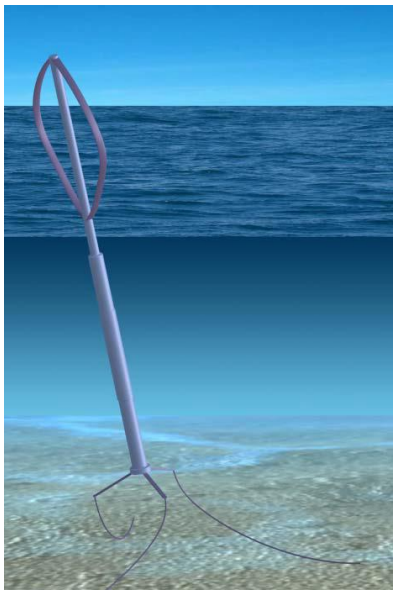

Figure 4-2: Illustrative picture of the DeepWind concept, retrieved from [10]

4.3 VertiWind

VertiWind is a VAWT project launched in 2006 by Nénuphar, where EDF Enginers Nouvelles and Technip have later joined as partners. The concept consist of an innovative rotor assembly placed in the middle of a semi-submersible floater, which ensures that the center of gravity and center of buoyancy of the system coincides on a vertical centerline. The rotor consists of three blades with four levels of support struts, where each blades has a heliaxial twist of 120° that minimizes the torque variations during a full rotation. The concept also comprises of a direct-drive permanent magnet generator, reducing the number of components on the turbine's driveline [11]. A prototype is scheduled to be in operation in 2017, followed by a pilot farm of 13 turbines installed 23 kilometers from shore [12].

Figure 4-3: Illustrative picture of the VertiWind concept, retrieved from [12]

4.4 Aerogenerator X

Wind Power Ltd. proposed the aerogenerator X concept in 2010. It featured a 10 MW vertical axis wind turbine with the rotor blades configured in a V-shape extending from the center of the structure. At the time of writing, Wind Power Ltd. has set a goal of providing 1 GW of offshore wind power by 2020. However, the concept heave featured a slow progress due insignificant sufficient funds, but Wind Power Limited insists that the project is still moving towards is 2020 ambitions [13].

Figure 4-4: Illustrative picture of the aerogenerator X concept, retrieved from [13]

4.5 Gwind

The Gwind is a VAWT concept based on actively using gyroscopic effects to suppress critical motions. A prototype named “Spinwind 1” was built to explore the motion characteristics of the VAWT used in relation with a Spar buoy [14]. Besides its low center of gravity, the concept features the benefit of using gyro stabilization, which may eliminate motions at natural periods in pitch and roll according to laboratory tank test concluded in 2012. Gwind’s business plan follows a three-step strategy [15] including:

1. Constructing a 250 kW prototype for in fjord fish farms
2. Constructing first single-unit FVAWT for powering platforms
3. Full multi-unit wind farm development.

Figure 4-5: Illustrative picture of the Gwind concept, retrieved from [14]

4.6 SKWID

The SKWID is a hybrid power generation concept proposed by Modec, capable of utilizing both the kinetic energy from ocean currents and ocean winds for power production. It features a Darrieus turbine above the sea level and a Savonius turbine below the sea level. These two turbines are connected to a central gearbox and generator assembly, allowing for electricity generation from currents, winds or both at the same time. The floating support structure is circular in shape, featuring a large diameter and low draft, where the Savonius turbine works as ballast in order to facilitate stability. [16]. However, the two SKWID prototypes installed off the coast of the Japanese island Kyushu, have capsized [17], illustrating some possible flaws in the design.

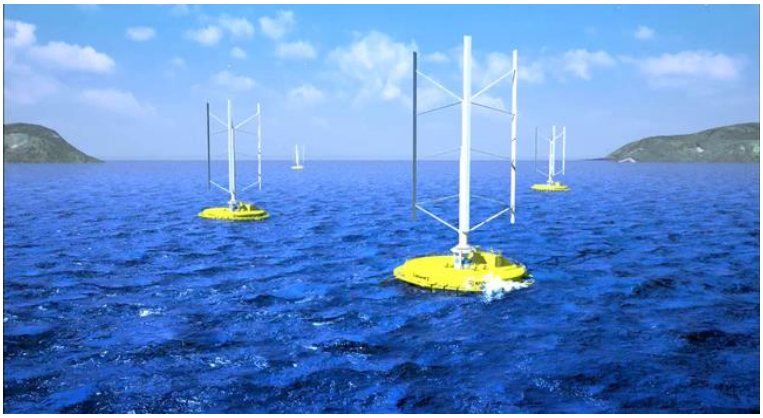

Figure 4-6: Illustrative picture of the SKWID concept, retrieved from [17].

5 Theory

The following section presents the theory utilized in this thesis. Wind theory and theory related to wind turbines is presented first, before the concept of static stability of floating offshore structures is introduced. Relevant wave theory will follow, before a rather comprehensive section regarding vessel response in regular and irregular sea states is presented. The theory section will be concluded by an introduction to station keeping systems, where emphasis is placed on the catenary mooring system.

5.1 Wind

Wind is a highly variable resource with respect to time and space. On a global scale, wind is generated due to a differential heating of the earth's surfaces, which will be greatest on landmasses near equator. The air particles in the hot regions will rise towards the atmosphere and circulate to the cooler areas, resulting in a large-scale global wind-circulation pattern [18]. This pattern is however disturbed on a continental scale by the distribution of landmasses and oceans. On a local scale, the wind-pattern is further altered by local topography. Coastal regions will also experience a local sea breeze on sunny days due to differential heating between the sea and land [18].

These variations can also be regarded on a timescale. Differences in wind speed of several days are referred to as synoptic variations, while differences on an hourly time scale are described as Diurnal variations. Wind speed variations on a shorter time scale, down to minutes or seconds, are known as turbulence [18].

It is useful to evaluate the instantaneous wind climate as a mean wind speed component with superimposed turbulent fluctuations [18]. The mean wind speed is a measure of the wind's intensity and is important for the energy potential for the turbine, while the turbulence is a measure of the wind's variability and is important when establishing short-term peak loading for structural design of the turbine.

5.1.1 Mean wind component

The mean wind component is obtained by averaging the wind speed over a specified period, often set to 10 minutes. On such time scales, the mean wind speed can often be assumed constant and acting in one prevailing direction [19]. The mean wind speed will however vary with vertical height above ground or sea level, which is often described trough an idealized model profiles. The three most commonly applied profiles includes the logarithmic profile, the power law profile and the Frøya model [19]. The power law profile will be utilized in the presented work, given as [19]:

$$U(z) = U_{10}(10) \cdot \left(\frac{z}{H}\right)^{\alpha} \qquad \textit{Eq. 5-1}$$

The coefficient α depends on the terrain roughness, and is typically given in standards and recommended practices.

5.1.2 Turbulent wind component

The turbulent fluctuations are, as previously stated, variations in the wind climate on the shortest time scales. The two main sources of turbulence are friction with the earth surface and a variation in air-particle density with height, caused by differential heating of the air masses [18]. Generally, turbulence can be decomposed into three components, one per direction in a catenary coordinate system. In the prevailing wind direction, the turbulence can be regarded as the natural variability in the wind speed about the mean value. As there is no mean wind component in the lateral and vertical direction, the turbulence component fluctuates around zero in these directions.

Turbulence is often quantified by turbulence intensity given as [19]:

$$I = \frac{\sigma}{U(z)} \;\; ; \;\; where \qquad \textit{Eq. 5-2}$$

$$\sigma = \text{standard deviation of the wind speed}$$

5.1.3 Wind force

Wind forces arises as the interaction between the wind particles and an external surface creates a pressure field on the surface. The wind load arising from the wind pressure field can generally be divided into three force components, a drag force acting in the prevailing wind direction, a lift force acting in the across-wind direction and a tangential force acting in the vertical direction. Note that the tangential force arises due to friction forces and is only be significant when considering large wind exposed areas [19].

The sectional lift and drag forces may be calculated as [19]:

$$f_{d,l} = \frac{1}{2} \cdot \rho_{air} \cdot C_A \cdot U_{tot}^2 \cdot D \;\; ; \;\; where \qquad \textit{Eq. 5-3}$$

$$C_A = \text{shape coefficient in the applicable direction}$$

$$D = \text{typical cross sectional dimension in the applicable direction}$$

$$U_{tot} = \text{total wind velocity}$$

The expression above considers the total wind velocity, comprising of the mean wind component and the turbulence component. This makes the sectional lift and drag forces fluctuating in nature. It is often convenient to separate the wind loads into a mean component and a fluctuating component. The shape coefficient is a non-dimensional coefficient derived from experiments, which are generally dependent upon the shape of the wind exposed structure and in some cases the Reynolds number, given as:

$$R_e = D \cdot \frac{U(T,z)}{\nu} \;\; ; \;\; where \qquad \textit{Eq. 5-4}$$

$$\nu = \text{kinematic viscosity of fluid}$$

5.2 Wind turbines

Modern wind turbines uses kinetic energy in the wind to generate electrical energy. This is done through an energy converter, usually known as a rotor, which transforms the kinetic energy into mechanical rotation that drives a generator. Furthermore, modern wind turbines is generally classified according to rotor's axis of rotation [20], which may be either horizontal or vertical. A presentation of the two different windmill concepts will follow, where more emphasis is placed towards describing vertical axis wind turbines. However, some general principles of the conversion of kinetic energy to mechanical torque will be discussed first, as this is similar to both type of turbine.

5.2.1 Energy potential

The available power of moving air passing through the rotor area is given as [20]:

$$P_0 = \frac{1}{2}\rho_{air} \cdot U_W^3 \cdot A_{swept} \; ; \; where \qquad \textit{Eq. 5-5}$$

$$\rho_{air} = \text{density of air}$$

$$U_W = \text{undisturbed free air velocity}$$

$$A_{swept} = \text{swept area}$$

The swept area is defined as the projected surface on a vertical plane created by the rotational blades, and will be dependent upon the type of turbine under consideration.

Furthermore, the mechanical power output of the rotor is expressed as [20]:

$$P_M = \frac{1}{4}\rho \cdot A_{swept}(U_W^2 - U_2^2) \cdot (U_W + U_2) \; ; \; where \qquad \textit{Eq. 5-6}$$

$$U_2 = \text{velocity behind the rotor}$$

The ratio between the mechanical power extracted from the rotor and the available power of the undisturbed air stream is represented by a power coefficient (C_P), given as [20]:

$$C_P = \frac{P_M}{P_0} = \frac{1}{2}\left[1 - \left(\frac{U_2}{U_W}\right)^2\right] \cdot \left[1 + \frac{U_2}{U_W}\right] \qquad \textit{Eq. 5-7}$$

Plotting this interrelationship graphically, the maximum possible power coefficient is found to be $C_P = 0.593$, which occurs for $U_2/U_W = 1/3$. Albert Betz was the first to derive this expression, and it is consequently often referred to as the "Betz factor". Note that the Betz factor assumes a turbine working with zero losses in a two dimensional frictionless airflow, and will therefore represents a theoretical ideal limit for the power coefficient. Expressing the mechanical power generated from the rotor through the power coefficient gives:

$$P_M = \frac{1}{2}C_P\rho_{air}A_{swpt}U_W^3 \qquad \textit{Eq. 5-8}$$

The mechanical power potential is therefore proportional to the wind speed in the third power.

Another important parameter to control in order to achieve an optimum power production is the tip-speed ratio, given as the tangential velocity of the rotor blades divided by the undisturbed free stream velocity [20]:

$$\Phi = \frac{U_\omega}{U_W} = \frac{\omega r}{U_W} \;\; ; \;\; where \qquad \textit{Eq. 5-9}$$

$$U_\omega = \text{tangential velocity of the rotor blade}$$

$$\omega = \text{rotational velocity of rotor blade}$$

A too low tip-speed velocity will allow much of the free-stream velocity to pass through the turbine undisturbed, and thus lead to a poor exploitation of the possible wind energy. Similarly, a too high tip speed ratio will block the free-stream wind velocity and force more of the air to flow past on the outside of the turbine [21].

5.2.2 Horizontal axis wind turbine (HAWT)

A horizontal axis wind turbine features a horizontal axis of rotation, i.e. axis of rotation aligned with the incoming wind. The configuration of key components, including rotor, drive train, generator and the yaw system is illustrated in Figure 5-1.

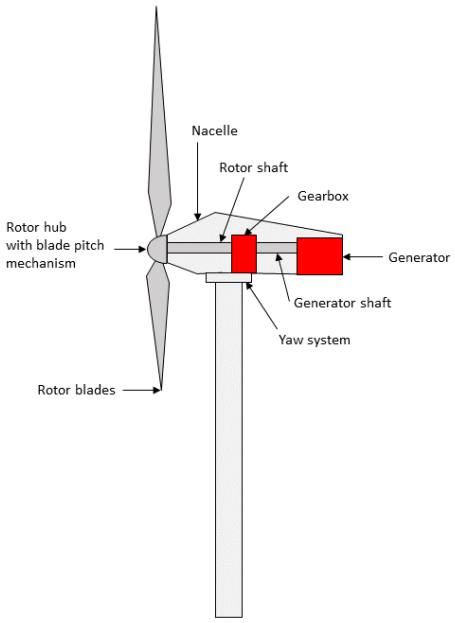

Figure 5-1: Simplified illustration of a HAWT, inspired from [20]

The rotor consists of a set of rotor blades, two or three blades are most common [6], and a hub to which the blades are connected. The hub may also contain mechanisms to pitch the blades about their longitudinal axis to control the rotor speed and power output. The mechanical torque is transferred to the drive train, consisting of a rotor shaft, a gearbox and a generator drive shaft, before being converted into electrical energy at the generator. A yaw system is also needed in the HAWT configuration to ensure that the rotor always faces the direction of the incoming wind.

5.2.3 Vertical axis wind turbines (VAWT)

There exist several rotors with a vertical axis of rotation, each with their own distinct features. The rotor depicted in Figure 5-2 is referred to as a Darrieus-rotor, and was one of the first promising designs to utilize turbine blades in a vertical configuration for the generation of electricity.

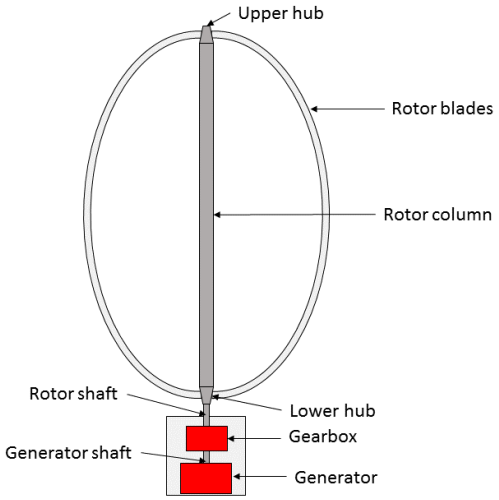

Figure 5-2: Simplified illustration of a VAWT, inspired from [6]

As may be observed, a VAWT comprises of similar components as described for the HAWT, but their configuration is completely different due to the different axis of rotation. Mechanical work generated by the rotor is transferred to a vertical oriented rotor column, which transfer the work to the generator located at the base of the turbine. The design usually consist of either two or three blades that is curved into an approximate *troposkien* shape in order to minimize bending stresses during a rotation. The blades are rigidly connected to an upper and lower hub in a symmetrical configuration around the rotor column [6]. Other design of VAWT includes the H-rotor and the Savonius turbine, as illustrated in Figure 5-3.

The H-rotor is based on the Darrieus-rotor, but the *troposkien* shaped is replaced with straight vertical blades attach to the rotor column by struts. This simplifies the fabrication of the blades, but leads a higher aerodynamic drag due to the presence of the struts [20].

A Savonius turbine utilizes drag force to drive a rotor, whereas the two aforementioned turbines utilizes lift force to drive a rotor. The design normally features two or three scoops that, due to the curvature, experience less drag moving against the wind compared to movement with the wind. The Savonius turbine is however not suitable electricity generation due to a relatively low power coefficient. All modern wind turbines therefore uses lift driven rotors [20].

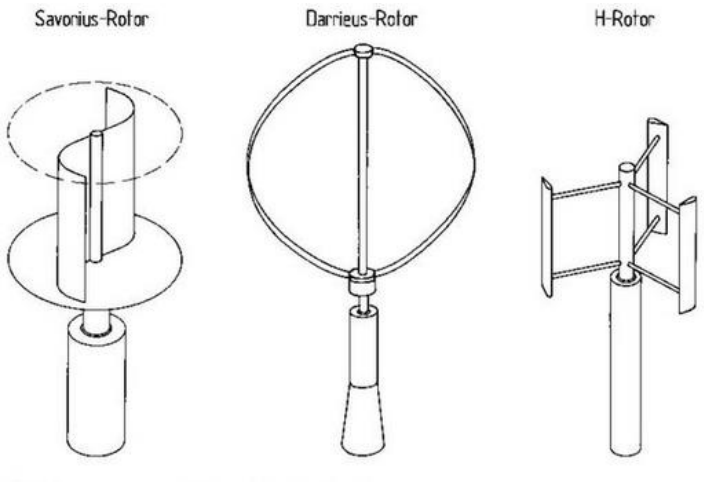

Figure 5-3: Three primary design of VAWT, retrieved from [20]

5.2.3.1 Aerodynamics of vertical axis wind turbines

In order to utilize the lift force to drive the rotor, the rotor blades is shaped like an airfoil. Figure 5-4 depicts a cross-sectional view of such a geometry, where applied velocities and resultant aerodynamic forces are also presented.

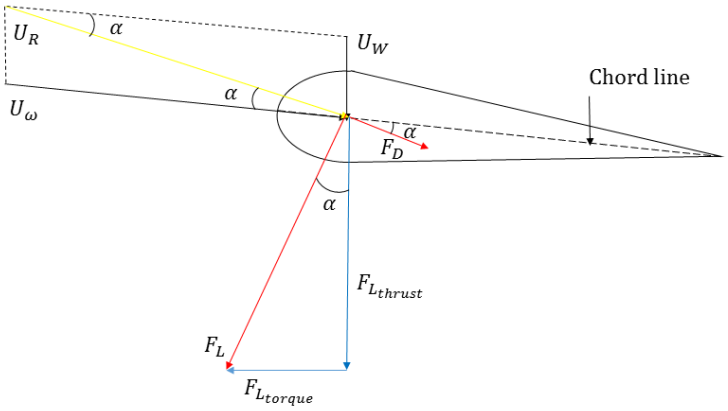

Figure 5-4: Cross-sectional view of airfoil with velocity vectors and resulting aerodynamic forces

$\overrightarrow{U_W}$ is the undisturbed free airstream velocity vector and $\overrightarrow{U_\omega}$ is the tangential velocity vector of the advancing rotor blades. The resultant velocity vector $(\overrightarrow{U_R})$ is obtain by taking the vectorial sum of $\overrightarrow{U_W}$ and $\overrightarrow{U_\omega}$ as follow:

$$\overrightarrow{U_R} = \overrightarrow{U_W} + \overrightarrow{U_\omega} \qquad \textit{Eq. 5-10}$$

The angle of attack (α) is given as the angle between the resultant velocity and the airfoil chord line, ref. Figure 5-4. As the peripheral velocity of the airfoil will always be in-line with the airfoils chord line, the angle of attack is also represented as the angle between the peripheral velocity and the resultant velocity.

The aerodynamic force can be decomposed into a drag force (F_D) and a lift force (F_L), as discussed in section 5.1.3. These force components may be separated further into a torque force working in the plane of rotation and a thrust force working perpendicular to the plane of rotation. The total torque and thrust force may be obtained by superposing the decomposed components in the appropriate direction, i.e.:

$$F_{torque} = F_L \cdot \sin(\alpha) - F_D \cdot \cos(\alpha) \qquad \textit{Eq. 5-11}$$

$$F_{thrust} = F_L \cdot \cos(\alpha) + F_D \cdot \sin(\alpha) \qquad \textit{Eq. 5-12}$$

The torque drives the turbine. As may be observed from Eq. 5-11, the lift force increases the torque while the drag force breaks the torque. Modern airfoils therefore features an extremely favorable lift-to-drag ratio [20] to gain a higher torque.

As the blade advances and changes its orbital position (θ), the orientation of the peripheral velocity is altered as it always follows the chord line. This implies that the angle of attack (α) will continuously change during one rotation. The angle of attack also changes direction from the upwind region $(\theta = 0° \rightarrow \theta = 180°)$ to the downwind region $(\theta = 180° \rightarrow \theta = 360°)$, which alters the direction of the lift force. The rotor will therefore generate a maximum torque at two points during one rotation, leading to the variation in torque with θ illustrated in Figure 5-5. It may also be observed that there exist short sections with negative torque, but the mean generated torque from a single blade during one rotation is still positive [20].

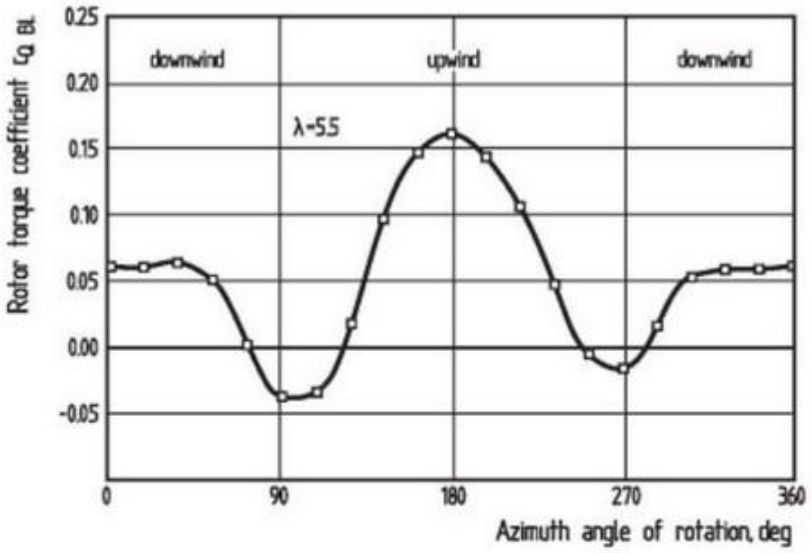

Figure 5-5: Variation of torque for a single rotor blade during one rotation in a VAWT, retrieved as Fig. 6.64 in [20]

The variation in torque during one rotation makes the VAWT prone to fatigue issues. However, modern VAWT designs have alleviated this problem by configuring the turbine to gives a smoother torque profile during one rotation.

5.3 Stability

Stability of a floating structure encompasses its up-righting properties when brought out of equilibrium by a disturbance in the form of a force and/or moment from environmental loads [22]. Figure 5-6 illustrates a cross sectional view of a barge in an inclined position, which will be used to derive important features regarding static stability. Note that the obtained relations is transferable to a Spar buoy. The notations used in Figure 5-6 is explained in Table 5-1.

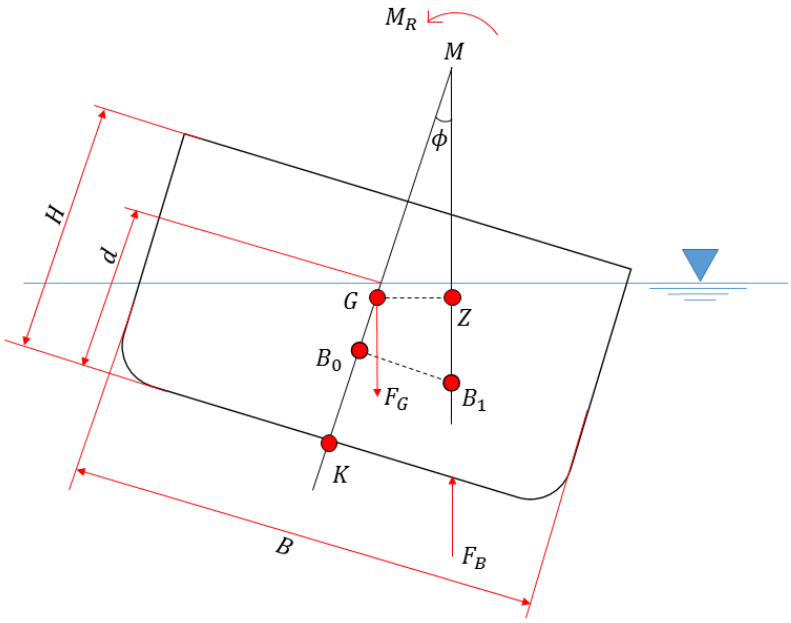

Figure 5-6: Cross sectional view of inclined barge for explanation of static stability, inspired from [23]

Table 5-1: Explanation of notations used in Figure 5-6

Notation	Explanation
M	Metacenter
G	Center of gravity
B_0	Center of buoyancy in equilibrium position
B_1	Center of buoyancy in inclined position
K	Keel
Z	Projection of G onto a vertical line through B_1
H	Height of barge
d	Draft
B	Width of barge
F_B	Buoyancy force
F_G	Gravity force
M_R	Up-righting moment

As the barge is in its initial horizontal position, the center of buoyancy (CoB) and center of gravity (CoG) is aligned on a vertical line. The buoyancy force (F_B), given as the weight of displaced water by the vessel, will be equal and act in the opposite direction of the gravity force (F_G) according to Archimedes' principle. The vessel is therefore in static equilibrium. Forces from wind, waves and currents gives rise to an inclination moment, which will tilt the vessel.

The inclination moment is given as:

$$M_I = F_I \cdot a \cdot \cos(\phi) \;\; ; \;\; where \qquad \textit{Eq. 5-13}$$

$$F_I = \text{inclination force arising from wind, waves and current}$$

$$a = \text{moment arm of inclination force}$$

$$\phi = \text{inclination angle}$$

The $\cos(\phi)$ term is needed to reduce the moment-arm as the inclination angle increases.

The center of buoyancy will be relocated in the inclined position, as the center of buoyancy will always be located in the center of the submerged volume [23]. The intersection between two vertical lines going through the center of buoyancy in the equilibrium position and the inclined position is defined as the metacenter. Furthermore, as the gravity force and buoyancy force does no longer act in the same vertical line, a up righting moment will be generated from the buoyancy force with a moment arm equal to the horizontal distance from G to Z. From Figure 5-6, it can be realized that the up righting moment is given as:

$$M_R = F_B \cdot \overline{GZ} = \nabla \rho g \cdot \overline{GM} \cdot \sin(\phi) \qquad \textit{Eq. 5-14}$$

$\overline{GM}$, the metacenter height, is the vertical distance between center of gravity and the metacenter, and ∇ is the submerged volume.

As the buoyancy force will always be positive, the metacenter height $(\overline{GM})$ is the governing parameter that determines the properties of the righting moment, and thus the stability. The following may be stated [23]:

- If $\overline{GM} > 0 \rightarrow M_R > 0$, the vessel will move to the initial position if the inclining moment is taken away, and initial stability is obtained
- If $\overline{GM} = 0 \rightarrow M_R = 0$, the vessel will not move to the initial position when the inclining moment is taken away, the barge is in a state of indifferent equilibrium.
- If $\overline{GM} < 0 \rightarrow M_R < 0$, the vessel will continue to incline even when the inclination moment is taken away. The vessel may find a new stable position at another inclined angle, but will not go back to its original position.

From the geometry presented in Figure 5-6, it may be realized that the metacenter height is given as:

$$\overline{GM} = \overline{KB} + \overline{BM} - \overline{KG} \qquad \textit{Eq. 5-15}$$

In case of a Spar buoy featuring different sections, the distance from keel to center of buoyancy $(\overline{KB})$ has to be derived based on the submerged volume and center of buoyancy of each individual section in the following manner:

$$\overline{KB} = \frac{\sum_{i=1}^{N} \nabla_i \cdot z_i}{\sum_{i=1}^{N} \nabla_i} \;\; ; \;\; where \qquad \textit{Eq. 5-16}$$

$$z_i = \text{vertical distance from keel to CoB of individual section}$$

$\overline{BM}$ is the distance between the center of buoyancy and metacenter (often referred to as the metacenter radius), and is given as the area moment of inertia in the water plane divided by the submerged volume [23]:

$$\overline{BM} = \frac{I}{\nabla} \qquad \textit{Eq. 5-17}$$

When establishing the distance between the keel and center of gravity ($\overline{KG}$), the CoG may alter its position depending on how the vessel is loaded. To calculate the vertical position of the CoG, the following formula apply:

$$CoG_{vertical} = \frac{m_{initial} \cdot z_{initial} + \sum m_{added} \cdot x_{added}}{m_{initial} + \sum m_{added}} \;\; ; \;\; where \qquad \textit{Eq. 5-18}$$

$$m_{initial} = \text{initial (i. e. empty vessel) mass}$$

$$z_{initial} = \text{inital (i. e. empty vessel) vertical position of the CoG}$$

$$m_{added} = \text{mass of individual added objects}$$

$$z_{added} = \text{vertical position of CoG of the individual added objects}$$

5.4 Waves

Ocean waves are characterized by irregularities and randomness regarding shape, length, height and velocity of propagation [19]. Such a sea state may be described by a random wave model, which sums several individual wave components featuring varying amplitudes, frequencies and directions. There are several wave theories used to describe a single wave component, including linear wave theory, stokes wave theory, stream function theory, cnoidal wave theory and solitary wave theory [24]. Linear wave theory, often referred to as Airy theory, is the simplest wave model. It describes regular waves expressed by a sine function, which is a result from linearizing the boundary conditions when solve the Laplace equation [23]. It should be noted that linear wave theory only provides wave kinematics from the SWL ($z = 0$) to the sea bottom ($z = -d_0$), and information above the SWL needs to be estimated by mathematical models, e.g. constant stretching or Wheeler stretching.

The simplest random wave model to generate an irregular sea state is the linear long-crested model, which sums numerous sinusoidal wave components described by the Airy wave theory.

The linear long-crested model is given as [19]:

$$\xi(t) = \sum_{i=1}^{N} A_i \cdot \sin(\omega_i t - k_i x + \varepsilon_i) \;\; ; \;\; where \qquad \textit{Eq. 5-19}$$

$$\xi(t) = \text{free surface elevation}$$

$$A_i = \text{wave amplitude of i}^{\text{th}}\text{ component}$$

$$\omega_i = \text{wave angular frequency of i}^{\text{th}}\text{ component}$$

$$k_i = \text{wave number of i}^{\text{th}}\text{ component}$$

$$\varepsilon_i = \text{phase angle of i}^{\text{th}}\text{ component}$$

It is often reasonable to assume that a Gaussian process with zero mean can describe the free surface elevation presented in Eq. 5-19. The individual wave crests will then follow a Rayleigh distribution as long as the process is relatively narrow-banded [25], and the random wave amplitudes may be expressed by a wave spectrum in the following manner [19]:

$$A_i^2 = 2 \cdot S_\xi(\omega_i) \cdot \Delta\omega_i \ ; \ \text{where} \qquad \textit{Eq. 5-20}$$

$$S_\xi(\omega_i) = \text{wave spectrum}$$

$$\Delta\omega_i = \omega_i - \omega_{i+1} = \text{difference between sucsessive frequencies}$$

Further details about wave spectrums are discussed in section 5.4.2.1. The process of generating time dependent regular waves, which are summed to form an irregular sea state, is illustrated in Figure 5-7.

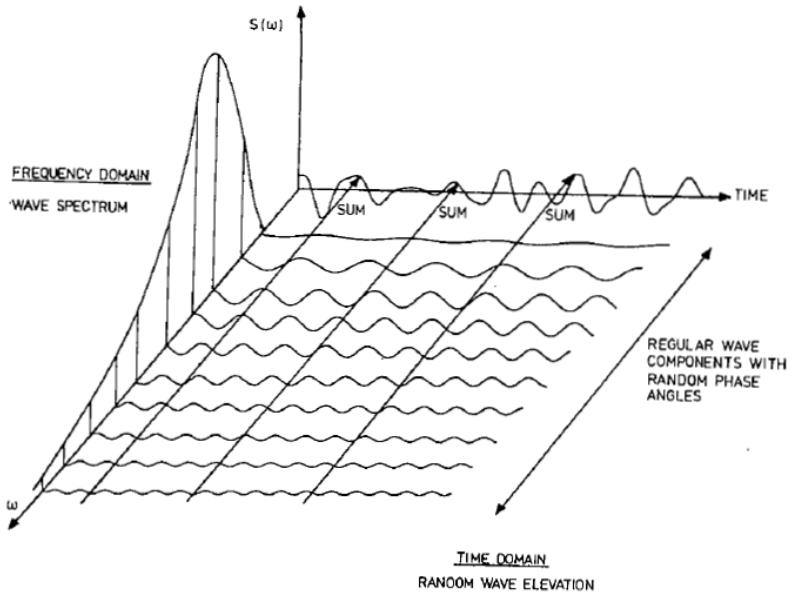

Figure 5-7: Illustration of the relation between a frequency domain and time domain representation of waves, retrieved from [26]

5.4.1 Linear wave theory

As indicated in the linear long-crested wave model, the surface elevation process from linear wave theory is described through the following formula [23]:

$$\xi(t) = A \cdot \sin(\omega t - kx) \qquad \textit{Eq. 5-21}$$

A set of equation describing the horizontal and vertical velocities and accelerations may be derived from the potential function associated with the linear wave model. Assuming deep-water waves, these equations are given as [23]:

$$u = \text{horizontal velocity} = A \cdot \frac{kg}{\omega} \cdot e^{kz} \cdot \sin(\omega t - kx) \quad \textit{Eq. 5-22}$$

$$\dot{u} = \text{horizontal acceleration} = A \cdot kg \cdot e^{kz} \cdot \cos(\omega t - kx) \quad \textit{Eq. 5-23}$$

$$v = \text{vertical velocity} = A \cdot \frac{kg}{\omega} \cdot \sin(\omega t - kx) \quad \textit{Eq. 5-24}$$

$$\dot{v} = \text{vertical acceleration} = -A \cdot kg \cdot e^{kz} \cdot \sin(\omega t - kx) \quad \textit{Eq. 5-25}$$

The wave number (k) is expressed as [23]:

$$k = \frac{2\pi}{\lambda} \quad \textit{Eq. 5-26}$$

The wavelength may be related to the wave period by the dispersion relation, which for deep-water waves gives:

$$\lambda = 1.56T^2 \quad \textit{Eq. 5-27}$$

5.4.2 Statistical description of waves

5.4.2.1 Short term wave condition

Short-term wave conditions assumes a stationary sea elevation process for a duration of 20 minutes up to 6 hours [19], which implies that the sea state may be characterized by a significant wave height and spectral peak period. The significant wave height (H_s) is defined as the average wave height of highest 1/3 waves in the period evaluated, and is mathematically given as [19]:

$$H_s = 4 \cdot \sigma_\xi^2 \;\; ; \;\; where \quad \textit{Eq. 5-28}$$

$$\sigma_\xi^2 = \text{variance of surface elevation process}$$

Irregular sea states in stationary conditions can be described by a wave spectrum. A wave spectrum describes the distribution of energy in a sea state over different frequencies [23], defined as:

$$S_\xi(\omega_n) = \sum_{\omega_n=1}^{\omega_n+\Delta\omega} \frac{\xi^2(\omega_n)}{2 \cdot \Delta\omega} \quad \textit{Eq. 5-29}$$

As the frequency band approaches zero ($\Delta\omega \to 0$), the wave spectrum converges towards a continuous curve.

An applicable wave spectrum for the area of interest is not always available and analytical expressions are therefore often used in practice. There are several suggested forms of such analytical wave spectra,

where their applicability depend upon the geographical area, local bathymetry and severity of the sea state [19]. Two wave spectra, which are frequency applied to describe wind seas [19], includes the Pierson Moskowitz spectrum and JONSWAP spectrum.

The Pierson-Moskowitz spectrum assumes a fully developed sea state, and is given as [19]:

$$S_{PM}(\omega) = \frac{5}{16} \cdot H_s^2 \cdot \omega_p^4 \cdot \omega^{-5} \cdot e^{-\frac{5}{4}\left(\frac{\omega}{\omega_p}\right)^{-4}} \;\; ; \;\; where \qquad \textit{Eq. 5-30}$$

$$\omega_p = \text{angular spectral peak frequency} = \frac{2\pi}{T_p}$$

The JONSWAP spectrum does not assume a fully developed sea state, but rather describes a continuous developing sea state through non-linearity and wave to wave interactions. This is achieved by implementing an additional factor to the Pierson Moskowitz spectrum, a peak enhancement factor, making the spectrum more pronounced. The JONSWAP spectrum is given by [19]:

$$S_J(\omega) = A_\gamma \cdot S_{PM}(\omega)\gamma^{e^{-\frac{1}{2}\left(\frac{\omega-\omega_p}{\sigma\cdot\omega_p}\right)^2}} \;\; ; \;\; where \qquad \textit{Eq. 5-31}$$

$$\gamma = \text{peak shape parameter}$$

$$\sigma = \text{spectral width parameter} = \begin{matrix} \sigma_a \text{ for } \omega \leq \omega_p \\ \sigma_b \text{ for } \omega > \omega_p \end{matrix}$$

$$A_\gamma = 1 - 0.287 \cdot \ln(\gamma)$$

Average values for the JONSWAP experimental data includes [19]: $\gamma = 3.3$, $\sigma_a = 0.07$, $\sigma_b = 0.09$. Also, note that if $\gamma = 1$, the JONSWAP spectrum reduces to the Pierson Moskowitz spectrum.

5.4.2.2 Long term wave conditions

Long-term description of the wave environment implies modelling the sea elevation process in terms of months or years. To do this, the joint frequency of significant wave height and spectral peak periods needs to be evaluated [26], which may be done in terms of generic distributions or scatter diagrams for the governing sea state parameters.

Examples where a long-term wave distribution is of importance includes [26]:

- establishing the design sea state, i.e. 50 or 100 year wave
- evaluating the percentage of time an marine operation may be performed
- obtaining the long term probability responses of offshore vessels

5.5 Vessel response

An offshore floating vessel is a system containing a floater, mooring lines and potentially risers that responds dynamically to time varying loads in a generally complex manner [27]. The term response generally covers the induced motions of the vessel and the induced loads on the vessel. The following section gives a presentation of the imposed wave loads on an offshore floating structure, before the dynamic motions will be discussed with focus on the equation of motion. However, before going into detail about the dynamic responses, some clarification about the rigid body motions and an associated coordinate system is needed.

5.5.1 Rigid body motions

The dynamic motions for a floating vessel is generally decomposed into six degrees of freedom (DOF), including three translational motions and three angular motions. The translational motions includes surge, sway and heave, while the three angular motions are termed roll, pitch and yaw. The orientation of the rigid body motions in a Cartesian coordinate system is illustrated in Figure 5-8 for a VAWT placed on a Spar buoy. The surge axis is often set to coincide with the mean wind direction in offshore wind turbine applications [4].

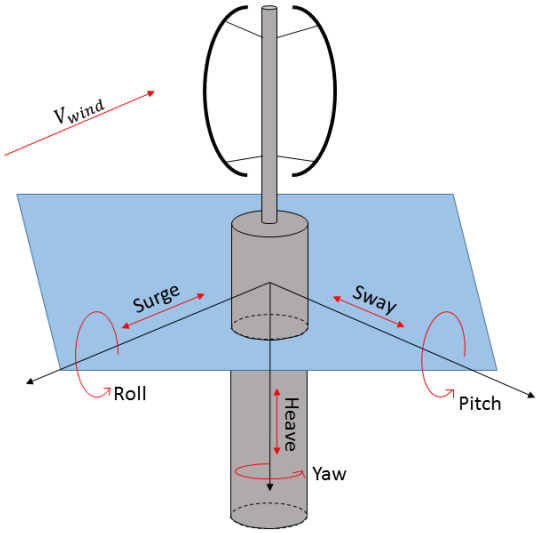

Figure 5-8: Illustration of the six DOF of a VAWT on a Spar buoy foundation

It should be noted that the Spar's symmetry around a vertical center axis makes the surge and sway motions equal. The same applies for pitch and roll. These are therefore often used interchangeably in the presented work. Furthermore, it is common practice in ocean engineering and naval architecture to express the translational motion in surge, sway and heave as η_1, η_2 and η_3, and the rotational motions in roll, pitch and yaw are as η_4, η_5 and η_6. Similar relations applies for the hydrodynamic forces in the respective DOFs.

The motions of floating structures may further be divided into wave-frequency (WF) motion, high frequency (HF) motion and low frequency (LF) motion. WF motions are excited linearly with waves in the frequency range of significant wave energy, and causes the largest wave loads on the floating structures [26] [19]. Exited linearly implies that the wave induced motions and loads are linearly proportional to the wave amplitude. These motions may be described through linear theory, which will be described in the following. A short section about the HF and LF motions are presented near the end this section.

5.5.2 Linear hydrodynamic forces

A consequence of the linear assumption is that the response in an irregular sea state may be obtained by superposing the responses in incident regular waves featuring different amplitudes, wavelengths and propagation. It is therefore sufficient to analyze a structure in incident regular waves when assessing linear force components. The hydrodynamic loads in regular waves are often divided into two sub-categories [26]:

1) Forces and moments on the vessel arising from regular waves when the vessel is fully restrained. These forces are referred to as wave excitation loads, and contains the Froude-Krylov force and diffraction effects.
2) Forces and moments on the vessel arising from forced oscillation of the structure in the different degrees of freedom. There are no excitation waves, but the structure oscillates with the same frequency as the excitation waves. These loads are identified as added mass, damping and hydrostatic stiffness.

Due to the linearity, the forces arising in 1) and 2) can be added together to form a total hydrodynamic force in an incident regular wave.

5.5.2.1 Wave excitation forces

The Froude-Krylov force arises as the accelerated motion of the fluid far away from the restrained structure generates a pressure gradient, which in turn produces an additional force on the body [28].

The diffraction force arises as the presence of the structure disturbs the incident waves. An outwards reflection wave is generated when the incident waves impinges on the body. The wave fronts is also bent around on vessel's sheltered side, generating so-called diffracted waves. The disturbance of the radiation waves and diffraction waves changes the pressure field around the body, which generates the diffraction force [28]. The flow around a cylinder in the diffraction flow regime is unseparated, and the diffraction forces may be analyzed by potential theory in most situations [28].

5.5.2.2 Hydromechanical loads

The added mass, damping and hydrostatic stiffness load terms are commonly referred to as hydromechanical loads [22]. The forced oscillation of a floating structure generates outgoing waves that results in an oscillating pressure field on the body surface. The added mass and damping forces/moments may be obtained by integrating this pressure field over the wetted surface, which can formally be expressed in the i^{th} degree of freedom as [26]:

$$F_i = A_{ij} \cdot \frac{d^2}{dt}\eta_i + B_{ij} \cdot \frac{d}{dt}\eta_i \;\; ; \;\; where \qquad \textit{Eq. 5-32}$$

$$i = 1,2,\dots,6$$

The damping force is proportional to the velocity of the forced oscillations, and may be understood as the amount of energy that is withdrawn from the forced oscillations by the outgoing waves [22]. The added mass force is proportional to the acceleration of the forced oscillations, and may be understood as the mass of the fluid around a body that is accelerated with the movement of the body due to the

action of pressure [28]. This does however not mean that added mass is a finite amount of fluid that oscillates rigidly with the body. Rather, the influenced fluid will oscillate with different fluid particle amplitudes that decays with distance to the body, eventually becoming negligible [26]. A_{ij} and B_{ij} are the added mass and damping coefficients. Added mass and damping forces can arise in one direction due to motion in a different direction, and there is thus a total of 36 added mass and damping coefficients. These are generally presented in 6x6 matrices as:

$$\boldsymbol{A} = \begin{bmatrix} A_{11} & A_{12} & A_{13} & A_{14} & A_{15} & A_{16} \\ A_{21} & A_{22} & A_{23} & A_{24} & A_{25} & A_{26} \\ A_{31} & A_{32} & A_{33} & A_{34} & A_{35} & A_{36} \\ A_{41} & A_{42} & A_{43} & A_{44} & A_{45} & A_{46} \\ A_{51} & A_{52} & A_{53} & A_{54} & A_{55} & A_{56} \\ A_{61} & A_{62} & A_{63} & A_{64} & A_{65} & A_{66} \end{bmatrix} \quad \textit{Eq. 5-33}$$

$$\boldsymbol{B} = \begin{bmatrix} B_{11} & B_{12} & B_{13} & B_{14} & B_{15} & B_{16} \\ B_{21} & B_{22} & B_{23} & B_{24} & B_{25} & B_{26} \\ B_{31} & B_{32} & B_{33} & B_{34} & B_{35} & B_{36} \\ B_{41} & B_{42} & B_{43} & B_{44} & B_{45} & B_{46} \\ B_{51} & B_{52} & B_{53} & B_{54} & B_{55} & B_{56} \\ B_{61} & B_{62} & B_{63} & B_{64} & B_{65} & B_{66} \end{bmatrix} \quad \textit{Eq. 5-34}$$

The coefficients may be interpreted as the added mass or damping in the i^{th} direction due to a unit acceleration or unit velocity in the j^{th} direction. The added mass and damping coefficients generally depends on frequency of oscillations and the shape of the body [26].

It is often possible to simplify the added mass and damping matrices. The symmetrical shape of a Spar buoy around both the xz-plane and yz-plane makes several of the coefficients zero-valued [29], leading to the added mass and damping matrices observed below.

$$\boldsymbol{A} = \begin{bmatrix} A_{11} & 0 & 0 & 0 & A_{15} & 0 \\ 0 & A_{22} & 0 & A_{24} & 0 & 0 \\ 0 & 0 & A_{33} & 0 & 0 & 0 \\ 0 & A_{42} & 0 & A_{44} & 0 & 0 \\ A_{51} & 0 & 0 & 0 & A_{55} & 0 \\ 0 & 0 & 0 & 0 & 0 & 0 \end{bmatrix} \quad \textit{Eq. 5-35}$$

$$\boldsymbol{B} = \begin{bmatrix} B_{11} & 0 & 0 & 0 & B_{15} & 0 \\ 0 & B_{22} & 0 & B_{24} & 0 & 0 \\ 0 & 0 & B_{33} & 0 & 0 & 0 \\ 0 & B_{42} & 0 & B_{44} & 0 & 0 \\ B_{51} & 0 & 0 & 0 & B_{55} & 0 \\ 0 & 0 & 0 & 0 & 0 & 0 \end{bmatrix} \quad \textit{Eq. 5-36}$$

The Spar buoy's symmetries also makes the surge-surge elements, A_{11} and B_{11}, to be equal to the sway-sway elements, A_{22} and B_{22}. The same applies to the roll-roll elements, A_{44} and B_{44}, and the pitch-pitch elements, A_{55} and B_{55}. Furthermore, for a vessel with zero forwards speed situated in an environmental state without current, the added mass matrix and damping matrix are symmetric along its diagonal, i.e. $A_{ij} = A_{ji}$ and $B_{ij} = B_{ji}$ [26]. It is therefore sufficient to gain expression for seven added mass coefficients and damping coefficients for the floater studied in the presented work.

The restoring forces for a freely floating body arises due to hydrostatic and mass considerations. As for the added mass and damping force, the restoring force and moment in the i[th] DOF may be expressed as [26]:

$$F_i = C_{ij} \cdot \eta_i \;\; ; \;\; where \qquad \textit{Eq. 5-37}$$

$$C_{ij} = \text{restoring coefficients}$$

As may be observed, the restoring forces is proportional to the motion of the forced oscillations. The restoring coefficients may be expressed in a 6x6 hydrostatic stiffness matrix as [19]:

$$\boldsymbol{C} = \begin{bmatrix} 0 & 0 & 0 & 0 & 0 & 0 \\ 0 & 0 & 0 & 0 & 0 & 0 \\ 0 & 0 & \rho g S & \rho g S_2 & -\rho g S_1 & 0 \\ 0 & 0 & \rho g S_2 & \rho g (S_{22} + \nabla z_b) - M g z_g & -\rho g S_{12} & -\rho g \nabla x_b + M g x_g \\ 0 & 0 & -\rho g S_1 & -\rho g S_{12} & \rho g (S_{11} + \nabla z_b) - M g z_g & -\rho g \nabla y_b + M g y_g \\ 0 & 0 & 0 & -\rho g \nabla x_b + M g x_g & -\rho g \nabla y_b + M g y_g & 0 \end{bmatrix}; \qquad \textit{Eq. 5-38}$$

$$x_b, y_b, z_b = \text{position of CoB in x, y and z direction}$$

$$S = \text{water plane area}$$

$$S_i = \text{first moment of inertia of water plane}$$

$$S_{ij} = \text{second moment of inertia of water plane}$$

Static equilibrium requires the center of gravity and center of buoyancy to coincide on the same vertical line, implying that $x_b = x_g$ and $y_b = y_g$. As a consequence, $C_{46} = C_{64} = C_{56} = C_{65} = 0$. Furthermore, in the case of a symmetrical body with the coordinate system on a vertical line that intersects the center of gravity, $S_1 = S_2 = S_{12} = 0$, resulting in the following hydrostatic stiffness matrix for the studied geometry:

$$\boldsymbol{C} = \begin{bmatrix} 0 & 0 & 0 & 0 & 0 & 0 \\ 0 & 0 & 0 & 0 & 0 & 0 \\ 0 & 0 & \rho g S & 0 & 0 & 0 \\ 0 & 0 & 0 & \rho g (S_{22} + \nabla z_b) - M g z_g & 0 & 0 \\ 0 & 0 & 0 & 0 & \rho g (S_{11} + \nabla z_b) - M g z_g & 0 \\ 0 & 0 & 0 & 0 & 0 & 0 \end{bmatrix} \qquad \textit{Eq. 5-39}$$

5.5.2.3 Hydrodynamic classification of structures

All of the effects discussed above may be of significance when determining the wave induced loads on offshore structures. However, some load terms can often be neglected, and illustrations like the one depicted in Figure 5-9 is a useful tool for determining which loads effects are significant in the particular situation.

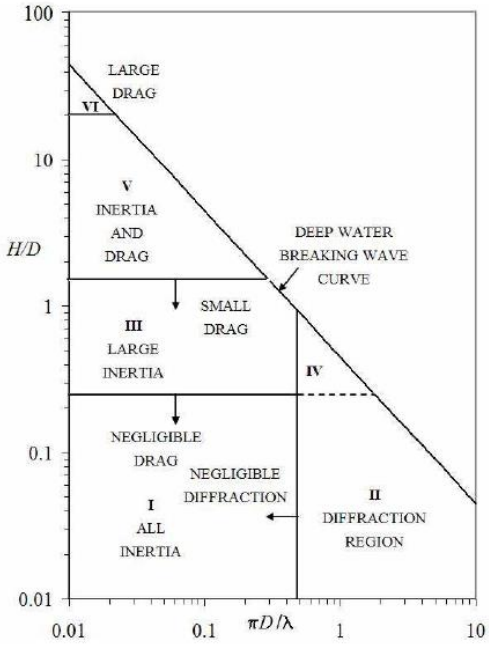

Figure 5-9: Different wave force regimes, retrieved from [19]

The parameters in Figure 5-9 are as follows:

$$D = \text{characteristic dimension}$$

$$\lambda = \text{wave length}$$

$$H = \text{wave height}$$

The importance of different hydrodynamic effects therefore depends on the wave environment studied. If the characteristic dimension is small compared to the wavelength, drag and inertia terms are most significant and diffraction is negligible as the wave are allowed to pass the structure relatively undisturbed. Such structures are often referred to as small volume or transparent structure (regime I, III, V, and VI in Figure 5-9).

As the characteristic dimension increases, waves are not allowed to pass the structure undisturbed, and differential forces increases in importance. These structures are referred to as large volume structures or hydrodynamically compact structures (regime II and IV in Figure 5-9).

5.5.2.4 Small volume structures

A structure can be characterized as a small volume structure when $\lambda > 5D$ [19]. Hydrodynamic forces are then calculated using the Morison's equation, which is a sum of the inertia force proportional to the acceleration and the drag force proportional to the square of the velocity.

The Morison's load formula in the normal direction for a fixed cylinder is given by [19]:

$$f_N(t) = \rho C_M A \cdot a + \frac{1}{2}\rho C_D \cdot D \cdot v_n \cdot |v_n| \;\; ; \;\; where \qquad \textit{Eq. 5-40}$$

$$A = \text{cross sectional area } [m^2]$$

$$a = \text{acceleration } [m/s^2]$$

$$D = \text{typical cross sectional dimension}$$

$$v_n = \text{velocity in normal direction from waves and current}$$

$$C_M, C_D = \text{hydrodynamic coefficients}$$

Note that the expression above is given as force per unit length, where the total hydrodynamic loads may be estimated by summing up the sectional forces along the length of the structure.

In case of a moving cylinder in waves and currents, the Morison's equation may be expressed through the relative velocity and acceleration formulation, which results in the following formulation [19]:

$$f_N(t) = \rho A a + \rho C_a A \cdot a_r + \frac{1}{2}\rho \cdot C_D D \cdot v_r \cdot |v_r| \;\; ; \;\; where \qquad \textit{Eq. 5-41}$$

$$v_r = v - \dot{r} = \text{velocity of fluid relative to structure}$$

$$a_r = a - \ddot{r} = \text{acceleration of fluid relative to structure}$$

Note that the use of the relative velocity is valid for $r/D > 1$, where r is the structure's displacement amplitude. If $r/D < 1$, the validity of the relative velocity formulation depends on the term:

$$V_R = v \cdot T_n/D \;\; ; \;\; where \qquad \textit{Eq. 5-42}$$

$$v = \frac{\pi H_s}{T_z} = \text{approximate particle velocity close to wave surface}$$

$$T_n = \text{period of structural oscillations}$$

$$D = \text{characteristic dimension}$$

The following applies [19]:

$V_R \geq 20$	Relative velocity is recommended
$10 \leq V_R < 20$	Relative velocity may lead to an over-estimation of the damping if displacement is less than one diameter
$V_R < 10$	Recommended to discard the relative velocity if the displacement is less than one diameter, and use the formula presented for a fixed cylinder.

It becomes prominent that the magnitude of the hydrodynamic forces is highly dependent upon the hydrodynamic coefficients (C_D, C_M). It is therefore of most importance to appoint appropriate hydrodynamic coefficient in order to obtain correct estimates of the imposed loadings. These coefficients are based on experiments and dependents upon the geometry, Reynolds number, Keulegan-Carpenter number and surface roughness [19].

5.5.2.5 Large volume structures

Structures are characterized as large volume structures if $D > \frac{\lambda}{6}$. These structures will significantly disturb the wave field, causing wave diffraction and wave radiation [26]. The most common numerical method for solving diffraction problems is the boundary element method (BEM), where the velocity potential in the fluid domain is represented by a distribution of sources over the mean wetted surface [19]. The potential flow problem may also be solved using the finite element method (FEM).

5.5.3 The equation of motion

The six rigid body motions presented in the introduction to this section may be written in a vector form as:

$$\vec{\eta}(t) = [\eta_1(t), \eta_2(t), \dots, \eta_6(t)]^T \qquad \textit{Eq. 5-43}$$

The equation of motion for a linear rigid body with respect to an earth-bound coordinate system follows from Newton's second law. The vector equations for the six motions about the center of gravity are thus given as [22]:

$$\vec{F} = \frac{d}{dt} \cdot \boldsymbol{M}\vec{\dot{\eta}} \qquad \textit{Eq. 5-44}$$

$\vec{F}$ is a time dependent vector containing all of the forces acting on the structure, while $\boldsymbol{M}$ is a 6x6 matrix representing the inertia properties of the system. Assuming that the system features linear characteristics, the force vector may be separated into the forces discussed in section 5.5.2, i.e. wave excitation loads and hydromechanical loads [22]. It is reminded that the added mass force is proportional to the body's acceleration, damping force is proportional to the body's velocity, and hydrostatic stiffness force is proportional to the body's motion. Collecting the opposing terms on the left hand side of equation Eq. 5-44, the linear equation of motion becomes:

$$[\boldsymbol{M} + \boldsymbol{A}] \cdot \ddot{\vec{\eta}} + \boldsymbol{B} \cdot \dot{\vec{\eta}} + [\boldsymbol{C} + \boldsymbol{K}]\vec{\eta} = \vec{X} \qquad \textit{Eq. 5-45}$$

$\boldsymbol{A}, \boldsymbol{B}, \boldsymbol{C}$ is the 6x6 matrices containing the added mass, damping and restoring coefficients, as presented in section 5.5.2.2. $\boldsymbol{K}$ is a 6x6 matrix containing information about the mooring stiffness, while $\vec{X}$ is a 6x1 vector containing the external wave excitation forces in each mode of motion. As may be observed, the added mass, damping and restoring loadings, along with contributions from the vessel's inertia properties and mooring system, opposes the wave excitation forces.

Table 5-2 shows the type of response in the six DOF for the most common type of floating foundations used for offshore wind turbine concepts. "C" refers to compliant motion with displacements in the order of meters [4], while "R" refers to restrained motion with displacements in the order of centimeters.

Table 5-2: Typical floating support structures used for OWT with their respective motions characteristics in the six DOF. C=compliant and R=restrained, reproduced from [4]

Type	Surge	Sway	Heave	Roll	Pitch	Yaw
Deep Draught Floaters (DDFs)	C	C	C	C	C	C
Semi submersibles	C	C	C	C	C	C
Tension Leg Platforms (TLP)	C	C	R	R	R	C

The Deep Draught Floaters represent classic, truss & cell Spar, deep draught semis and buoys, and is thus the class that is evaluated in the presented works. The motion in all DOF is therefore of a compliant nature and expected to be several meters.

The equation of motion can generally be solved in either a frequency domain or a time domain.

5.5.3.1 Frequency domain analysis

The concept of generating an irregular sea state from regular wave components was illustrated in section 5.4. If linearity is assumed, the vessel response, i.e. displacement, velocity and acceleration, is linearly proportional to the incident wave amplitudes. Similarly to the irregular wave generation, the responses in an irregular sea state may be obtained superpose the response gained from different incident regular waves with varying amplitudes, phases and propagation. This is the principle of the frequency domain analysis. It therefore assumes linearity, and only linear wave responses may be studied in a frequency domain analysis. It is however a very computational effective method, and takes less time to perform than a time domain analysis [19]. The equation of motion presented above is in a frequency domain formulation, while one method of solving the equation of motion in the time domain is presented in the next section.

5.5.3.2 Time domain analysis

The time domain analysis solves the equation of motion with respect to time. This is necessary when studying a system that possesses non-linear elements, as the superposition principle of the frequency domain analysis is no longer valid. Examples of non-linear elements includes non-linear viscous damping, forces and moments due to currents and higher order load terms associated with high frequency motions and low frequency motions [22]. A time domain analysis offers a higher insight to the system's response, but is also more computational demanding than the frequency domain analysis. There are several methods of solving the equation of motion in time domain, one of which is the Cummins equation, presented in Eq. 5-46. For the full derivation of this equation, reference is made to [22].

$$(M + A) \cdot \ddot{\eta}_i + \int_0^{\infty} B(\tau) \cdot \dot{\eta}_i (t - \tau) \cdot d\tau + C \cdot \eta_i = X_i(t) \;\; ; \;\; where \qquad \textit{Eq. 5-46}$$

$$t, \tau = \text{time}$$

$$B(\tau) = \text{retardation function derived from damping}$$

$$X_i = \text{external forces in i}^{\text{th}} \text{ DOF at time t}$$

5.5.4 Response in irregular waves

As already indicated, the response in irregular waves may be obtained by analyzing the response in regular waves comprising of different amplitudes, phases and possibly direction, and summing the contributions to form an irregular response time series [26]. This process is illustrated in Figure 5-10 for the heave response of an offshore structure. The left side of the figure presents the generation of the irregular sea state as described in section 5.4, while the right side of the figure represents the resultant heave motions of the vessel. As may be observed, each of the regular wave components is transferred to a vessel response by a frequency dependent amplitude characteristic function along with the associated phase characteristic. These characteristics are known as the transfer function, or the response amplitude operator. The response characteristics are described through a frequency dependent response spectrum, which is given as [22]:

$$S_\eta(\omega) = \left|\frac{\eta_i}{A}(\omega)\right|^2 \cdot S_\xi(\omega) \;;\; where \qquad \textit{Eq. 5-47}$$

$$S_\eta = \text{response spectrum}$$

$$\left|\frac{\eta_i}{A}(\omega)\right| = \text{transfer function}$$

$$S_\xi(\omega) = \text{wave spectrum}$$

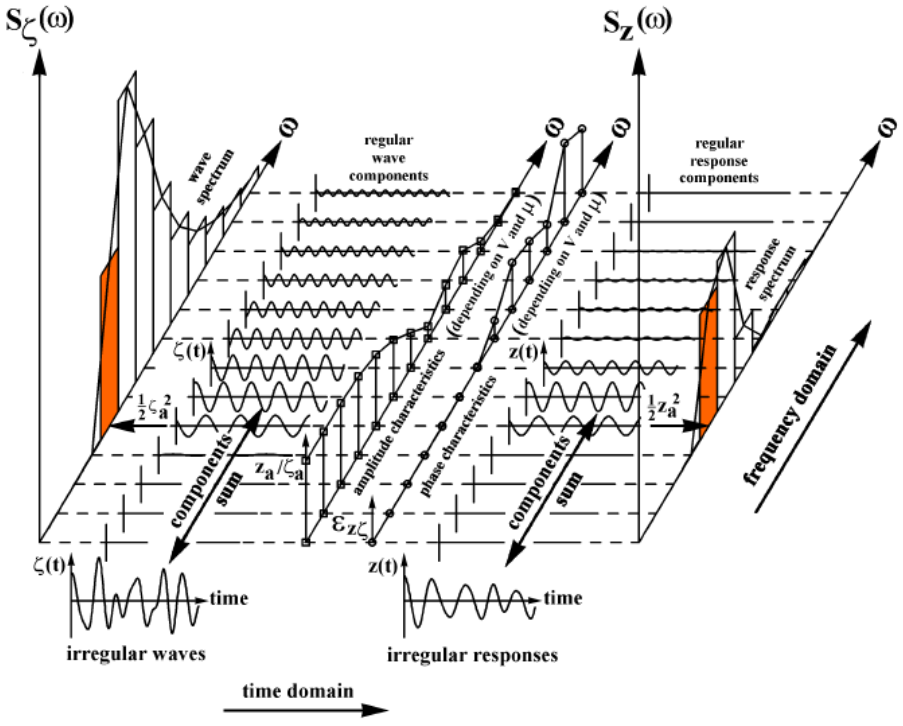

Figure 5-10: Principle of obtaining waves induced responses, retrieved from [22]

5.5.4.1 Response amplitude operators

As indicated in the previous section, the response of an offshore floating system is described through the response amplitude operator (RAO) and an associated wave spectrum that represents the particular site. As a response may generally be a motion or a load, there exists load RAOs and displacement RAOs. These are given as the ratio of either displacement or force, over the wave amplitude of the studied wave component, i.e.:

$$RAO_{Displacement} = \frac{\eta_{i,a}}{A_j} \;\; ; \;\; where \qquad \textit{Eq. 5-48}$$

$$\eta_i = \text{displacement amplitude in i}^{\text{th}}\text{ DOF}$$

$$A_j = \text{amplitude of j}^{\text{th}}\text{ wave component}$$

$$RAO_{Load} = \frac{F_{i,a}}{A_j} \;\; ; \;\; where \qquad \textit{Eq. 5-49}$$

$$F_i = \text{Load amplitude in the i}^{\text{th}}\text{ direction}$$

The response amplitude operators are derived from the equation of motion for the particular system. The principal will be presented in short terms for the displacement RAO in heave for a circular cylinder. For the full derivation, reference is made to [22].

The heave response due to regular wave excitations is given as:

$$\eta_3 = \eta_{3,a} \cdot \cos(\omega t + \varepsilon_{3\xi}) \qquad \textit{Eq. 5-50}$$

Inserting this into the equation of motion, and relating the external wave excitation forces to the added mass, damping and restoring coefficients through the reduced wave elevation process, results in the following displacement RAO in heave [22]:

$$\frac{\eta_{3,a}}{A} = e^{-kd}\sqrt{\frac{(c_{33} - a_{33}\omega^2)^2 + (b_{33}\omega)^2}{(c_{33} - (m_{33} + a_{33}) \cdot \omega^2)^2 + (b_{33}\omega)^2}} \;\; ; \;\; where \qquad \textit{Eq. 5-51}$$

$$A = \text{wave amplitude}$$

$$k = \text{wave number}$$

$$d = \text{draft of cylinder}$$

$$\omega = \text{angular frequency of wave component}$$

In addition, the associated phase shift is given as [22]:

$$\varepsilon_{3\xi} = \tan^{-1}\left(\frac{-m \cdot b_{33}\omega^3}{(c_{33} - a_{33} \cdot \omega^2) \cdot (c - (m_{33} + a_{33}) \cdot \omega^2) + (b_{33} \cdot \omega)^2}\right) \;\; ; \;\; \in \;\; [0\,;2\pi] \qquad \textit{Eq. 5-52}$$

The motional behavior of this heaving cylinder may be divided into three frequency areas [22].

1. The low frequency area features high wave periods large wavelengths. The structure will then tend to float on top of the waves, leading to a 1.0 displacement RAO, i.e. the heave amplitude is equal to the wave amplitude.
2. The natural frequency area features wave frequencies that approaches the natural frequency of the vessel, yielding resonance motions. The resonance motions are dominated by the damping term in the system. Depending on the amount of damping, these motions can be relative severe and will generally impose displacement amplitudes > 1.0. A phase shift of $-\pi$ also occurs in this frequency area
3. The high frequency area features motions that are dominated by the mass term in the system. The waves does not impose large motions on the vessel, as there exist several crest and troughs in the length of the vessel in the propagation direction. The displacement amplitudes will therefore be small and will approach zero for high enough frequencies. A second phase shift also occurs in this frequency range.

5.5.5 Higher order load terms

As previously stated, offshore floating structures may experience high frequency (HF) and low frequency (LF) motions. Unlike the linear wave response, HF and LF motions occurs due to higher order, nonlinear, wave load terms. However, the higher order load terms are normally small, and their contributions are therefore most important near the natural period of the system [19], i.e. at resonance.

High frequency resonance motions, also known as ringing and springing, may occur for tension leg platforms (TLPs) and for slender gravity based structures (GBS) [19]. These are therefore not of relevance for the present problem description and will not be considered further. LF-motions may however cause resonance motions in surge, sway and yaw for a moored system [26]. These responses are caused by slowly varying wave, winds and current loads [19], and are therefore often termed slow-drift motions. The wave induced drift force consists of two contributions, one from inviscid effects and one from viscous effects. The inviscid force is proportional to the square of the wave amplitude, making it a second order wave force. In an irregular sea state, this force is given as [19]:

$$F_{WA}^{(2-)} = \mathrm{Re}\sum_{i,j}^{N} a_i a_j H^{(2-)} \cdot (\omega_i,\, \omega_j) \cdot e^{i(\omega_i - \omega_j)t} \;\; ; \;\; where \qquad \textit{Eq. 5-53}$$

$$a_i, a_j = \text{individual wave components}$$

$$H^{(2-)} = \text{quadratic drag function (QTF)}$$

$$\omega_i - \omega_j = \text{difference frequencies}$$

Computer tools exist for calculating the quadratic drag functions. These are second-order problems requiring discretization of the free surface in addition to the vessel's surface [19].

As discussed in the previous section, most damping in wave frequency response is due to the radiation of free surface waves. However, as the motion frequencies becomes low the structure radiates less wave energy, and radiation damping is therefore normally negligible for slow drift motions [19]. The damping in these problems thus comprises from wave drift damping, viscous damping and damping due to variation of the wind loads with the velocity of the structure, which are all non-linear damping terms.

5.5.6 Natural period

An important aspect for any floating system is to avoid large resonance motions. As stated in the introduction to this section, the largest response on offshore structures occurs at the same frequencies as the waves, i.e. wave frequency response. It is therefore normal to design offshore structures and their moorings to have natural periods well outside the periods featuring substantial wave energy [19], which is often in the range of 5 to 25 seconds [4].

The natural period for a floating offshore vessel is given as [30]:

$$T_j = 2\pi\sqrt{\frac{M_{jj} + A_{jj}}{C_{jj} + K_{jj}}} \qquad \textit{Eq. 5-54}$$

Where j is the DOF in question and $M_{jj}, A_{jj}, C_{jj}\ and\ K_{jj}$ are elements of the mass, added mass, hydrostatic stiffness and mooring stiffness matrices presented throughout this chapter.

The uncoupled natural period, i.e. no mooring lines attach, in surge is given by:

$$T_1 = 2\pi\sqrt{\frac{M_{11} + A_{11}}{C_{11}}} \qquad \textit{Eq. 5-55}$$

Referring to the hydrostatic stiffness matrix presented in section 5.5.2.2, it is realized that $C_{11} = 0$. Thus, the natural periods for an uncoupled system in surge is undefinable, it will go towards infinity as C_{11} approaches 0. The same applies to sway motions due to the symmetries of the Spar. Note that similar relations may be discovered for natural periods in yaw, as $C_{66} = 0$.

Thus, there is only definable uncoupled natural periods in heave, roll and pitch. These are given as:

$$T_3 = 2\pi\sqrt{\frac{M + A_{33}}{\rho g S}}\ ;\ where \qquad \textit{Eq. 5-56}$$

$$S = \text{water plane area}$$

$$T_4 = 2\pi\sqrt{\frac{Mr_{44}^2 + A_{44}}{\rho g V \cdot \overline{GM_T}}}\ ;\ where \qquad \textit{Eq. 5-57}$$

$$r_{44} = \text{roll radius of gyration}$$

$$\overline{GM_T} = \text{transverse metacentric height}$$

$$T_5 = 2\pi\sqrt{\frac{Mr_{55}^2 + A_{55}}{\rho g V \cdot \overline{GM_L}}}\ ;\ where \qquad \textit{Eq. 5-58}$$

$$r_{55} = \text{pitch radius of gyration}$$

$$\overline{GM_L} = \text{longitudinal metacentric height}$$

It should be noted that due to the symmetries of the Spar buoy, $r_{44} = r_{55}$, $\overline{GM_T} = \overline{GM_L}$ and $A_{44} = A_{55}$, implying that the natural periods in roll and pitch are the same in the presented work. The metacentric height presented in the formulas above is the same parameter discussed in section 5.3. The roll and pitch natural periods will therefore decrease with an in increase in $\overline{GM}$, and a compromise to obtain sufficient static stability and ensure suitable natural periods is therefore often needed.

Table 5-3 shows typical natural periods for the most common deep-water floaters in a coupled system, i.e. mooring lines attached.

Table 5-3: Typical natural periods of coupled deep water floaters, retrieved from [19] as Table 7-1

DOF	FPSO	Spar	TLP	Semi
Surge	> 100	> 100	> 100	> 100
Sway	> 100	> 100	> 100	> 100
Heave	5-12	20-35	< 5	20-50
Roll	5-30	50-90	< 5	30-60
Pitch	5-12	50-90	< 5	30-60
Yaw	> 100	> 100	> 100	> 50

The compliant motion in the horizontal plane yields a high natural period in surge, sway and yaw for all floater types [4]. Clearly, these periods are well outside the range containing energetic waves. Avoiding resonance in heave, roll and pitch is therefore of greatest importance in most applications. However, even though the natural periods is moved outside the frequency range of energetic waves, some resonance responses will always appear due to the non-linear load effects discussed in the previous section [19].

5.6 Station keeping

A station keeping system has the purpose of maintaining a desired position of an offshore floating vessel. There is various techniques for station keeping, including dynamic positioning (DP), taut mooring, catenary mooring or a tendon system of tethers used on a tensioned-leg platform (TLP) [4]. Catenary mooring systems using chain and wire or a taut mooring system using fiber ropes are most common for a turbine system featuring compliant motions [4]. This introduction will limit itself to the catenary mooring, as it is the system utilized in the presented work.

The term “catenary mooring” originates from the resulting shape of a free hanging line under the influence of gravity, as illustrated in Figure 5-11. The sea keeping is provided by the suspended mooring line weight and changes in the line’s configuration with the dynamic response of the vessel [23]. Mooring lines comprises of either chain or rope, where the ropes are available in steel (wire), natural fiber and synthetic fiber [26]. The line is often segmented with a combination of the aforementioned line types to get a heavy line at the bottom by using chains, and a lighter line close to the water surface. This ensures greater stiffness and a lighter mooring cable than using chain alone [26].

The loads arising in the mooring lines due to the dynamic responses are transferred to anchors installed at the seabed. The applicable anchor solution is highly dependent upon the soil conditions at the actual site and has to be determined on a case-by-case basis [4]. Traditional gravity anchors are however not designed to withstand a vertical load, as this tends to pull out the anchor [23]. A horizontal load acting on the anchor should therefore absorb the entirety of the line load. A surplus of mooring line resting on the seabed ensures that no vertical load is applied to the anchor.

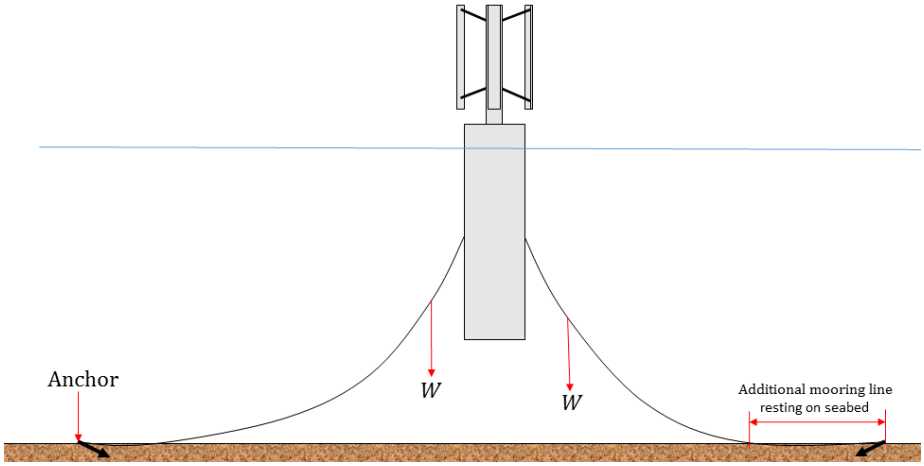

Figure 5-11: Illustration of the catenary mooring line concept

Some floating offshore wind turbine concepts features low yaw stiffness, which may require the use of "crowfoots" to ensure suitable operation. A crowfoots configuration implies that each mooring lines have two connection points to the floating structure, as was observed in the illustrative picture of Statoil's Hywind pilot presented in section 4.1. Sufficient yaw stillness is necessary for the evaluated concept in the presented work. A VAWT generates torque around the vertical centerline, and the torque is transferred to the supporting structure about the yaw axis. Spar buoys generally have low yaw resistance, and the use of additional yaw stiffeners seems indispensable.

It may also be noted that catenary mooring is less suitable for deep-waters, as the weight of the catenary increases due to the greater line length needed to reach the seabed. Less ballast mass may then be included in the system, as much of the surplus buoyancy is used to accommodate for the large mooring line weight. Furthermore, mooring lines are prone to fatigue damage since the touchdown point changes constantly as the vessel reacts dynamically with the environmental loads [23].

6 Concept description and parameter definition

The turbine concept evaluated in the presented work will be introduced in the following section, including the rotor and the studied floater geometry. The rotor's geometry, dimension, key data for power generation and its mass distribution is presented in section 6.1. The floating system comprises of a Spar buoy, for which the diameter and draft shall be altered to study what effect this imposes on the system's hydrostatic and hydrodynamic performance. Numerical values of the floater geometry is therefore not presented in the following section, but the studied variable parameters is introduced. A naming system for systematically distinguish between the different floaters is also presented along with some assumptions of the mass distributions of the floaters.

6.1 Rotor

In collaboration with the thesis supervisor, it was decided to study a turbine in the MW class in order to evaluate a representative industrial turbine system. However, at the time of writing commercially available vertical axis rotor designs were only in the small scale for use in cities and for private households. It was of great importance to establish a realistic VAWT rotor design in the MW class, as the rotor's dimension and weight distribution will have a direct influence on the metacentric height and the dynamic performance of the system. A rotor design in the MW class is presented in [21], which is designed to represent the equivalent vertical axis counterpart to the 2.3 MW Hywind HAWT. Even though this is not a commercially available rotor, and a full-scale model has not tested its applicability (CFD calculations were performed in [21] to assess the rotors performance), it was the most detailed design acquired at the time of writing. This design will consequently be used in the presented work.

6.1.1 Rotor geometry and dimension

The concept presented in [21] features an H-rotor design with three NACA 0021 airfoils orientated symmetrically around the rotor column. The rotor diameter is 55 meters and the blade length is 99 meters to form a total swept area of 5500 m^2. These dimensions were established to ensure a power output of 2.3 MW with a realistic power coefficient of 0.4 at an undisturbed wind velocity of 12 m/s, using Eq. 5-8. It should be noted that in order to keep the tip-speed ratio constant, the proposed design in [21] featured a smaller diameter at the bottom and a larger diameter at the top of the rotor, resulting in a tapered rotor along the vertical axis. For simplicity, this effect was not included in the presented work, and the diameter was set to the mean diameter of 55 meters.

The rotor column features a total length of 112 meters, in order to form an air gap of 23 meters between the mean sea level and the lowermost point of the rotor blades. A sufficient airgap is of most importance as the rotor blades are not designed to withstand severe hydrodynamic loads by, for example, a 50-year wave. However, the diameter and thickness of the rotor column were not specified in [21]. As an approximation, the rotor column diameter was set to 4 meters with a wall thickness of 20 mm in accordance with DeepWind's 2 MW concept turbine [31]. Detailed dimensions of the struts supporting the vertical oriented airfoils was also missing in [21]. The struts were therefore approximated to have an outer diameter of 1.0 meter and a wall thickness of 20 mm.

Wind turbines also have different operational conditions, which is general dependent upon the environmental conditions. For low wind speeds, the turbine idles until the wind velocity reaches the so-called cut-in velocity. The turbine then starts to generate electricity and is in a power producing state. The system continues producing power until the cut-out wind, where the turbine is either parked or allowed to idle to minimize adverse structural and fatigue damage in such extreme winds. The proposed

rotor design features a cut-in and cutout wind speed 5 m/s and 25 m/s, respectively. The rated wind speed, i.e. the wind speed which 2.3 MW power output is achieved, is 12 m/s. Above this value, the rotor is stalled to give a constant rotational wind speed and consequently a constant power output. The identified optimum tip-speed ratio was found to be three according to CFD simulations performed in [21]. This gives a rated rotational speed of 12.50 RPM according to Eq. 5-9.

A summary of the specification of the vertical axis rotor design is presented in Table 6-1.

Table 6-1: Rotor parameters

Parameter	Value	Unit
Rated power	2.3	MW
Rated wind speed	12	m/s
Cut-in wind speed	5	m/s
Cut-out wind speed	25	m/s
Solidity	0.3	-
Tip-speed ratio	3	-
Rated rotational speed	12.5	RPM
Rotor diameter	55	m
Blade length	99	m
Air gap	23	m
Rotor column diameter	4	m
Rotor column thickness	20	mm
Struts diameter	1	m
Struts thickness	20	mm

6.1.2 Rotor mass distribution

In [21], the rotor mass was set to 54 tons in accordance to the rotor assembly used on the Hywind HAWT. This assumption may however prove to be inappropriate as each blade on the equivalent VAWT is 59 meters longer compared to the Hywind pilot design. It was therefore decided to establish a more accurate estimate for the rotor's mass. Furthermore, as will be discussed in section 8.2, accurate estimates of the moment of inertia of the rotor assembly is needed to generate reliable frequency dependent added mass and damping matrices, displacement RAOs and load RAOs in HydroD. It was therefore decided to model the rotor assembly in Autodesk Inventor Professional 2015 to get accurate predictions of the total mass, center of gravity and mass moment of inertias. The resulting model can be observed in Figure 6-1.

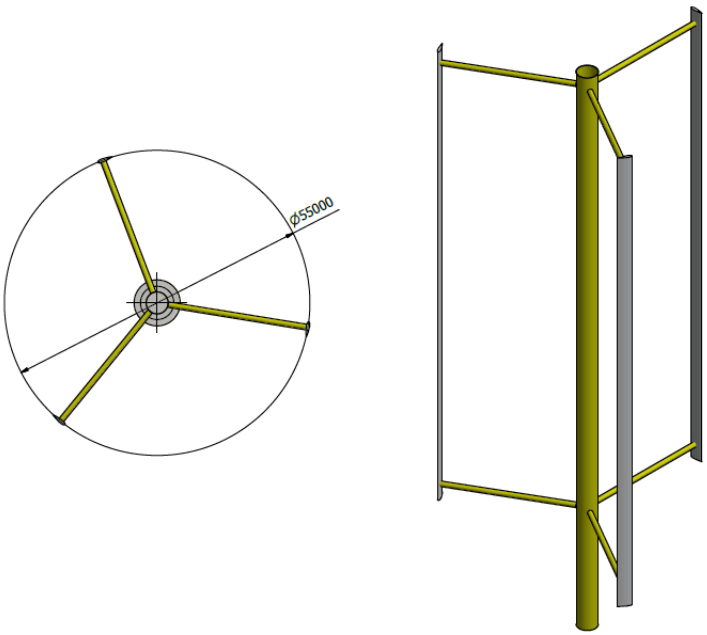

Figure 6-1: Illustration of rotor assembly, constructed in Inventor Professional 2015

The steel density was set to represent a generic density of 7850 kg/m^3. The steel parts include the rotor column and six struts, for which the dimensions are presented in the previous section. Based on the background research performed in relation with the state of art section, it was realized that most airfoils used in wind turbine applications are made of a glass reinforced epoxy resin composite (GRE), which has a typical density of 1850 kg/m^3 [32]. The airfoil cross section was modelled according to the specified NACA 0021 profile with a chord length of 2.75 meters by using an online airfoil calculator [33], which generates numerous points in an x-y coordinate system to represent the specified airfoil's periphery. However, airfoils used in turbine applications comprises of skeleton frame to reduce the weight while still giving a stiff structure. Modelling the airfoils as a solid section and using the typical density for the GRE material would therefore lead to an overestimation of the blade weight. Detailed schematics of a skeleton frame of the NACA0021 wing was unfortunately not acquired, and an assumption regarding the fraction of the airfoil area that is covered with material had to be made. This was set to 20%. The obtained results for the Inventor model can be observed in Table 6-2.

Table 6-2: Rotor data extracted from Inventor 2015

Parameter	Value	Unit
Mass	398587.74	kg
CoG, relative to bottom of rotor column	58.9	m
Ixx, with respect to CoG	5.296E+8	kgm^2
Iyy, with respect to CoG	5.296E+8	kgm^2
Izz, with respect to CoG	1.003E+8	kgm^2

It should be noted that the authenticity of the established rotor data presented in Table 6-2 is highly dependent upon the validity regarding the assumptions made about the amount of area the skeleton frame covers, along with the rotor column and the support struts diameter and thickness. These assumptions will have a direct effect on the location of center of gravity, and thus stability. Furthermore, the structural integrity of the rotor column and struts was not assessed in the presented work due to

time limitations. There is therefore a possibility of these sections being under-dimensioned, leading to an unfeasible rotor design. However, even though it was desirable to acquire a realistic as possible VAWT rotor, the presented design still works as a baseline with reasonable accuracy for a first evaluation of the floating turbine system hydrostatic and hydrodynamic performance.

6.2 Floater

As the Spar buoys principal hull parameters shall be altered throughout the analysis, numerical values will not be specified in this section. Rather, explanation of the viable floater parameters will be presented, along with a naming system for systematically distinguish between the different floaters.

6.2.1 Floater geometry

The geometry and associated variable parameters of the Spar buoy evaluated in the presented work is depicted in Figure 6-2.

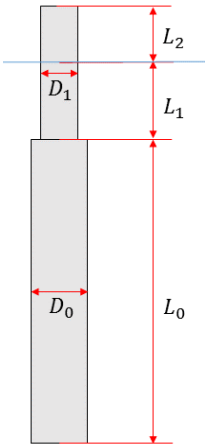

Figure 6-2: Illustration of floater geometry and parameters

Based on the research performed in relation to the state of art section, it was seen that floating turbine concepts utilizing Spar buoys features a larger diameter at the bottom part of the floater and a smaller diameter for the top part of the floater. This is true for the Hywind demo project [9], Hywind Scotland project [7] and the Spar floater developed in phase IV of the OC3 project [29]. The smaller diameter reduces the water plane area, which minimizes the hydrodynamic loadings from waves and ensures favorable natural periods in heave. The larger diameter facilitates a large amount of displacement, which is necessary for accommodating a sufficient ballast mass to ensure satisfactory stability characteristics. This effect was therefore implemented into the floating geometries studied in the presented work. It is therefore possible to alter the upper diameter (D_1) and lower diameter (D_0) independently. It is of course still possible to study a floater containing only one diameter throughout the whole draft by setting $D_0 = D_1$. It should be noted that the aforementioned turbine concepts using two diameters featured a conical region to join the discontinuities. As can be observed from Figure 6-2, this effect is not implemented to the floater geometry studied in the presented work in order to ease the calculations related to the spreadsheet analysis.

The draft comprises of the lengths L_0 and L_1. As illustrated in Figure 6-2 L_0 represents the length of the floater section featuring the larger diameter (D_0), while L_1 represent the length of the submerged section of the smaller diameter (D_1). The smaller diameter extends above the SWL to represent the

floater's freeboard, and the upper section is consequently divided into two length (L_1 and L_2) to separate the draft and freeboard.

All the parameters presented in Figure 6-2 are alterable in the spreadsheet calculations. However, some of the parameters be set as constant values in order to reduce the number of parameters studied. This includes the freeboard (L_2), draft of the smaller diameter (L_1) and the smaller diameter itself (D_1). The reason for this is related to the design criteria for these parameters. For example, the freeboard is set to ensure that wave crests related to extreme sea states can pass the structure without risk of imposing hydrodynamic slamming loads to the top of the platform, or to the rotor assembly [4]. The main purpose of the lower diameter near the wave zone is to minimize the imposed hydrodynamic loadings on the structure. These parameters are therefore related to the environmental condition, and it is thus appropriate to set these parameters constant, as all floaters shall operate in similar environmental conditions.

The freeboard evaluated in the presented work is set to 10 meters, in accordance to the freeboard used on the OC3 phase IV floater presented in [29]. This turbine system features a larger power output with a horizontal axis rotor and is thus not directly comparable to the turbine system evaluated here. However, the freeboards should still be similar as both turbines are designed for offshore applications at locations featuring similar conditions.

In order to minimize the hydrodynamic loadings, the top section's diameter should be as small as possible. This will be 4 meters, as the top section cannot be smaller than the diameter of the rotor column. Furthermore, the imposed loads due to waves is most severe around the SWL, before decaying with depth due to the nature of deep-water waves. The length of the top geometry should therefore be set to ensure that the most severe forces are exerted onto the smaller diameter. However, this length cannot be too large, as a long upper section would require more volume to be displaced near the floater's keel to obtain suitable displacement. This will lower the CoB position and reduce $\overline{KB}$, which will consequently decrease the metacentric height according to Eq. 5-15 and lead to poor stability characteristics. It was therefore decided to set L_1 to 10 meters, based on the design of the OC3 Hywind floater [29]. At this depth, the velocities and accelerations in the studied environmental conditions are reduced by approximately 30%.

The wall thickness will have a direct result on the weight of the floater, and consequently the amount of ballast that can be accommodated for the given displacement. It was therefore desirable to get realistic estimates of this parameter. However, this demands detailed strength analysis for each floater, which there was simply not enough time to perform. The wall thickness was consequently set to the constant value of 25 mm, in accordance to information presented in [21]. The validity of this assumption is of course debatable from a structural integrity point of view, i.e. whether the set thickness will actually be feasible for a given floater. However, the thickness in the presented work represents a baseline for which tendencies for the altered floater geometry may be identified. Further work built on these results may then establish a more detailed estimate of the wall thickness in order to represent a more optimized floater where structural integrity can be guaranteed.

A bottom plate, middle plate and top plate have also been included as a part of the floater with the same specified thickness. The bottom plate is designed to flush with the bottom part of the floater, meaning it features a diameter of $D_0 - 2 \cdot t_w$. The middle plate is placed at the transition between the two diameters, and is designed to flush to the inner diameter of the bottom section and outer diameter of top section. The plate consequently features an outer diameter of $D_0 - 2 \cdot t_w$ and an inner diameter of D_1. The top plate flushes with the top of the floater and features an outer diameter of $D_1 - 2 \cdot t_w$. The three plates and their dimensions are depicted in Figure 6-3.

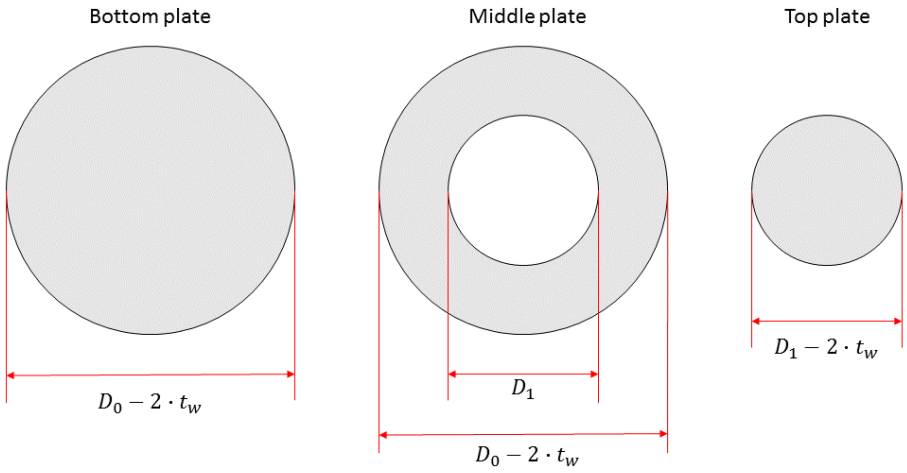

Figure 6-3: Illustration of bottom plate, middle plate and top plate

The floater geometries to be altered in the further analysis is therefore D_0 and L_0 to from an array of floater geometries featuring different drafts and diameters. In order keep track of all the established geometries, a common naming system is generated based on the parameters D_0, L_0, D_1 and L_1. The suggested naming system is presented in Table 6-3.

Table 6-3: Suggested naming system for floaters

D_0	-	L_0	x	D_1	-	L_1

For example, a floater termed "6-65x4-10" features a diameter and draft of the lower section equal to 6 meters and 65 meters, respectively. The upper section comprises of a diameter and draft equal to 4 meters and 10 meters, as discussed above. The total draft is then 70 meters, and the total length of the floater (including the freeboard) is 80 meters.

6.2.2 Floater mass distribution

The mass of floater is estimated by assessing a generic steel density of 7850 kg/m^3 multiplied with the material volume for each individual part of the floater presented above. As the thickness is uniformly distributed along the length of the floater, the center of gravity for each individual section of the floater will coincide with the geometrical center of the respective section.

7 Selected environmental conditions

In order to evaluate the floating system performance, realistic environmental conditions has to be established. The term environmental condition covers virtually all natural phenomena occurring on a particular site [4]. However, only wind and waves conditions is included in the presented work, excluding environmental conditions such as current, marine growth, tidal effects and sea ice.

It was desired to study the turbine's performance in two environmental conditions, one representing a typical operating condition and one representing an extreme environmental condition where the turbine is in its parked position.

7.1 EC1: Operating environmental condition

In order to represent the operating environmental condition, a 10-minute average wind speed at hub height was selected between the cut-in and cutout velocity of the rotor. This is in accordance with information specified for load case 1.1 and 1.2 in DNV-OS-J101: Design of offshore wind turbine structures. These load conditions also specifies that a normal turbulence model should be used to model the turbulence components acting simultaneously with the mean wind profile. The model represents the turbulence in terms of characteristic standard deviation of wind speed, which is defined as the 90% quantile in the probability distribution of the standard deviation of the wind speed at hub height averaged over 10 minutes [24]. Modelling the turbulence component often demands comprehensive computer simulations in the time domain [19], as the turbulent component is highly random in nature. As time was rather spent to obtain an accurate hydrodynamic model, turbulence was neglected all together and the wind climate was consequently only modelled by the mean wind component. In can thus be stated that due to time limitation, the wind is assessed in a simplified manner in the presented work, and focus is rather put into simulating the hydrodynamic effects accurately.

The operational loading conditions in DNV-OS-J101 also specifies that that the wave condition should be assessed with the concurrent mean wind speed, as an typical operating condition contains wind generated waves. This is done through a joint probability distribution, where the significant wave height (H_s) is selected as the expected value given a mean wind speed. The spectral peak period (T_p) shall, according to DNV-OS-J101, be set to the value giving the highest loads or load effects for the established H_s. However, structural integrity is not evaluated in the presented work, and the spectral peak period is therefore set to the expected value of the joint probability distribution of T_p conditioned on H_s, which again is conditioned on the given mean wind speed. In this way, a typical operational environment was truly represented. The wind and waves is assumed to be aligned, forming a collinear operational environment.

Furthermore, an environmental state is characterized by a specific duration, e.g. 10-minutes for the average wind speed and 3-6 hours for the short-term wave condition. According to DNV-OS-J101, a reference period of one hour should be used for the environmental state when evaluating the response of an offshore turbine. Appropriate conversions of U_{10} and H_s should be performed in case the reference period for these parameters are different from one hour [24].

The 1-hour mean wind speed was set to 14 m/s at hub height 78.9 meters to represent an environment where the rotor is operating at its rated rotation speed, and thus it rated power. The corresponding values for the significant wave height and spectral peak period, established from the joint probability distribution generated on data from the Statfjord site in the North Sea, can be observed in Table 7-1. The values are based on environmental conditions presented in [34], where an identical approach was performed to generate the operational environmental condition.

Table 7-1: Presentation of environmental condition 1: Operating condition

Environmental condition	Wind condition	Wave conditions		Wind and wave directionality
	U_w [m/s]	H_s [m]	T_p [s]	
1	14	3.62	10.29	Co-directional in one direction

7.2 EC2: Extreme environmental condition

In order to represent an extreme environmental condition to evaluate the systems survivability, a mean wind component of 50 m/s is elected along with the associated significant wave height and spectral peak period. As with environmental condition 1, turbulence is not be assessed. This leads to the environmental condition presented in Table 7-2.

Table 7-2: Presentation of environmental condition 2: Extreme condition

Environmental condition	Wind condition	Wave conditions		Wind and wave directionality
	U_w [m/s]	H_s [m]	T_p [s]	
2	50	12.90	14.10	Co-directional in one direction

7.3 Physical parameters

The physical environmental parameters used in the analysis is presented in Table 7-3. These was kept constant through all analysis, including the spreadsheet calculations, HydroD analysis and OrcaFlex simulations.

Table 7-3: Physical environmental parameters used in the analysis process

Parameter	Value	Unit
Air, density	1.226	kg/m^3
Air, kinematic visc.	$1.462 \cdot 10^{-5}$	m^2/s
Sea, density	1025	kg/m^3
Sea, kinematic visc.	$1.19 \cdot 10^{-6}$	m^2/s

8 Method of analysis

As stated in section 2, the presented work aims to study the effect of varying principal hull parameters of a Spar buoy foundation for vertical axis wind turbine (VAWT) in the MW-class. This will be achieved in stages.

First, spreadsheet calculations will be performed for a number of geometries featuring different diameters and drafts. The spreadsheet gives means of efficiently study several geometries, but limit itself in evaluating static stability, estimates of natural period and estimates of static heel angle. These results are used to evaluate the effect of varying the principal hull parameters on the floating system's hydrostatic performance, while also forming the base to establish three promising geometries to be analyzed in a more comprehensive dynamic simulation. The results from the dynamic simulations are used to evaluate what effect different drafts and diameters have on the system's hydrodynamic performance. However, in order to execute the dynamic simulations, frequency dependent added mass and damping matrices, displacement RAOs and load RAOs needs to be established, for which the hydrodynamic analysis software HydroD is used. As will be explained in detail in the following section, accurate estimates of the system's mass and inertia properties must be obtained to gain reliable outputs from the HydroD analysis. The three identified floaters from the spreadsheet calculations are therefore modelled in Inventor 2015 to gain accurate estimates of the inertia properties. Furthermore, HydroD requires an FE-model generated from an independent software, for which GeniE was used. The analysis process is illustrated in Figure 8-1.

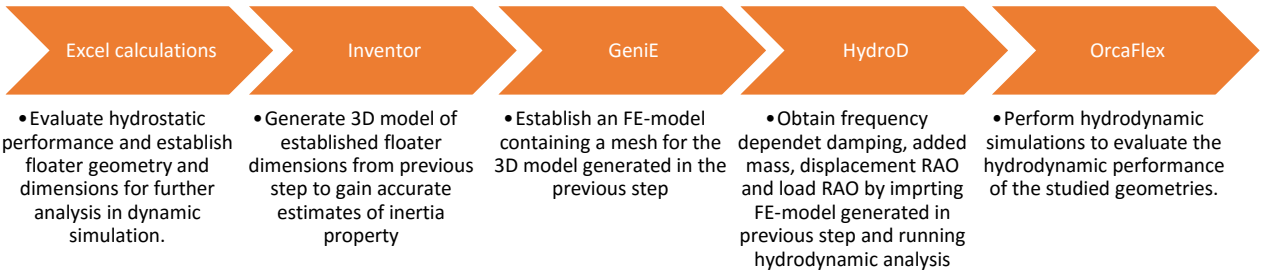

Figure 8-1: Illustration of the analysis process

How the individual steps in the analysis procedure was performed is explained in detail in the following sections.

8.1 Spreadsheet calculations

The spreadsheet calculation was generated in excel 2013 to study various floater geometries with respect to static stability, natural periods and static heeling angle to evaluate the hydrostatic performance and identify candidates to be studied further in the dynamic simulations. The set-up of the spreadsheet is presented in the following.

8.1.1 Metacentric height

The metacentric height was established using Eq. 5-15, which is dependent upon the systems center of gravity, center of buoyancy and metacenter radius.

The center of gravity relative to the keel was established by using Eq. 5-18, where the mass and local CoG location of the rotor, individual sections of the floater, gearbox and generator assembly and ballast were evaluated. The mass distributions and center of gravity of the rotor and floater is presented in section 6. The gearbox and generator assembly was assumed to feature a mass of 82 tons, similar to the drivetrain assembly used in the Hywind pilot project. The assembly was placed to make the local CoG coincide with the SWL, as made possible by the VAWT design. The ballast mass was set as the differential mass between the system (including floater, rotor and gearbox/generator assembly) and the mass of displaced fluid in order to obtain a static equilibrium position with a freeboard of 10 meters. The ballast density was assumed to be 3300 kg/m^3, according to the work performed in [21].

The CoG positions relative to the keel for each individual component is illustrated in Figure 8-2, where the abbreviations in the figure are explained in Table 8-1.

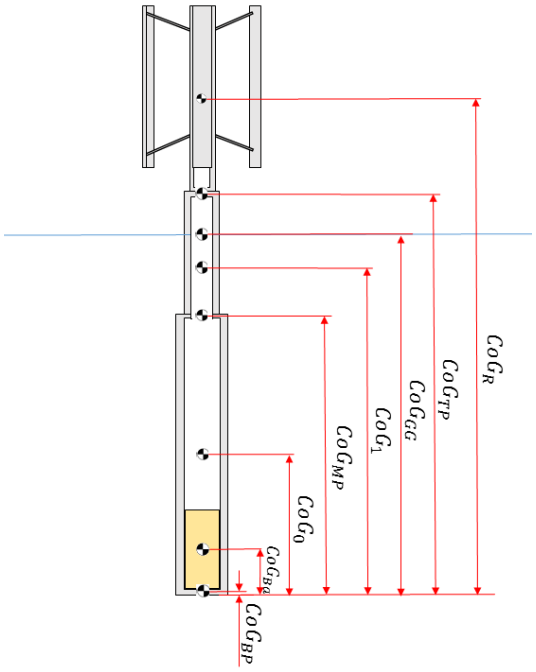

Figure 8-2: Illustration of location of local CoG from keel of each individual section and components

Table 8-1: Explanation of abbreviations used in Figure 8-2

Parameter	Explanation
CoG_{BP}	Center of gravity of bottom plate
CoG_{Ba}	Center of gravity of ballast
CoG_0	Center of gravity of bottom part of floater
CoG_{MP}	Center of gravity of mid-plate
CoG_1	Center of gravity of top part of floater (included freeboard)
CoG_{GG}	Center of gravity of generator and gearbox
CoG_{TP}	Center of gravity of top plate
CoG_R	Center of gravity of rotor

The keel to buoyancy of the system ($\overline{KB}$) was obtained using equation Eq. 5-16 and evaluating the displaced volume and the position of the local center of buoyancy (CoB) relative to the keel of each submerged section of the floater.

Lastly, the metacentric radius was obtained by evaluating the area moment of inertia of the water plane, and the total displacement of the floater. Using the notation of the floater parameters presented in section 6.2.1, $\overline{BM}$ becomes:

$$\overline{BM} = \frac{\frac{\pi}{64} D_1}{\frac{\pi}{4} D_0 \cdot L_0 + \frac{\pi}{4} D_1 \cdot L_1} = \frac{D_1}{16 \cdot (D_0 \cdot L_0 + D_1 \cdot L_1)}$$

8.1.2 Natural periods

As stated in section 5.5.6, avoiding resonance is a key aspect in any offshore construction, and estimates of the natural periods are thus of great assistance when determining possible candidates to be evaluated in the dynamic simulations. Mooring lines was however not included in the spreadsheet calculations, making the natural period in surge, sway and yaw undefinable, as illustrated in section 5.5.6. The natural periods in heave, roll and pitch was therefore investigated in the spreadsheet analysis. These are however often of most concern, as a Spar buoy features coupled natural periods in surge, sway and yaw over 100 seconds. It is reminded that the pitch and roll natural periods are equal due to the symmetries of the Spar, and the natural period in pitch was only evaluated in the spreadsheet analysis.

8.1.2.1 Heave

The uncoupled natural period in heave for a freely floating vessel was presented in section 5.5.6, and is dependent upon mass of the system, water plane area and added mass in heave. The system mass and water plane area was easily obtained from the rotor mass and floater geometry discussed in section 6. However, as stated in section 5.5.2.2, the added mass is generally dependent on frequency and shape of the structure. Obtaining the frequency dependent added mass requires specialized software utilizing potential theory, which is too comprehensive for the purpose of the spreadsheet calculations. The added mass in heave was consequently estimated as the weight of a hemisphere with diameter equal to the bottom diameter of the floater.

8.1.2.2 Pitch

The uncoupled natural period in pitch for a freely floating structure was presented in 5.5.6, and is dependent upon the radius of gyration in pitch, mass of the system, displaced volume, metacentric height and added mass in pitch.

The mass of the system and displaced volume was established during the establishment of metacentric height, and only the radius of gyration and added mass in pitch had to be established to gain an estimate of the natural period in pitch.

The radius of gyration in pitch is given as:

$$r_{55} = \sqrt{\frac{I_{yy}}{M}} \;\; ; \;\; \text{where} \qquad \textit{Eq. 8-1}$$

$$I_{yy} = \text{mass moment of inertia around y} - \text{axis for the entire system}$$

$$M = \text{mass of system}$$

The mass moment of inertia of the total system was computed by acquiring expressions for the moment of inertia for each individual section, and relating these to the system's center of gravity through Steiner's formula. The hollow cylindrical parts of the floater, including the bottom section, top section and the mid-plate was regarded as thick-walled cylinders with open ends, while the solid cylindrical part of the floater, including the bottom plate, top plate and the ballast column, was regarded as solid cylinders. The generator was assumed to be a point mass located on the vertical centroid axis, while inertia terms for the rotor had already been established through the Inventor model.

The added mass in pitch was estimated using strip theory. Strip theory divides the submerged part of a body into a number of strips with infinitesimal length, where an expression for the two-dimensional added mass coefficient is obtained for each strip in the desired DOF. The three-dimensional added mass coefficient is then approximated by integrating the results from each strip [26]. However, the variation of flow in the cross-sectional plane should be much larger than the variation of the flow in the longitudinal direction for the strip theory to be applicable [26]. This is not the case at the end of the submerged body, and is the reason for not evaluating the added mass in heave through the strip theory.

In case of a constant cross section over a length d, the added mass in pitch for a Spar buoy using the strip theory is given as [26]:

$$A_{55} = \frac{\rho \pi D^2}{4} \cdot \left(\frac{d^3}{12} + d \cdot \overline{BG}^2 \right) \qquad \textit{Eq. 8-2}$$

8.1.3 Static heeling angle

The static heeling angle is represented as the angle that makes the inclination moment equal to the up righting moment. As the up-righting moment is highly dependent upon the metacentric height, the static heeling angle is an indication of sufficient $\overline{GM}$.

In order to estimate the heeling angle, expression of loads induced from waves and wind needs to be established to get an estimate of inclination moment.

8.1.3.1 Wind forces

As stated in section 7, the fluctuating part of the wind environment has been neglected in the presented work due to time limitations, and the wind force was calculated based on the mean wind component. Furthermore, as presented in section 5.2.3.1, the aerodynamic forces on a VAWT varies during one

rotation due to a time dependent variation in the angle of attack. These dynamic effects were not implemented in the spreadsheet, as it is a static analysis. It was therefore decided to calculate the inclination moment arising the mean wind force on a rotor that is assumed parked in the position observed in Figure 8-3. Note that only drag force acting on the freeboard of the floater, the rotor column and the rotor blades will give an inclination moment in this situation.

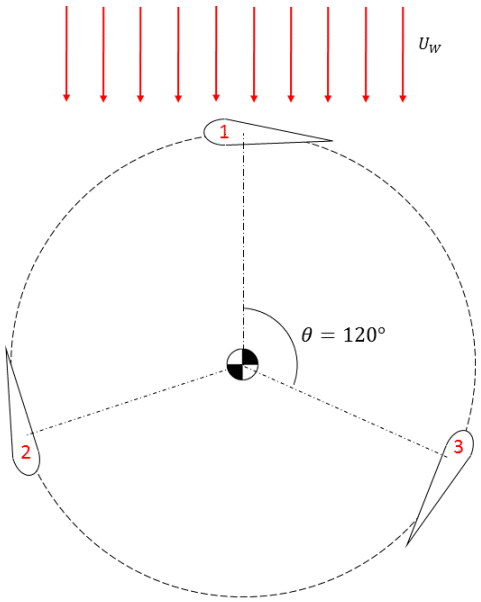

Figure 8-3: Illustration of stalled position of the rotor evaluated in the spreadsheet analysis

The mean wind speed profile was established for the environmental conditions presented in section 7 by using the power-law profile, as stated applicable by [19]. In order to calculate the mean drag force by using Eq. 5-3, appropriate shape coefficients had to be assigned for each wind-exposed section. This was done in accordance to DNV-RP-C205, which states that the shape coefficient for circular cylinders may be set according to Figure 8-4. This figure depicts the shape coefficient as a function of Reynolds number and cylinder roughness.

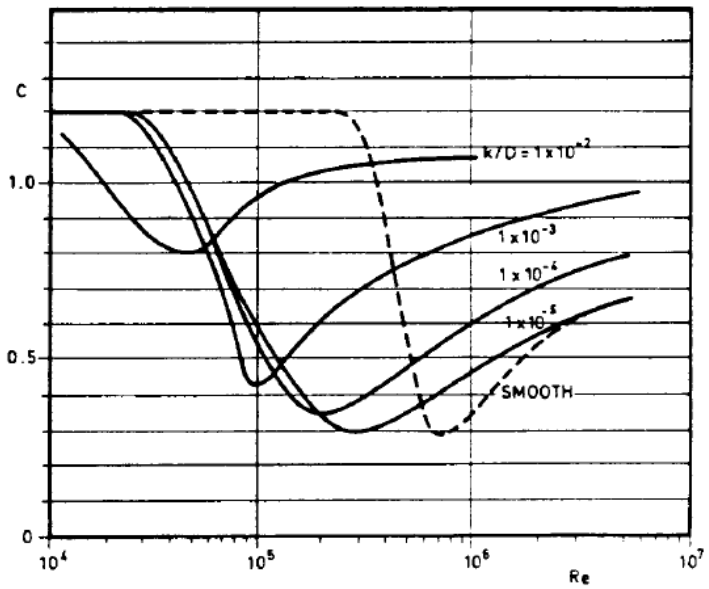

Figure 8-4: Shape coefficient as a function of Reynolds number and surface roughness, retrieved as Figure 6-6 in [19]

However, this shape coefficient is for cylinders with infinite length and needs to be modified for a cylinder with finite length by a reduction factor, given as the ratio between member length and characteristic cross-sectional dimension (l/d). Note that for members where free flow around one end is prevented due to the presence of another structure, the ratio l/d shall be doubled when determining the reduction factor [19]. This is the case for the rotor column, which is connected to the floater at the bottom of the column. Furthermore, the shape coefficient shall be set as the shape coefficient for infinite length when flow around both ends of the member is prevented [19]. This is the case for the freeboard of the floater, where airflow is denied at the bottom due to the presence of the ocean and at the top due to the presence of the rotor column. Numerical values for the reduction factor as a function of l/d is presented in Table 8-2. Case A and B refers to a circular cylinder in subcritical flow and a circular cylinder in supercritical flow, respectively.

Table 8-2: Values of the reduction factor, retrieved as Table 6-2 in [19]

l/d	2	5	10	20	40	50	100
A	0.58	0.62	0.68	0.74	0.82	0.87	0.98
B	0.80	0.80	0.82	0.90	0.98	0.99	1.00

The shape coefficient for the rotor column and freeboard was then established by evaluating the mean Reynolds number acting on these sections and reading the appropriate values from Figure 8-4 and Table 8-2. The surface roughness was selected to $k = 1 \cdot 10^{-4}\, m$ to represent a roughness between uncounted steel and highly corroded steel.

An airfoil feature a rather complex cross-section, and appropriate shape coefficients was difficult to obtain. The airfoils was consequently regarded as flat plates with length = 2.75 m and width = 0.5775m, corresponding to the airfoils chord length and maximum thickness of the NACA0021 profile. However, a flat plate stagnates the airflow considerably more compared to an airfoil cross-section, meaning that the shape coefficient for flat plates are higher than for an airfoil. The resulting air forces acting on the rotor blades will therefore be somewhat overestimated in the spreadsheet calculations. This will however be of less significance, as it is done for all studied floater geometries. The tendencies of altering the draft and diameter on the system's hydrostatic performance will therefore still be valid, along with the comparison basis of electing three potential floaters for further evaluation in a dynamic simulation. Furthermore, the horizontal struts used in an H-rotor to support the airfoils was assumed to be included in the overestimated shape coefficients of the flat plates, and was consequently not regarded in the estimation of the mean wind force.

In the stalled position illustrated in Figure 8-3, airfoil number 1 features a projected area of $A_1 = 2.75\ m^2/m$, while airfoil 2 and 3 features a projected area normal to the velocity of $A_{2,3} = 2.75m \cdot \sin(30°) = 1.375\, m^2/m$.

The obtained shape coefficients and the associated projected area in the wind direction is presented in Table 8-3.

Table 8-3: Projected area and shape factor for calculating drag wind force

Part	Projected area ⊥ wind vector	Shape coefficient EC1	Shape coefficient EC2
Rotor column	4 m^2/m	0.6938	0.7930
Freeboard	4 m^2/m	0.6938	0.7930
Airfoil 1	2.75 m^2/m	2	2
Airfoil 2,3	1.375 m^2/m	2	2

Note that the shape coefficient for flat plates are not dependent upon Reynolds number and will consequently be the same in both environmental conditions.

After obtaining the shape coefficients, the total wind exposed structure was divided into sections of 1 meter, where the mean wind force was calculated for each particular section.

8.1.3.2 Wave forces

The wave environment in the spreadsheet calculations was modelled using linear wave theory with the environmental parameters presented in section 7. The wave amplitude was set to half of the significant wave height, while the period was set to the spectral peak period for the different environmental states. As mentioned in section 5.4.2.1, the significant wave height has the physical interpretation of the average of the one-third largest waves observed in the sea state, and the spectral peak period is the period containing the most energetic waves in the sea state. The chosen representation of the incident linear wave, for which the wave forces was calculated, was therefore somewhat conservative, even though the studied linear wave does not represent the largest wave in the sea state.

It was decided to use the Morison's load formula in the normal direction for a fixed cylinder in order to get estimates of the hydrodynamic loadings. As mentioned in section 5.5.2.4, the cross-sectional dimension has to be sufficiently small for the Morison's equation to be a suitable estimate of the hydrodynamic loads, i.e. $D \leq 0.2\lambda$. Using the dispersion relation for deep-water linear waves, the wavelength in the studied environmental condition 1 is found to be:

$$\lambda = 1.56 \cdot 10.29^2 s^2 = 165.18\, m$$

Note that EC1 was used when evaluating the limiting diameter, as it features the smallest period among the environmental conditions and is therefore most critical.

The largest diameter on the floater can therefore not exceed 33.04 meters for the Morison's equation to be valid. Furthermore, in order to use the Morison's equation for a fixed structure for a cylinder that is in reality free to move, V_R has to be less than 10 and the member displacement amplitude has to be less than one diameter, as discussed in section 5.5.2.4. This will probably not be fulfilled in a realistic scenario, as Spar features compliant motions in all degrees of freedom, as presented in section 5.5.3. However, the spreadsheet calculations is a simplified analysis featuring static conditions, and it was assumed that the Morison's equation for a fixed structure was applicable.

After some initial trials, it was discovered that all relevant floaters featured a low KC-number, making the inertia term dominating. The maximum wave force was therefore obtained by evaluating a surface elevation process that passes the SWL. The added mass coefficient was set as 1.0, as stated applicable for low KC-numbers in DNV-RP-C205. The force distribution was obtained by discretizing the submerged part of the floater in sections of 1 meter, and applying the Morison's equation with the appropriate horizontal maximum acceleration for each section.

8.1.3.3 Estimation of static heel

After estimates of the wind and wave loads acting on the structure was obtained, the inclination moment was calculated. Note that the floaters rotates around the metacenter position, also known as the pitch center. The inclination moment was therefore assessed by multiplying the sectional forces induced from the wind and waves with the appropriate moment arm relative to the floating geometry's metacenter, and summing all the contributions. It should also be noted that the hydrodynamic loads

acting below the metacenter would counteract some of the inclination caused by the wind and hydrodynamic forces acting above the metacenter. This situation is illustrated in Figure 8-5, where the resultant forces are depicted with their associated moment arm. The total inclination moment is therefore obtained by subtracting the moment resulting from the hydrodynamic loadings below the metacenter to the inclination moment imposed from the wind forces and hydrodynamic loads acting above the metacenter.

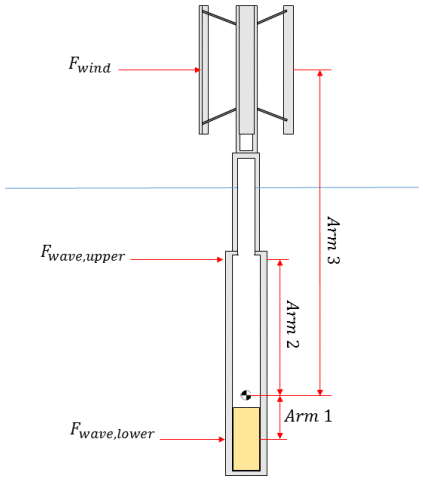

Figure 8-5: Illustration of resultant forces with associated moment arms

The static heeling angle was finally obtained by setting the inclination moment equal to the up righting moment, and solving for the static heeling angle, yielding:

$$M_R = M_I \rightarrow \nabla \rho g \cdot \overline{GM} \cdot \sin(\phi) = M_I \cdot \cos(\phi) \rightarrow$$

$$\phi = \tan^{-1}\left(\frac{M_I}{\nabla \rho g \cdot \overline{GM}}\right) \qquad \text{Eq. 8-3}$$

8.2 Dynamic analysis

As stated in the introduction to this section, the dynamic analysis comprises of generating 3D models in inventor and finite element models in GeniE, performing a HydroD analysis and running the OrcaFlex simulations. The procedure performed in each step is presented in the following. It is reminded that the following presentation is of a generic nature, and the presented figures are from the initial trials of the programs, and does not necessarily represent the floater that shall be studied.

8.2.1 Inventor

The 3D models for the floaters was generated based on dimensions established through the spreadsheet calculations for floaters showing suitable potential regarding metacentric height, natural periods and static heel angles. The steel density was set to 7850 kg/m^3, in accordance with the information given in 6.2. The total system was modelled by importing the 3D model for the rotor assembly previously constructed and a 3D model for the ballast column and generator into an assembly

containing the evaluated floater geometry. The height of the ballast column was obtained from the spreadsheet, which was calculated to achieve an equilibrium position with a freeboard of 10 meters.

An advantage of generating a 3D model in inventor is that it may be imported into the GeniE software in the form of a .SAT file, where the FE-model is generated. To avoid over-complicating the FE model, it was decided to include the floater's outer geometry in the imported SAT file. Components like the rotor, ballast and generator was therefore excluded in the in the 3D model used in GeniE. However, these components have their own masses and inertias, which must be included in HydroD to get representative hydrodynamic coefficients for the turbine system. This was achieved by extracting values for the mass, center of gravity and radius of gyration in the x, y and z-directions from the inventor model comprising of the total turbine system (including rotor, floater, ballast and generator), and use these values as input in the "MassModel" in HydroD. This gave means of representing the entire turbine system in HydroD, while only including the floater geometry in the FE-model. The inventor process is illustrated in Figure 8-6.

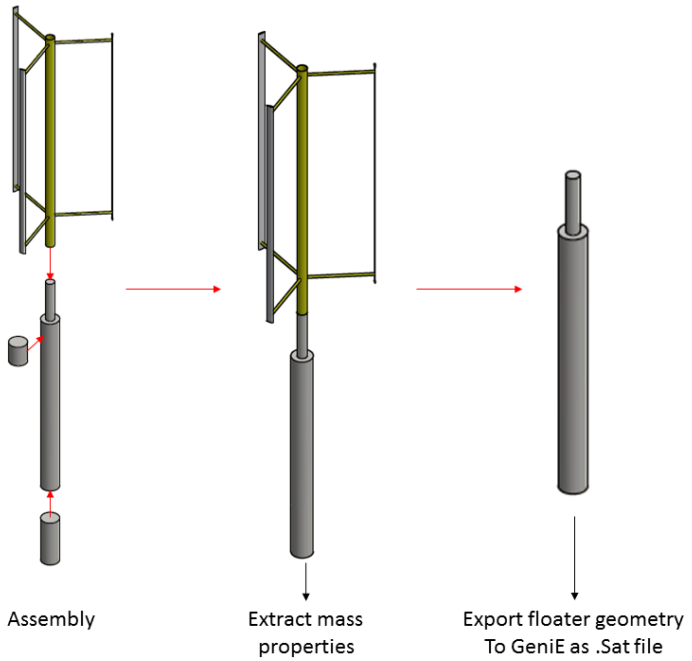

Figure 8-6: Illustration of work process in Inventor

8.2.2 GeniE

The modelling process in GeniE will be explained in the following. Note that all presented figures are obtained during the initial trail in GeniE, and does not necessarily represent the floater that shall be studied in HydroD. The presented figures are therefore for illustration purpose only.

Importing the SAT file to the workspace in GeniE generated surface structures for both the outer inner geometry to represent the floater. Attempts were made to keep both surfaces in the generated FE-model. However, this led to an unnecessarily extensive mesh model, as GeniE applied a mesh to both surfaces. No hydrodynamics were to be calculated on the inside of the model, and including the mesh on the inner surface only resulted in an increases computation time and memory requirements. It was therefore decided to delete the inner surface and rather apply a wall thickness of 25 mm to the outer

geometry to represent the floating structure. In this way, GeniE only applied a mesh to the outer surface, increasing the functionality of the FE-model.

Wet surfaces was then specified in order to apply a hydro dummy pressure on these surfaces. This must be implemented so HydroD recognizes where to apply hydrodynamic calculations. Panels assigned with a wet surface are also automatically cut in the waterline by HydroD [35]. Wet surface property should therefore be assigned to all surfaces that goes above all relevant waterlines to ensure that hydrodynamic computation is performed for the entire instantaneous submerged structure. For this reason, wet surfaces were specified for the entire floating structure, as can be observed in Figure 8-7. The dummy pressure was then inserted under load cases, by selecting the "Dummy Hydro Pressure" option and applying this to the specified wetted surface. The resulting hydro dummy pressure may be observed in Figure 8-8.

Figure 8-7: Applied wet surfaces in the FE-model, marked in blue

Figure 8-8: Applied hydrodynamic dummy load, marked in orange

A mesh could finally be established. An appropriate mesh is key for generating reliable results. A satisfactory mesh features elements that do not deviate from their original shape. A coarse mesh size often imposes such deviation and irregularities, as the mesh tries to represent the specified body with few elements. A finer mesh will often contain fewer irregularities, however at the cost computation time and memory requirements of the hardware. It is thus common to perform a convergence study to identify the needed fineness of the mesh to generate reliable results. Different mesh fineness may be obtained by adjusting the element length in GeniE, which is the length of one mesh element.

One completed FE-model with the applied dummy hydro pressure and a generated mesh is presented in Figure 8-9.

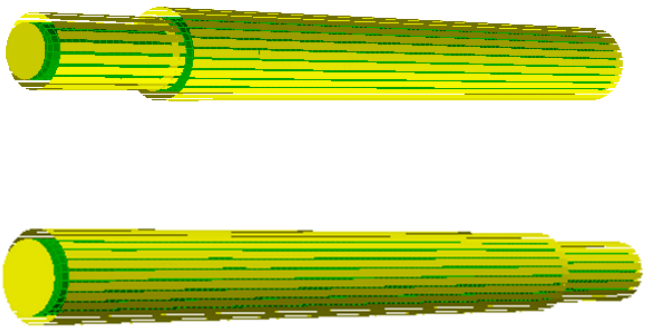

Figure 8-9: Illustration of completed FE-model

8.2.3 HydroD

HydroD utilizes “wizards”, which guides the user through the necessary steps to set up an analysis [35]. There are in general three wizards available in HydroD, including Stability wizard, Wadam wizard and Wazim wizard. The wizard applicable for establishing the frequency dependent added mass, damping and RAOs is the Wadam wizard. The first option was to select between four main model configurations, including panel model, Morison model, composite model and the dual model. The panel model is used for large submerged volumes for calculation of hydrostatic and hydrodynamic forces from potential theory [35]. The Morison model is applicable for calculation of hydrodynamic loads on slender structures using the Morison’s equation [36]. The composite model is a combination of the panel model and Morison model, and evaluates hydrodynamic forces on structures containing both large volume elements and small volume elements [36]. The dual model is also a combination of the panel model and Morison model, but is applicable when both potential theory and Morison’s equation shall be applied to the same part of the model [36].

For the purpose of modelling the Spar buoy, the panel model was selected. First, inputs regarding the domain of the analysis, what model to use in the analysis and what outputs to include in the analysis was specified in the “settings” tab of the wizard. A frequency domain analysis was selected. As only linear wave responses are evaluated in the presented work, obtaining the desired output in the frequency domain is sufficient, ref. section 5.5.3.1. Furthermore, it was specified to use the element model for the analysis, which enables the finite element model generated in GeniE to be imported. After the wizard set up was completed, it systematically went through 11 steps of needed input to perform the analysis.

Step 1: *Create direction set*

The direction set was taken from 0 to 180 degrees with 30 degrees increment to form a total of 7 directions to be evaluated.

Step 2: *Create frequency set*

The frequency set was created with the first value of 0.5s, last value of 25s, and an increment of 0.5s to form a total of 50 frequencies to be included in the analysis. This was done to ensure that the generated frequency set captured all periods containing relevant wave energy, while also obtaining enough data points to generate reliable results in OrcaFlex.

Step 3: *Create location*

The location specifies the density and kinematic viscosity of air and the water, along with the water depth at the location. The depth was set to 320 meter to represent a typical operation site for the offshore turbine system, while the other physical parameters was set according to the information given in section 7.3.

Step 4: *Create frequency domain condition*

The frequency domain condition was generated by specifying the direction and frequency sets created in step 1 and 2. A wave amplitude may also be specified at his stage, but this setting is only relevant for Wasim [35] and was consequently not altered in the presented analysis.

Step 5: *Create hydro model*

The hydro model represents the offshore structure, where inputs like the panel model and mass model will be integrated at later stages. The structure was first characterized as a floating unit, before a

baseline z-position, an AP (aft perpendicular) x-position and a FP (forwards perpendicular) x-position was specified. These position parameters were set to zero, as they are only relevant when specifying a trim and heel angle from the AP and FP position, which was not done in the presented work.

Step 6: *Create panel model*

The FE-model created in GeniE was imported into HydroD at this stage. It is possible to specify symmetry around the XZ-plane, YZ-plane or both for the imported model. This reduces calculation time and memory requirements, as the FE-model may be modelled as one-half or one-fourth of the total model. This was however not done for the presented analysis and these options were consequently left un-checked. The model was then translated in the z-direction to represent the appropriate draft of the studied floater.

Step 7: *Create loading condition*

A loading condition in HydroD is defined by the z-coordinate of the waterline, trim and heeling angles. The z-waterline was set to z=0, in order to be consistent with inputted draft in step 6. The trim and heeling angles was also set to zero to represent an initial stable floater.

Step 8: *Create mass model*

At this stage the mass properties, position of center of gravity and the radius of gyration in the x, y and z-directions were specified. As discussed in section 8.2.1, it was desired to represent the entire turbine system including ballast, generator and rotor assembly by using only the floating geometry as the panel model. These parameters were consequently specified as user defined inputs in accordance with the results gained in the Inventor models.

Step 9: *Create damping matrix*

This damping matrix is for additional damping [35], and is left blank in the presented analysis.

Step 10: *Create run*

A Wadam run contains all the information required to execute the Wadam analysis [35]. The run dialog is divided into three tabs, “input”, “execution directives” and “output directory”.

In the input tab, a single body analysis was specified as only one structure was included in this analysis. The hydro model was then set to the model generated in step 5, and the loading conditions was specified to the loading conditions established in step 7. Lastly, the environmental condition was set to the condition specified in step 4.

The execution directives tab specifies numerous instructions to the program of how to perform the analysis concerning global response, structural loads and data checks with appropriate standards. Not all options will be presented here, but it is informed that the characteristic length and the motion reference point were altered. The characteristic length is used to make the outputs non-dimensioned, and is often set to the largest horizontal distance between two points on the average immerged surface [35]. This was therefore set to the appropriate diameter of the studied floater. Furthermore, it is of most importance to be consistent with the motion reference point in the OrcaFlex simulation and HydroD, as results are only valid for that reference point. This was set to coincide with the global origin in the analysis, which coincides with the SWL at the middle of the evaluated floater.

Step 11: *Run analysis*

8.2.4 Orcaflex

It was decided to model a vessel from scratch in the OrcaFlex simulations in order to maximize the results established in the HydroD analysis. The modelling procedure will be evaluated in the following.

8.2.4.1 General

General data includes specification of the units used in the analysis, integration method and time steps, and the simulation's ramp-up time and duration. The units were set to the basic SI-units to be consistent with the outputs gained from the HydroD analysis.

The ramp up time was specified to 100 seconds to allow the waves to be sufficiently generated before data is gathered. The simulation time was set to 3600 seconds, as the environmental state given in section 7 uses an average period of one hour according to specifications given in DNV-OS-J101 [24].

OrcaFlex offers two integration schemes, explicit and implicit. The explicit integration solves the equation of motion for each free body and line node, which is integrated using forward Euler integration. This process is repeated for each time step, which typically has to be very short to form a stable integration process [37]. The implicit integration solves the equation of motion for the entire system, rather than evaluating each node in the model. This demands an iterative solution method for each time step, which generally increases the computation time per time step compared to the explicit method. However, the implicit scheme is stable for longer time steps, which often results in an overall lower computation time [37]. The implicit method however have some limitations and none of the following elements can be included in the analysis when using implicit integration method:

- Superimposed motions
- Time domain VIV models
- Seabed damping
- Soil damping
- Line clashing

Superimposed motions gives the vessel an offset from the initial position, which is not of relevance in the presented simulation. The same may be stated for the line clashing, which is used to model contact between two lines, while the time domain VIV model is outside the scope of work. Seabed damping and soil damping might have some influence on the behavior of the mooring lines. However, mooring lines gain their primary restoring force by the suspended line weight and changes in the line's configuration with the dynamic response of the vessel, and the additional forces from seabed damping and soil damping is deemed low in comparison. This makes the implicit model suitable for performing the dynamic simulations. The time step in the implicit model has a default value of 0.1s. Some systems may require shorter time step to give reliable results, while other system may give suitable results with longer time steps [38]. Orcina strongly recommends performing a sensitivity study of the time step to ensure accuracy of the results.

8.2.4.2 Environmental conditions

The sea elevation process was represented using the JONSWAP spectrum, with a peakadness factor of $\gamma = 3.3$ and spectral width parameters of $\sigma_a = 0.07$ and $\sigma_b = 0.09$. These values represent the average of experimental data collected under the JONSWAP project, thus modelling a typical North Sea environmental state. The significant wave height and spectral peak period for the two studied environmental conditions are presented in section 7. It should also be noted that OrcaFlex uses a

pseudo-random wave generation process through a user specified seed [39]. The randomness of the generated process is then only dependent upon the randomness of the initial seed, where the same seed gives the same process [39]. This is a useful consequence for the evaluated problem description in the presented work, as it implies that the exact same wave trains may be generated between the analyses of the different floaters. This makes the maximum, minimum and mean responses imposed from the waves comparable.

The kinematic viscosity and sea density was set to the values presented in section 7.3, in order to be consistent throughout the different analysis.

It is also possible to generate a wind environment in the OrcaFlex simulation. However, this implies that the H-rotor represented in section 6.1 has to be modelled accurately in the OrcaFlex environment to obtain accurate estimates of the aerodynamic loads. This is a relatively complex and time demanding task, and it was consequently decided to model the wind environment in a simplified manner through a constant point load representing the mean wind force. The load could be set according to the wind force estimate obtained in the spreadsheet calculation. However, as stated in section 8.1.3.1, this is a relatively conservative estimate and does not accurately represent the wind-induced loadings on the H-rotor. More accurate estimates of the mean wind force is presented in [21], where CFD simulations were performed on the rotor evaluated in the presented work. The resultant values are presented in Table 8-4.

Table 8-4: Mean wind force resulting from CFD simulations presented in [21]

Wind speed [m/s]	Wind force [kN]	Operational condition
12	365	Operation
60	1200	Parked

The wind force resulting from the 12 m/s operational condition will be used to model the wind force in environmental condition 1, while the resulting force from the 60 m/s parked condition will be used to represent the wind force in environmental condition 2. As may be observed from section 7, EC 1 features a wind speed of 14 m/s, while EC 2 features a wind speed of 50 m/s. The mean wind forces therefore originates from a wind speed that is slightly different from originally intended. However, the resultant wind forces are still deemed more accurate than the estimates in the spreadsheet calculations, and will consequently be used to model the wind forces in OrcaFlex. A point load applied at the middle of the rotor blades, corresponding to 72.5 meters, was used to model the specified wind forces.

8.2.4.3 Constructing a new vessel

Creating a new vessel type in OrcaFlex implies that all relevant inputs have to be defined from scratch. This includes the structural mass and inertia properties, displacement RAOs, load RAOs, hydrostatic stiffness matrix, and frequency dependent added mass and damping matrices. These properties were obtained in the HydroD analysis. However, HydroD uses WADAM for the hydrodynamic computations, which has a native output format that is largely incompatible for import to OrcaFlex [40]. The suggested solution from Orcina is to add markup text in the .LIS file generated by HydroD. The desired output must then be located in the .LIS and the markup text added to all outputs. An alternative solution, not proposed in the OrcaFlex user manual, was to export the needed output to separate text files using the Postresp feature in HydroD, and import these text files into Excel. The parameters could then be modified to match the OrcaFlex setup of each input, and simply be copied from Excel and pasted directly into OrcaFlex. The latter method was selected in the presented work, as it was believed to be less work

intensive than adding the markup text to all desirable outputs, while also bringing the benefit of being able to fully modify and plot the RAOs, added mass and damping as desired.

The frequency dependent displacement RAOs and load RAOs was imported for the 7 directions studied, and the added mass and damping matrices were quantified for the 50 frequencies contained in the frequency set specified in HydroD. The structural properties was set according to the gained output from the respective Inventor model. Note that the floating geometries was modelled make the local coordinate system to coincide with the global coordinate system, which is located in the SWL. The reference point for the inputted results from HydroD was set to (0, 0, 0) to be consistent with the reference point specified in the HydroD analysis.

Note that wave drift quadratic drag functions (QTFs) and sum frequency QTFs may be specified when constructing a new vessel. These are used in order to capture the higher term load effects discussed in section 5.5.5. However, such QTFs was not obtained in the HydroD analysis due to time limitations, and will consequently not be evaluated in the OrcaFlex analysis. The slow drift effect that compliant floating structures are prone to experience is therefore not assessed in the presented work. The included loads in the OrcaFlex model is therefore: applied loads, first order wave loads and added mass and damping loads. This enables to assess the wave frequency responses, i.e. linear wave response, discussed in section 5.5.

8.2.4.4 Mooring lines

The mooring lines can be modelled in OrcaFlex by using “Lines”. These are flexible linear elements with the primary intention to model cables, chains and similar structures [41]. It may be noted that the lines are generated by using a lumped mass model, implying that they consist of a series of lump masses joined together by a massless spring. The lumped masses are termed nodes and the joining springs are termed segments. The properties of the segments is represented at the nodes of the segment’s end [41]. It is therefore necessary to specify the number of segments each mooring line section shall comprise in order to achieve sufficient fineness between the nodes at the line. The two line ends are referred to as End A and End B, whereas each can be regarded as free, fixed, anchored or connected to a vessel. The two ends are essentially treated in the same way, but the numbering of segments always starts at End A [41]. Furthermore, OrcaFlex provides the option of modelling attachment on the lines in form of clump weights (either buoyant or heavy components) and drag chains. The effects discussed above is illustrated in Figure 8-10.

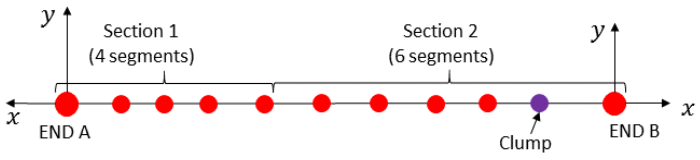

Figure 8-10: Line model in OrcaFlex, inspired from [41]

For the mooring line configuration in the presented work, it was decided to use three lines separated 120 degrees apart, as this is what was commonly observed for similar concepts through the state of the art research. Furthermore, the mooring line tension is sensitive to the direction of the environmental loading [4]. The lines are therefore oriented such that the environmental loadings acts in the most unfavorable direction in order to assess the dynamic response in a worst-case scenario. This will be the

mooring orientation presented in Figure 8-11, where mooting line 1 is oriented directly into the incoming wave and wind loadings, while mooring line 2 and 3 is in the lee-side of the incoming forces.

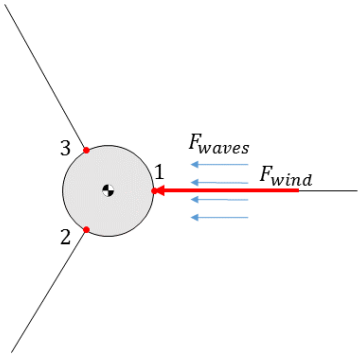

Figure 8-11: Illustration of mooring line orientation

The needed input to specify the mooring system includes the connection points to vessel, radius to anchor point, un-stretched mooring line length, line mass per unit length, and other relevant mechanical properties.

It was originally intended to study different mooring line configurations in order to obtain an optimum station keeping system, as this has an influence on the hydrodynamic response of the floaters. The effect of varying the floaters draft and diameter would then be assessed by comparing the structure's hydrodynamic performance using the optimum mooring configuration identified for each floater. However, establishing the needed hydrodynamic inputs to the OrcaFlex model was more time consuming than initial planned, and the problem description was consequently reduced to perform the dynamic simulations with one common mooring line configuration. This however makes it necessary to establish a mooring line configuration that gives similar characteristics for all studied geometries, so one floater does not comprise of a more beneficial mooring line configuration with respect to dynamic motions than other studied floaters. This ensures that the difference in hydrodynamic behavior is only related to the differences in geometry, i.e. draft and diameter, and is thus in line with the problem description.

The common mooring line configuration needs to feature equal line tension, horizontal connection force and vertical connection force and arc length to touchdown point in the static sea state. This may easily be achieved by specifying an applicable radius to anchor point, un-stretched mooring line length, mass per unit length and a connection point relative to the seabed, and keeping this constant throughout the analysis. However, as previously stated, the studied Spars pitches and rolls around their respective metacenter positions, which will be different between the studied geometries due to the parametric change. The mooring lines imposes additional restoring moments in pitch and roll, and it needs to be ensure that these moments are of the same magnitude between each studied floater. In other words, the connection point must be set to a fixed distance relative to the metacenter so the moment arm in the restoring moments are equal. In the presented work, the connection point was set to coincide with the different geometries' metacenter, as done in [29] and [21]. The mooring lines does therefore not impose any additional restoring moment in pitch and roll, making the resulting motions solely based on properties of each individual floater.

However, this makes the arc-length to touchdown point and line tension different between the studied floaters if the radius to anchor point, un-stretched mooring line length and mass per unit length is held constant as stated above. At first, it was believed that the un-stretched mooring line length could be altered to give equal line tension and arc length to touchdown point in a static state, and therefore

achieve identical mooring line configuration between the floaters. However, even though similar tensions in the connection point were achieved, the decomposed force components were different between the studied geometries. Floaters featuring a metacenter position closer to the seabed gained higher horizontal force and consequently smaller vertical force, leading to more favorable surge characteristics and less favorable heave characteristics induced from the mooring system. The opposite may be stated for floaters featuring a metacenter position closer to the sea surface. As already mentioned, the arc-length to touchdown point was set to be similar between the studied geometries to gain alike tensions at the connection point by altering the un-stretched mooring line length. However, the vertical distance from seabed to the connection point was different between the studied geometries due to the varying position of the metacenters. This resulted in a varying angle between the outgoing mooring line and the Spar's vertical centerline, leading to the difference in the decomposed force components at the connection point. Clearly, this is not in line with the set goal of isolating the difference in hydrodynamic performance to the geometrical features of each individual studied floater. The mass per unit length could possibly be altered to achieve the same vertical and horizontal force component, while still obtaining the same arc length to touchdown point in the static analysis. However, this would lead to an inaccurate basis for comparison in the dynamic simulation, as some floaters would then obtain larger restoring forces per unit suspended mooring line. The only solution to make the mooring system 100% equal between the studied floaters, while still connecting the lines in the floater's metacenters, was to alter the water-depth so each analysis featured the same water depth relative to the connection points. The identical mooring system was then achieved by keeping the line mass density, un-stretched mooring line length and the distance to anchor point relative to the studied geometry's periphery constant between the analyses.

These parameters therefore had to be determined to achieve a suitable mooring line configuration. The design criterion for the mooring system was to avoid vertical pull-up loads in the anchor in the extreme environmental condition, i.e. have some excessive mooring line resting on the seabed in the one-hour storm scenario presented in section 7.2. Some initial trials were performed with the mooring configuration used on the OC3 phase IV floater, as a relatively detailed description of this system is available. The properties for the OC3 Hywind mooring system is presented in Table 8-5 [29].

Table 8-5: Initial mooring line properties, presented in [29]

Parameter	Value	Unit
Number of mooring lines	3	-
Angle between adjacent lines	120	°
Depth to anchor points below SWL	320	m
Radius to anchor point from platform centerline	853.87	m
Mooring line diameter	0.09	m
Un-stretched mooring line length	902.2	m
Mooring line mass density	77.7066	kg/m
Mooring line extensional stiffness	384 240 000	N

However, these initial trials resulted in vertical loads in the anchor point, and the mooring system used on the OC3 Hywind floater was consequently not suitable to absorb the imposed loadings of the extreme environmental condition in the analysis performed in the presented work. It was therefore decided to establish a suitable mooring line through a series of trials. These trials will be discussed further and presented in section 11.2. Note that the mooring line diameter and extensional stiffness

was set according to the information presented in Table 8-5, while the mooring lines Poisson ratio and Torsional stiffness was set to 0.5 and 80000 Nm^2, as suggested by the line type wizard in OrcaFlex. The trials therefore only assesses the radius to anchor point, un-stretched mooring line length and line mass density needed to give zero vertical pull-up force in the anchor.

8.2.4.5 Other inputs

Other inputs included in the OrcaFlex model includes:

- Seabed was modelled as a flat plane.
- The anchored end's height above seabed coordinate was set to zero to model mooring lines resting on the seabed without penetration.
- A linear seabed model was selected. The seabed resistance is then modelled as a spring in both normal and tangential direction, proportional to the penetration of the mooring line [42]. However, the mooring lines are modelled to rest on the seabed without penetration, making this parameter of less importance. The stiffness was consequently left to the standard value of 100 kN/m.
- Water depth was varied to give identical mooring lines, as discussion above.
- Mooring lines were categorized as general, which applies to all elements that shall not be modelled as a homogeneous pipe or pipe-in-pipe or pipe-on-pipe constructions [43].
- The compression was set to limited in the mooring lines, implying that OrcaFlex does not allow compressive load greater than the Euler load [44].
- Drag, lift and added mass coefficients in the normal and axial direction for the mooring lines were left to their default values. A detailed evaluation of these coefficients are of less importance as the mooring lines are not severely affected by moving water particles, as current is not evaluated in the presented work and the mooring lines are connected far from the sea surface. The default values includes a drag coefficients of 1.2 in the normal directions (x and y-directions) and 0.0080 in the axial direction (z-direction), a lift coefficient of zero in all directions, and an added mass coefficient of 1.00 in the normal directions and zero in the axial direction.
- The lines were segmented into lengths of 2 meters, which was deemed sufficiently fine for all relevant purposes.
- The friction coefficient between the seabed and mooring lines were set to 0.69, to model a muddy seabed with sand according to information given in [45]. Note that the coefficient was set to the sliding coefficient instead of the breakout coefficient for conservative reasons.
- The connection stiffness was set to zero to represent a flexible connection between the mooring lines and the Spar buoy, which is free to rotate with no resistance. This may not be the most realistic illustration of the connections, but is deemed applicable for modelling the system's global response.
- A structural damping in the mooring line in the form of a Rayleigh damping was not included, as this quantity is usually negligible for subsea lines [46].
- All other inputs were left to their default values.

9 Result, spreadsheet calculation

As previously mentioned, the aim with the spreadsheet calculation is to evaluate a number of floating geometries to study the effect of varying the floater's draft and diameter on the system's hydrostatic performance and obtain geometries that will be studied further in dynamic simulations. Some design criteria therefore needs to be specified to ensure that realistic and promising geometries are selected for the dynamic simulations.

9.1 Design criteria

With the aforementioned statements in mind, the following criteria has been identified for the spreadsheet calculations.

- Natural periods should be well above the periods containing significant wave energy. However, the natural periods in surge, sway and yaw are undefinable in the spreadsheet calculation, and the natural periods in heave, pitch and roll will therefore only be evaluated. It was decided to demand natural periods in these DOFs of 25 seconds or more, as is common design procedure according to [26].
- A positive $\overline{GM}$ should be ensured in order to obtain a stable floater. The desired magnitude of $\overline{GM}$ is assessed trough the static inclination angle.
- Static inclination angle should not exceed 5 degrees in environmental condition 1 and 25 degrees in environmental condition 2. These values were established based on initial trials of a modified version of the Hywind test pilot floater. The term "modified" is used as the tapered region between the two diameters was neglected to be consistent with the parameters presented in section 6.2.1. By setting the static heel criterion similar to the output gained for this proven concept ensures a floating system with suitable heeling characteristics. It may be noted that in the static heeling angles obtained in the spreadsheet calculations are relatively conservative, as the airfoils are modelled as flat plates and the modelled linear wave is based on significant wave height and spectral peak period.

9.2 Identifying initial displacement

The needed displacement in order to achieve a suitable floating system with respect metacentric height and static heeling angle is evaluated first. The spreadsheet is constructed such that the amount of ballast is set to the differential mass between the floater, generator and rotor and the displacement. The displacement therefore has a direct influence on the amount of ballast, which influences the position of the system's CoG and metacentric height. For simplicity, the floaters studied in this section are modelled as a single column Spar buoy comprising of only one diameter, meaning that D0 = D1.

For the purpose of evaluating needed displacement, it was decided to generate 36 floater combinations with drafts varying from 25 to 150 meters with 25 meters increment, and diameters varying from 5 to 10 meters with 1-meter increment. The resulting metacentric height for the different draft and diameter combinations is presented in Table 9-1.

Table 9-1: Resulting metacentric height for the 36 studied cases to evaluate initial displacement

		Draft					
		150	125	100	75	50	25
Diameter	5	17.96	8.24	-2.46	-15.14	-32.73	-70.03
	6	27.68	18.43	8.52	-2.74	-17.35	-45.36
	7	35.55	22.72	15.10	4.65	-8.22	-30.82
	8	37.39	28.56	19.37	9.43	-2.35	-21.50
	9	40.06	31.33	22.31	12.71	1.67	-15.16
	10	41.99	33.33	24.43	15.07	4.55	-10.62

These values are also graphically illustrated in Figure 9-1, where the metacentric height is plotted versus the drafts and diameters. The intersections in the diagram represents the data points presented in Figure 9-1. There are also lines included in the figure indicating where the surface plot intersects $\overline{GM} = 0$ and $\overline{GM} = 20$.

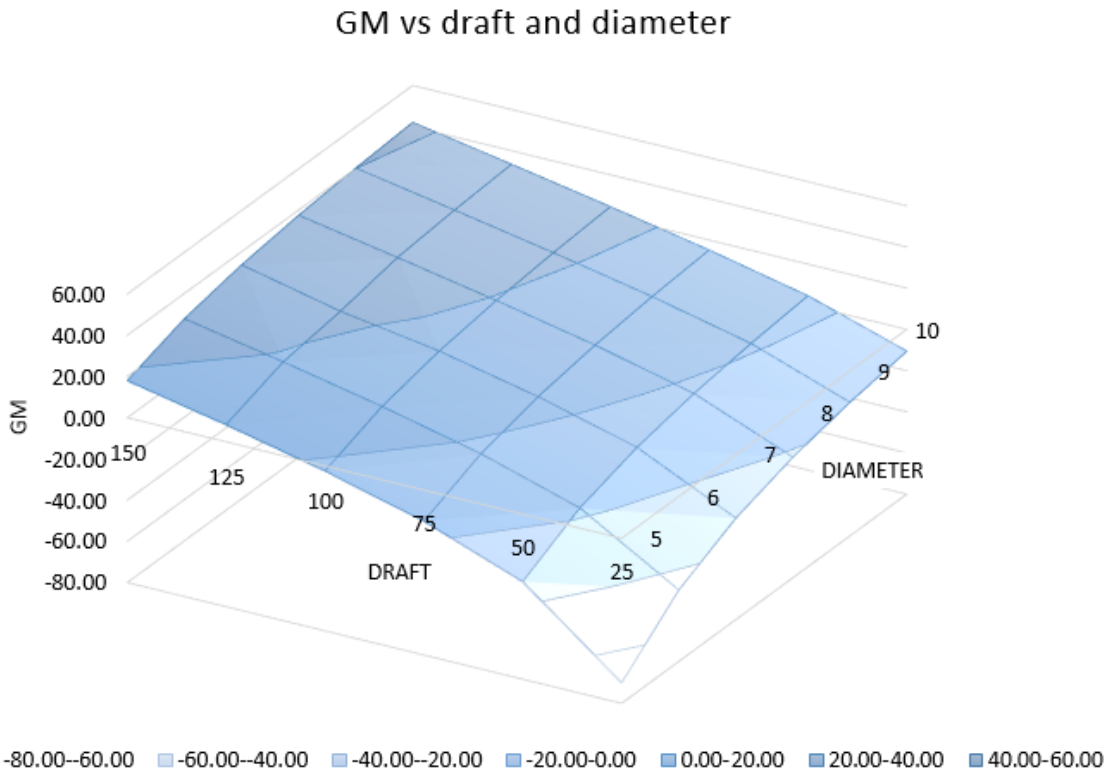

Figure 9-1: 3D plot of metacentric height vs diameter and draft

From the intersection line $\overline{GM} = 0$, it may be observed what floater combinations gives a positive metacentric height. For example, a diameter of 5 meters demands a draft of 125 meters in order to obtain a positive metacentric height, while a diameter of 9 meters needs a 50 meters draft. However, a positive $\overline{GM}$ does not necessarily mean a sufficient $\overline{GM}$. The needed magnitude of the metacentric height may be evaluated by the static heeling angle.

The static heeling angle in environmental condition 1 for diameters 7 to 10 and drafts 150 to 75 meters is presented in Figure 9-2. The other drafts and diameters combinations are not included in the figure as the series contained some floaters with negative metacentric height, which breaks down the inclination angle calculations in the spreadsheet analysis. The magnitude of the inclination angle in the

figure is color coded, where the blue area represents 0 to 5 degrees of inclination and the yellow area indicates 15 to 20 degrees of inclination.

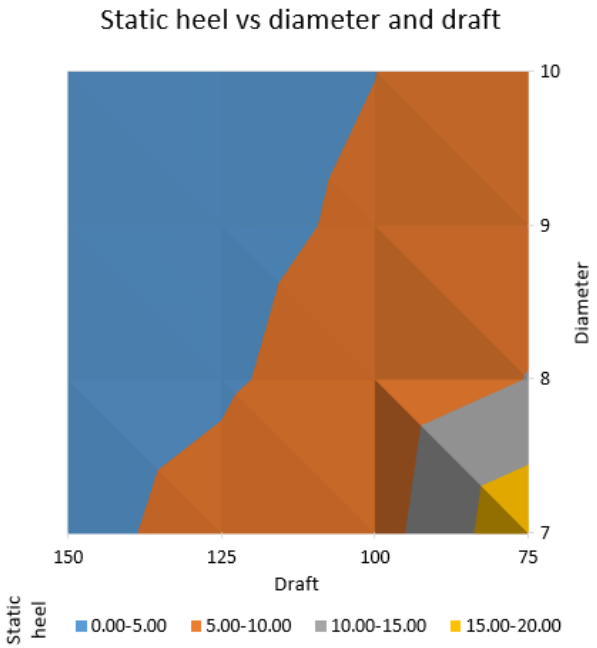

Figure 9-2: Static heel vs draft and diameter

In order to meet the static heel criterion in environmental condition 1 of 5 degrees, the floater combination has to be on the intersection of the blue and orange area. In order to evaluate which floaters this includes, the draft and diameter combinations with associated static heel in environmental condition 1 presented in Table 9-2.

Table 9-2: Diameter and draft combinations with the associated static heeling angle in EC1

		Draft			
		150	125	100	75
Diameter	7	4.34	5.80	7.80	18.97
	8	3.86	4.71	6.19	10.15
	9	3.59	4.29	5.42	7.80
	10	3.41	4.03	4.97	6.72

As may be observed, the draft and diameter combinations 7x125, 8x100, 9x100 and 10x75 is on the limit of satisfying the static heel criterion, and will therefore be evaluated further to gain indications of the needed displacement in order to give satisfactory floater characteristics. The displacement and metacentric height of the aforementioned floater combinations is presented in Table 9-3.

Table 9-3: Critical floater combination displacements and associated metacentric height

Floater	Displacement [tons]	$\overline{GM}$
7x125	**4733.59**	**22.72**
8x100	**5152.21**	**19.37**
9x100	**6520.77**	**22.31**
10x75	**6037.75**	**15.07**

The needed displacement is therefore in the range of:

$$\nabla_{\text{estimate}} = [4500 \text{ tons}, 6500 \text{ tons}]$$

It may be noted that metacentric height and heeling angle is not solely dependent upon the amount of displaced volume, but also on the floater geometry. This effect is clearly illustrated from the values presented in Table 9-3, where floater combination 7x125 features the highest metacentric height, while still displacing the least amount of volume among the presented floater combinations. Evaluating the needed displacement based on $\overline{GM}$ is therefore a rather complex task, as $\overline{GM}$ is heavily dependent on a number of parameters. Nevertheless, the efforts made above still gives reasonable indications of the floating systems needed displacement.

However, only one displacement should be evaluated to isolate the effect of varying the diameter and draft on the floating system's performance. It was decided to study a displacement of 5300 tons, as this is the displacement of the proven Hywind test pilot. Furthermore, this represents a displacement value approximately in the middle of the obtained displacement range. For detailed results of the 36 floaters studied to identify the needed displacement, reference is made to Appendix A.

9.3 Parametric study

In this section, the diameter and draft of the lower section of the floater (D_0, L_0) will be altered in order to study the effect this implies on the system's hydrostatic performance. The section also aims at establishing floater geometries that satisfies the design criteria stated in section 9.1, which may be used for further evaluation in the dynamic simulations. The single column approximation made in the previous section is discharged, and D_1 and L_1 is set to the numerical values discussed in section 6.2.1, i.e. 4 and 10 meters, respectively.

A set of 6 floaters were established by altering the drafts from 150 meters to 25 meters with 25 meters increment, and obtaining the needed diameter of the bottom section to give a displacement of 5300 tons. The upper draft limit of 150 meters was set to make the studied floaters applicable to more locations, as high drafts demand deeper water depths on the particular site to accommodate the floater and the associated mooring system used for station keeping purposes. The lower limit of 25 meters was a consequence of the specified increment.

The resultant geometries are presented in Table 9-4. For the floater naming system, reference is made to section 6.2.1, Table 6-3.

Table 9-4: Studied geometries in the spreadsheet analysis

Floater	D_0 [m]	L_0 [m]	D_1 [m]	L_1 [m]	Displacement [tons]
6.78-140x4-10	6.78	140	4	10	5309.66
7.47-115x4-10	7.47	115	4	10	5294.79
8.45-90x4-10	8.45	90	4	10	5302.13
9.94-65x4-10	9.94	65	4	10	5298.92
12.67-40x4-10	12.67	40	4	10	5298.05
20.69-15x4-10	20.69	15	4	10	5298.04

It may be noted that there exist some deviations in the displacement from the 5300 tons target. More significant digits on the bottom diameter could have been included to obtain displacement values closer to the 5300 tons. However, it was decided to keep the significant digits to only two, as including more digits did not seem appropriate from a tolerance perspective, and accept the featured deviations from the target value.

The calculated mass and stability parameters of the specified geometries are presented in Table 9-5.

Table 9-5: Comparison of key parameters for the studied floaters

Floater	Floater mass [tons]	Ballast mass [tons]	KG [m]	BM [m]	KB [m]	GM [m]	Ratio d/D
6.78-140x4-10	645.98	4183.09	42.07	0.0024	71.82	29.75	22.12
7.47-115x4-10	593.79	4220.41	35.42	0.0024	59.02	23.60	16.73
8.45-90x4-10	538.19	4283.35	28.81	0.0024	46.21	17.41	11.83
9.94-65x4-10	476.45	4341.88	22.35	0.0024	33.41	11.07	7.55
12.67-40x4-10	409.89	4407.57	16.02	0.0024	20.61	4.59	3.95
20.69-15x4-10	371.39	4446.06	9.86	0.0024	7.80	-2.05	1.21

From the table, it may be realized that there is a strong tendencies of a high draft and low diameter floater obtains higher metacentric height than low draft and high diameter floaters. This is illustrated in Figure 9-3, depicting the resulting $\overline{GM}$ versus the draft-to-diameter ratio for the six studied floater combinations, see Table 9-5. Note that the ratio was obtained by dividing the total draft with the diameter of the lower section of the floater (D_0), as the diameter of the upper section is kept constant. This trend will be covered in greater detail in the discussion section.

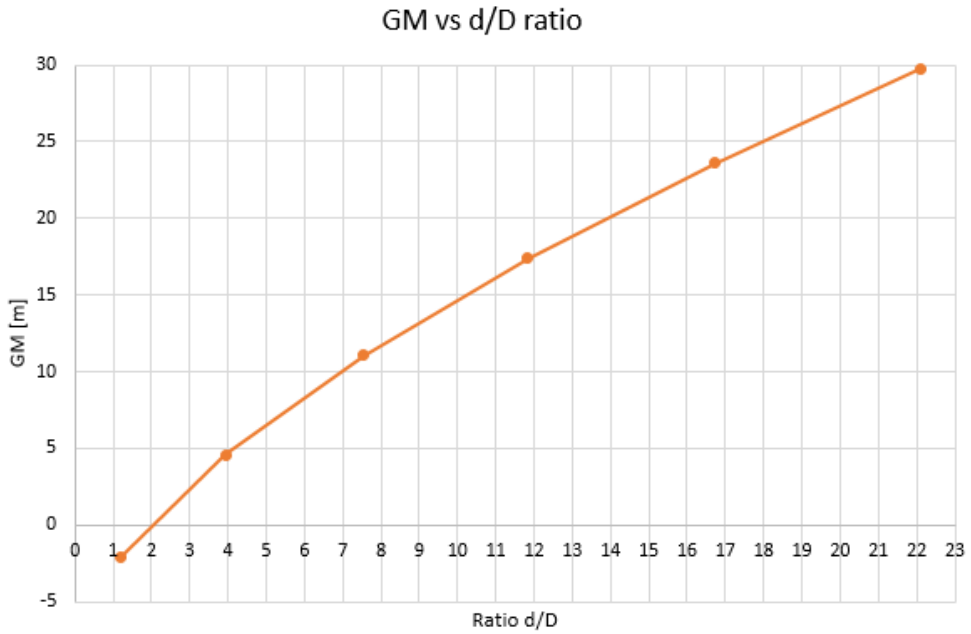

Figure 9-3: Metacentric height as a function of draft-to-diameter ratio for the studied geometries

The resulting static heeling angles and natural periods for the studied geometries are presented in Table 9-6. Note that the natural period in roll is not included in the table, as this is equal to the natural period in pitch due to the symmetries of the Spar buoy. Furthermore, the natural period in pitch and static heel

angles for floater 20.69-15x4-10 is not included as the associated $\overline{GM}$ was negative, implying that the formulas for these parameters breaks down in the spreadsheet analysis.

Table 9-6: Natural periods and static heel angle for the studied floaters

Floater	Static heel [deg]		Natural periods [s]	
	EC1	EC2	Heave	Pitch
6.78-140x4-10	**2.70**	**15.70**	**41.05**	**28.91**
7.47-115x4-10	**3.01**	**17.50**	**41.10**	**27.66**
8.45-90x4-10	**3.45**	**20.33**	**41.32**	**26.74**
9.94-65x4-10	**4.23**	**26.20**	**41.69**	**26.99**
12.67-40x4-10	**6.85**	**44.14**	**42.73**	**32.65**
20.69-15x4-10	N/A	N/A	**48.97**	N/A

As may be observed, floaters with higher drafts and smaller diameter generally obtains a lower static heel angle in both environmental conditions. This effect is illustrated in Figure 9-4, depicting the static heel angle in environmental condition 1 on the left axis and environmental condition 2 on the right axis as a function of the draft-to-diameter ratio for each floater.

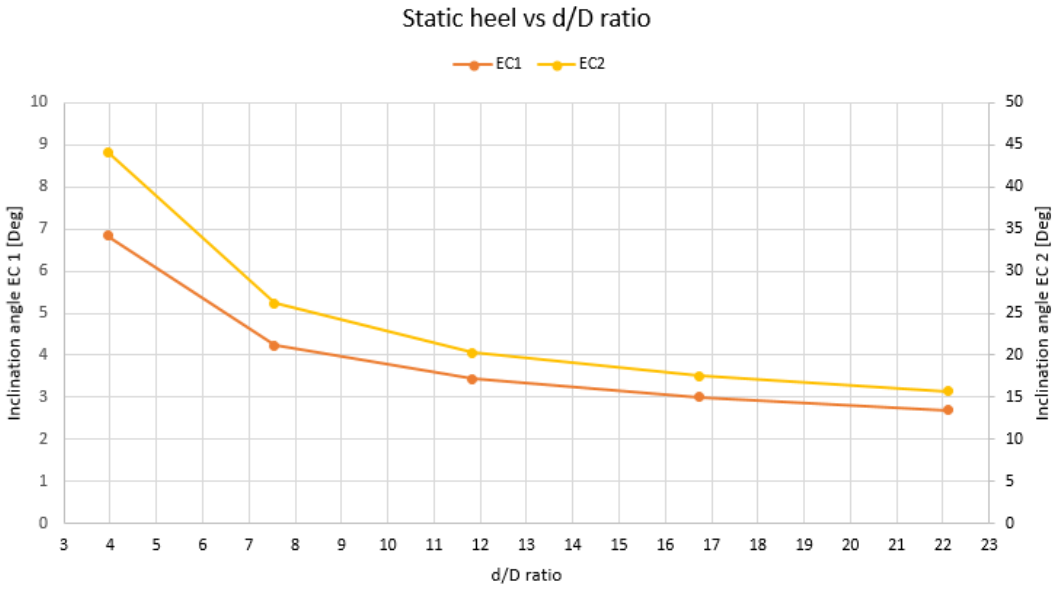

Figure 9-4: Static heel vs d/D ratio for the studied floaters in both environmental conditions

It may also be realized by observing Table 9-6 that all floater combinations features natural periods in heave, pitch and roll over 25 second, consequently fulfilling the requirement of natural periods.

Based on the presented results, it may be it may be concluded that floater 6.78-140x4-10, 7.47-115x4-10 and 8.45-90x4-10 satisfies all of the criteria specified in section 9.1, and is suitable for further evaluation in the dynamic simulations. The other floaters fails to fulfill the static heeling criterion in either EC1 or EC2. Floater 9.94-65x4-10 however fulfills the specified criterion in EC1, and is close to fulfilling it in EC2. In order to evaluate a broader specter of draft-to-diameters ratios to better evaluate the effect of varying the principal hull parameters on the system's hydrodynamic performance, it was decided to include floater 9.94-65x4-10 in the dynamic analysis. However, establish the needed input and running the hydrodynamic simulation is a relatively time consuming task, and it was therefore desired to keep the number of studied floaters in the dynamic simulations to three. Floater 6.78-140x4-10 was consequently discarded for further analysis, in favor of floater 9.94-65x4-10. A summary of the

established floaters for further evaluation is presented in Table 9-7. For full results of the six studied geometries in this section, reference is made to Appendix A.

Table 9-7: Summary of floaters for further evaluation

Floater	$\overline{GM}$	Natural periods		Static heel angle	
		Heave	Pitch	EC1	EC2
7.47-115x4-10	23.60	41.10	27.66	3.01	17.50
8.45-90x4-10	17.41	41.32	26.74	3.45	20.33
9.94-65x4-10	11.07	41.69	26.99	4.23	26.20

An illustrative representation of these floaters modelled in Inventor is presented in Figure 9-5. As stated in section 8.2.1, the total mass, center of gravity and radius of gyration in the x, y and z-directions needs to be extracted from the inventor models representing the total turbine system (including rotor, floater, ballast and generator) for further use in HydroD. These values are given in Table 9-8. For values with increased accuracy, reference is made to Appendix B.

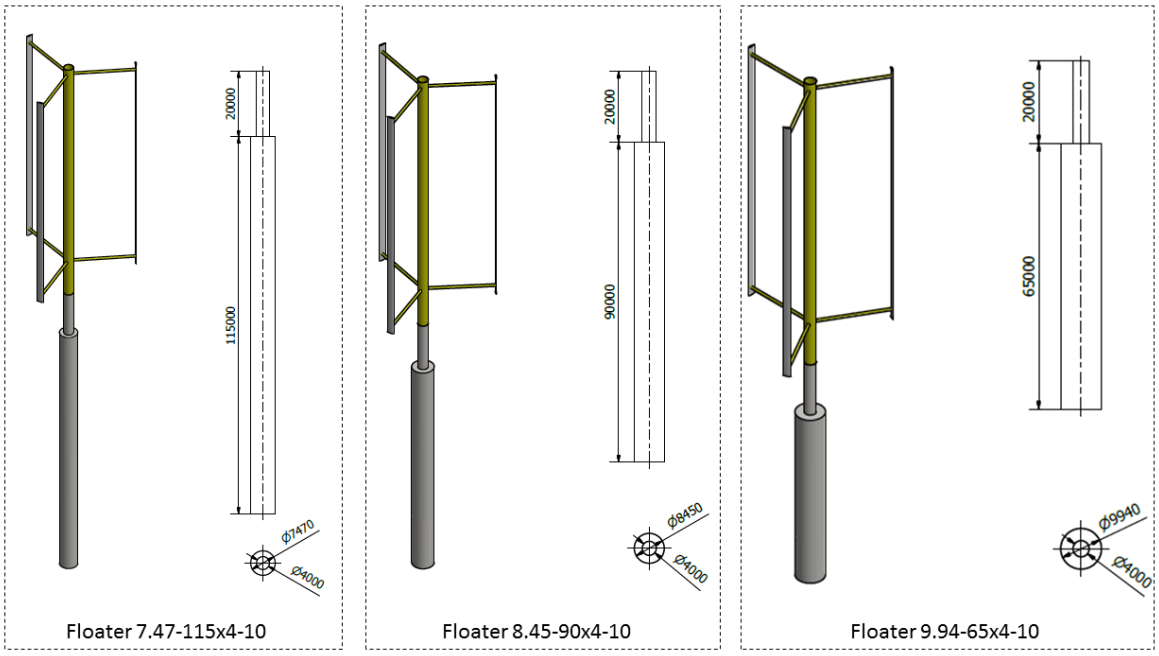

Figure 9-5: Illustration of identified floaters for further evaluation

Table 9-8: Resulting inertia properties from the Inventor models comprising of the entire turbine system

Floater	CoG relative to keel (x, y, z) [m]	Total mass, included ballast [tons]	Radius of gyration (Rx, Ry, Rz) [m]
7.47-115x4-10	(0, 0, 35.27)	5294.78	(52.31, 52.31, 5.09)
8.45-90x4-10	(0, 0, 28.66)	5302.13	(45.28, 45.28, 5.26)
9.94-65x4-10	(0, 0, 22.19)	5298.93	(38.58, 38.58, 5.55)

10 Result, HydroD

The outputs from the hydrodynamic analysis in HydroD includes frequency dependent added mass and damping matrices, displacement RAOs and load RAOs, which will be presented in the following. However, as stated in section 8.2.3, a convergence study should be performed in relation to the finite element method to ensure the validity of the results. A convergence study will therefore be presented first for the three floaters obtained in section 9.3, before the results from the deemed converged solution are presented in section 10.2.

10.1 Convergence study

It was decided to use the damping coefficients for the basis of the convergence study. Added mass could also be used for this purpose, but this quantity features less variation with respect to frequency than damping, making it difficult to assess the convergence. As stated in section 5.5.2.2, the symmetries of the Spar buoy makes some damping modes equal in magnitude and possibly opposite in direction. This applies to damping B11 being equal to B22, B24 being equal in magnitude but opposite in direction to B15 and B55 being equal to B44. The other modes are zero for a Spar buoy. The convergence study will therefore base itself on the damping modes in surge-surge (B11), sway-roll (B24), heave-heave (B33) and pitch-pitch (B55).

It may be noted that floater 8.45-90x4-10 features two more mesh models compared to the convergence study performed in relation with floater 7.47-115x4-10 and 9.94-65x4-10. The convergence study was performed for this floater first, where it was observed that some of the mesh models (3, 4 and 5) featured similar number of panels. There are consequently small differences in these models, and mesh model 3 and 4 was therefore excluded for floater 7.47-125x4-10 and 9.94-65x4-10 in order to ease the workload. Furthermore, the convergence study for floater 8.45-90x4-10 was performed for a different frequency set than floater 7.47-125x4-10 and 9.94-65x4-10. An initial frequency range from 0.05 rad/s to 5 rad/s with increments of 0.1 rad/s was specified, as it was believed to capture all relevant periods that may be encountered in the specified environmental conditions. However, after the convergence study had been performed and the outputs had been extracted from HydroD, it turned out that the specified frequency set did not contain enough values in the higher frequency range, i.e. lower periods, for OrcaFlex to generate reliable results. The frequency set was therefore reevaluated to a lower value of 0.5 seconds and an upper value of 25 seconds, with a 0.5-second increment. It was decided to base the convergence study for floater 7.47-125x4-10 and 9.94-65x4-10 on this frequency set in order to study the convergence of the solution at the frequency range used in OrcaFlex. It was unfortunately not enough time to redo the convergence study of floater 8.45-90x4-10 with the improved frequency set, which is the reason for the presented convergence studies bases itself on different frequencies. This should however not alter the conclusions of the convergence study, as the significant damping values are present at frequencies included in both frequency sets.

10.1.1 Floater 7.47-115x4-10

In order to generate different mesh models with varying fineness, i.e. number of elements, 5 mesh densities were used. These are presented in Table 10-1, where the element length specifies the length of one mesh element. A smaller element results in a finer mesh.

Table 10-1: Mesh densities used in the convergence study

Mesh density	Element length [m]
1	1.5
2	1.0
3	0.8
4	0.6
5	0.4

For the convergence study of floater 7.47-115x4-10, a total of five mesh models was generated with an increased fineness. These are presented in Figure 10-1, where a color-coding scheme has been implemented to illustrate what mesh density is applied to the particular section of the model. The density numbering presented in the bottom right in Figure 10-1 is set to match the numbering system presented in Table 10-1. Mesh model 1 therefore features a mesh comprising of an element length of 1.5 meter applied to all sections, while mesh model 5 comprises of a mesh with element length 0.6 meters applied to the bottom section and 0.4 meters applied to the top section.

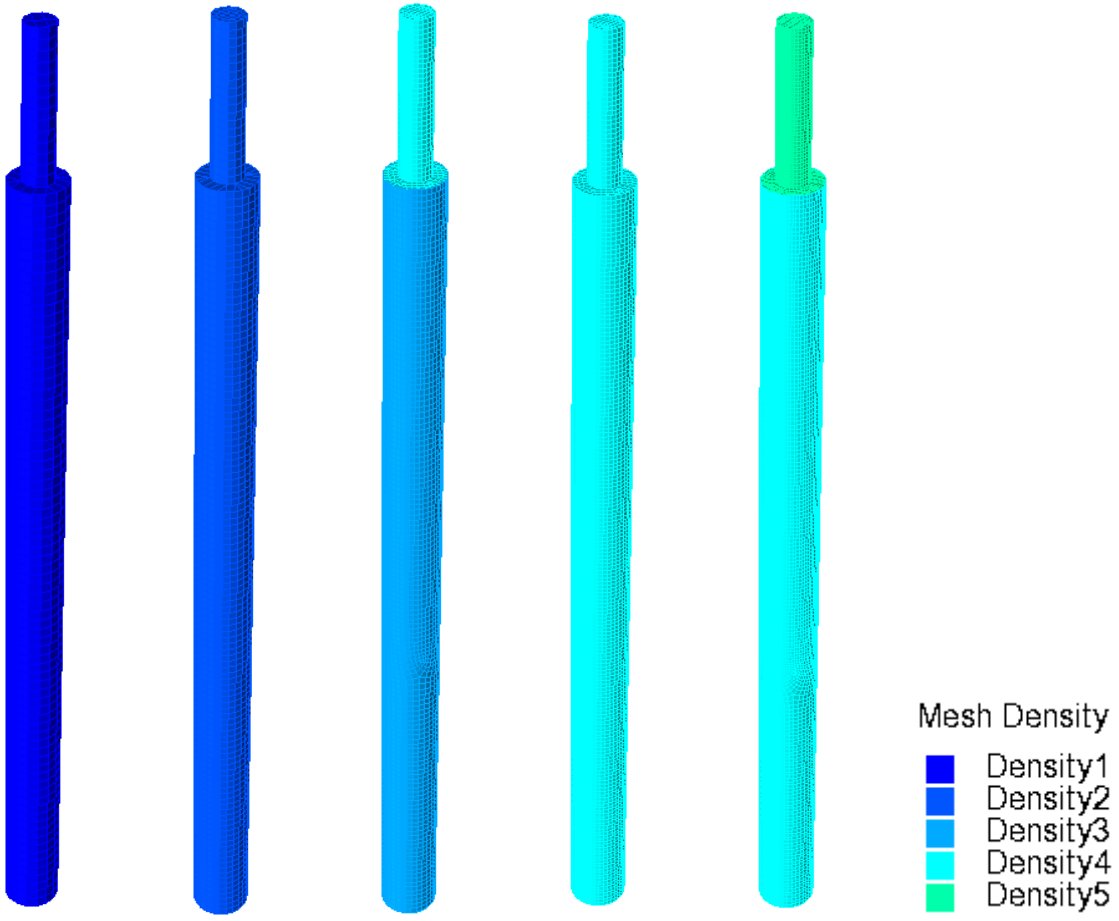

Figure 10-1: Illustration of mesh models used in the convergence study for floater 7.47-115x4-10

The resulting number panels for each mesh is presented in Table 10-5, along with the resulting freeboard, water-plane area and metacentric height recognized by HydroD

Table 10-2: Presentation of mesh properties and resulting floating characteristics for the different mesh models, floater 7.47-115x4-10

Mesh model	Number of panels	Execution time [s]	Freeboard [m]	Δz [%]	GM [m]	ΔGM [%]
1	1426	-	-	-	-	-
2	3150	226	4.93	50.7	24.5366	3.41
3	6181	4771	7.68	23.2	24.1531	1.79
4	8712	9232	8.19	18.1	24.0291	1.27
5	12210	18054	8.86	11.4	23.9578	0.97

As may be observed there is a steady increase in the number of panels between the mesh models, which is generally desirable in a convergence study to evaluate the converging characteristics of the solution. The execution time also increases with the number of panels, where mesh model 5 featured a computation time of about five hours. Furthermore, there was an issue of HydroD recognizing too little displaced volume in the equilibrium position obtained in the spreadsheet analysis with a freeboard of 10 meters. HydroD consequently increased the draft to displace more volume until it obtained what it recognized as an equilibrium position according to Archimedes' principal. This reduced the freeboard, which may be observed in Table 10-2. Mesh model 1 did not converge, as HydroD failed to obtain an equilibrium position before the entire vessel was submerged.

This issue presented above is related to the mesh models generated in GeniE and HydroD. The mesh elements are constructed by drawing a straight-line segment between the nodes in the FE-model. This implies that curved or twisted surfaces will be represented with planar panel elements [36]. The circular shape of the Spar buoy are therefore generated by forcing planar panel elements onto the periphery of the geometry, resulting in deviations from the perfect circular shape, as illustrated in Figure 10-2.

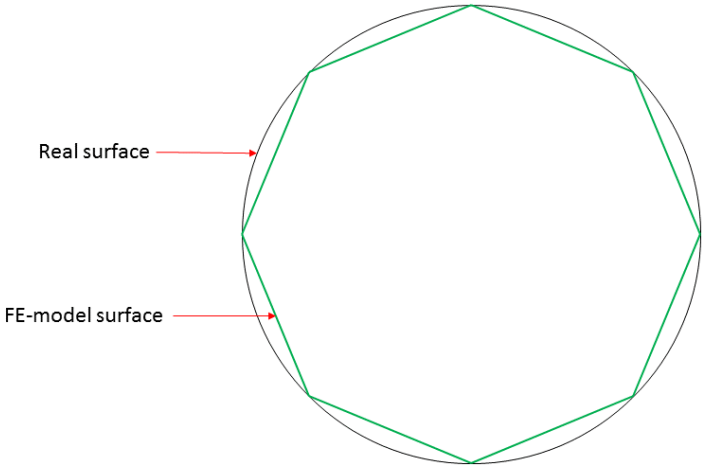

Figure 10-2: Illustration of the generated FE model circular surface

As this effect is present over the entire draft of in the model, the differences in displacement between the HydroD analysis and the spreadsheet calculation is relative noticeable.

This effect is alleviated with a finer mesh, as may be observed from the Δz column in Table 10-2, presenting the difference between the obtained freeboard and the target freeboard of 10 meters. This alleviation occurs as a finer mesh contains more mesh elements used to model the periphery of the Spar buoy, thus improving the representing the circular shape. There is also a general overestimation of the metacentric height present in the mesh models, as illustrated by $\Delta\overline{GM}$, representing the difference between the resulting $\overline{GM}$ from each mesh model and the target metacentric height obtained in the spreadsheet analysis. As more of the floater is submerged, the position of the center of buoyancy is increased, increasing $\overline{KB}$ and consequently $\overline{GM}$. The difference in metacentric height compared to the spreadsheet calculation therefore reduces with an increased mesh fineness, as a more correct draft is obtained.

The resulting frequency dependent potential damping coefficients are presented in Figure 10-3. Mesh model 1 is not included, as the solution did not converge for this coarse mesh.

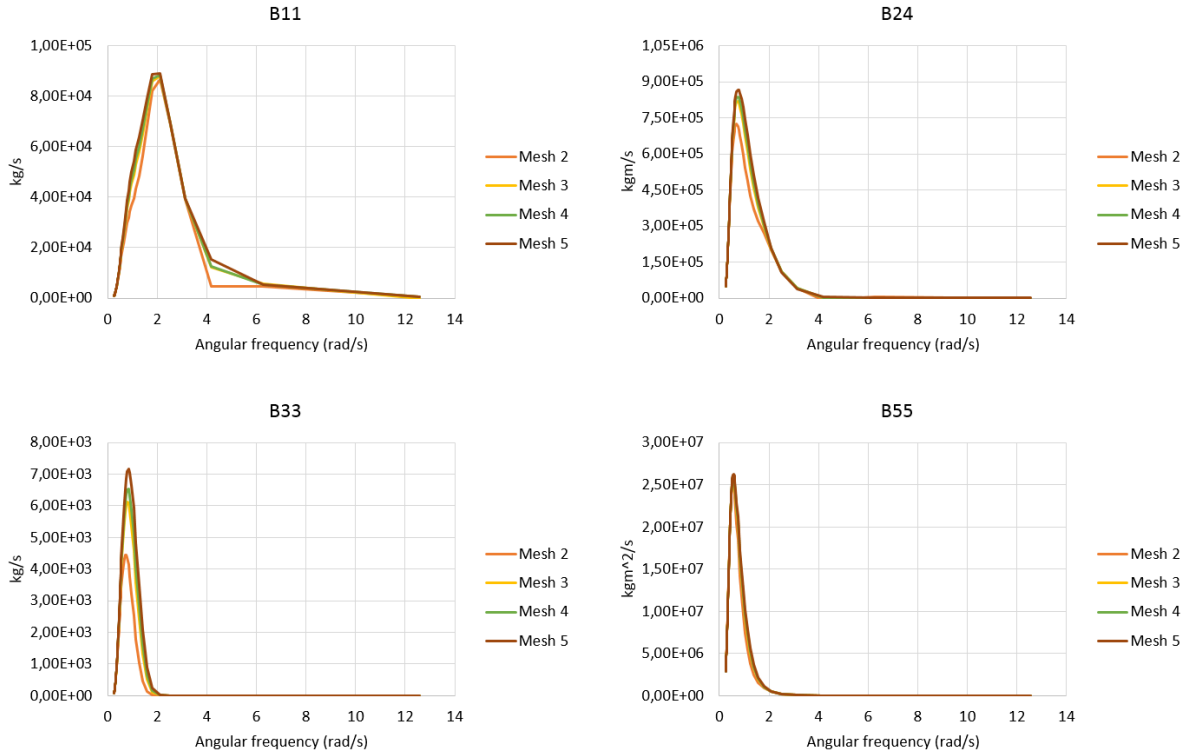

Figure 10-3: Damping resulting from each finite element model, floater 7.47-115x4-10

The figure shows strong indications that the solution has converged for the damping in pitch-pitch (B55), as there is little observable difference between the studied mesh models. More deviations are however present for damping in surge-surge (B11), sway-roll (B24) and heave-heave (B33). Damping B11 generally features a good compliance in the lower frequency range (0 to 0.5 rad/s) and higher frequency range (6 to 12 rad/s), but deviations are present elsewhere in the plot. These deviations appears to be decreasing with an increasing mesh fineness, where mesh model 4 and 5 seems to feature a respectable compliance throughout the entire frequency set. Damping mode 24 also features decent conformity between the studied mesh models, but some deviations may be observed in the frequency band 0.5 rad/s to 2 rad/s. These differences seems to be decreasing with an increased mesh fineness, and there appears to be small deviations between the results gained from mesh model 3 to 5. Damping mode B33 appears to be the damping mode containing the largest relative difference between the studied mesh models, where the maximum value increases with an increased mesh fineness. The difference is largest

between mesh model 2 and 3, before an increased conformity is achieved between mesh models 3 to 5.

In order to get a better understanding of the plot presented in Figure 10-3, averaged difference values between each studied mesh model is presented in Table 10-3. The values were generated by obtaining the difference in percent between mesh model "i" and mesh model "$i-1$" for each frequency, summing each contribution and dividing on the total number of frequencies studied.

Table 10-3: Average difference in damping values for each mesh model, floater 7.47-65x4-10

Damping	Mesh 2 to 3	Mesh 3 to 4	Mesh 4 to 5
B11	9.11 %	1.60%	2.37%
B24	6.50%	1.19%	1.66%
B33	78.07%	5.29%	8.44%
B55	4.20%	0.70%	1.01%

Damping B11 generally features small differences between the studied mesh models, illustrating the conformity that was observed in Figure 10-3. The difference is most severe between mesh model 2 and 3, where the largest differences were observed between frequencies 0.50 rad/s and 1.8 rad/s and 4.0 rad/s to 6.0 rad/s. The average difference decreases for the comparison of mesh model 3 to 4, and 4 to 5 to values below 3%. It may therefore be stated that the solution converges with reasonably accuracy in B11 for mesh model 3, which is in accordance to the observed tendencies in Figure 10-3.

Damping B24 features similar patterns to damping B11, with the largest difference between mesh models 2 to 3, before the difference significantly decreases for the comparison of mesh model 3 through 5. The largest deviations was observed in the frequency range of 0.5 rad/s, 2.0 rad/s, as was indicated in Figure 10-3. As the comparison of mesh model 3 to 4 features a difference of 1.19%, it may be stated that damping mode B24 converges for mesh model 3.

Damping B55 features the highest differences between mesh model 2 and 3, where most of the deviations are observed at the frequency range 0.7 rad/s to 2 rad/s. The difference between mesh model 3 to 4 and 4 to 5 is generally small, and it may be stated that the solution converges for damping B55 at mesh model 3.

As may be observed from Table 10-3, B33 features the worst convergence characteristics between the featured damping modes with large differences present in all comparison cases. The average difference giving in percentage may however be somewhat misleading for the heave-heave damping. As the other damping modes generally featured large values in the third power or higher throughout the entire studied frequency band, B33 featured several data points with small, insignificant values, especially in the higher frequency region. This implies that an insignificant increase or decrease in these small values between the studied mesh models may lead to a tremendous increase or decrease in percent value. Studying the difference for mesh model 2 to 3 for example, as this featured the highest average difference; a deviation of 963.32% is present at frequency 2.513 rad/s, even though the difference in the numerical value between the cases is only 0.072875 kg/s. As these small values are so sensitive to numerical change, it was decided to base the convergence study for this damping mode on the maximum values obtained from each mesh models. The resulting difference may be observed in Table 10-4. It is stressed the sensitivity of small values on the average difference values is not present in the other damping modes, as these generally featured higher values throughout the frequency band. The comparison presented in Table 10-6 is therefore still valid for B11, B24 and B55.

Table 10-4: Difference in maximum value for damping mode B33, floater 7.47-115x4-10

Damping	Mesh 2 to 3	Mesh 3 to 4	Mesh 4 to 5
B33 [max]	37.59%	6.46%	10.00%

As may be observed, the maximum value features a steady increase with an increased mesh fineness, as was observed in Figure 10-3. This indicates a somewhat poor convergence characteristic, as the increase is relatively large in all comparison cases. However, as indicated in Table 10-2, running the hydrodynamic analysis in HydroD for the finer meshes takes a relative long time, where the increase in number of panels seems to be disproportionate to the increase computation time. Due to time limitations, it was decided to assess mesh model 5 as sufficiently converged regarding the damping values in heave-heave.

Based on the discussion above, it may be realized that mesh model 3 seems to converge the solution for damping mode B11, B24 and B55. This is however not the case for damping mode B33, where a steady increase in maximum values with increase mesh fineness was observed. Furthermore, mesh model 3 features a difference of 23.2% from the target freeboard. Due to the convergence characteristics of damping mode B33 and a desire to obtain a model with a freeboard closer to the target value, mesh model 5 was selected for the establishment of the frequency dependent RAOs and added mass and damping matrices for the presented floater.

10.1.2 Floater 8.45-90x4-10

For floater 8.45-90x4-10, a total of seven different mesh models were generated for the convergence study, which are presented in Figure 10-4. Note that the same color-coding scheme as presented in section 10.1.1 is embedded with the same mesh densities as previously used, ref. Table 10-1.

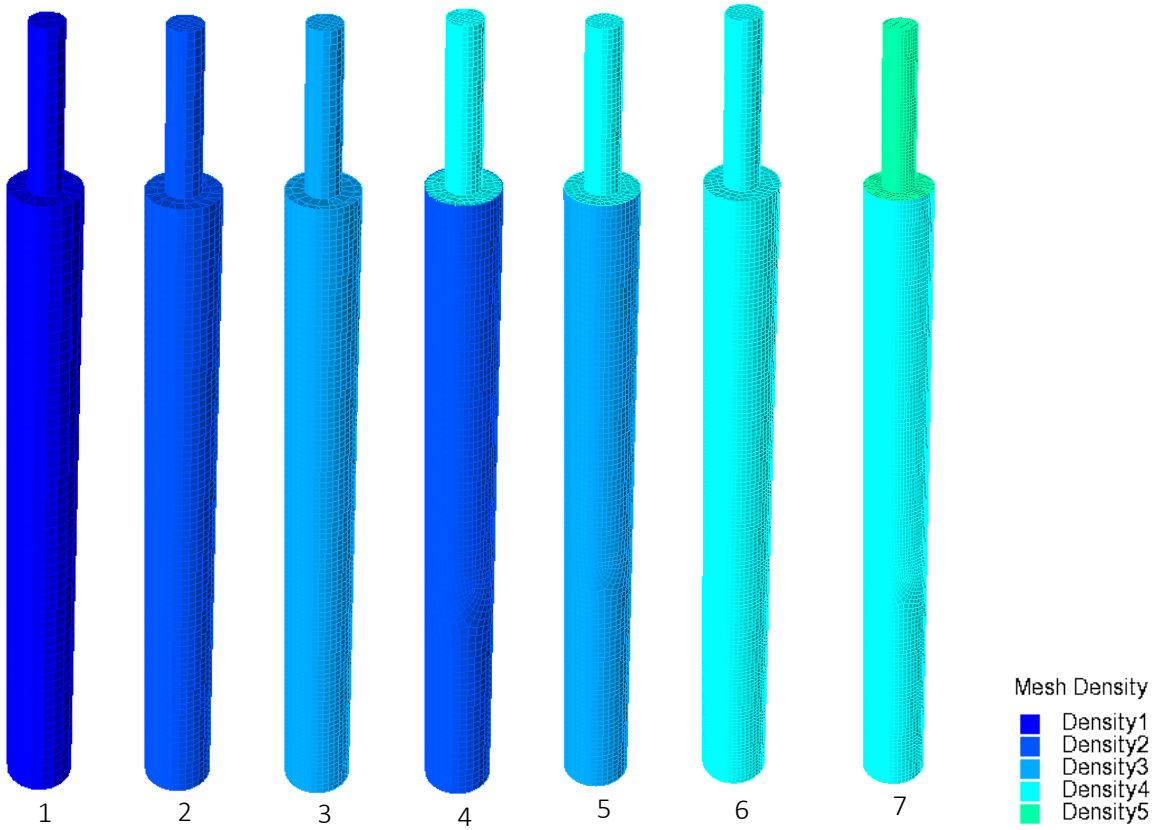

Figure 10-4: Illustration of mesh models used in the convergence study for floater 8.45-90x4-10

The resulting number panels for each mesh model is presented in Table 10-5, along with the resulting freeboard, and metacentric height obtained in the HydroD analysis. As previously stated, Δz resembles the difference in freeboard compared to the desired freeboard of 10 meters, while ΔGM is the difference in metacentric height from the HydroD analysis and the spreadsheet calculations.

Table 10-5: Presentation of mesh properties and resulting floating characteristics, floater 8.45-90x4-10

Mesh number	Number of panels	Execution time [s]	Freeboard [m]	Δz [%]	GM [m]	ΔGM [%]
1	1282	-	0.64	93.6	-	-
2	2945	200	6.18	38.2	18.0314	2.54
3	4436	525	7.40	26.0	17.8770	1.69
4	4558	613	7.81	21.9	17.8832	1.73
5	5686	2651	8.18	18.2	17.8135	1.34
6	7976	8190	8.60	14.0	17.7318	0.89
7	11151	15324	9.10	9.0	17.6886	0.65

As can be observed, the present convergence study also contains the issue of HydroD recognizing a lower displaced volume in the equilibrium position obtained from the spreadsheet calculation. This is most severe for mesh model 1, which only obtains a freeboard of 0.64 meters in the recognized static equilibrium state. This was deemed unacceptable, and the analysis for this mesh model was consequently not performed. The freeboard approaches the target value of 10 meters as the mesh fineness increases. This is related to the increasing number of panels used to represent the circular periphery, as discussed in section 10.1.1. The increased submergence of the mesh models also induces a difference in metacentric height compared to the spreadsheet calculations. This deviation is reduced with an increased mesh fineness, as a more correct draft is obtained.

The resulting frequency dependent potential damping coefficients are presented in Figure 10-5. Mesh model 1 is not included due to the unacceptable freeboard.

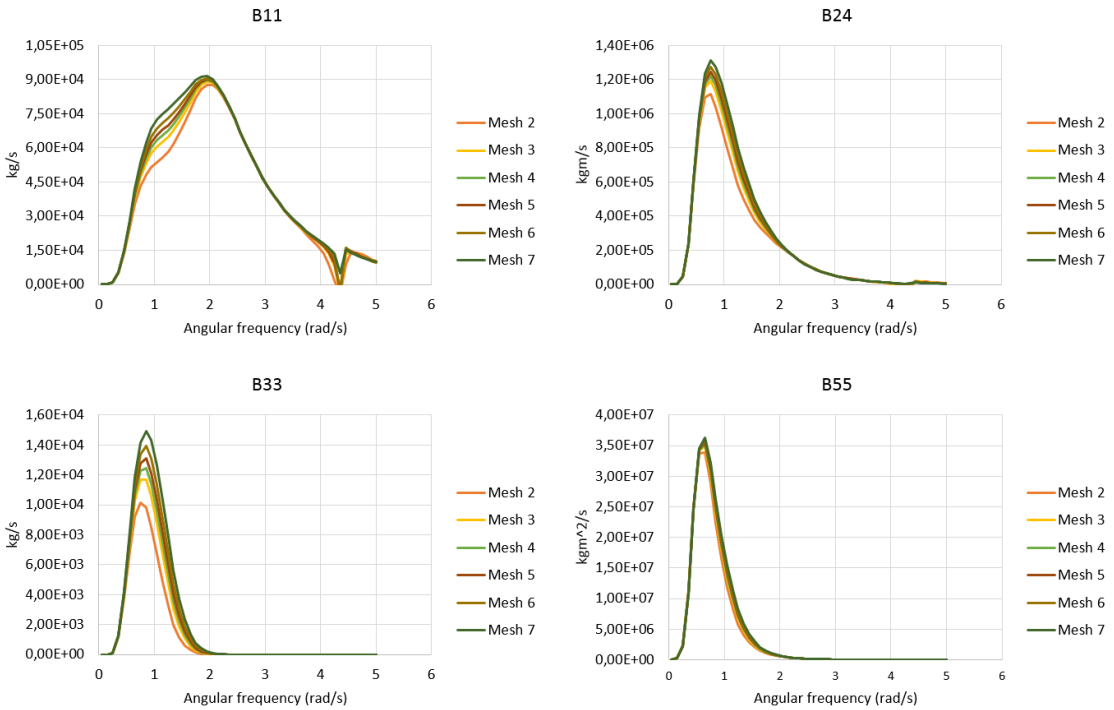

Figure 10-5: Damping resulting from each finite element model, floater 8.45-90x4-10

There is strong indication of damping in pitch-pitch (B55) has converged, as the differences between the studied mesh models are relative small. More deviations are however present for damping in sway-roll (B24), heave-heave (B33) and surge-surge (B11). B11 features a decent compliance in the lower frequency range (0 to 0.5 rad/s) and mid frequency range (2.0 to 4.0 rad/s), but deviations are present elsewhere in the plot. Mesh models 2 through 6 also obtains negative values at frequencies around 4.3 rad/s, where an abnormal dip is present, as may be observed from Figure 10-5. Damping in surge-surge can in reality never be negative [26], indicating some flaws with these mesh models.

Damping mode B24 generally features a decent conformity between the studied mesh models, but there are some deviations present at similar in the frequency range 0.5 rad/s to 2 rad/s. These seems to decrease with an increased mesh fineness, where mesh model 6 and 7 features a decent compliance throughout the studied frequency set. Also note that negative values are present for mesh 2 through 6, due to an abnormal dip around frequency 4.3 rad/s. Negative damping is not physically possible for this damping mode, indicating some flaws with these mesh models.

B33 seems to feature the highest relative difference for the studied damping modes, where the maximum value generally increases with an increased mesh fineness.

In order to get a better understanding of the presented plot, averaged difference values in percentage between the studied mesh models is presented in Table 10-6. The values were obtain in a similar fashion as described in section 10.1.1. It should also be noted that the comparison for damping B33 was based on maximum values, due to the small number's sensitivity to numerical change.

Table 10-6: Average difference in damping values for each mesh model, floater 8.45-90x4-10

Damping	Mesh 2 to 3	Mesh 3 to 4	Mesh 4 to 5	Mesh 5 to 6	Mesh 6 to 7
B11	12.94 %	1.99%	-0.16%	2.51%	1.85 %
B24	6.07 %	-10.17%	2.96%	2.54%	2.94%
B33 [max]	15.04%	6.41%	5.14%	6.34%	7.4%
B55	12.16%	0.78%	1.33%	1.06%	2.06%

Damping B11 generally features small differences between the studied mesh models, emphasizing the decent compliance observed in Figure 10-5. The largest differences are present between mesh model 2 and 3, where most deviations were observed in the frequency range 0.5 rad/s to 2.0 rad/s. As the difference between mesh models 5 to 7 is under 3%, it may be stated that B11 has sufficiently converged for mesh model 5.

Damping B24 features the largest deviations between mesh model 3 and 4. Furthermore, the difference is negative, even though the values seems to be increasing according to Figure 10-5. The negative difference may be explained by an observable deviation of -400.48% at frequency 4.15 rad/s, which is approximately in the abnormal dip observed in Figure 10-5. The average difference decreases for the comparison of mesh models 5 through 7, to values under 3%. This is deemed sufficiently accurate to make the solution converge.

Damping B55 features some variations between mesh model 2 and 3, but the differences are generally small between mesh models 3 to 7. It may be stated that damping B55 already converges for mesh 3, as was indicated in Figure 10-5.

The maximum value for damping B33 features a steady increase with an increased mesh fineness. This indicates a somewhat poor convergence characteristic, as the increase is relatively significant in all

comparison cases. However, it was decided to assess mesh model 7 as sufficiently converged for the damping in heave-heave due to time limitations, as discussed in section 10.1.1.

Based on the discussion above, mesh model 5 seems to converge the solution in B11, B24 and B55 with reasonably accuracy. However, this mesh model features negative values in B11 and B24, indicating some potential flaws. It also features a difference in freeboard of 18.2%, while leading to a poor convergence of damping mode B33. It was therefore decided to select mesh model 7 for the establishment of the frequency dependent input into OrcaFlex, as it contained no negative values throughout the studied frequency set, while also featuring the best convergence characteristics for B33.

10.1.3 Floater 9.94-65x4-10

For floater 9.94-65x4-10, 5 mesh models were generated for the purpose of the convergence study. The studied mesh models are illustrated in Figure 10-6, where the color-coding scheme and the mesh densities are the same as embedded in section 10.1.1 and 10.1.2.

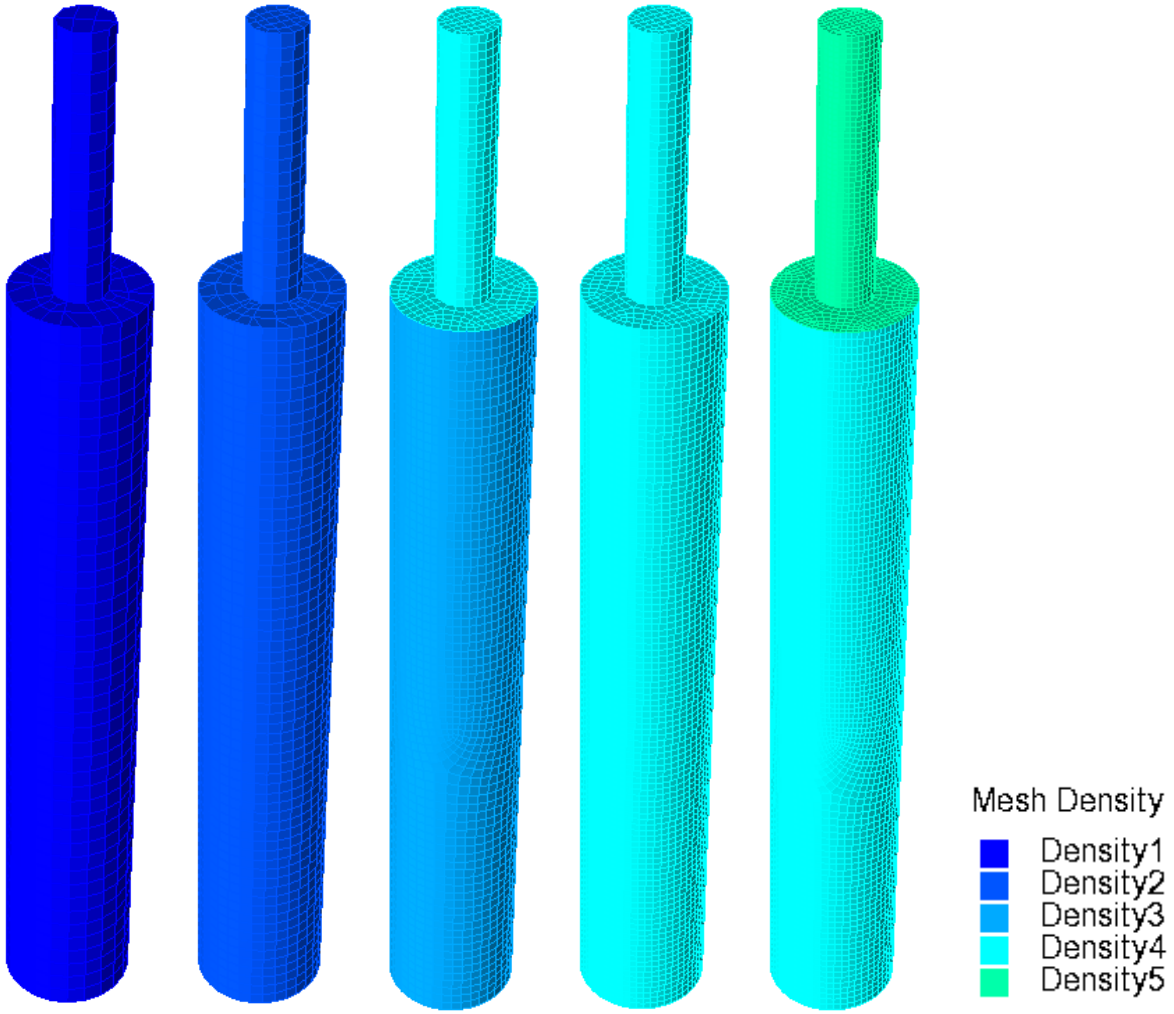

Figure 10-6: Illustration of mesh models used in the convergence study for floater 9.94-65x4-10

The resulting amount of nodes and panels, execution time, freeboard and metacentric height for each mesh model is presented in Table 10-7.

Table 10-7: Presentation of mesh properties and resulting floating characteristics for the different mesh models, floater 9.94-65x4-10

Mesh number	Number of panels	Execution time [s]	Freeboard [m]	Δz [%]	GM [m]	ΔGM [%]
1	1184	45	3.50	65.0	11.8410	5.22
2	2562	159	7.00	30.0	11.5045	2.45
3	5104	665	8.62	13.8	11.3663	1.27
4	7128	5998	8.94	10.6	11.3205	0.87
5	9984	11572	9.32	6.8	11.2964	0.66

Not surprisingly, the tendency of HydroD recognizing too little displaced volume is also present throughout this convergence study. The effect is most pronounced for mesh model 1, where a freeboard of 3.50 was acknowledged as the equilibrium position in HydroD, a 65% difference from the target value. However, this is a significant improvement compared to the previously studied geometries featuring the mesh density. The analysis for mesh model 1 was consequently performed in the current mesh study. The freeboard increases with an increased mesh fineness, as more planar elements are used to model the periphery of the Spar buoy. The target freeboard of 10 meter is however never obtained throughout the studied mesh models, where mesh model 5 features the closes freeboard of 9.32 meters. The deviations in freeboard also leads to deviations in the metacentric height, as a larger portion of the draft is submerged; lowering the location of the CoB. This effect is alleviated with an increased mesh fineness, where mesh 5 features the lowest difference of 0.66% compared to target value obtained in the spreadsheet calculation.

The resulting frequency dependent damping for mesh model is presented in Figure 10-7.

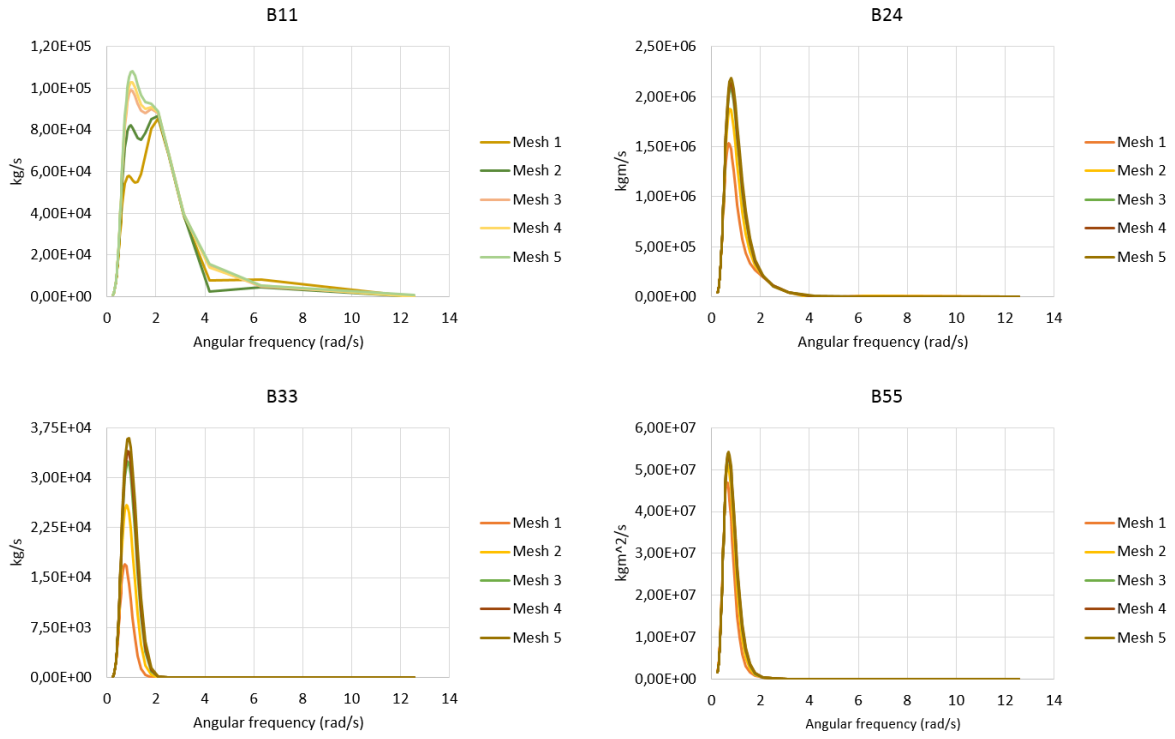

Figure 10-7: Damping resulting from each mesh model, floater 9.94-65x4-10

The figure indicates that damping mode B55 converges for an early mesh model, as the difference between mesh model 2 and 5 seems to be relatively small. Damping in surge-surge (B11), sway-roll (B24) and heave-heave (B33) however features some differences between the mesh models. Damping B11 generally shows decent compliance in the lower frequency range (0 to 0.5 rad/s) and the higher frequency range (6 to 12 rad/s), but deviations are present elsewhere in the plot. This is especially true for frequencies between 0.5 to 2 rad/s and 3 to 6 rad/s. However, the differences seems to decrease with increasing mesh fineness, and mesh model 3 to 5 generally shows respectable conformance throughout the entire frequency band.

Damping B24 also features relative decent conformity, with some deviations present in the frequency range 0.5 to 2 rad/s. The differences is however most pronounced between mesh model 1 and 3, where mesh model 3 to 5 illustrates a respectable compliance through the entire frequency set.

Damping B33 seems to feature the poorest convergence characteristics among the studied damping modes, as was the case for the other floaters. The maximum value gradually increases with an increase in mesh fineness. The differences are however most severe between mesh model 1 through 3.

In order to get a better understanding of the presented plots, averaged differences between the mesh models are presented in Table 10-8. The values were obtain in a similar fashion to what was described in section 10.1.1 The convergence values for damping B33 is based on the resulting maximum values from each mesh model due to the sensitivity of low numbers.

Table 10-8: Average difference in damping values for each mesh model for floater 9.94-65x4-10

Damping	Mesh 1 to 2	Mesh 2 to 3	Mesh 3 to 4	Mesh 4 to 5
B11	15.02%	7.43%	1.39%	1.76%
B24	10.07%	4.60%	0.92%	1.06%
B33 [max]	51.94%	25.68%	4.62%	5.76%
B55	5.76%	2.01%	0.44%	0.37%

B11 features a relatively large difference between mesh model 1 to 2 and 2 to 3, where the most severe deviations were observed in the frequency range 0.5 to 1.50 rad/s and 4.0 to 12.5 rad/s. The differences decreases in the comparison of mesh model 3 to 4, and it may therefore be stated that mesh 3 sufficiently converges damping mode B11 with reasonable accuracy.

A similar behavior may be observed for damping B24, where the most severe differences are observed between mesh models 1 to 3. The variations between mesh models 3 through 5 are generally low, indicating that mesh model 3 converges the solution with reasonable accuracy.

Damping 55 features a relatively low increase in average comparison values with an increase in mesh fineness, illustrating the good conformity throughout the dataset as was observed in Figure 10-7. As the difference between mesh model 2 and 3 is only 2.01%, it may be stated that the solution has converged for mesh model 2 with reasonable accuracy for damping B55.

The differences in maximum value for B33 between mesh model 1 to 2 and 2 to 3 are relative severe, obtaining an average difference of 51.94% and 25.68 %, respectively. The differences decreases for mesh model 3 through 5, but the deviations are still relative significant, indicating a somewhat poor convergence characteristic. Nevertheless, it was decided to assess mesh 5 as sufficiently converged for all practical reasons for damping in heave-heave due to time limitations.

Based on the discussion above, it may be realized that mesh model 3 seems to converge the solution for damping mode B11, B24 and B55. This is however not the case for damping mode B33, where a

steady increase in maximum values with an increase mesh fineness was observed. Furthermore, mesh model 3 features a difference of 13.8% from the target freeboard. Due to the convergence characteristics of damping mode B33 and a desire to obtain a model with a freeboard closer to the target value, mesh model 5 was selected for the establishment of the frequency dependent input to OrcaFlex.

10.2 Output from HydroD

The results from HydroD that will be utilized as input for the hydrodynamic simulation in OrcaFlex includes the displacement RAO, load RAO, frequency dependent added mass matrices, frequency dependent damping matrices and hydrostatic stiffness matrix. These outputs resulting from each of the deemed converged mesh models will be presented in the following. It should be noted that data were extracted from a frequency band of 0.251 rad/s to 12.566 rad/s, corresponding to the period range of 0.5s to 25s specified in section 8.2.3. This is also true for floater 8.45-90x4-10, even though the convergence study based itself on a different frequency set. Furthermore, the obtained damping matrices are derived from potential theory, implying that viscous effects are not included in the presented damping values. In actual viscous fluid, friction will cause an additional non-linear damping. However, as stated in 5.5.5, the viscose damping is used to dampen HF and LF resonance motions, which are non-linear motions. Such responses are not evaluated in the presented work, and only the radiation damping is needed to accurately model the in linear response.

10.2.1 Floater 7.47-115x4-10

10.2.1.1 Hydrostatic stiffness

The resulting hydrostatic stiffness matrix obtained in HydroD for floater 7.47-115x4-10 is presented below.

$$\boldsymbol{C_{F7.47-65x4-10}} = \begin{bmatrix} 0 & 0 & 0 & 0 & 0 & 0 \\ 0 & 0 & 0 & 0 & 0 & 0 \\ 0 & 0 & 1.26\text{E}+5 & 1.98\text{E}+1 & -8.28\text{E}-2 & 0 \\ 0 & 0 & 1.98\text{E}+1 & 1.24\text{E}+9 & -1.99\text{E}-2 & -1.31\text{E}+2 \\ 0 & 0 & -8.28\text{E}-2 & -1.99\text{E}-2 & 1.24\text{E}+9 & -7.47\text{E}+2 \\ 0 & 0 & 0 & 0 & 0 & 0 \end{bmatrix}$$

As discussed in section 5.5.3, the only non-zero hydrostatic stiffness coefficient for a symmetrical body is C_{33}, C_{44} and C_{55}. However, several "zero-elements" obtains a numerical value in the matrix. This may be explained by HydroD recognizing a small offset in the center of buoyancy from the vertical centerline of x=2.519E-6m and y=1.439E-5m. This is most probably related to the representation of the circular cross-section in HydroD, discussed in section 10.1.1. Nevertheless, the offset imposes a small first and second moment of inertia of the water plane, giving numerical values to coefficients C_{34}, C_{35}, C_{45} and their symmetrical counterparts. However, these coefficients generally obtains insignificant values when compared to the coefficients along the diagonal. Coefficients C_{46} and C_{56} are however more significant, obtaining values of -131 kgm^2/s^2 and -747 kgm^2/s^2, respectively.

As presented in section 5.5.2.2, these coefficients are given as:

$$C_{46} = -\rho g \nabla x_b + M g x_g$$

$$C_{56} = -\rho g \nabla y_b + M g y_g$$

As the displaced volume is relatively large for the studied floater, a small offset in center of buoyancy x and y position (x_b, y_b) leads to the relatively significant damping value. Furthermore, the hydrostatic stiffness matrix should be symmetrical around the diagonal, implying that C_{64} and C_{65} should obtain the same values as C_{46} and C_{56}. This is however not the case. The explanation for this is of a rather speculative nature, but it seems that HydroD does not recognize any imposed damping forces in the yaw DOF, and consequently sets all coefficients on the sixth column to zero.

Nevertheless, the non-zero deviations in the hydrostatic stiffness matrix should not impose significant error to the OrcaFlex simulation, as only the damping coefficients from the third row and column to the fifth row and column is imported into the OrcaFlex model. Coefficients C_{46} and C_{56} are therefore not included into the OrcaFlex simulations.

10.2.1.2 Frequency dependent added mass and damping

The added mass and damping coefficients is imported into OrcaFlex as 6x6 matrices for all frequencies specified in the frequency set, giving a total of 50 input matrices for both added mass and damping. The 100 matrices will not be presented here for practical reasons, but the frequency dependent plots for the damping modes and added mass coefficients in interest are presented instead. As stated in section 10.1, it is sufficient to study the damping mode B11, B24, B33 and B55, as other damping modes are either zero or equal and possibly opposite in magnitude. The same also applies to the added mass coefficients. The frequency dependent damping plots are presented in Figure 10-8.

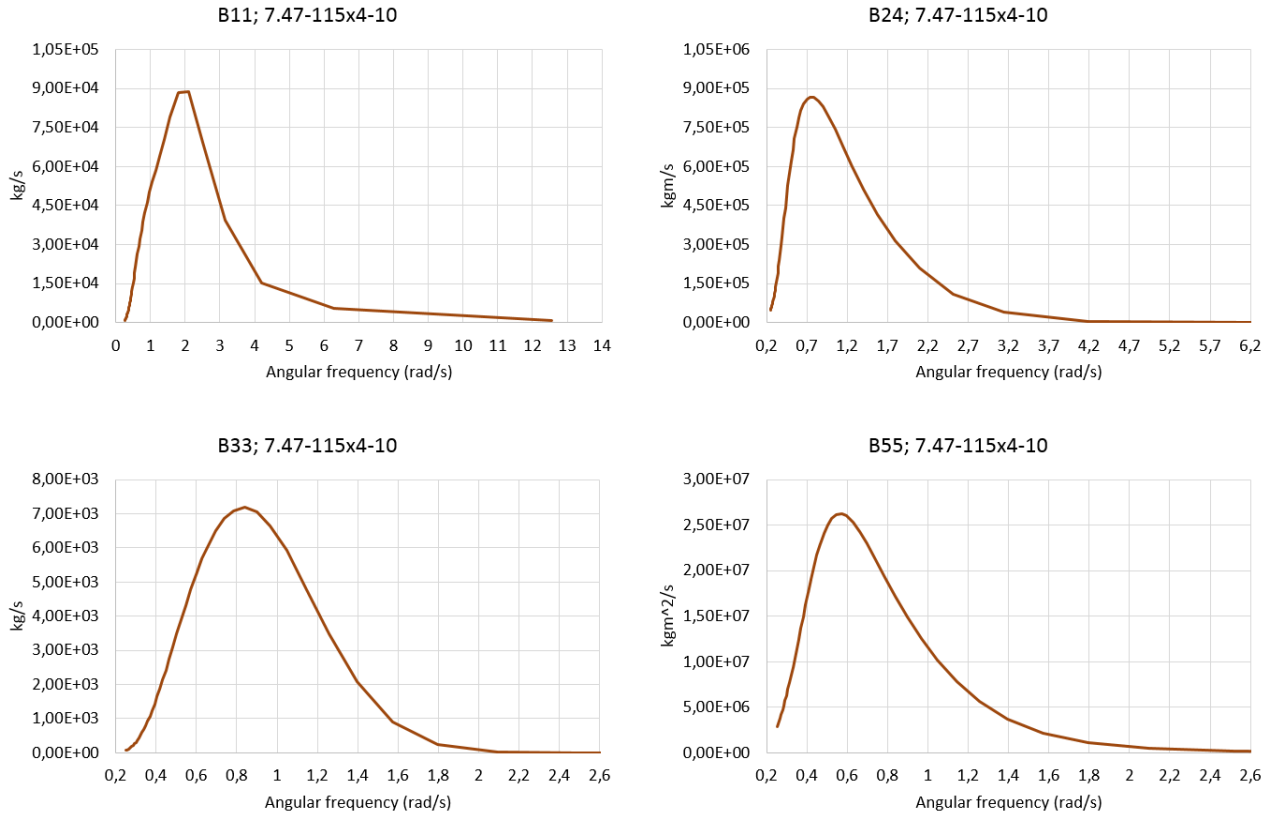

Figure 10-8: Frequency dependent damping for floater 7.47-115x4-10

As may be observed there are generally insignificant damping in all modes at the lowest frequency in the frequency set, corresponding to a wave period of 25 seconds. The values increases rather rapidly towards a maximum value as the frequency is increased, before becoming insignificant again at certain frequencies. Damping mode B11 features numerical values throughout the entire frequency set, but the most significant damping occurs between frequencies 0.25 rad/s to 4.0 rad/s, corresponding to 1.5 seconds and 25 seconds. Damping in heave and pitch becomes insignificant after 2.6 rad/s, or 2.5 seconds, while damping in sway-roll obtains the most relevant values prior to frequency 4.2 rad/s, corresponding to a period of 1.5 seconds. It therefore seems that radiation waves with long periods and short periods does not transport significant energy away from the system, and the noteworthy damping generally occurs for wave periods between 3 to 25 seconds.

The added mass plots in the same modes as illustrated for damping, is presented in Figure 10-9.

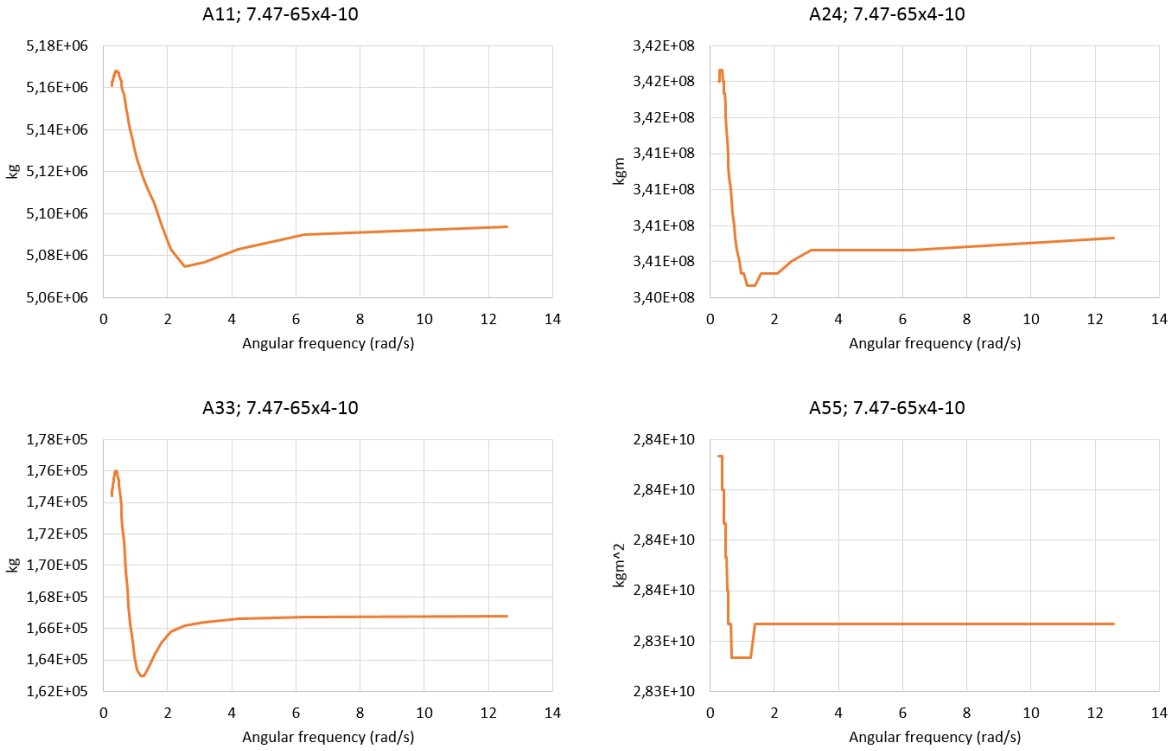

Figure 10-9: Frequency dependent added mass for floater 7.47-115x4-10

As may be observed there is generally lower variance with respect to frequency for the added mass compared to the damping, as was stated in the introduction to this section. There is consequently significant added mass throughout the studied frequency set. As a general trend, it seems that the highest added mass values occurs at lower frequencies, before becoming more or less constant in the higher frequency range. OrcaFlex refers to this effect as the infinite-frequency added mass. If the data are consistent, the added mass plots vs frequencies should converge towards the infinite frequency added mass [47]. The obtained added mass values from HydroD therefore seems reliable, as the convergence is present.

10.2.1.3 Displacement RAOs

The displacement RAO for floater 7.47-115x4-10 as a function of frequency in each DOF is presented in Figure 10-10. As stated in section 8.2.3, a total of 7 wave directions were specified in HydroD, implying that there are a total of 7 different displacement RAOs for each DOF, one for each wave direction.

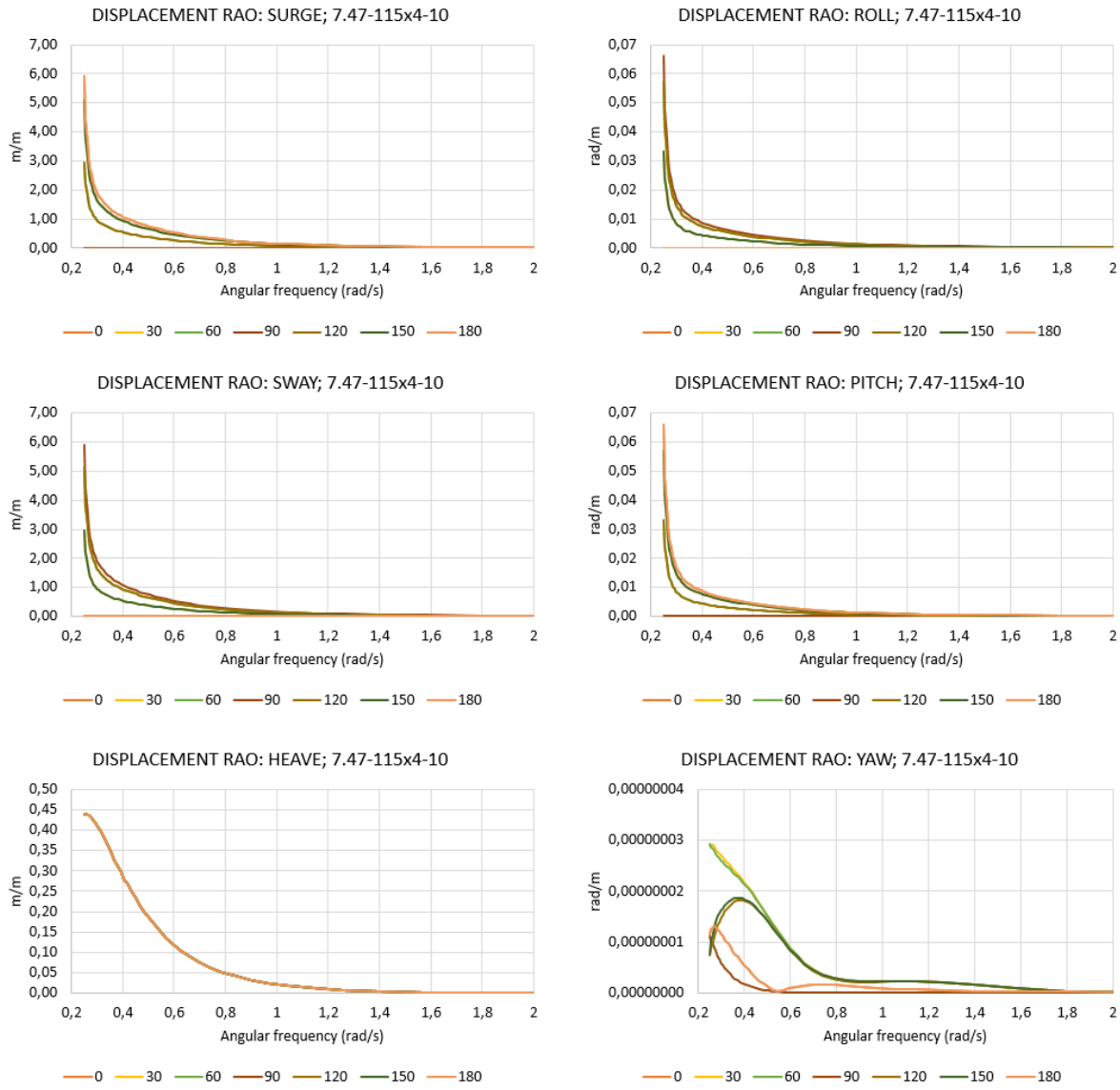

Figure 10-10: Displacement RAOs in the six DOFs for floater 7.47-115x4-10

As may be observed, the highest displacements in surge occurs with a wave direction of 0 degrees, as the incoming waves coincides with the surge direction. The values gradually decreases as the angle of attack is altered, before becoming zero at a wave heading of 90 degrees as would be expected by the definition of this motion. It may also be noted that the displacement RAO is symmetrical around 90 degrees wave headings, due to the symmetrical shape of the Spar buoy. This implies that the RAO for a 60-degree angle of attack is equal to the RAO for a 120-degree angle of attack, etc.. Furthermore, the surge and sway displacement RAO equal, but shifted 90 degrees. This implies that sway gains its maximum displacements at a wave heading of 90 degrees and zero displacements for 0 and 180 degrees wave headings, as would be expected from the definition of this motion. It may also be noted that the surge and sway displacement RAO features a relative severe maximum value of about 6 m/m at frequency 0.251 rad/s, corresponding to a period of 25 seconds. The amplitude values rapidly decreases

as the frequency is increased, before becoming insignificant at 1.0 rad/s. Most of the wave excitation motions in surge and sway therefore occurs between periods 6s to 25s.

The displacement RAOs in heave is equal for all angles of attack, indicating that this motion is independent upon the direction of the incoming waves. This is as expected, since it is a horizontal motion for a system with symmetry around a vertical center axis. The RAO features the largest displacement amplitudes in the lower frequency range, before steadily decreasing with an increase in frequency and becoming insignificant frequency 1.6 rad/s, corresponding to a period of 4.0 seconds.

Pitch and roll is, as with surge and sway, equal in magnitude, but shifted 90 degrees with respect to wave heading. Pitch therefore obtains the largest displacements at wave heading 0 and 180, while no motions are being imposed for a 90 degrees wave heading. The opposite applies for roll, i.e. the largest displacements occurs at a wave heading of 90 degrees, while no displacements eventuates at headings 0 and 180 degrees. The largest displacement amplitude of 0.062 rad/m are observed at the lowest frequency in the frequency set, corresponding to a 25 seconds period. The displacements rapidly decreases as the frequency is increased, before being insignificant at a frequency of around 1.0 rad/s, corresponding to 6 seconds.

The plot generally reveals a somewhat erratic behavior for the yaw motions. However, the displacement amplitudes are very small and the erratic behavior may be regarded as numerical noise, and the displacement amplitudes are zero for all relevant purposes.

As may be realized from the discussion above, the displacement RAOs in surge, sway, roll and pitch obtained the largest value at a wave period of 25 seconds, where the displacement amplitude significantly increased at a relatively short frequency band, i.e. a sudden increase. In order to discuss this effect, the natural periods for the system recognized by HydroD is presented in Table 10-9.

Table 10-9: Eigen values obtained in the HydroD analysis for floater 7.47-115x4-10

Eigen mode	Period [s]	Frequency [rad/s]
Surge	Infinite	Infinite
Sway	Infinite	Infinite
Heave	41.5	0.151
Roll	26.3	0.239
Pitch	26.3	0.239
Yaw	Infinite	Infinite

The natural periods in roll and pitch are fairly close to the 25-second wave period, and resonance motions may explain the sudden increase in displacement amplitudes. However, HydroD identifies natural period in surge and sway as infinite, which is in line with the discussion presented in section 5.5.6 regarding an unmoored free-floating system. Clearly, a 25-second wave period is far from infinite, but the structure seems to be exited heavily regardless in larger wave periods. This was confirmed by a trial analysis containing wave periods up to 100 seconds, leading to a 60 m/m displacement at the larger periods. It should be noted that a wave period of 100 seconds is not typically observable, and was just set to evaluate the surge and sway displacement characteristics. The high displacements value may be related to the low restoring forces in surge and sway in the HydroD analysis, due to the absence of a mooring system.

The sudden increase in displacement amplitude the 25-second period was not observed in the heave RAO, as the natural period is significantly higher than the wave period, i.e. there are no resonance

motions present in heave. Intuitively, it may seem important to obtain displacement RAOs featuring a frequency set that captures the resonance motions. However, this is not a necessity, as the specified period set of 0.5 seconds to 25 seconds includes all relevant wave periods generated by OrcaFlex in both environmental conditions. In other words, the specified environmental conditions does not contain waves with larger periods than 25-seconds, and the specified frequency set is therefore sufficient.

Furthermore, most displacement RAOs became insignificant after an angular frequency of 1.0 rad/s. As presented in section 5.5.4.1, motions generally becomes insignificant in the higher frequency area, as several crests and troughs are present over the cylinders diameter. This behavior is therefore expected.

10.2.1.4 Load RAOs

The load RAOs for floater 7.47-115x4-10 as a function of frequency is presented in Figure 10-11 for each degree of freedom. As with the displacement RAOs, seven directions were studied, leading to seven load RAOs in each DOF.

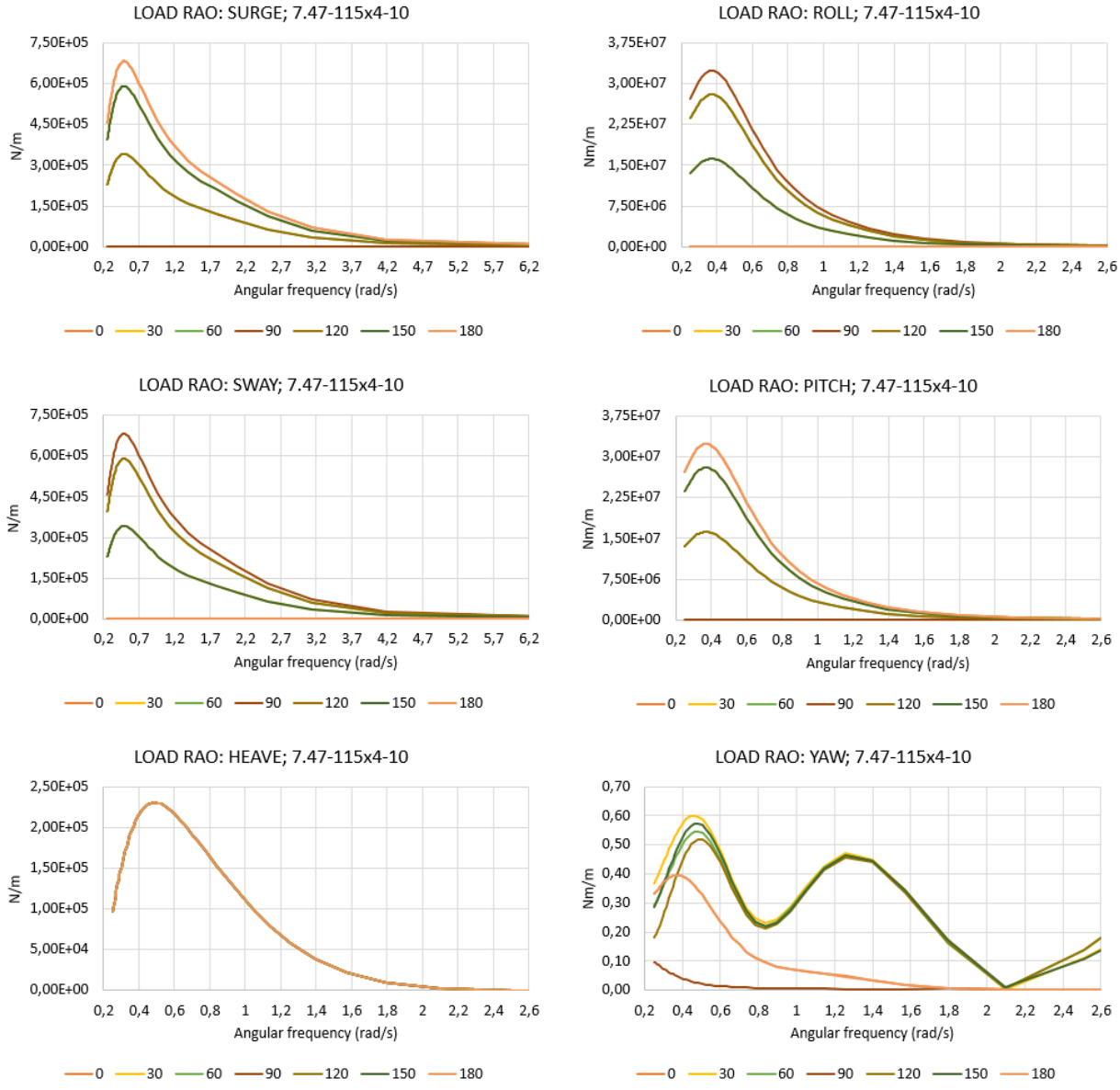

Figure 10-11: Load RAO in the six DOF for floater 7.47-115x4-10

Loads in surge is highest with a wave heading of 0 and 180 degrees, as these angles coincides with the surge direction. The values gradually decreases before being zero for a wave heading of 90 degrees, as would be expected by the definition of this DOF. The load RAOs in sway are equal to surge, but shifted 90 degrees with respect to wave heading, implying that the maximum loadings occurs for a wave heading of 90 degrees and no loads are imposed for wave headings 0 and 180 degrees. As indicated in the figure, most of the significant hydrodynamic loadings occurs at frequencies between 0.25 and 4.2 rad/s, corresponding to 1.5 to 25 seconds.

The load RAO in heave is independent upon wave direction, due to the symmetrical properties of the Spar buoy. Most of the significant hydrodynamic loadings occurs between frequencies 0.25 rad/s to 2.0 rad/s, corresponding to a period of 3 to 25 seconds.

The roll and pitch load RAOs are equal but shifted 90 degrees with respect to wave heading, due to the definition of these DOFs. This implies that the most severe hydrodynamic loadings in pitch occurs at wave headings 0 and 180 degrees, while no loads arises for a 90-degree wave heading. The opposite applies for the wave forces in roll. The most noteworthy hydrodynamic loadings occur at a similar frequencies observed for heave.

As with the displacement RAO, the load RAO in yaw generally features some erratic behavior, obtaining non-zero values that varies with the wave heading. However, the values are relatively small, and the erratic behavior may be regarded as numerical noise.

10.2.2 Floater 8.45-90x4-10

10.2.2.1 Hydrostatic stiffness

The hydrostatic stiffness matrix obtained in HydroD is presented below.

$$\boldsymbol{C_{F8.45-90x4-10}} = \begin{bmatrix} 0 & 0 & 0 & 0 & 0 & 0 \\ 0 & 0 & 0 & 0 & 0 & 0 \\ 0 & 0 & 1.26\text{E}+5 & -1.36\text{E}+2 & -3.92\text{E}-1 & 0 \\ 0 & 0 & -1.36\text{E}+2 & 9.19\text{E}+8 & -4.44\text{E}0 & -2.80\text{E}+3 \\ 0 & 0 & -3.92\text{E}-1 & -4.44\text{E}0 & 9.19\text{E}+8 & -2.12\text{E}+3 \\ 0 & 0 & 0 & 0 & 0 & 0 \end{bmatrix}$$

As was observed for floater 7.47-115x4-10, there are coefficients in the hydrostatic stiffness matrix that obtains a numerical value, which should, per definition, be zero. This is related to the same issue presented in section 10.2.1.1, i.e. there is a small offset in the center of buoyancy position recognized by HydroD from the vertical centerline. However, this should not impose any significant errors in OrcaFlex, as coefficients C_{46} and C_{56} are not imported, and coefficients C_{34}, C_{35}, C_{45} and their symmetrical counterparts features significantly lower values compared to the coefficients on the diagonal.

10.2.2.2 Frequency dependent added mass and damping

The frequency dependent damping and added mass plots for the selected modes is presented in Figure 10-12 and Figure 10-13, respectively.

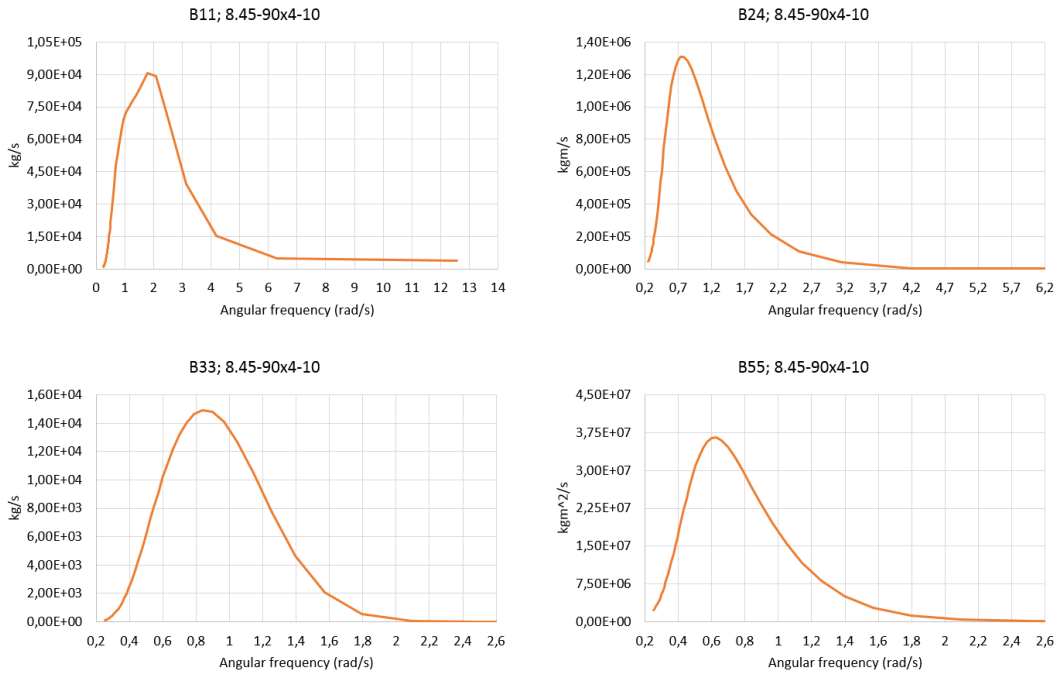

Figure 10-12: Frequency dependent damping for floater 8.45-90x4-10

As may be observed, the damping in all of the presented modes are highly dependent upon the angular frequency of the generated waves. As was observed for the previously evaluated floater, there is a general trend of low damping values in the lower frequency range, i.e. wave periods near 25 seconds. The damping values then increases relatively rapidly towards the maximum value before becoming insignificant at different frequencies. Damping B11 features numerical values throughout the entire frequency set, but most substantial damping is observed in the frequency range 0.25 rad/s to 4 rad/s, corresponding to wave periods of 1.5 seconds to 25 seconds. The other damping modes generally features a narrower frequency range of significant damping. For example, damping in heave and pitch becomes insignificant at frequency 2.2 rad/s, or 3 seconds, while B24 features irrelevant damping after 4.2 rad/s, corresponding to 1.5 seconds.

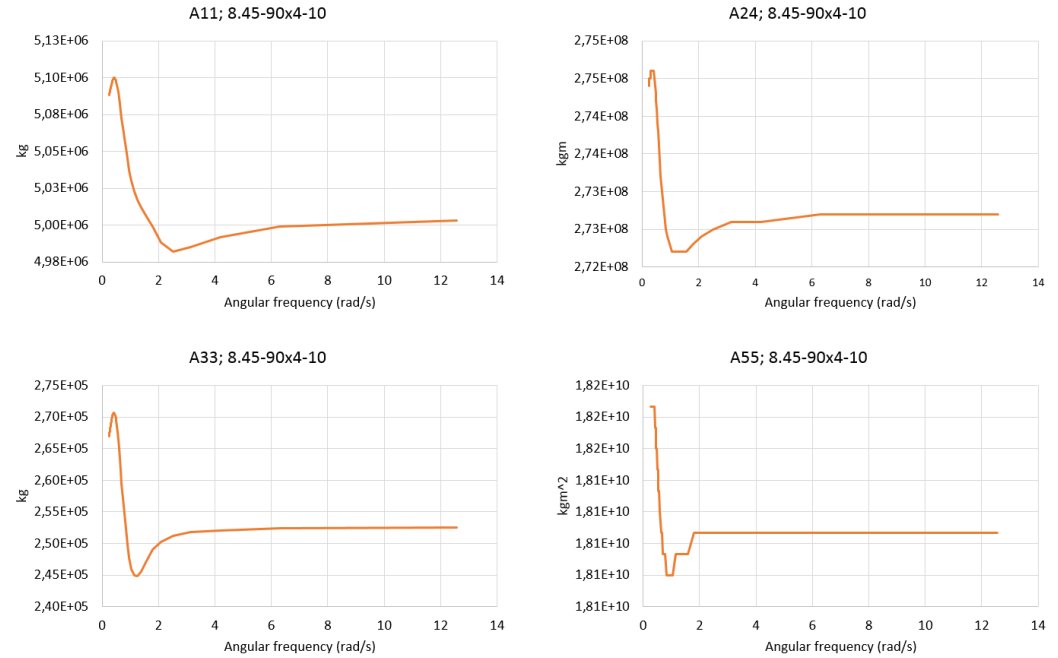

Figure 10-13: Frequency depended added mass for floater 8.45-90x4-10

The added mass does not vary significantly with respect to frequency, and there are therefore significant added mass throughout the studied frequency set. As a general trend, the added mass seems to be largest in the lower frequency range, i.e. higher periods, before becoming approximately constant for higher frequencies. It may therefore be stated that the added mass data for the present floater is reliable, as a convergence towards the infinite frequency added mass value is present.

10.2.2.3 Displacement RAOs

The displacement RAOs for each seven wave headings in the six degrees of freedom for the present floater are presented in Figure 10-14.

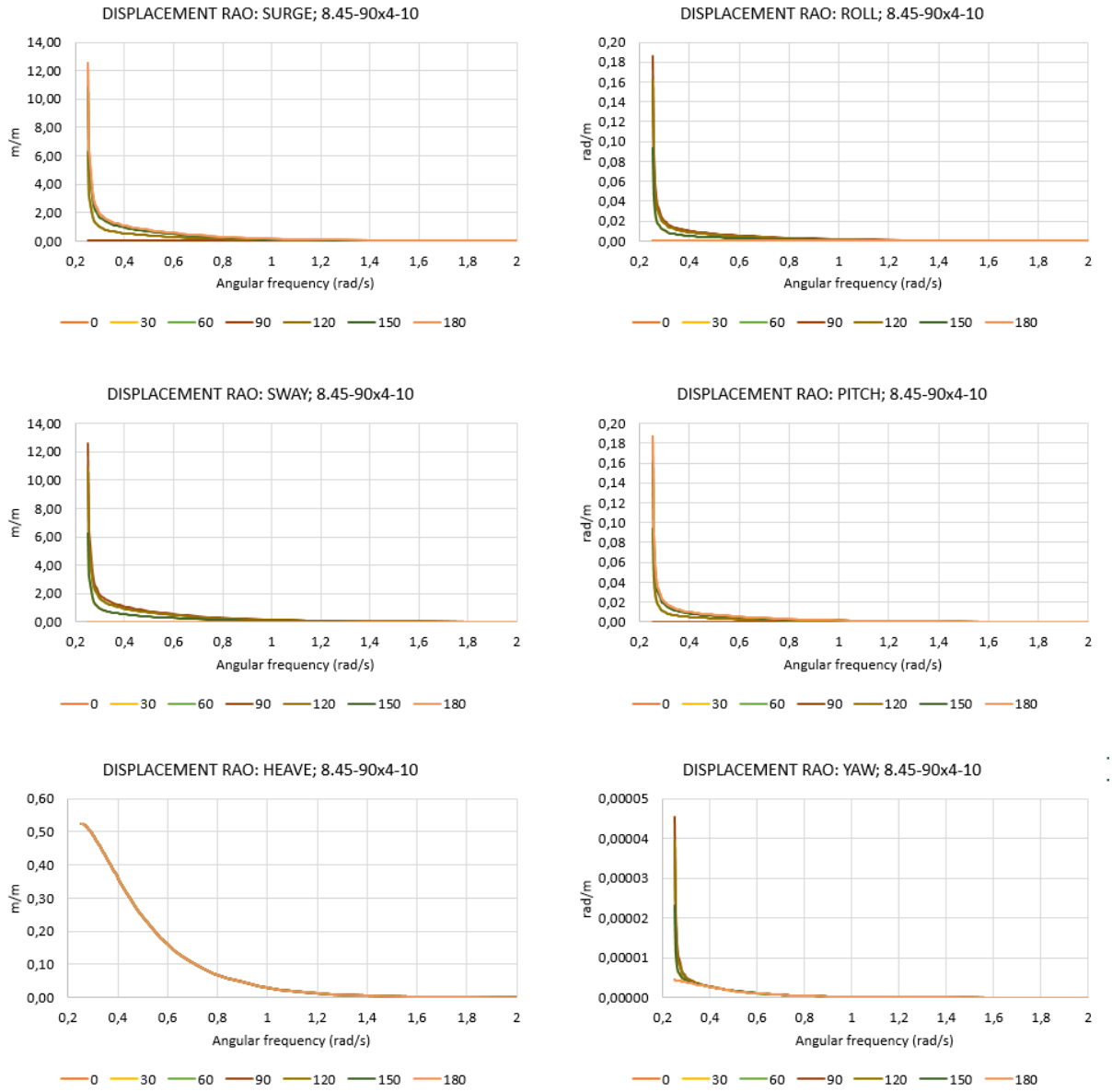

Figure 10-14: Displacement RAOs in the six DOFs for floater 8.45x90-4x10

Similarly to the displacement RAOs obtained for floater 7.47-115x4-10, surge and sway is equal, but shifted 90 degrees. Surge therefore gains its maximum value at wave headings 0 to 180 degrees, and minimum value with a wave heading of 90 degrees, where the opposite applies for sway. There is a relatively severe displacement amplitude of 12.55 m/m present at frequency 0.251 rad/s, corresponding

to a period of 25 seconds. The most significant displacement amplitudes occurs in the frequency range 0.251 rad/s to 1.0 rad/s, corresponding to a period range of 6 to 25 seconds.

The heave motions independent upon the incoming wave direction, due to the symmetrical shape of the Spar buoy. The structure experiences the largest excitations in heave for low angular frequency, i.e. high wave periods, before the displacement becomes insignificant at 1.2 rad/s, corresponding to wave period of around 5 seconds.

The roll and pitch displacements RAOs are equal, but shifted 90 degrees due to the definition of these motions. Pitch therefore obtains the maximum amplitude with a wave heading of 0 and 180 degrees, and a minimum value for wave heading of 90 degree, where the opposite applies for roll. The largest displacement of 0.1866 rad/m occurs at the lowest frequency in the frequency set, corresponding to a period of 25 seconds. The displacement amplitude rapidly decreases with an increase in frequency, before becoming insignificant at frequency 1.0 rad/s, corresponding to a wave period of about 6 seconds.

The displacements values in yaw is insignificant, and may be regarded as zero for all relevant purposes.

As may be realized from the discussion above, the displacement RAOs in surge, sway, roll and pitch features a sudden and rapid increase at wave frequency 0.251 rad/s, corresponding to 25 second. Observing the eigen values presented in Table 10-10, it may be realized that the natural period in roll and pitch is relatively close to the 25-second wave period. The sudden increase in displacement amplitude may therefore be explained as resonance motions between the structure and the waves. This explanation does not hold in surge and sway, as HydroD recognizes the natural periods as infinite. However, as explain in section 10.2.1.3, the structure seems to be heavily excited in these DOFs for high wave periods. Furthermore, the sudden increase in displacement amplitude was not observed in heave, as the natural period is far from the highest wave period in the dataset.

Table 10-10: Eigen values obtained in the HydroD analysis for floater 8.45-90x4-10

Eigen mode	Value [s]
Surge	Infinite
Sway	Infinite
Heave	41.49
Roll	25.5
Pitch	25.5
Yaw	Infinite

10.2.2.4 Load RAOs

The load RAOs for the seven studied wave directions in the six degrees of freedom is presented in Figure 10-15.

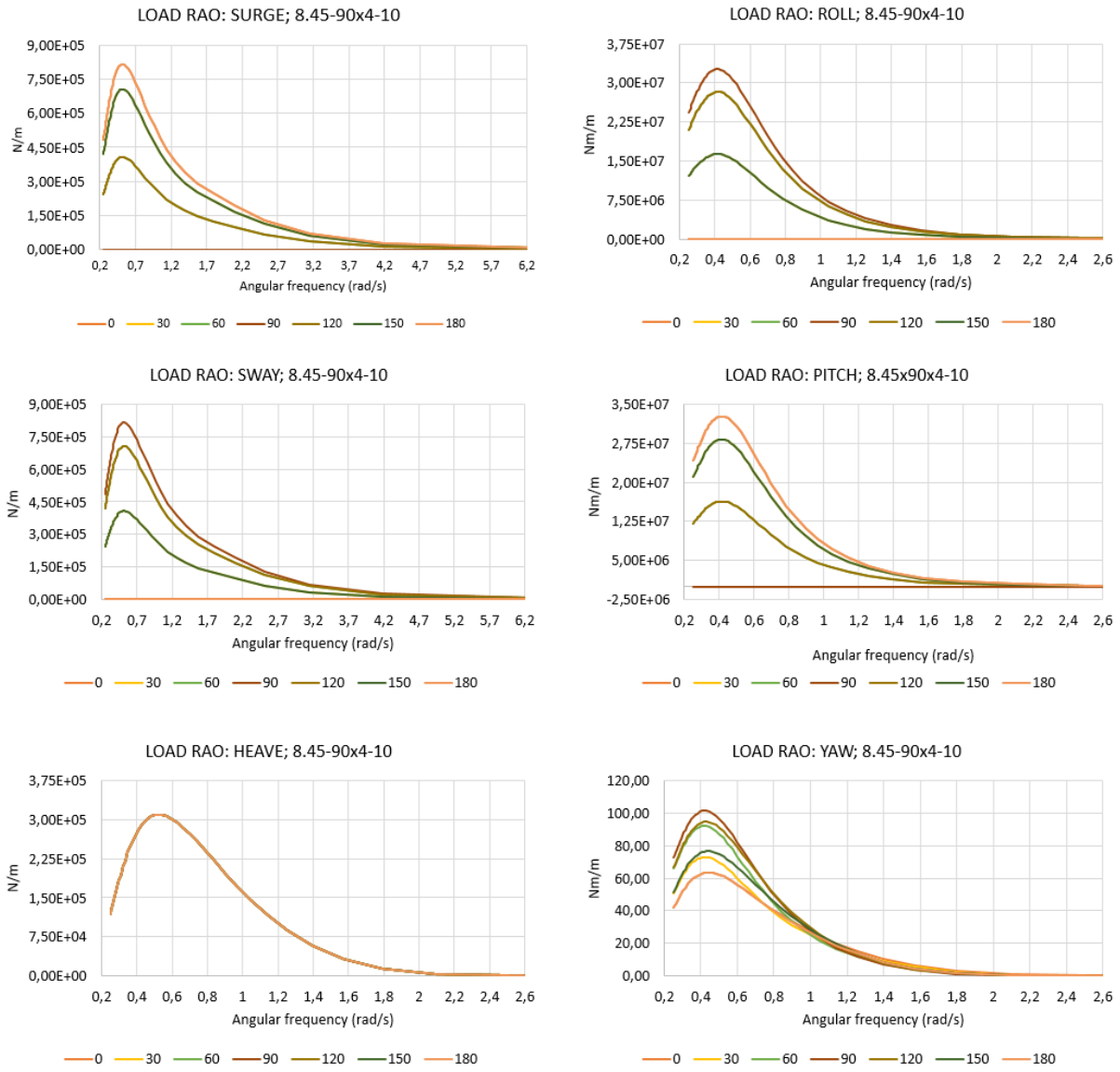

Figure 10-15: Load RAO in the six DOF for floater 8.45-90x4-10

The load amplitudes in surge are highest for a wave heading of 0 and 180 degrees, and zero for a wave heading of 90 degrees. The load RAO in sway is equal to that obtained for surge, but shifted 90 degrees with respect to wave heading. As may be observed from the figure, the most relevant hydrodynamic loadings in these DOFs occurs for wave frequencies between 0.25 rad/s to 4.2 rad/s, corresponding to wave periods of 1.5 and 25 seconds.

The load RAO in heave is independent upon the incoming wave directions, as this is a vertical DOF for a body featuring symmetry around a vertical centerline. The load amplitudes becomes insignificant for an angular frequency of 2.2 rad/s, or about 3 seconds.

The load RAO in pitch and roll features the largest load amplitudes at wave headings 0/180 and 90 degrees, respectively. The most noteworthy hydrodynamic loadings occurs at similar wave frequencies observed for the heave load RAO, i.e. between periods 3 to 25 second.

The load RAOs in yaw should be zero due to the symmetrical shape of the Spar buoy. However, this is not the case for the presented floater, where a maximum value of 101.5 Nm/m is observed for a wave heading of 90 degrees. This is a significant increase compared to floater 7.47-115x4-10, which obtained insignificant load amplitudes. The reason for this increase is somewhat uncertain, but it is believed to be related to the generated mesh models, and most probably due to the circular shape being modelled by planar elements. However, the values are still relatively small and should not impose any errors in the hydrodynamic simulations. This was confirmed after the OrcaFlex analysis had been performed, where the maximum yaw motion induced from the waves was 0.25 degrees in environmental condition 2.

10.2.3 Floater 9.94-65x4-10

10.2.3.1 Hydrostatic stiffness

The hydrostatic stiffness matrix for floater 9.94-65x4-10 resulting from mesh model 5 is presented below.

$$\boldsymbol{C_{F9.94-65x4-10}} = \begin{bmatrix} 0 & 0 & 0 & 0 & 0 & 0 \\ 0 & 0 & 0 & 0 & 0 & 0 \\ 0 & 0 & 1.26\text{E}+5 & -1.51\text{E}+2 & -4.59\text{E}-1 & 0 \\ 0 & 0 & -1.51\text{E}+2 & 5.87\text{E}+8 & 7.57\text{E}-2 & -3.77\text{E}+3 \\ 0 & 0 & -4.59\text{E}-1 & -7.57\text{E}-2 & 5.87\text{E}+8 & -1.54\text{E}+3 \\ 0 & 0 & 0 & 0 & 0 & 0 \end{bmatrix}$$

As may be observed, the tendency of "zero-coefficients" gaining a numerical value is also present for this floater, due to the same reasons as previously discussed. This should however not impose any significant errors to the hydrodynamic simulation, as coefficients C_{46} and C_{56} are not imported to OrcaFlex, and coefficients C_{34}, C_{35}, C_{45} and their symmetrical counterparts are generally small compared to the coefficients on the main diagonal.

10.2.3.2 Frequency dependent damping and added mass

The frequency dependent damping and added mass for the relevant modes is presented in Figure 10-16 and Figure 10-17, respectively.

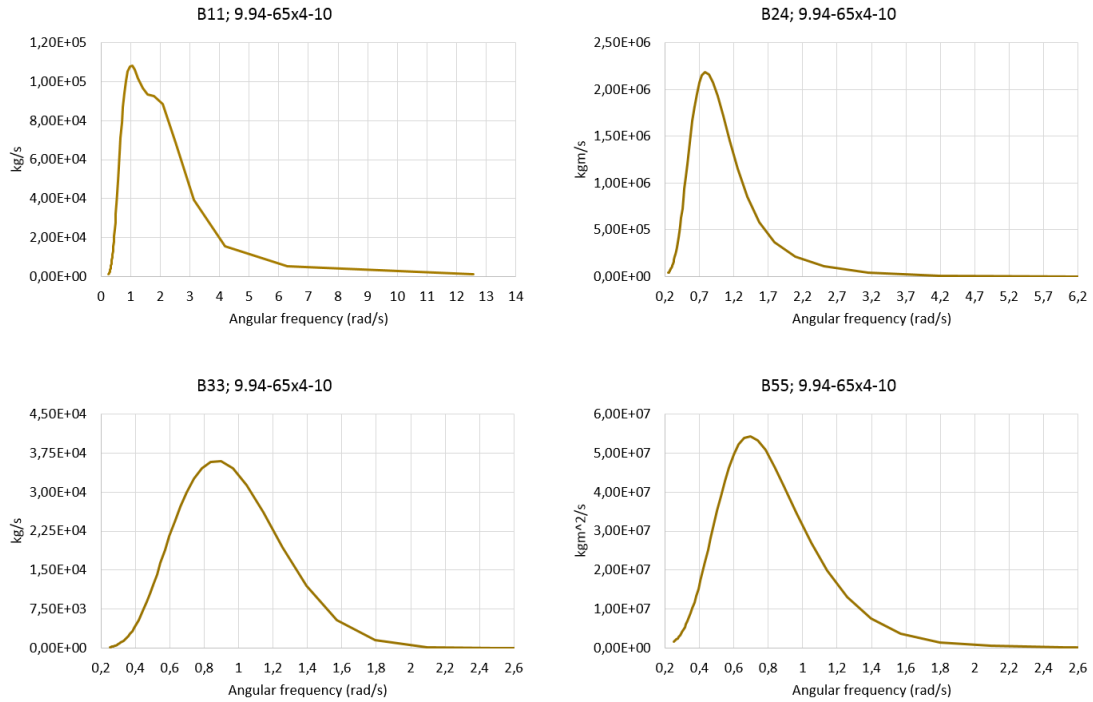

Figure 10-16: Frequency dependent damping for floater 9.94-65x4-10

The damping values are highly dependent upon the wave frequency. As was observed for the other floaters, there are insignificant damping in the lower frequency area, before it increases relatively rapidly towards the maximum value with an increase in wave frequency and becomes insignificant at higher frequencies. Significant damping in B11 occurs in the frequency range 0.25 rad/s to 4.0 rad/s (1.5 seconds to 25 seconds), while B33 and B55 generally becomes insignificant at 2.2 rad/s (3 seconds). B24 features irrelevant damping after an angular frequency of 4.2 rad/s, corresponding to 1.5 seconds.

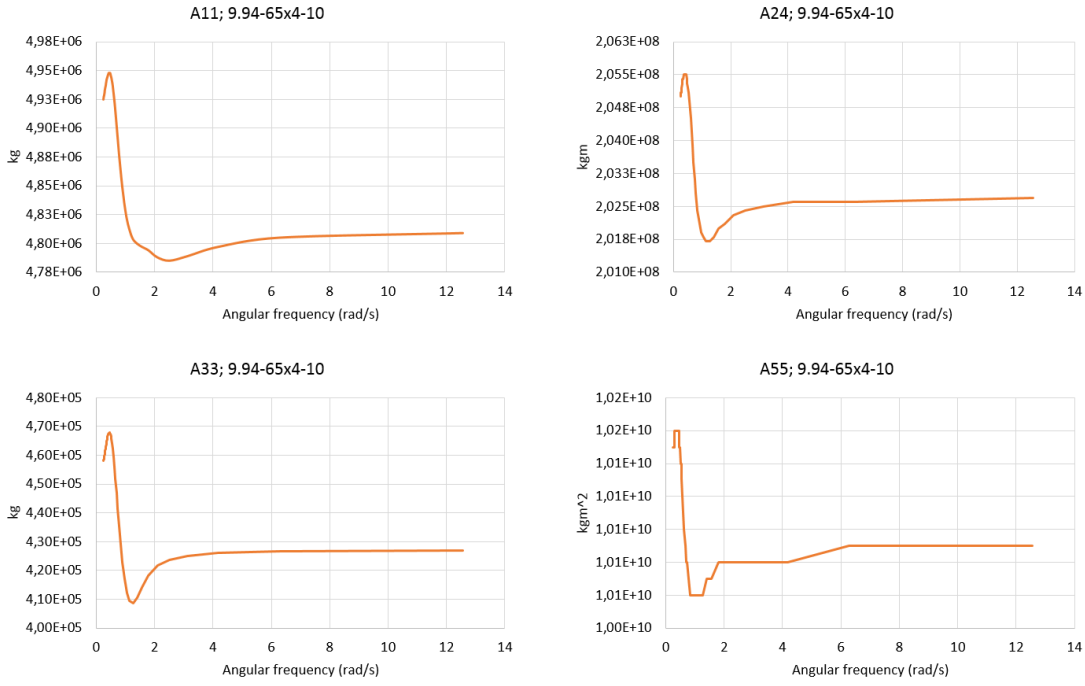

Figure 10-17: Frequency dependent added mass for floater 9.94-65x4-10

The added mass values does not vary to the same extent with respect frequency as the damping. There are consequently significant damping values throughout the frequency set. Similarly to the trend observed for the other floater, the added mass seems to be largest in high period waves, before becoming more or less constant at higher frequencies. As the plots converges towards the infinite frequency added mass, it may be stated that the added mass values obtained in HydroD is reliable.

10.2.3.3 Displacement RAO

The resulting displacement RAO in all DOFs for floater 9.94-65x4-10 for the seven wave headings is presented in Figure 10-18.

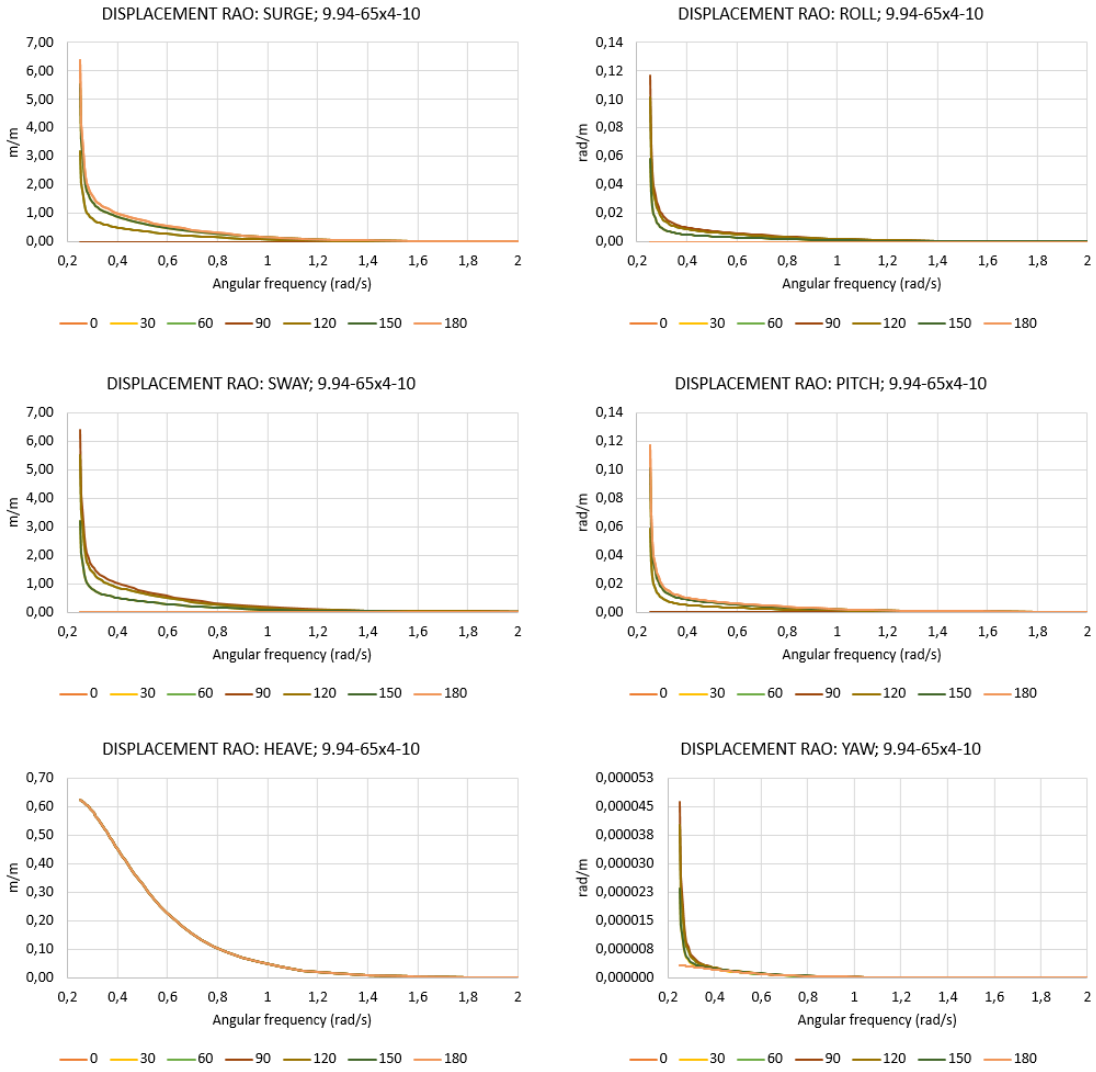

Figure 10-18: Displacement RAO is the six DOFs for floater 9.94-65x4-10

Similar tendencies as previously observed are also present for this floater. The surge and sway displacement RAOs are equal but shifted 90 degrees, as is the case with roll and pitch, while the heave RAO is independent upon the incoming wave direction and yaw displacements are generally insignificant. The frequency ranges containing significant displacement amplitudes are 0.25 rad/s to 1.0 rad/s (6 to 25 seconds) in surge, sway, roll and pitch and 0.25rad/s to 1.4 rad/s (4 to 25 seconds) in heave. There is also a relative sudden increase in surge, sway, roll and pitch displacement amplitudes around frequency 0.25 rad/s, corresponding to a wave period of 25 seconds. From Table 10-11, showing the natural periods for the present floater in the heave, roll and pitch recognized by HydroD, it may be

realized that the natural periods in roll and pitch are relatively close to the 25 seconds wave period. The sudden increase in displacement amplitude at this frequency may therefore be explained as resonance motions. The same does not hold for surge and sway, as the natural period is recognized as infinite in HydroD. However, the structure seems to be heavily exited in large wave periods regardless, which is most probably related to the low restoring in these DOFs in HydroD, as mooring lines were not implemented to the model.

Table 10-11: Eigen values obtained in HydroD analysis for floater 9.94-65x4-10

Eigen mode	Value [s]
Heave	42.6
Roll	25.7
Pitch	25.7

10.2.3.4 Load RAO

The load RAO for the seven wave directions in each DOFs is presented in Figure 10-19.

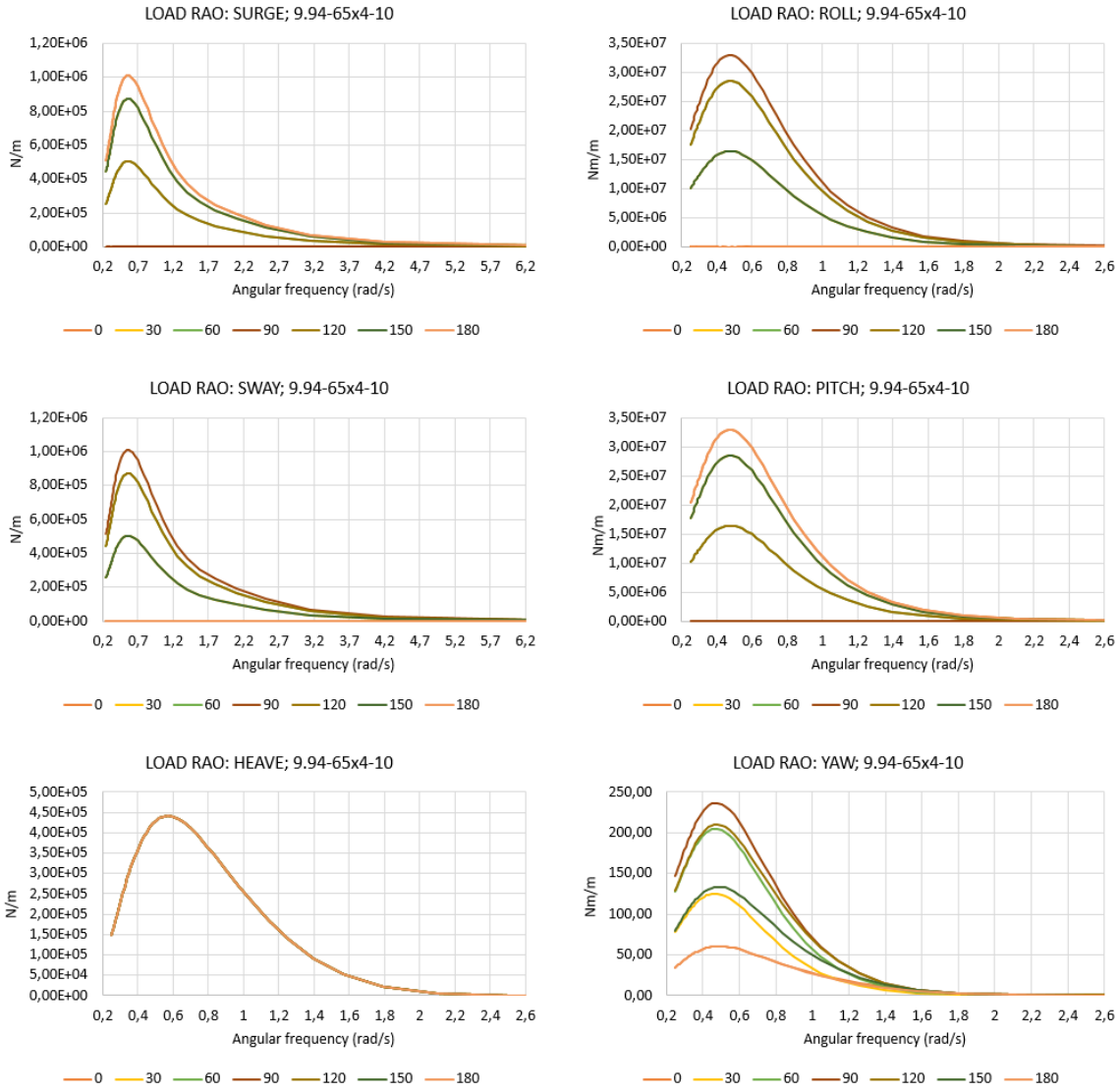

Figure 10-19: Load RAO in the six DOF for floater 9.94-65x4-10

Similar tendencies as was observed for the other floaters are also present in the featured load RAOs. The surge and sway load RAO is therefore equal, but shifted 90 degrees, where the same applies in roll and pitch. Surge and pitch therefore obtains the maximum load amplitude at wave headings of 0 and 180 degrees, while zero force is imposed at a wave heading of 90 degrees. The opposite applies for sway and roll. Heave is also independent upon wave directions due to the symmetrical properties of the Spar buoy. Most hydrodynamic loading occurs for angular frequencies between 0.25 rad/s to 4 rad/s (1.5 to 25 seconds) in surge and sway, 0.25 rad/s to 2 rad/s (3 to 25 seconds) in roll and pitch and 0.25 rad/s to 2 rad/s (3 to 25 seconds) in heave. The load amplitudes in yaw however features an additional increase compared to floater 8.45-90x4-10. Again, this deviation from the zero value is most probably related to some features with the mesh models. Nevertheless, the values are relatively small and should not impose any significance in the hydrodynamic simulation. This was later confirmed, as the maximum yaw motion due to the waves in environmental condition 2 was 0.06 degrees.

11 Results, OrcaFlex

The results from the OrcaFlex simulations will be presented in the following. However, an initial discussion of the direction of the incoming environmental loadings and studied parameters in the simulations seems appropriate. The trials needed to establish a suitable mooring line configuration, as discussed in section 8.2.4.4, will be covered in section 11.2, before the results are finally presented in section 11.3 through 11.5.

11.1 Studied parameters in OrcaFlex

In the presented work, the motions in the six DOFs, the resultant freeboard and air-gap and the mooring line tension and arc-length to touchdown point are evaluated for the basis of measuring the hydrodynamic performance of the studied floaters. Figure 11-1 illustrates the modelling environment in OrcaFlex. As may be observed, the direction of the wave propagation is to the negative x-direction. As the environmental conditions features a collinear wave and wind, the wind load is set to coincide with the propagation of the waves. Also note that the mooring line 1 is set to be directly oriented into the incoming environmental loadings, as discussed in section 8.2.4.4.

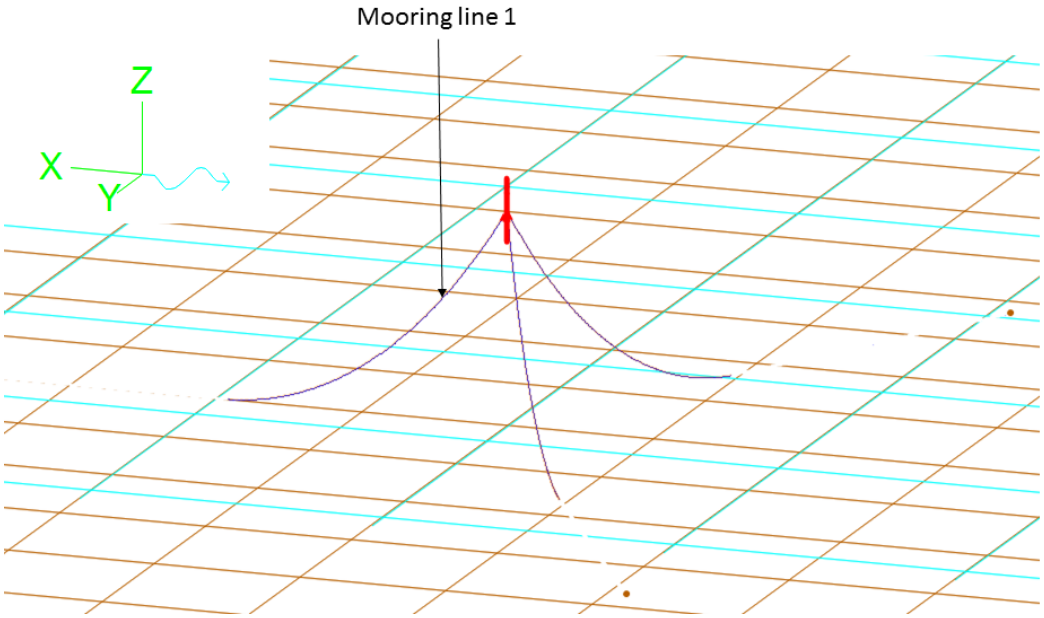

Figure 11-1: Illustration of OrcaFlex modelling environment

Due to the direction of the incoming environmental loading, motions in sway and roll will be negligible, and will consequently not be studied in the presented work. It is however reminded that surge and sway, and roll and pitch motions will feature equal motion characteristics due to the symmetric shape of the Spar buoy. The obtained results in surge and pitch is therefore directly transferable to sway and roll, respectively.

The yaw motions induced from the waves is insignificant due to the symmetries of the Spar buoy. This is illustrated in Figure 11-2, depicting a time series of the yaw motion for floater 9.94-65x4-10 in environmental condition 2 with only the wave loads applied.

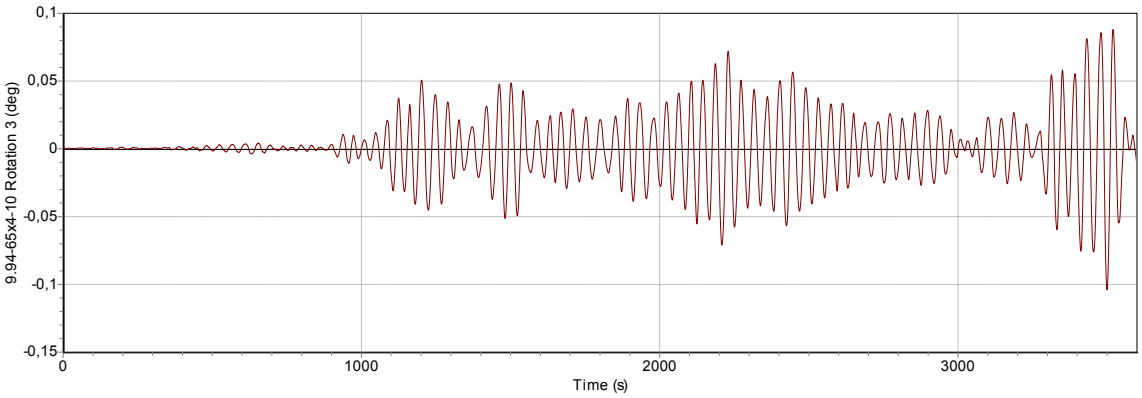

Figure 11-2: Time series of yaw motion with only wave loads applied in EC2, floater 9.94-65x4-10

However, yaw motions is important to control for a Spar buoy used in offshore wind turbine applications, especially for a VAWT. As mentioned in section 5.6, the generated torque in a VAWT is transferred to the support structure around the yaw axis. Yaw motions are also induced on structure due to an asymmetric force distribution about the rotor diameter, imposed by the turbulent variation in wind. However, turbulence is not considered in the presented work, and the yaw motions are therefore mainly induced from the generated torque. Spar buoys features relatively low yaw stiffness compared to other floating foundations and often requires additional yaw stiffness. On Statoil's Hywind pilot HAWT, this is achieved by implementing crowfoots connections between the mooring lines and the vessel. The DeepWind concept utilizes torque arms to extend the moment arm of the mooring lines to achieve a higher resistance to yaw motions [10]. In the OC3 Hywind floater, the yaw stiffness was modelled as a yaw spring with stiffness 98340 kNm/rad to represent a crowfoot connection similar to that used on Staoil's Hywind pilot [29].

Attempts were made of implementing the yaw spring used on the OC3 floater into the OrcaFlex model as an additional hydrostatic stiffness. However, OrcaFlex only allows hydrostatic stiffness to be specified in heave, roll and pitch, as the stiffness components in surge sway and yaw are all normally zero [48]. Further efforts were made of searching in papers and forums of a method of implement an external yaw stiffness into OrcaFlex, but to no avail. It was also attempted to model the crowfoot configuration presented in [49] to implement a realistic yaw stiffness to the model. However, this had to be abandoned due to time limitations.

Using the information presented in section 6.1 regarding the rotor's power output and rated rotational speed, the maximum torque imposed by the rotor may be found in the following manner:

$$T_{\max} = \frac{2300\ kW \cdot 60 \frac{sec}{\min}}{2\pi \cdot 12.5\ RPM} = 1786\ kNm$$

Trying to run an analysis in the operational condition with the maximum applied around the floater's local z-axis, results in relatively severe yaw rotations. This is illustrated in Figure 11-3, depicting a time series of the yaw motions for floater 9.94-65x4-10.

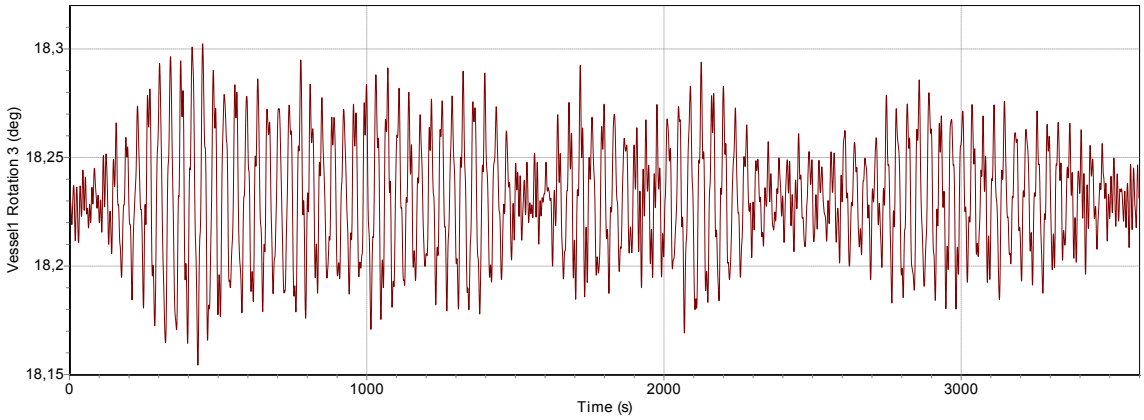

Figure 11-3: Time series of yaw motions with torque applied in EC1, floater 9.94-65x4-10

The mooring line configuration without additional yaw stiffness does not manage to counteract the imposed torque before a rotation of about 18.22 degrees. The small fluctuations around the mean value is caused by the waves as was observed in Figure 11-2. The large yaw seems to contaminate the other studied results, as the mooring lines are severely rotated away from their initial intended position. In other words, the excessive yaw motions needs to be controlled in the dynamic simulations in order to obtain realistic results for the other hydrodynamic performance parameters. As the implementation of sufficient yaw stiffness into the OrcaFlex model was not successful, it was decided to exclude the operational torque on the floater in environmental condition 1, leading to a model that assesses the turbine system as parked in both environmental conditions. The yaw motions in the presented work will therefore only be induced from the waves, which are significantly smaller compared to realistic state with the turbine running. It should however be noted that not obtaining realistic yaw motions in the simulations does not have a significance on the motions in the other DOFs, as yaw rotations does not augment wave excitation forces in the other DOFs and there is no internal couplings between yaw and other DOFs due to the symmetries of the Spar buoy. The radiation force couplings in yaw-pitch and yaw-surge are also a magnitude of five orders smaller than the radiation forces in surge-surge and pitch-pitch [50]. In other words, even though yaw motions is more or less disabled in the analysis, the induced motions in the other DOFs should still be representative of a realistic scenario. The significance of disabling the torque is therefore that the assessment of sufficient platform yaw stiffness for accommodating the VAWT in an operation condition may not assessed.

The motions that will be used as hydrodynamic performance parameters are therefore surge, heave and pitch. Note that due to the set wave propagation and wind load direction, the surge and pitch motions will be registered as negative in the OrcaFlex results.

The resultant freeboard and air-gap are also important performance parameters to consider. As stated in section 6.2.1 sufficient freeboard is a necessity in order to prevent severe hydrodynamic loadings acting on the rotor column of the VAWT. In a traditional VAWT, the rotor column transfers the mechanical work to the gearbox and generator assembly, meaning that it is directly connected to these components. An insufficient freeboard may therefore damage also damage the gearbox and generator assembly along with associated bearing systems. The air-gap shall fulfill a similar purpose as the freeboard, but is set to ensure that no hydrodynamic loadings acts on the airfoils, as these are not designed to withstand such loadings. The air-gap and freeboard will however only be assessed in the extreme environmental condition (EC 2), as the sufficiency of these parameters is only critical in this condition.

Lastly, the effective tension along with the arc-length to touchdown point obtained in the hydrodynamic simulations are evaluated. These parameters are a direct indication of the magnitude of the imposed motions, and will therefore give strong indications of the hydrodynamic performance. The effective tension is evaluated at the connection point to the vessel to study the maximum tension in the line. Note that the time series of the effective tension will only be evaluated for mooring line 1, as this is directed into the incoming wind and waves and is therefore most critical in relation to effective tension and arc-length to touchdown point. Statistical values (maximum, minimum, mean and standard deviation) for mooring line 2 and 3 are however presented in a table at the end of each section.

11.2 Identifying line configuration

As stated in section 8.2.4.4, the un-stretched mooring line length, line mass density and radius to anchor point must be established through trials to gain a suitable mooring line configuration. These trials will be presented in the following. As all floaters will feature an equal mooring line configuration by altering the water depth and radius to anchor point relative to the Spar buoys periphery, it is sufficient to base the trials on one of the three floater geometries established from the spreadsheet analysis. It was decided to use floater 9.94-65x4-10 for this purpose. Furthermore, in order to reduce the number of variables, it was decided to set the radius to anchor point to 853.87 meters, in accordance with the OC3 Hywind floater, and use an un-stretched mooring line length equal to three times the water depth based on a rule of thumb. The water-depth for the presented floater was set to 320 meters, resulting in an un-stretched mooring line length of 960 meters. The mooring lines mass density is therefore to be altered in the trials until a mooring configuration that gave no vertical pull-up force in the anchor is established. The established mooring line mass density and the set un-stretched mooring line length of 960 meters will then be used on the other two floaters (7.47-115x4-10 and 8.45-90x4-10), but the water-depth will be increased corresponding to the difference in metacenter position between the two aforementioned floaters and floater 9.94-65x4-10. The radius to anchor point will also be reduced corresponding to the difference in radius between floater 9.94-65x4-10 and floaters 7.47-115x4-10 and 8.45-90x4-10. In this way, the exact same mooring line configuration is achieved between the studied geometries, and the difference in the hydrodynamic simulations will only be related to the difference in geometry, as discussed in section 8.2.4.4.

Using the information obtained in the spreadsheet calculations, the position of the metacenter with respect to sea surface is found to be -41.58 meters. Embedding the mooring line orientation around the circular Spar buoy as presented in section 8.2.4.4, i.e. mooring line 1 oriented directly into the incoming wind and waves and space the line 120 degrees apart from each other, the resulting mooring line orientation presented in Table 11-1 is obtained. Note that OrcaFlex uses the center of the mooring line as the reference coordinate. The z-position at the connection point is therefore set 0.045 meters above the seabed, corresponding to half of the mooring diameter, to model a situation where line rests on the seabed without any penetration.

Table 11-1: Mooring line orientation for floater 9.94-65x4-10

		Polar coordinates		
		R [m]	Theta [deg]	Z [m]
Mooring line 1	End A	4.97	0	-41.59
	End B	853.87	0	-319.95
Mooring line 2	End A	4.97	120	-41.59
	End B	853.87	120	-319.95
Mooring line 3	End A	4.225	240	-41.59
	End B	853.87	240	-319.95

It may be noted that the sufficient line mass density to give no vertical pull-up load in the anchor is assessed by studying the time history of the arc-length to touchdown point of mooring line 1, as this is the most critical line due to its direct orientation with the incoming wind and wave forces.

11.2.1 Trial 1, 100 kg/m

The first trail was performed by specifying a line mass density of 100 kg/m, which resulted in the time history of the arc-length to touchdown-point presented in Figure 11-4.

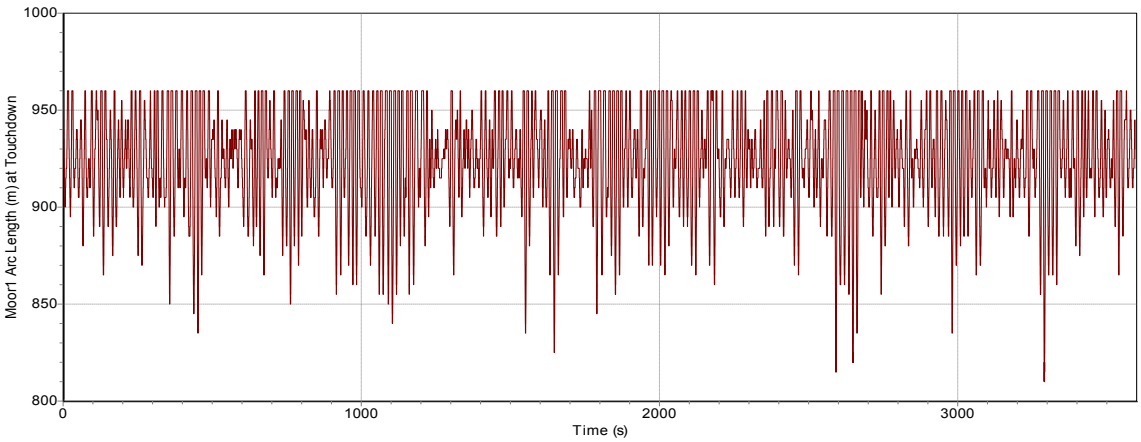

Figure 11-4: Time history of arc-length to touchdown point for mooring line 1, 100 kg/m line density

An arc-length of 960 indicates that the entire mooring line is suspended and there is consequently no mooring line resting on the seabed. This occurs relatively frequently, indicating that a line density of 100 kg/m is too small to absorb the associated forces in the extreme environmental condition without giving rise to vertical loads in the anchor with the given radius to anchor and un-stretched mooring line length.

11.2.2 Trial 2, 115 kg/m

The second trial featured a mass line density of 115 kg/m, which increases the tension at the connection point, enabling the mooring lines to counteract more of the imposed loadings from the environment. The resulting time history of the arc-length to touchdown point is presented in Figure 11-5. Again, an arc-length of 960 implies that the entire line length is suspended, giving rise to vertical loadings in the anchor.

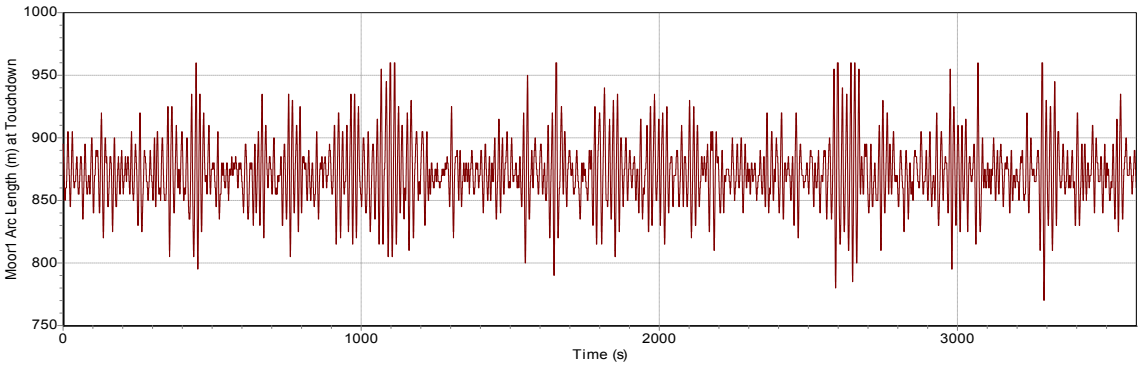

Figure 11-5: Time history of arc-length to touchdown point for mooring line 1, 115 kg/m line density

The time set reveals smaller arc-length to touchdown point compared to the initial trial, with a mean value of about 870 meters. However, there are some data points illustrating an arc-length of 960

meters, and there is consequently no additional line resting on the seabed. The featured line mass density is therefore insufficient to absorbing the loadings associated with the storm condition without giving vertical pull-up forces in the anchor.

11.2.3 Trial 3, 125 kg/m

The third trail was conducted with a line mass density of 125 kg/m. The resulting arc-length to touchdown point time series for mooring line 1 is presented in Figure 11-6.

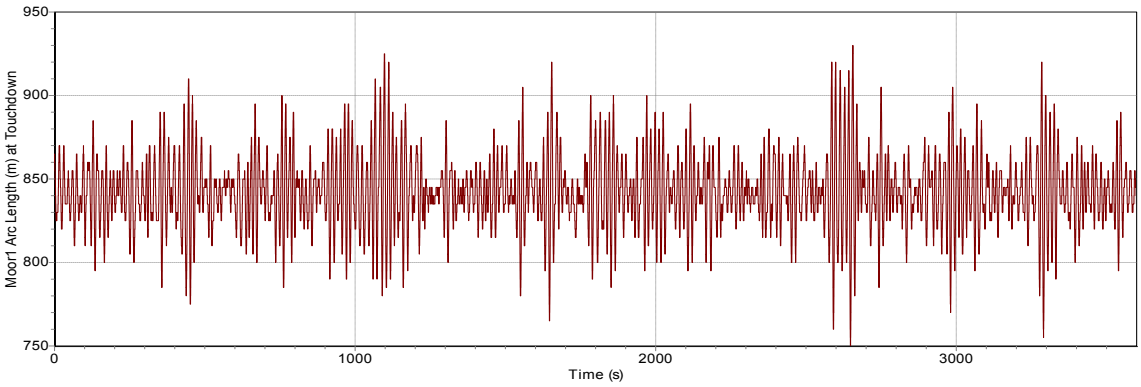

Figure 11-6: Time history of arc-length to touchdown point, 125 kg/m line density

As may be observed, the highest arc-length to touchdown point is about 930 meters, leading to an additional 30 meter of mooring line resting on the bottom. A line mass density of 125 kg/m is therefore applicable to avoid vertical pull-up loads in the anchor with the current mooring line setup. This line mass density, along with the un-stretched mooring line length of 960 meters will be used when establishing the mooring line configuration for the other two floaters. Relevant results from the static calculation for the featured mooring line configuration is presented in Table 11-2.

Table 11-2: Results from static analysis with mooring line mass density of 125 kg/m, floater 9.94-65x4-10

Parameter	Value	Unit
Static position (x, y, z)	(0, 0, -0.0001)	m
Line tension at connection	673.52	kN
Horizontal force at connection	350.45	kN
Vertical force at connection	575.16	kN
Line orientation angle	31.405	deg
Arc length to TDP	491	m
Mooring line mass	175.95	tons

The line orientation angle corresponds to the angle between the outgoing lines and the vertical center axis of the platform. The results presented in Table 11-2 may be used to verify that the mooring line configuration for the other floaters is indeed identical to the configuration presented above.

It may be noted that adding three mooring lines introduces an additional mass to the total system, resulting in a downwards translation of the vessel in the static equilibrium position. The inputted mass for the vessel model in OrcaFlex, originally based on mass estimates from the inventor models, therefore has to be reduced with an equal amount added by the mooring lines in order to obtain the intended freeboard of 10 meters in the equilibrium position. The mooring line total mass, i.e. from all three lines, is presented in Table 11-2.

11.3 Floater 7.47-115x4-10

The results from the dynamic simulation for floater 7.47-115x4-10 will be presented in the following, where the equal mooring configuration to the one obtained in the previous section will be presented first.

11.3.1 Mooring line configuration

From the spreadsheet calculations, it may be realized that floater 7.47x115-4x10 features a metacenter position relative to the sea surface of -65.98 meters and a radius the outer periphery of the Spar buoy of 3.735 meters. The water-depth must therefore be increased by 24.39 meters, while the radius to anchor point must be reduced by 1.235 meters in order to obtain the same mooring line configuration as presented in section 11.2.3. Using a spacing of 120 degrees between lines and orienting mooring line 1 directly into the wind and waves yields the mooring orientation presented in Table 11-3.

Table 11-3: Mooring line orientation for floater 7.47-115x4-10

		Polar coordinates		
		R [m]	Theta [deg]	Z [m]
Mooring line 1	End A	3.735	0	-65.98
	End B	852.635	0	-344.34
Mooring line 2	End A	3.735	120	-65.98
	End B	852.635	120	-344.34
Mooring line 3	End A	3.735	240	-65.98
	End B	852.635	240	-344.34

Using the un-stretched line length of 960 meters and the line mass density obtained in the previous section results in the static results presented in Table 11-4.

Table 11-4: Results from static analysis, floater 7.47-115x4-10

Parameter	Value	Unit
Static position (x, y, z)	(0, 0, -0.0001)	m
Line tension at connection	673.52	kN
Horizontal force at connection	350.45	kN
Vertical force at connection	575.16	kN
Line orientation angle	31.405	deg
Arc length to TDP	491	m
Mooring line mass	175.95	tons

As may be observed, line tension at connection point and the line orientation angle is the same as was observed in section 11.2.3, implying that the horizontal force and vertical force at the connection point is equal. The arc length to touchdown point obtain is also equal, conforming that the mooring line configuration is completely identical to the baseline established in section 11.2.3.

As stated in section 11.2, the vessel's mass in OrcaFlex is reduced with an equal amount added by the mooring lines to achieve a freeboard of 10 meters in the static position. This mass reduction is achieved by decreasing the amount of ballast, as the floater, rotor and generator features a constant mass that cannot be altered. This means that the OrcaFlex model features 175.95 tons less ballast mass than obtained in the spreadsheet analysis. This reduction will not alter the total system mass, but the vessel's

CoG position along with the vessel's moment of inertia tensor will be slightly different. These parameters must therefore be updated in the vessel's model prior to performing the dynamic simulations. Reducing the ballast mass with 175.95 tons in the Inventor model gives the center of gravity and moment of inertias presented in Table 11-5. For values with increased accuracy, reference is made to Appendix C.

Table 11-5: Revised center of gravity and moment of inertias for the dynamic simulation in OrcaFlex, floater 7.47-115x4-10

Parameter	Value	Unit
$\overline{KG}$	35.485	m
I_{xx}	1.448E10	kgm^2
I_{yy}	1.448E10	kgm^2
I_{zz}	1.357E8	kgm^2

Note that the altered center of gravity and inertias was not assessed in section 11.2, as the main purpose was to address a suitable line mass density rather than acquire accurate dynamic simulations.

11.3.2 Results, EC 1

The results from the operating environmental condition featuring a significant wave height of 3.62 meters, a spectral peak period of 10.29 seconds and a constant wind force of 365 kN applied at the center of the rotor blades (72.5 meters from the SWL) will be presented in the following. However, as stated in section 8.2.4.1, performing the hydrodynamic simulation using the implicit integration scheme requires a time step sensitivity analysis. The surge, heave and yaw motion, along with the tension in connection point are therefore compared between two analyses consisting of time step 0.1 seconds and 0.05 seconds. The resulting difference in minimum value, maximum value, mean value and standard deviation may be observed in Table 11-6.

Table 11-6: Comparison of results from simulations with time step 0.1 seconds and 0.05 seconds, EC1, floater 7.47-115x4-10

Parameter	Differential values			
	Min	Max	Mean	Std.
Surge	0.00057%	0.00465%	0.00030%	0.08119%
Heave	0.04858%	1.07413%	0.00013%	0.08490%
Pitch	0.02571%	0.03261%	0.00005%	0.09510%
Mooring line 1 tension	0.01818%	0.01720%	0.00002%	0.02332%
Mooring line 2 tension	0.00832%	0.00710%	0.00002%	0.00971%
Mooring line 3 tension	0.00831%	0.00710%	0.00002%	0.00971%

As may be observed there are only insignificance differences between the two simulations, where the maximum motions in heave features the largest deviations of 1.07%. A dynamic simulation with time step 0.05 is therefore deemed to sufficiently converge the solution for all relevant purposes.

The resulting motions in surge, heave and pitch are presented in Figure 11-7, Figure 11-8 and Figure 11-9, respectively. Note that the surge translation is evaluated at the pitch center, i.e. at z=-65.98 meters, in order to exclude the additional surge motions arising from a pitch rotation. Statistical values,

including maximum and minimum position, mean position and standard deviations from the time histories are also presented in Table 11-7.

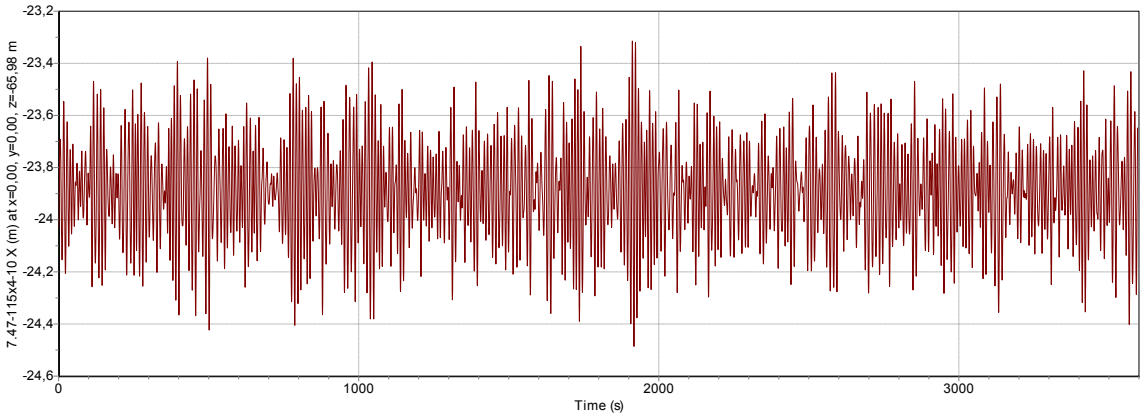

Figure 11-7: Surge motions at EC1, floater 7.47-115x4-10

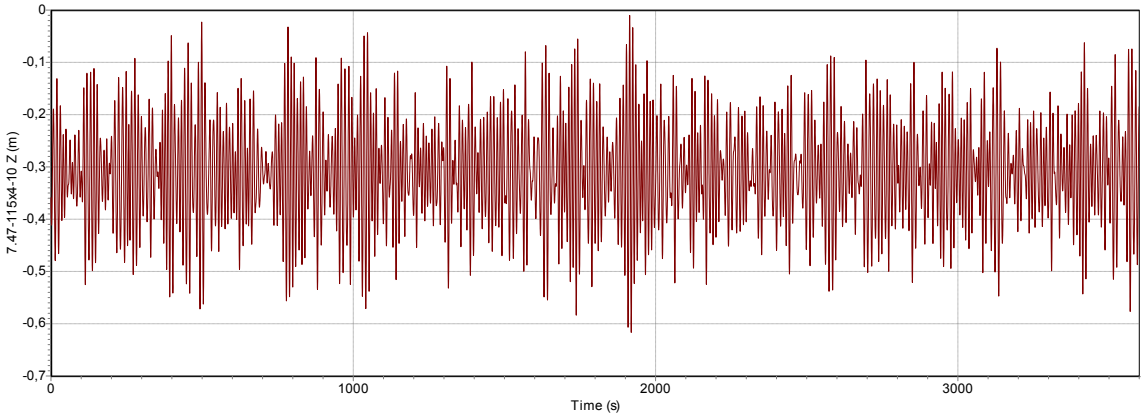

Figure 11-8: Heave motions at EC1, floater 7.47-115x4-10

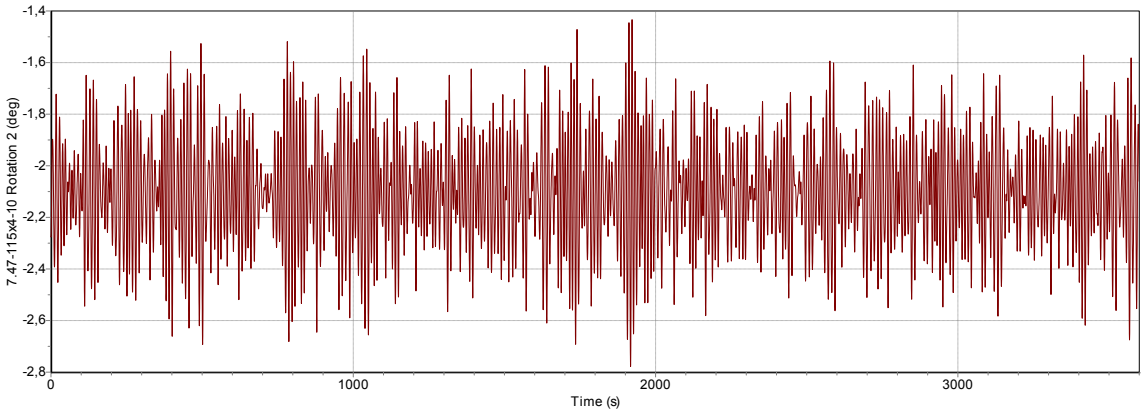

Figure 11-9: Pitch motions at EC1, floater 7.47-115x4-10

Table 11-7: Statistical values in surge, heave and pitch, EC1, floater 7.47-115x4-10

Parameter	Min	Max	Mean	Std.	Unit
Surge (0, 0, -65.98)	-23.314	-24.486	-23.890	0.183	m
Heave (0, 0, 0)	-0.0102	-0.617	-0.311	0.096	m
Pitch	-1.434	-2.778	-2.102	0.207	deg

As may be observed from Table 11-7, the mean position of the vessel in surge and pitch obtained during the simulation are significantly different from the initially stable position of 0 meters and 0 degrees. The waves are oscillatory in nature, meaning that they will impose oscillatory motions around a mean value. This implies that the waves does not cause the observable offset from the static position, and it must consequently be related to the applied wind load. This was confirmed by performing a static analysis comprising of only the wind load, which results in the stable surge position of -23.89 meters and the static pitch rotation of -2.10 degrees. It may therefore be stated that the constant applied wind load results in the observable offsets in surge and pitch from the initial stable position, and the waves imposes oscillatory motions around this mean value.

There is also an offset in the mean heave position when compared to the initially stable position of -0.0001 meters. This is most probably related to the obtained mean surge position will suspend more mooring line, consequently increasing the systems mass and translating the vessel downwards in heave. To evaluate this effect, Table 11-8 compares the arc-length to touchdown point of each individual mooring line in the static analysis to the mean arc-lengths obtained in the dynamic simulation.

Table 11-8: Comparison of arc-length to touchdown point in static and dynamic analysis

	Static Analysis	Dynamic Analysis (mean)
Mooring line 1	491.0 m	599.86 m
Mooring line 2	491.0 m	451.21 m
Mooring line 3	491.0 m	451.21 m

As may be observed, the reduction in arc-length to touchdown point for mooring line 2 and 3 is in total 79.58 meters, while the increase in arc-length to touchdown point for mooring line 1 is 108.86 meters. This will consequently increase the system's mass in the mean position induced from the wind load, leading to the observable average heave position in the dataset.

11.3.3 Results, EC 2

The resulting hydrodynamic performance parameter from the extreme environmental condition featuring a significant wave height of 12.9 meters, a spectral peak period of 14.1 seconds and a constant wind force of 1200 kN applied at the center of the rotor blades (72.5 meters from the SWL) are presented in the following. It was decided to include a time step sensitivity analysis in this environmental condition, as the more severe sea state may, or may not lead to an increased sensitivity for the integration time step. The resulting difference between two analysis featuring a time step of 0.1 and 0.05 seconds is presented in Table 11-9.

Table 11-9: Comparison of results from simulations with time step 0.1 seconds and 0.05 seconds, EC2, floater 7.47-115x4-10

Parameters	Differential values			
	Min	Max	Mean	Std.
Surge	0.00869%	0.01071%	0.00029%	0.04979%
Heave	0.01666%	0.39348%	0.00066%	0.06222%
Pitch	0.05509%	0.82745%	0.00017%	0.09532%
Mooring line 1 tension	0.06240%	0.06192%	0.00006%	0.03070%
Mooring line 2 tension	0.01478%	0.00854%	0.00026%	0.02152%
Mooring line 3 tension	0.00941%	0.01891%	0.00025%	0.02152%

As may be observed, the differences are insignificant, and the hydrodynamic simulation was consequently performed with a time step of 0.05 seconds.

The resulting surge, heave and pitch motion are presented in Figure 11-10, Figure 11-11 and Figure 11-12, respectively. The surge motions are evaluated at the pitch center (metacenter) in order to exclude the pitch induced surge motions. A summary of the results is presented in Table 11-10.

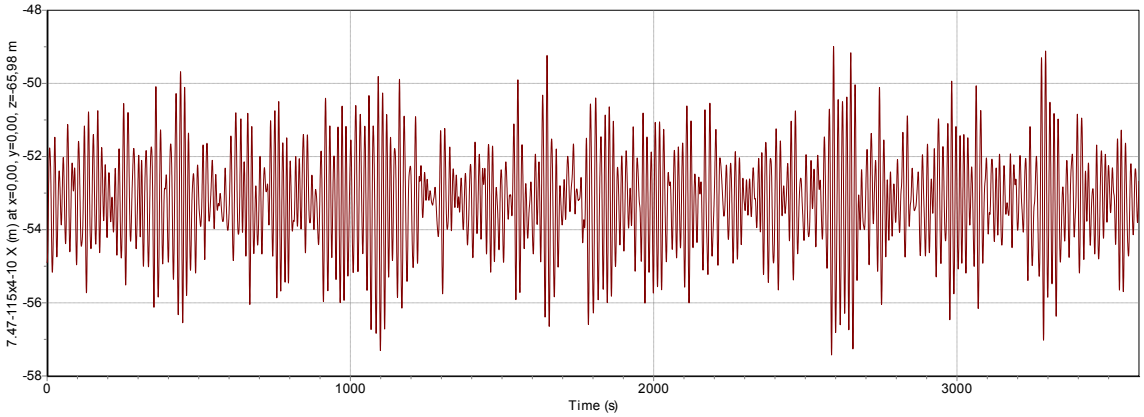

Figure 11-10: Surge motions at EC 2, floater 7.47-115x4-10

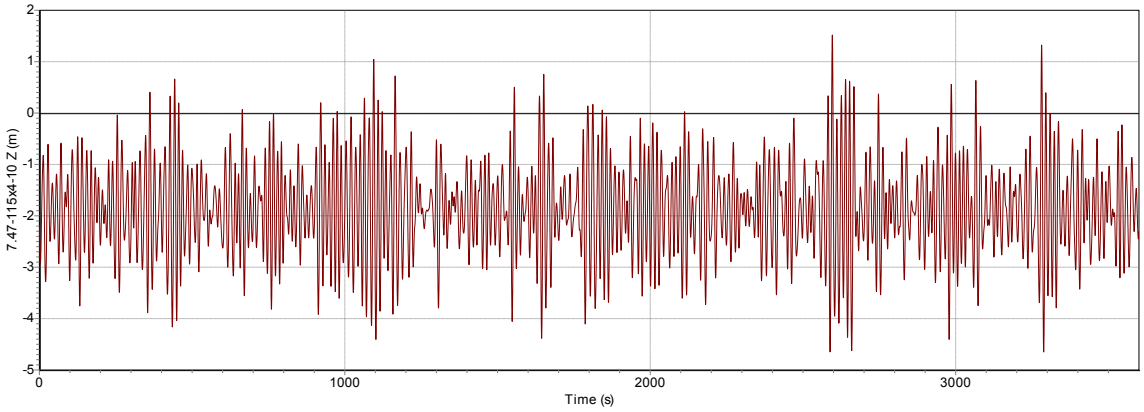

Figure 11-11: Heave motions at EC 2, floater 7.47-115x4-10

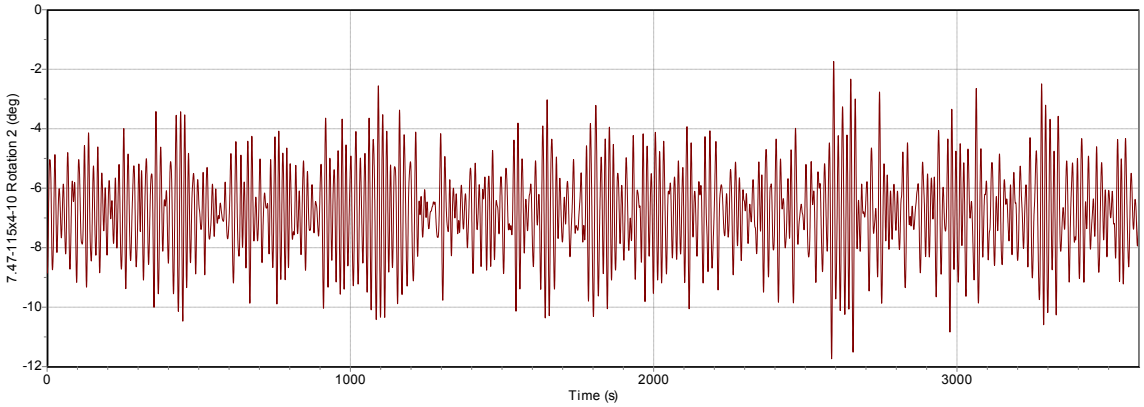

Figure 11-12: Pitch motions at EC 2, floater 7.47-115x4-10

Table 11-10: Statistical values for surge, heave and pitch, EC2, floater 7.47-115x4-10

Parameter	Min	Max	Mean	Std.	Unit
Surge (0, 0, -65.98)	-48.991	-57.426	-53.206	1.277	m
Heave (0, 0, 0)	1.519	-4.650	-1.865	0.878	m
Pitch	-1.737	-11.738	-6.812	1.407	deg

As may be observed, the increased wind load in EC 2 leads to a higher average surge position and static pitch angle compared to EC 1. The increased mean surge position also increases the length of suspended mooring line, resulting in the observable average heave position throughout the dataset. The more energetic waves also induces larger oscillatory motions around the mean values compared to environmental condition 1, as may be observed form the increased standard deviations for the present environmental condition.

The freeboard and air-gap plots are generated by studying the sea surface clearance for the respective location of the freeboard and air gap in the local coordinate system. As the local coordinate system translates and rotates with the body, the specified points will vary in position in the global coordinate system with time, thus generating a time dependent surface clearance plot. The motions affecting the resultant freeboard and air gap are heave and pitch. The heave motions dependency is self-explanatory, but some clarifications about the pitch motion's dependency is needed. A pitch rotation will translate the top of the floater and the airfoils towards the sea surface, as illustrated in Figure 11-13. It is therefore necessary to evaluate the resultant freeboard at the periphery of the Spar buoy, and the airgap at the lowermost point of the airfoils, as this will be the most critical points to assess with respect to submergence.

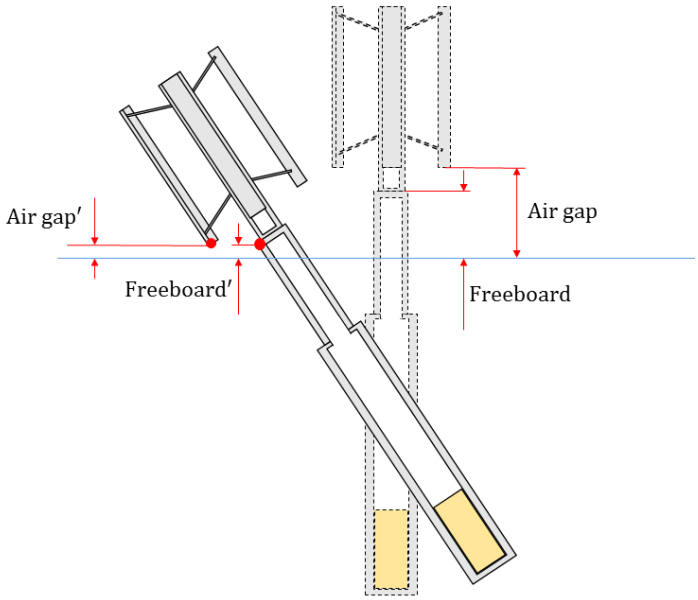

Figure 11-13: Illustration of the freeboard and air-gap's dependency on pitch motions

As the local coordinate system's origin is located in the center of the Spar buoy at the SWL, the critical points to evaluate are (-3.735, 0, 10) for the freeboard and (-22.5, 0, 23) for the airgap, indicated with red dots in Figure 11-13. Note that the coordinates in the x-axis is set to negative values as the incoming environmental forces acts in the negative x-direction. The resultant sea surface clearance plots are presented in Figure 11-14 and Figure 11-15 for the freeboard and air-gap, respectively. Statistical values throughout the simulations is also presented in Table 11-11.

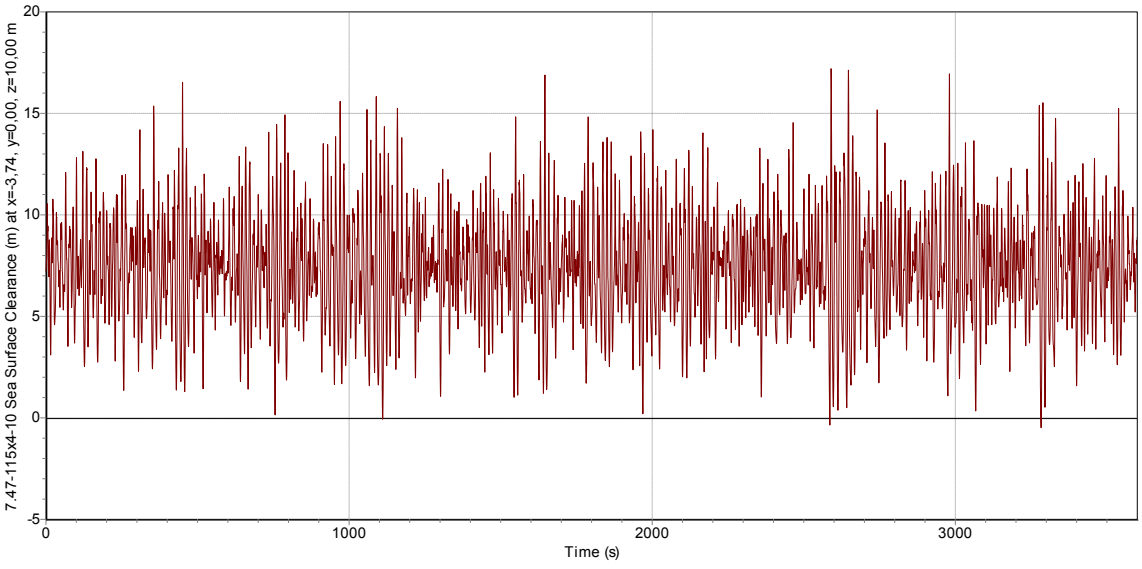

Figure 11-14: Resultant freeboard at EC2, floater 7.47-115x4-10

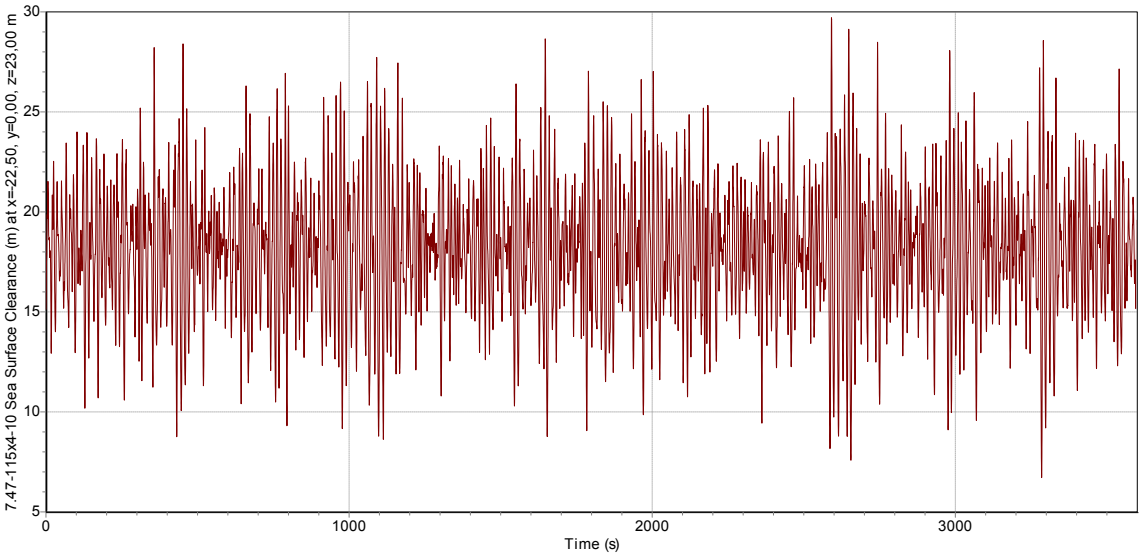

Figure 11-15: Resultant air-gap at EC2, floater 7.47-115x4-10

Table 11-11: Statistical values for freeboard and air-gap, EC2, floater 7.47-115x4-10

Parameter	Min	Max	Mean	Std.	Unit
Freeboard	-0.485	17.201	7.416	2.642	m
Air-gap	6.713	29.710	18.129	3.283	m

As may be observed, the freeboard features a mean value of 7.42 meters throughout the dynamic simulation, 2.58 meters lower than the static stable freeboard of 10 meters. The offset form the 10-meter freeboard may be explained by the mean heave position and the mean pitch angle obtained in the simulations. The minimum freeboard is -0.485 meters, implying that portions of the rotor column is submerged during the one-hour storm. Hydrodynamic loadings are therefore exerted onto the rotor-column, which might potentially damage the bearing systems and the gearbox and generator assembly, as previously discussed. The freeboard is therefore not acceptable, and should be increased for the present design.

The air gap features a mean value of 18.13 meters, which is 4.87 meters lower than the target value of 23 meters. Similar to the freeboard, this deviation is caused by the mean heave position and static pitch rotation induced from the applied wind load. The minimum air-gap throughout the simulation is 6.71 meters, and there is consequently some safety margins between the sea surface and the airfoils in the most critical instantaneous point in time. The air-gap of 23 meters therefore seems to be sufficient for floater 7.47-115x4-10.

The time series of arc-length to touchdown point and line tension at the connection point for mooring line 1 is presented in Figure 11-16 and Figure 11-17, respectively. As stated in section 11.1, mooring line 1 is the most critical line to study, as it is directed into the incoming wind and waves. Statistical values gained through the hydrodynamic simulations are presented in Table 11-12, where mooring line 2 and 3 are also included.

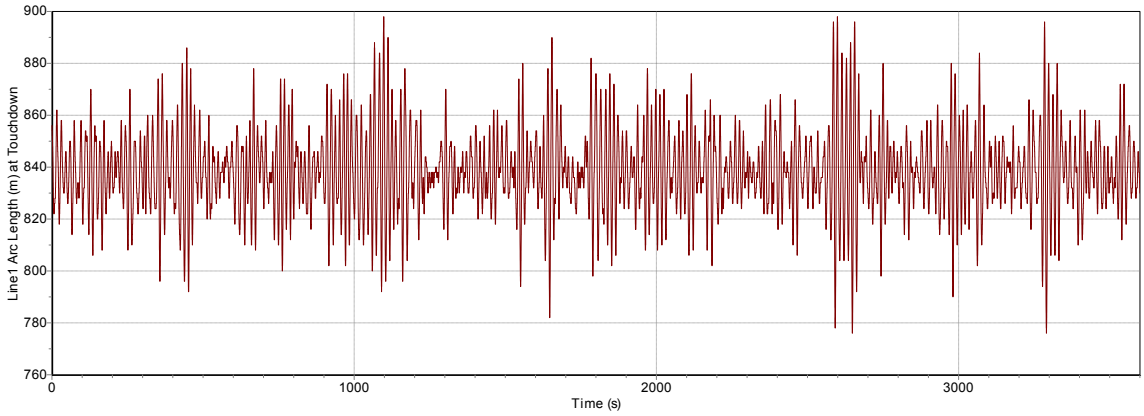

Figure 11-16: Resultant arc-length to touchdown point for mooring line 1 at EC2, floater 7.47-115x4-10

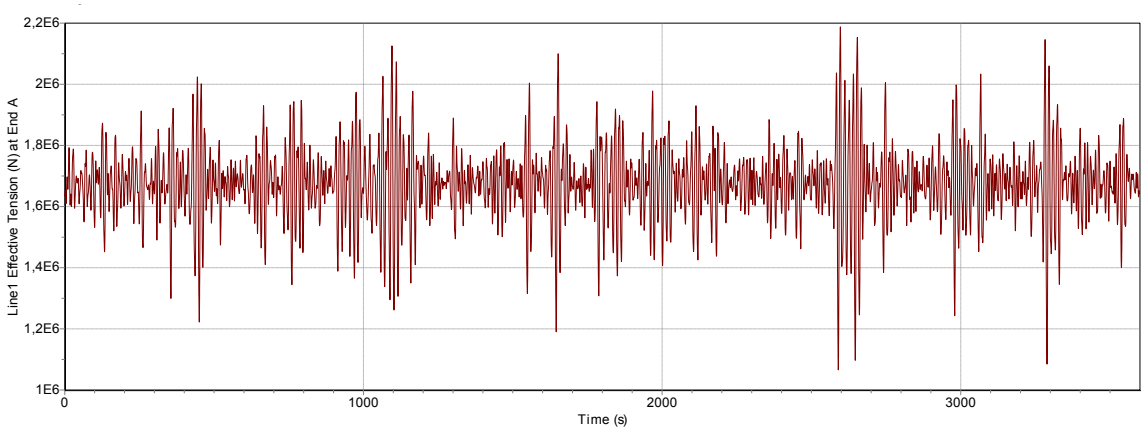

Figure 11-17: Resultant effective tension in mooring line 1 at EC2, floater 7.47-115x4-10

Table 11-12: Statistical values for effective tension and arc-length to touchdown point, EC 2, floater 7.47-115x4-10

Parameter	Min	Max	Mean	Std.	Unit
Arc-length to TDP mooring line 1	776.0	898.0	838.45	15.724	m
Effective tension mooring line 1	1065.61	2187.75	1675.76	117.97	kN
Arc-length to TDP mooring line 2	402.0	430.0	415.42	3.401	m
Effective tension mooring line 2	489.60	572.91	530.02	9.862	kN
Arc-length to TDP mooring line 3	402.0	430.0	415.42	3.401	m
Effective tension mooring line 3	489.54	572.91	530.02	9.862	kN

As may be observed, the translation in surge imposed by the storm wind load greatly increases the mean arc-length to touchdown point in mooring line 1 from the result obtained in the static analysis of 491.0 meters, where the opposite applies for mooring line 2 and 3. The maximum arc-length to touchdown point in mooring line 1 throughout the simulation is 898.0 meters. As the un-stretched line-length is 960 meters, there is a resultant minimum line-length of 62 meters resting on the seabed throughout the

simulations. This confirms that there is no vertical pull-up loads in the anchor during the 1-hour storm for the present floater, as was intended when establishing the mooring line configuration in section 11.2.

The increased arc-length to touchdown point in mooring line 1 results in higher effective tensions compared to line 2 and 3. The increased standard deviation for line 1 also indicates that the tension generally varies more in this line compared to line 2 and 3. The maximum tension in mooring line 1 is 2187.75 kN

11.4 Floater 8.45-90x4-10

11.4.1 Mooring line configuration

Floater 8.45-90x4-10 features a metacenter position relative to the sea surface of Z=-53.78 meters, and the water depth must be increased to 332.19 meters to achieve the same water depth relative to the connection point as the baseline presented in section 11.2.3. The radius to anchor point also needs to be reduced by 0.745 meters, as this corresponds to the difference in radius between the present floater and floater 9.94-65x4-10. Setting mooring line 1 directly into the incoming wind and waves yields the mooring configuration presented in Table 11-13.

Table 11-13: Mooring line orientation for floater 8.45-90x4-10

		Polar coordinates		
		R [m]	Theta [deg]	Z [m]
Mooring line 1	End A	4.225	0	-53.78
	End B	853.125	0	-332.14
Mooring line 2	End A	4.225	120	-53.78
	End B	853.125	120	-332.14
Mooring line 3	End A	4.225	240	-53.78
	End B	853.125	240	-332.14

The static parameters resulting from the presented mooring orientation with an un-stretched line length of 960 meters and a line mass density of 125 kg/m is presented in Table 11-14.

Table 11-14: Results from static analysis, floater 8.45-90x4-10

Parameter	Value	Unit
Static position (x, y, z)	(0, 0, -0.0001)	m
Line tension at connection	673.52	kN
Horizontal force at connection	350.45	kN
Vertical force at connection	575.16	kN
Line orientation angle	31.405	deg
Arc length to TDP	491	m
Mass of mooring lines	175.95	tons

All parameters are equal to the results obtained in section 11.2.3, and it may therefore be stated that the resultant mooring line configuration is identical to the baseline.

The updated center of gravity and moments of inertias after the additional 175.95 tons of mooring line mass has been subtracted from the vessel mass in Inventor is presented in Table 11-15. For accurate values of these parameters, reference is made to Appendix C.

Table 11-15: Revised center of gravity and moment of inertias for the dynamic simulation in OrcaFlex, floater 8.45-90x4-10

Parameter	Value	Unit
$\overline{KG}$	28.852	m
I_{xx}	1.087E10	kgm^2
I_{yy}	1.087E10	kgm^2
I_{zz}	1.452E8	kgm^2

11.4.2 Results, EC 1

A time step sensitivity analysis was also performed for the present floater geometry. Table 11-16 presents the resulting differences in surge, heave and pitch motion along with effective mooring line tension for two analysis comprising of time steps 0.1 seconds and 0.05 seconds.

Table 11-16: Comparison of results from simulations with time step 0.1 seconds and 0.05 seconds, EC1, floater 8.45-90x4-10

	Differential values			
	Min	Max	Mean	Std.
Surge	0.00292%	0.00180%	0.00023%	0.08114%
Heave	0.03473%	1.32339%	0.00042%	0.08436%
Pitch	0.02045%	0.05007%	0.00005%	0.09669%
Mooring line 1 tension	0.00744%	0.03953%	0.00001%	0.03642%
Mooring line 2 tension	0.01023%	0.00702%	0.00000%	0.00538%
Mooring line 3 tension	0.00703%	0.01022%	0.00000%	0.00540%

As may be observed, the differences are generally insignificant for the studied parameters, where the maximum translation in heave features the larges deviation of 1.32%. An analysis with time step 0.05 seconds is therefore deemed to sufficiently converge the solution, and will be used to perform the simulations.

The resultant surge, heave and pitch motions from the operational environmental condition is depicted in Figure 11-18 through Figure 11-20. It is reminded that the surge motions is evaluated at the pitch rotation center, i.e. metacenter, to exclude the pitch imposed surge motions. A summary of the time series is presented in Table 11-17.

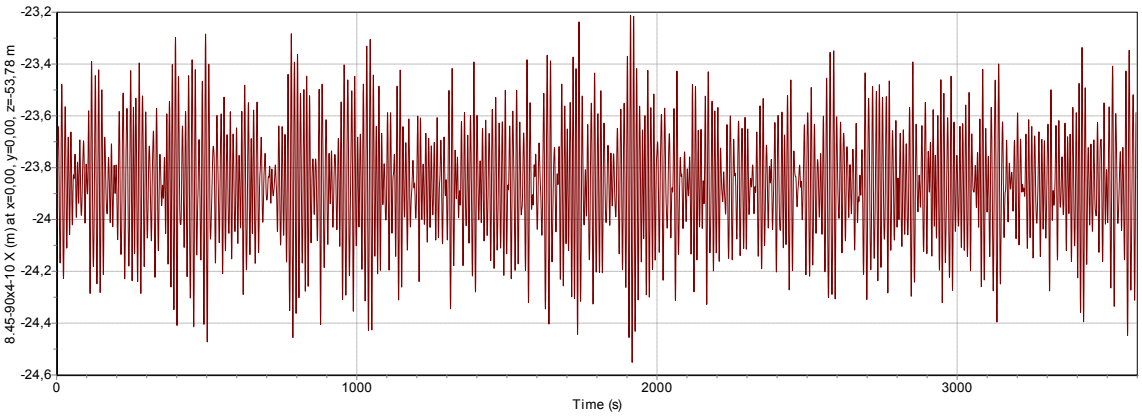

Figure 11-18: Surge motions at EC 1, floater 8.45-90x4-10

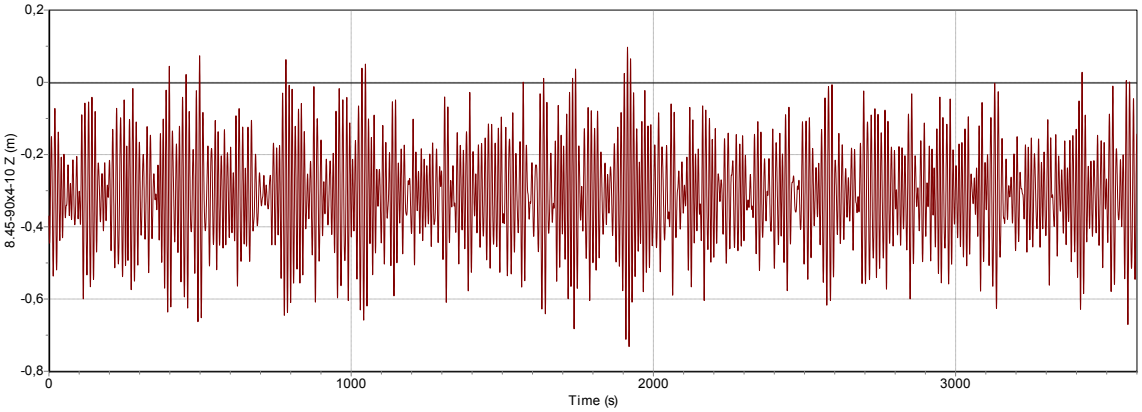

Figure 11-19: Heave motions at EC1, floater 8.45-90x4-10

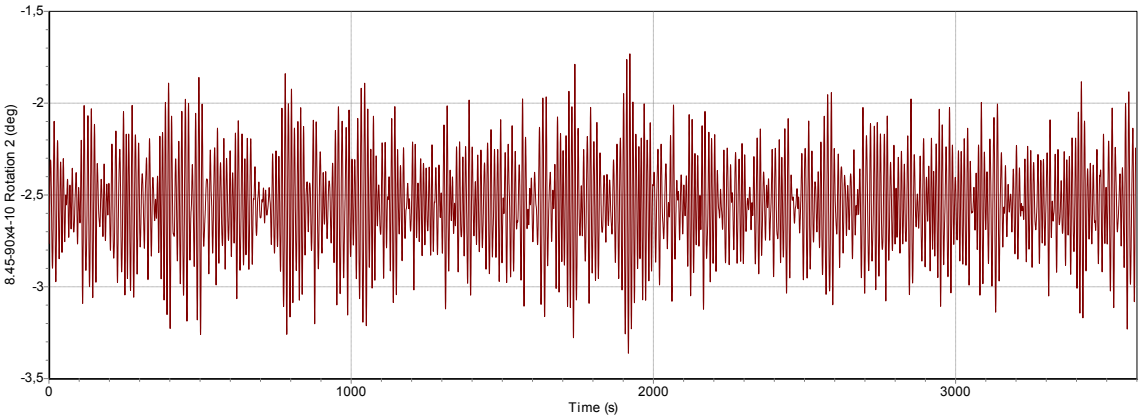

Figure 11-20: Pitch motions at EC1, floater 8.45-90x4-10

Table 11-17: Statistical values in surge, heave and pitch, EC 1, floater 8.45-90x4-10

Parameter	Min	Max	Mean	Std.	Unit
Surge (0, 0, -53.78)	-23.212	-24.552	-23.868	0.209	m
Heave (0, 0, 0)	0.0973	-0.732	-0.311	0.130	m
Pitch	-1.731	-3.362	-2.553	0.250	deg

As was observed for floater 7.47-115x4-10, the constant applied wind load leads to an offset from the initial stable position in surge and pitch. This offsets also suspends more mooring line initially resting on the seabed, resulting the mean heave position observed in the dataset.

11.4.3 Results, EC 2

A time step sensitivity analysis was also performed in environmental condition 2 for conservative reasons. The resulting differences in surge, sway, heave motions and effective mooring line tension at connection point between two analysis featuring a time step of 0.1 seconds and 0.05 seconds is presented in Table 11-18.

Table 11-18: Comparison of results from simulations with time step 0.1 seconds and 0.05 seconds, EC2, floater 8.45-90x4-10

	Differential values			
	Min	Max	Mean	Std.
Surge	0.00937%	0.02109%	0.00012%	0.07100%
Heave	0.05340%	0.32830%	0.00149%	0.13264%
Pitch	0.17034%	1.50875%	0.00120%	0.43379%
Mooring line 1 tension	0.10447%	0.07334%	0.00012%	0.03472%
Mooring line 2 tension	0.00071%	0.00161%	0.00012%	0.03432%
Mooring line 3 tension	0.00005%	0.00146%	0.00013%	0.03442%

As may be observed, the differences between the two analyses are generally small, where the maximum motions in pitch features the largest variation of 1.51%. The time step of 0.05 seconds is therefore deemed applicable to perform the dynamic simulation.

The resulting surge, pitch and heave motion in the 1 hour storm is presented in Figure 11-21 trough Figure 11-23. A summary of the results is presented in Table 11-19.

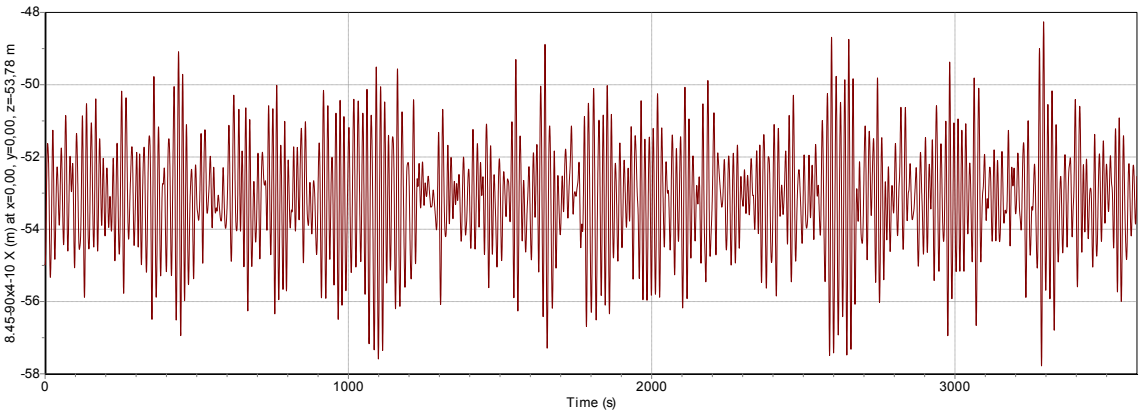

Figure 11-21: Surge motions at EC 2, floater 8.45-90x4-10

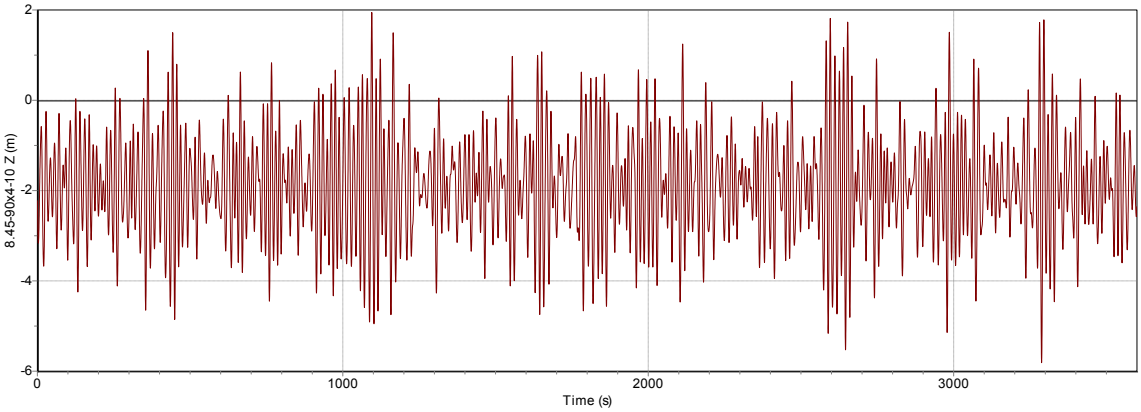

Figure 11-22: Heave motions at EC2, floater 8.45-90x4-10

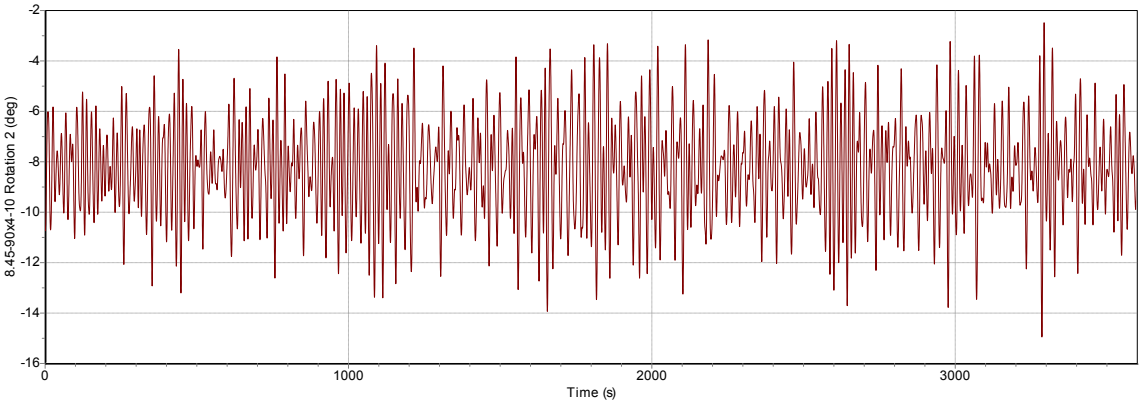

Figure 11-23: Pitch motions at EC 2, floater 8.45-90x4-10

Table 11-19: Statistical values in surge, heave and pitch, EC 2, floater 8.45-90x4-10

Parameter	Min	Max	Mean	Std.	Unit
Surge (0, 0, -53.78)	-48.258	-57.781	-53.146	1.425	m
Heave (0, 0, 0)	1.945	-5.812	-1.870	1.135	m
Pitch	-2.480	-14.949	-8.240	1.893	deg

As may be observed, the applied wind force of 1200 kN induces a more severe surge translation to the average position of -53.146 meters throughout the simulation. This also leads to a lower average heave position compared to the static state, as an increased line length is being suspended in the average surge position, increasing the weight of the system. The more energetic waves in this environmental condition imposes higher oscillatory motions around the mean values compared to EC 1, as may be observed form the increased standard deviations.

The sea clearance of the freeboard and the lowermost point of the blade is presented in Figure 11-24 and Figure 11-25, respectively. The plots are generated by evaluating the same locations as presented in section 11.3.3, due to the reasons discussed in that section. For the present floater, these positions in the local coordinate system are (-4.225, 0, 10) for the freeboard and (-22.5, 0, 23) for the airgap. A summary of the results is also presented in Table 11-20.

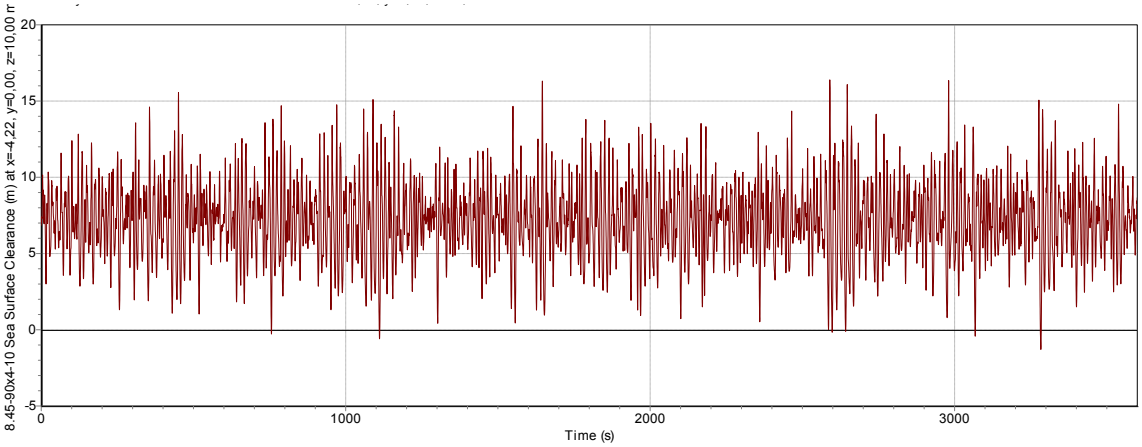

Figure 11-24: Resultant freeboard at EC2, floater 8.45-90x4-10

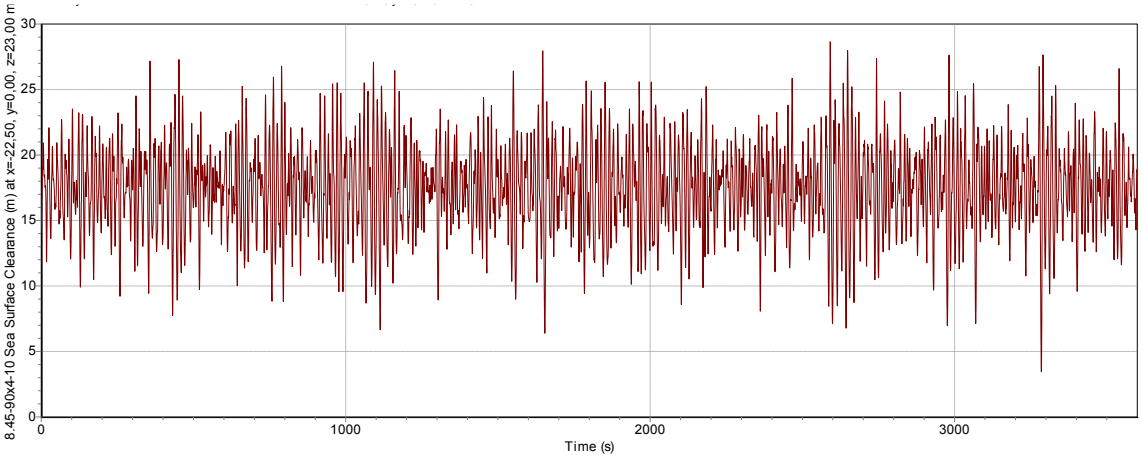

Figure 11-25: Resultant air-gap at EC 2, floater 8.45-90x4-10

Table 11-20: Statistical values for freeboard and air-gap, EC 2, floater 8.45-90x4-10

Parameter	Min	Max	Mean	Std.	Unit
Freeboard	-1.296	16.389	7.205	2.512	m
Air-gap	3.451	28.644	17.481	3.360	m

The average freeboard obtained throughout the 1-hour storm is 7.205 meters, 2.795 meters lower than the target freeboard of 10 meters. As explained in section 11.3.3, this is related to the mean heave and pitch position obtained in the dataset. The simulation reveals a minimum freeboard of -1.296 meters, implying that the entirety of the freeboard is used and the rotor-column is submerged during the 1-hour storm. The freeboard is consequently too small in the present design, and needs to be increased to avoid hydrodynamic loadings acting on the rotor-column.

The static pitch angle induced from the applied wind loads and the mean heave position results in a lower average air-gap throughout the simulation. However, the lowest sea clearance to the blades during the 1-hour storm is 3.451 meters, and the air-gap seems sufficient to withstand the storm conditions.

The time series of arc-length to touchdown point and effective tension in mooring line 1 is depicted in Figure 11-26 and Figure 11-27, respectively. A summary of the results are also presented in Table 11-21, where the values for mooring line 2 and 3 are also included.

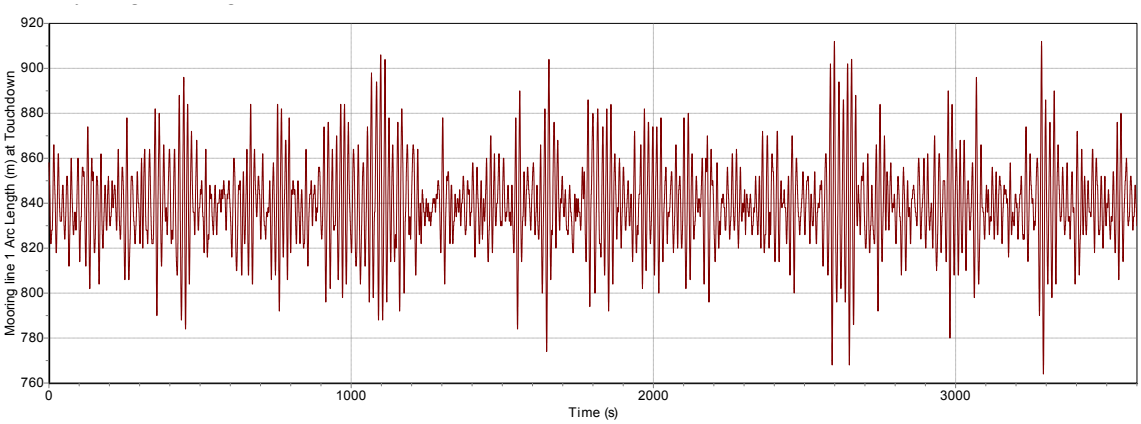

Figure 11-26: Resultant arc-length to touchdown point for mooring line 1 at EC2, floater 8.45-90x4-10

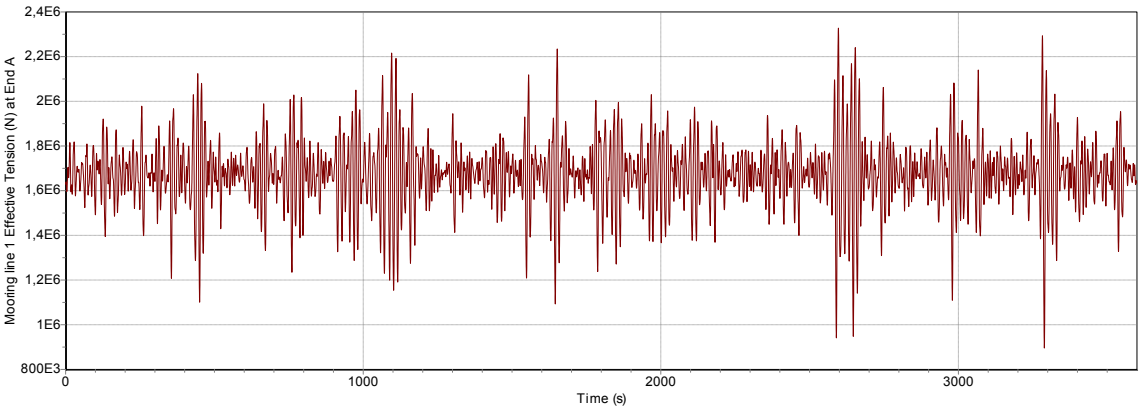

Figure 11-27: Resultant effective tension at connection point for mooring line 1 at EC2, floater 8.45-90x4-10

Table 11-21: Statistical values for arc-length to touchdown point and effective tension, EC 2, floater 8.45-90x4-10

Parameter	Min	Max	Mean	Std.	Unit
Arc-length to TDP mooring line 1	764.0	912.0	839.32	18.452	m
Effective tension mooring line 1	895.62	2327.67	1676.70	148.481	kN
Arc-length to TDP mooring line 2	398.0	432.0	415.39	4.367	m
Effective tension mooring line 2	471.76	587.48	529.98	13.396	kN
Arc-length to TDP mooring line 3	398.0	432.0	415.39	4.367	m
Effective tension mooring line 3	471.75	587.52	529.98	13.395	kN

As may be observed, the average surge position caused by the wind load in the extreme environmental condition suspends significantly more mooring line length in line 1 compared to the 491.0 meters arc-

length identified in the static analysis. The maximum arc-length to touchdown point throughout the simulation is 912.0 meters, leading to a minimum line length of 48 meters resting on the seabed. There will consequently be no vertical pull-up load in the anchor.

The mean effective tension is largest in mooring line 1, as it absorbs all of the imposed environmental loadings. This line also possesses the largest standard deviations, implying that the tension varies more compared to line 2 and 3. The maximum tension in line 1 is 2327.67 kN.

11.5 Floater 9.94-65x4-10

11.5.1 Mooring line configuration

The mooring line configuration for floater 9.94-65x4-10 is presented in section 11.2.3, as it was the floater used to identify the mooring line configuration by performing various trials. However, the results are restated here for ease of reference. Floater 9.94-65x4-10 features a metacenter position relative to sea surface of Z=-41.59 meters, which is used as the vertical coordinate of the connection point between the mooring line and vessel. Using the original water depth of 320 meters and the radius to anchor point of 853.87 meters yields the mooring line orientation presented in Table 11-22.

Table 11-22: Mooring line orientation for floater 9.94-65x4-10

		Polar coordinates		
		R [m]	Theta [deg]	Z [m]
Mooring line 1	End A	4.97	0	-41.59
	End B	853.87	0	-319.96
Mooring line 2	End A	4.97	120	-41.59
	End B	853.87	120	-319.96
Mooring line 3	End A	4.97	240	-41.59
	End B	853.87	240	-319.96

The static results for the presented mooring line configuration may be observed in Table 11-23.

Table 11-23: Results from static analysis, floater 9.94-65x4-10

Parameter	Value	Unit
Static position (x, y, z)	(0, 0, -0.0001)	m
Line tension at connection	673.52	kN
Horizontal force at connection	350.45	kN
Vertical force at connection	575.16	kN
Line orientation angle	31.405	deg
Arc length to TDP	491	m
Mass of mooring lines	175.95	tons

The revised center of gravity and moment of inertias by reducing the vessels mass equal to the suspended line mass in the static state is presented in Table 11-24. For accurate values of these parameters, reference is made to Appendix C.

Table 11-24: Revised center of gravity and moment of inertias for the dynamic simulation in OrcaFlex, floater 9.94-65x4-10

Parameter	Value	Unit
$\overline{KG}$	22.378	m
I_{xx}	7.881E9	kgm^2
I_{yy}	7.881E9	kgm^2
I_{zz}	1.615E8	kgm^2

11.5.2 Results EC 1

The time step sensitivity analysis for the present floater in environmental condition 1 is presented in Table 11-25. The analysis bases itself in comparing the results from analysis featuring time step 0.1 and 0.05 seconds, as done for the previous floaters.

Table 11-25: Comparison of results from simulations with time step 0.1 seconds and 0.05 seconds, EC1, floater 9.94-65x4-10

	Differential values			
	Min	Max	Mean	Std.
Surge	0.00315%	0.00317%	0.00003%	0.08197%
Heave	0.03872%	0.26896%	0.00013%	0.08507%
Pitch	0.01731%	0.03682%	0.00005%	0.09829%
Mooring line 1 tension	0.06404%	0.03501%	0.00006%	0.03120%
Mooring line 2 tension	0.00390%	0.02290%	0.00004%	0.00343%
Mooring line 3 tension	0.00390%	0.02290%	0.00004%	0.00343%

As may be observed, a halving in the integration time step generally results in insignificant differences between the two analyses, where the maximum heave motion features the largest variation of 0.27%. An integration time step equal to 0.05 seconds is therefore deemed to sufficiently converge the solution for all relevant purposes, and will be used to generate the results in the dynamic simulation.

The surge, heave and pitch motion for floater 9.94-65x4-10 in the operational environmental condition is presented in Figure 11-28 through Figure 11-30. It is reminded that surge is evaluated at the pitch rotation center, i.e. the metacenter, in order to exclude the pitch induced surge motions. A summary of the results is presented in Table 11-26.

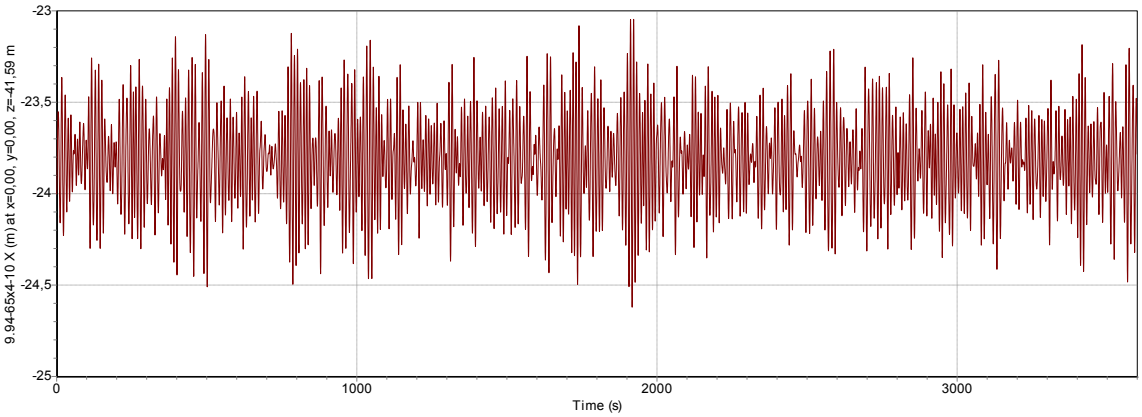

Figure 11-28: Surge motion at EC1, floater 9.94-65x4-10

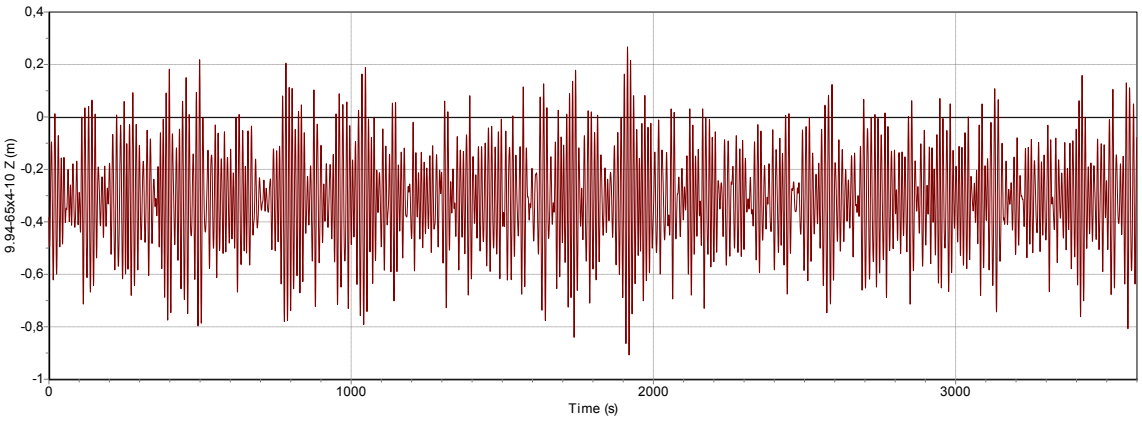

Figure 11-29: Heave motions at EC 1, floater 9.94-65x4-10

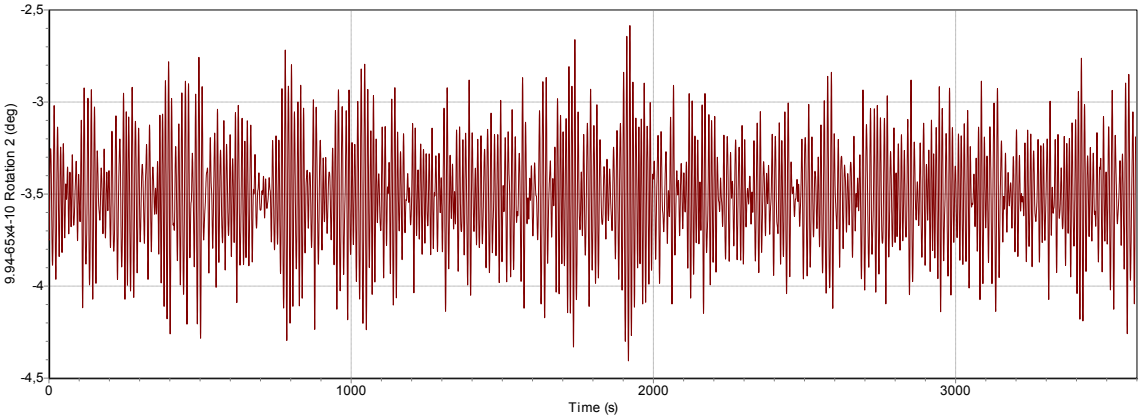

Figure 11-30: Pitch motions at EC 1, floater 9.94-65x4-10

Table 11-26: Statistical values in surge, heave and pitch, EC 1, floater 9.94-65x4-10

Parameter	Min	Max	Mean	Std.	Unit
Surge (0, 0, -41.59)	-23.046	-24.621	-23.813	0.244	m
Heave (0, 0, 0)	0.267	-0.908	-0.313	0.180	m
Pitch	-2.585	-4.407	-3.512	0.276	deg

Similarly to what was observed for the other two floaters, the applied wind loads induces a surge translation and pitch rotation different form the initial stable position. The surge translation leads to an increased mooring line mass, which alters the average heave position compared to the -0.0001 stable position.

11.5.3 Results EC 2

The resulting differences in surge, sway, heave and effective mooring line tension between two analysis featuring a time step of 0.1 and 0.05 seconds is presented in Table 11-27.

Table 11-27: Comparison of results from simulations with time step 0.1 seconds and 0.05 seconds, EC2, floater 9.94-65x4-10

	Differential values			
	Min	Max	Mean	Std.
Surge	0.00420%	0.00669%	0.00075%	0.04702%
Heave	0.08685%	0.18174%	0.00082%	0.03145%
Pitch	0.06627%	1.02150%	0.00113%	0.09627%
Mooring line 1 tension	0.11012%	0.07552%	0.00003%	0.03123%
Mooring line 2 tension	0.03946%	0.05569%	0.00053%	0.03045%
Mooring line 3 tension	0.04204%	0.05540%	0.00048%	0.03063%

As may be observed, the differences between the two analyses is insignificant, and a simulation featuring an integration time step of 0.05 seconds is deemed to sufficiently converge the solution.

The resultant surge, heave and pitch time history for the extreme environmental condition featuring a significant wave height of 12.9 meters, a spectral peak period of 14.1 seconds and a mean wind force of 1200 kN applied at 72.5 meters above the SWL is presented in Figure 11-31 through Figure 11-33. A summary of the obtained results is presented in Table 11-28.

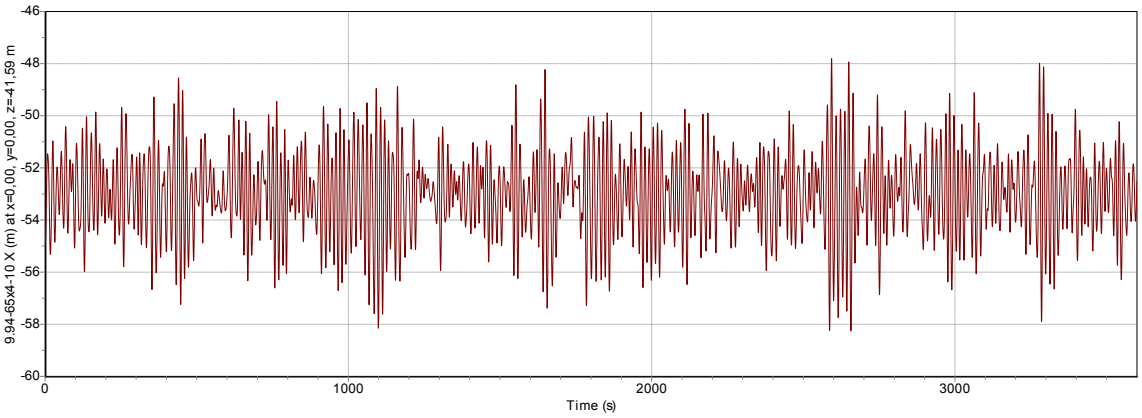

Figure 11-31: Surge motions at EC 2, floater 9.94-65x4-10

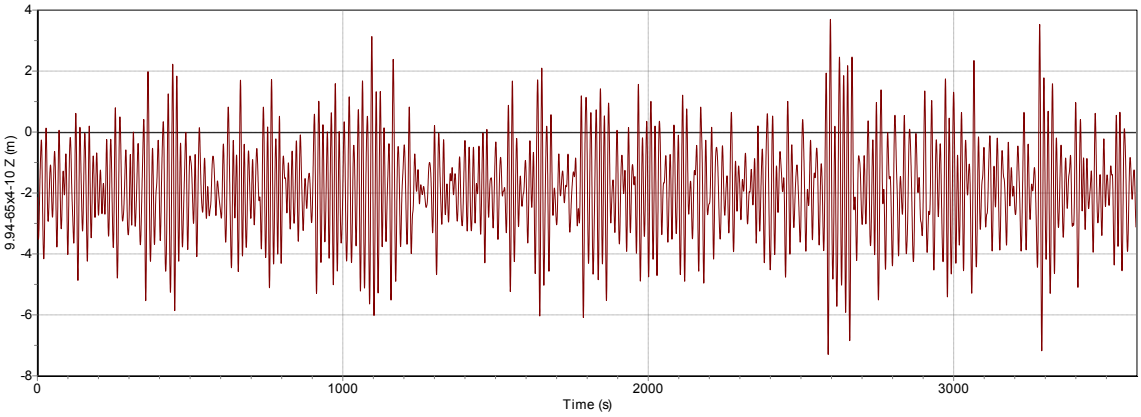

Figure 11-32: Heave motions at EC 2, floater 9.94-65x4-10

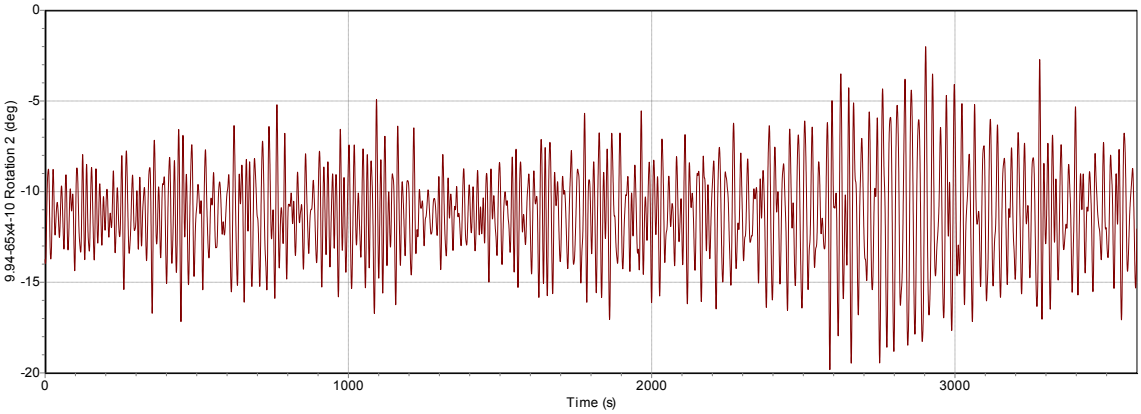

Figure 11-33: Pitch motions at EC 2, floater 9.94-65x4-10

Table 11-28: Statistical values in surge, heave and pitch, EC 2, floater 9.94-65x4-10

Parameter	Min	Max	Mean	Std.	Unit
Surge (0, 0, -41.59)	-47.807	-58.257	-52.980	1.577	m
Heave (0, 0, 0)	3.696	-7.298	-1.884	1.492	m
Pitch	-2.003	-19.816	-11.214	2.578	deg

The increased wind load induces a relatively severe translation in surge leading to the average surge position of -52.98 meters throughout the dataset. The large surge motions leads to an average downwards translation in heave, as more mooring chain is being suspended. The more energetic waves also imposes larger fluctuations around the mean values, as may be observed by the increase in standard deviation compared to environmental condition 1.

The resulting freeboard and air-gap is presented in Figure 11-34 and Figure 11-35, respectively. The evaluated locations are the same as before, i.e. the periphery of the buoy and the lowermost point of the airfoil. For the present floater, this corresponding to coordinates (-4.97, 0, 10) for the freeboard and (-22.5, 0, 23) for the air-gap. A summary of the results is also presented in Table 11-29.

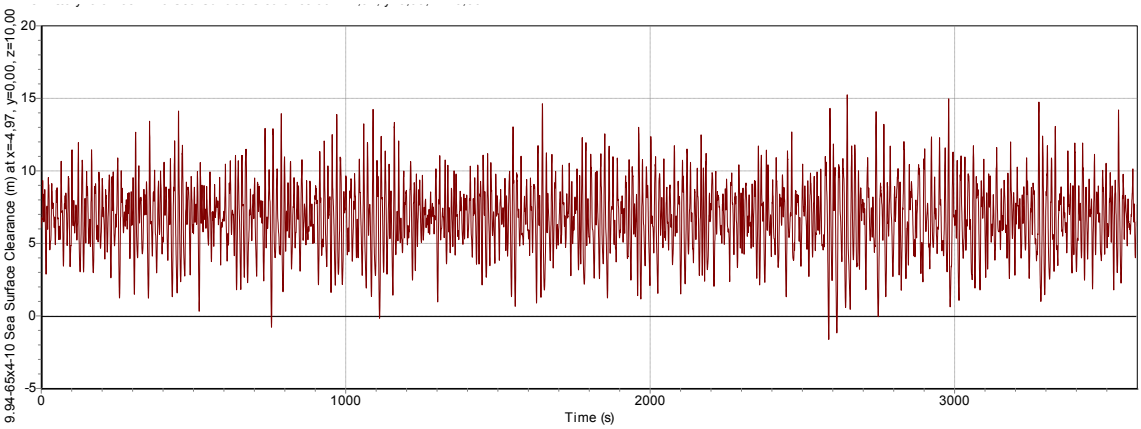

Figure 11-34: Resulting freeboard at EC2, floater 9.94-65x4-10

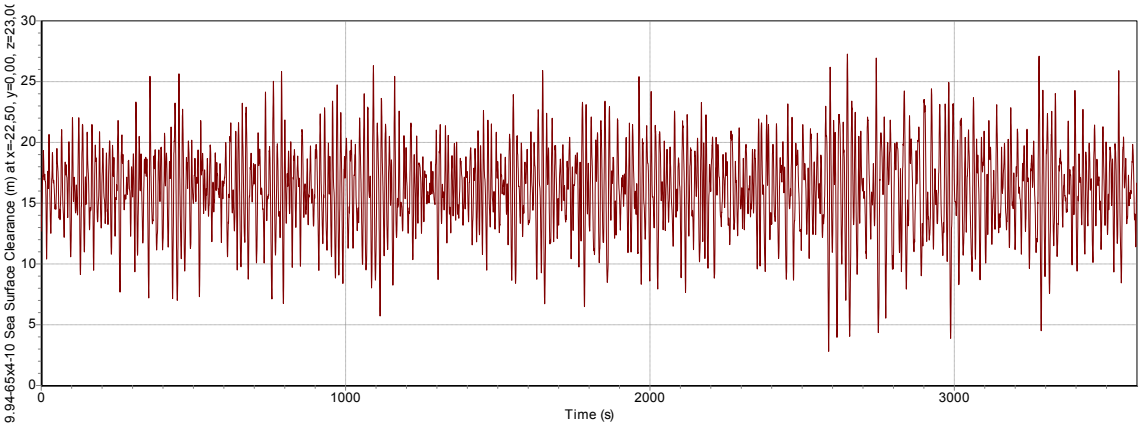

Figure 11-35: Resulting air-gap at EC2, floater 9.94-65x4-10

Table 11-29: Statistical values for freeboard and air-gap, EC 2, floater 9.94-65x4-10

Parameter	Min	Max	Mean	Std.	Unit
Freeboard	-1.624	15.249	6.748	2.357	m
Air-gap	2.797	27.269	16.112	3.483	m

As previously discussed, the mean position in heave and the static pitch rotation induced from the applied wind load leads to a reduced mean freeboard from the initial 10 meters. The more energetic waves induces oscillations around the mean value, leading to a minimum freeboard of -1.624 meters, indicating that hydrodynamic loadings are exerted onto the rotor column. As stated in section 11.3.3, this is not acceptable as it may damage components like the bearing assembly or the generator and gearbox assembly. The freeboard therefore needs to be increased for the presented floater.

The air-gap however remains positive throughout the dataset, with a minimum value that still features some safety margins. An air-gap of 23 meters therefore seems appropriate to avoid hydrodynamic loadings on the rotor-blades throughout the one-hour storm.

A time series of the arc-length to touchdown point and effective tension for mooring line 1 is presented in Figure 11-36 and Figure 11-37, respectively. A summary of the results is presented in Table 11-30, where the values obtained for mooring line 2 and 3 are also included.

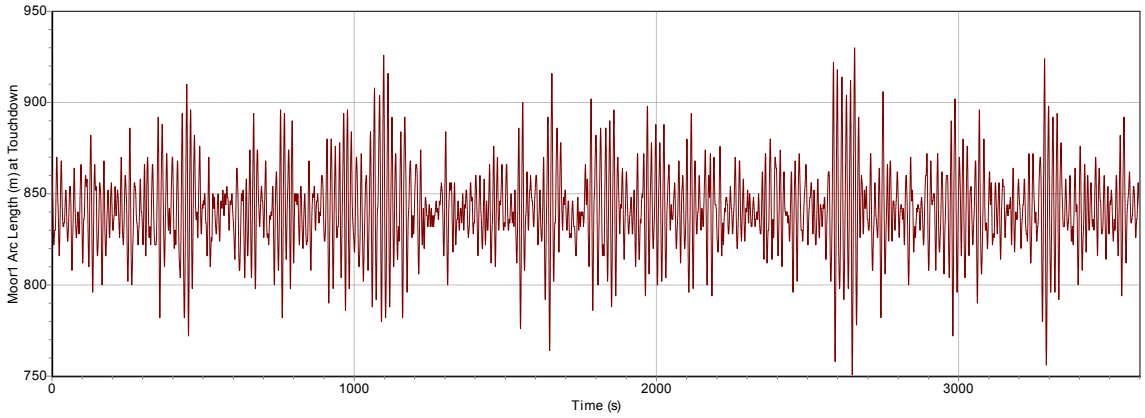

Figure 11-36: Resulting arc-length to touchdown point for mooring line 1 at EC2, floater 9.94-65x4-10

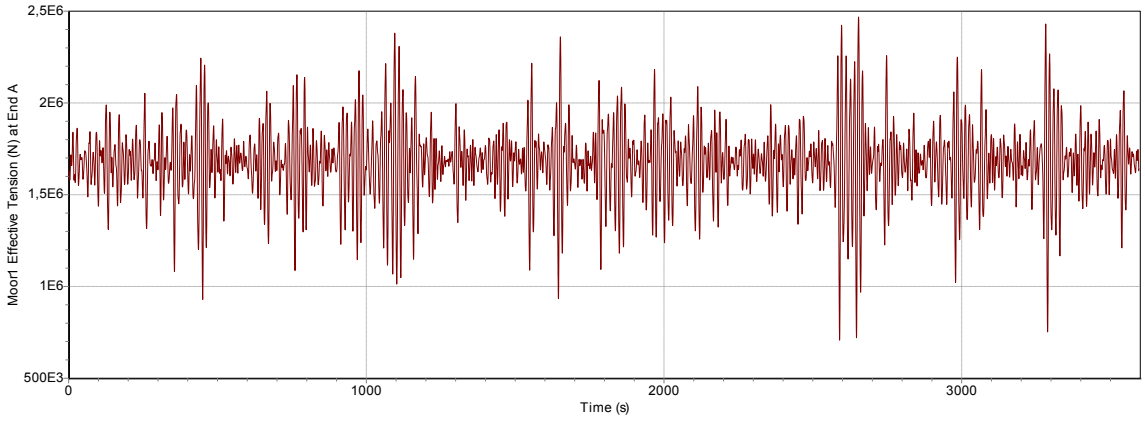

Figure 11-37: Resulting effective tension at connection point for mooring line 1 at EC2, floater 9.94-65x4-10

Table 11-30: Statistical values for arc-length to touchdown point and effective tension, EC 2, floater 9.94-65x4-10

Parameter	Min	Max	Mean	Std.	Unit
Arc-length to TDP mooring line 1	750.0	930.0	841.203	21.942	m
Effective tension mooring line 1	707.43	2468.23	1678.79	189.435	kN
Arc-length to TDP mooring line 2	390.0	440.0	415.499	5.733	m
Effective tension mooring line 2	439.83	627.10	530.17	18.856	kN
Arc-length to TDP mooring line 3	390.0	440.0	415.500	5.732	m
Effective tension mooring line 3	439.83	627.06	530.17	18.856	kN

As was observed for the other studied floaters, the severe surge motion results in a significantly higher average arc-length to touchdown point in mooring line 1 throughout the simulation compared to the results obtained in the static analysis. The maximum arc-length of 930.00 meters implies that there is a minimum line length of 30 meters resting on the seabed during the one-hour storm, and there is consequently no pull-up loads acting on the anchors.

The increased mean arc-length to touchdown point for mooring line 1 yields an average effective tension at the connection point throughout the simulation of 1678.79 kN. The waves imposes oscillatory tensions around the mean value, leading to maximum tension of 2468.23 kN during the 1-hour storm.

12 Discussion

The results obtained throughout the analysis process will be discussed in the following section. The results from the spreadsheet calculation are evaluated in section 12.1, whereas the results from the HydroD analysis are assessed in section 12.2. A discussion regarding the dynamic simulations will follow, before limitations and sources of error in the presented work are evaluated.

12.1 Spreadsheet analysis

The results presented in section 9.3 indicated a strong tendency of floaters comprising of higher draft and lower diameter gaining a higher metacentric height compared to floaters with a shallower draft and larger diameter. To assess this trend, the static stability parameters resulting from analysis of floater 6.23-140x4-10 and 20.69-15x4-10 is compared in Table 12-1, as these geometries represents the two extremes, i.e. highest draft and lowest diameter and lowest draft and highest diameter.

Table 12-1: Comparison of the two extreme floaters to assess metacentric height trend

Floater	KG [m]	BM [m]	KB [m]	GM [m]
6.78-140x4-10	42.07	0.0024	71.82	29.75
20.69-15x4-10	9.86	0.0024	7.80	-2.05

From this table it can be realized that floater 20.69-15x4-10 features a significantly lower center of gravity relative to the keel compared to floater 6.23-140x4-10. The low draft results in a shorter distance from keel to the individual center of gravities for each component, i.e. ballast, generator and gearbox, floater and rotor. The increased diameter also accommodates for a larger compartment surface area, which reduces the height of the ballast column, leading to a lower center of gravity position relative to keel for the ballast column. According to Eq. 5-15, a decrease in $\overline{KG}$ will be advantageous towards achieving a higher metacentric height, if this effect is isolated. However, the lower draft for floater 20.69-15x4-10 also results in a shorter distance between the center of buoyancy and keel compared to floater 6.78-140x4-10, which will have an adverse effect on the metacentric height. By observing the values presented in Table 12-1, it is realized that the difference in $\overline{KB}$ is greater than the difference in $\overline{KG}$ between the two floaters. This implies that $\overline{KB}$ features a greater increase than the $\overline{KG}$ values when the draft is increased, leading to an overall higher $\overline{GM}$ for the high draft-low diameter floaters. The opposite may be stated for the low draft high diameter floaters, i.e. the added benefit of achieving a lower center of gravity is counteracted by the larger reduction in $\overline{KB}$, reducing the overall metacentric height. Note that $\overline{BM}$ is identical for all floaters, as they comprise of the same water plane inertia and similar displacements. Furthermore, Spar buoys features a very small $\overline{BM}$, and it does not contribute significantly to the metacentric height.

There were also a tendency of a floater comprising of a high draft and low diameter experienced a lower static heel angle in both environmental conditions. As was discussed in section 8.1.3, the static heel is obtained by setting the inclination moment imposed from the environmental condition equal to the up-righting moment, and solving for ϕ. The imposed hydrodynamic and aerodynamic loadings calculated in the spreadsheet for the studied geometries are therefore presented in Table 12-2 in order to evaluate this trend.

Table 12-2: Imposed hydrodynamic loadings on each floater from the spreadsheet analysis

Floater	Hydrodynamic load		Aerodynamic load	
	EC 1 [MNm]	EC 2 [MNm]	EC 1 [MNm]	EC 2 [MNm]
6.78-140x4-10	48.106	118.542	24.861	317.103
7.47-115x4-10	41.553	94.679	22.879	291.820
8.45-90x4-10	33.614	68.970	20.898	266.551
9.94-65x4-10	23.650	41.832	18.916	241.277
12.67-40x4-10	11.742	15.707	16.935	216.004

As may be observed, floaters featuring a high draft experiences greater inclination moments, which may be explained by the difference in position of the metacenter, about which the inclination moment is calculated. Floaters with a high draft comprises of a greater distance from the metacenter position to the sea surface, which will increase the moment arm of the resultant wave and wind forces acting on the floater and rotor assembly, leading to the observed increase in inclination moment. From Eq. 5-14, it may be realized that the up-righting moment is a function of displaced volume and a moment arm, given as $\overline{GM} \cdot \sin(\theta)$. Since all floaters features similar displacements, the only difference in the up-righting moment will be the metacentric height. As the static heeling angles are smaller for the high draft-low diameter floaters, it may be stated that the larger metacentric height leads to a greater increase in the up-righting moment compared to the increase in inclination moment for these geometries. This explains the observable trend of a higher draft and lower diameter floater gaining more favorable static inclination angles. It may also be noted that inclination moment due to the wind is relatively severe in the spreadsheet calculation, especially in environmental condition 2. This is related to the rotor blades being modelled as flat plates rather than airfoils, emphasizes the statement made in section 8.1.3 that the static heeling angle obtained in the spreadsheet are relatively conservative estimates.

Furthermore, it might be expect that the floaters featuring a higher metacentric height would fare poorly regarding the natural period in pitch and roll, as these parameters are inversely proportional to the metacentric height. This is however not the case. Figure 12-1 presents the resultant natural period in pitch versus the draft-to-diameter ratio for the six floaters studied in the spreadsheet analysis. The ratio of just over 22 represents floater 6.78-140x4-10, while the ratio just under 4 represents floater 12.67-40x4-10. Note that floater 20.69-15x4-10 is not presented because the resulting metacentric height was negative, which means that the vessel fails to obtain satisfactory stability characteristics.

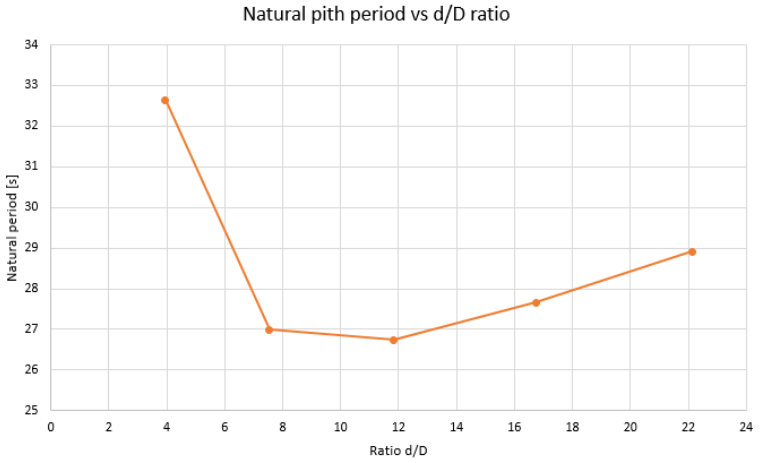

Figure 12-1: Natural pitch period vs d/D ratio for the six studied floaters

The natural period in roll and pitch decreases rapidly between floater 12.67-40x4-40 and 9.94-65x4-10, before increasing again between floater 8.45-90x4-10 and 6.78-90x4-10. The rather complex interrelation may be evaluated by considering the effect of varying the draft on the radius of gyration and added mass term in the natural roll/pitch period formula for a freely floating body. The other terms are not evaluated, as they are constant between each studied geometry.

If the draft is reduced, the mass moment of inertia around the y-axis for the entire system will decrease as the arm in Steiner's formula is reduced. This effect will decrease the radius of gyration of the system as illustrated in Figure 12-2, depicting the radius of gyration vs the draft-to-diameter ratio of each floater. An increase in R_{gyr} will reduce the natural period in roll/pitch, according to Eq. 5-56.

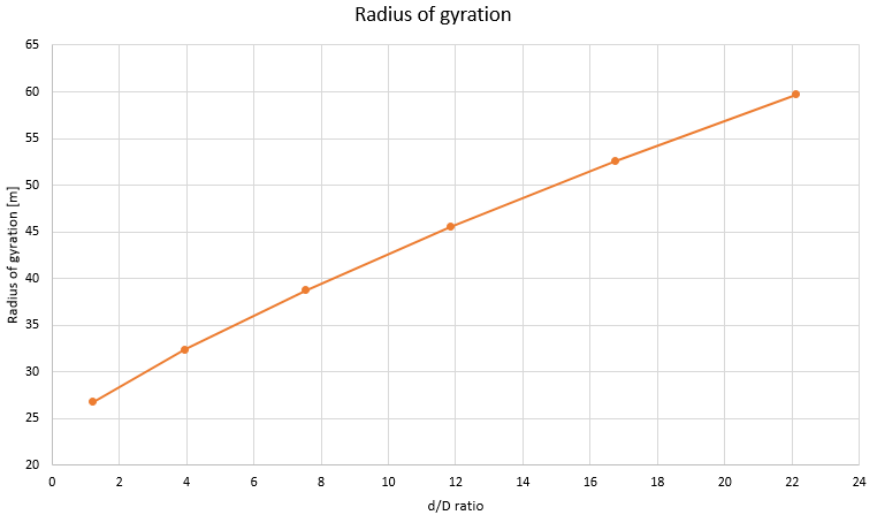

Figure 12-2: Radius of gyration vs draft-to-diameter ratio for the six studied floaters

The added mass in pitch was calculated in the spreadsheet analysis using strip theory, which results in a formula for pitch added mass on a Spar buoy that is dependent upon the draft in the third power. It is also proportional to the diameter of the structure, but only in the second power. The decrease in draft consequently gives an overall reduction in pitch added mass, as illustrated in Figure 12-3 depicting the added mass versus the draft-to diameter ratio for the studied floaters. This effect will also impose a reduction in the natural pitch/roll period of the floater.

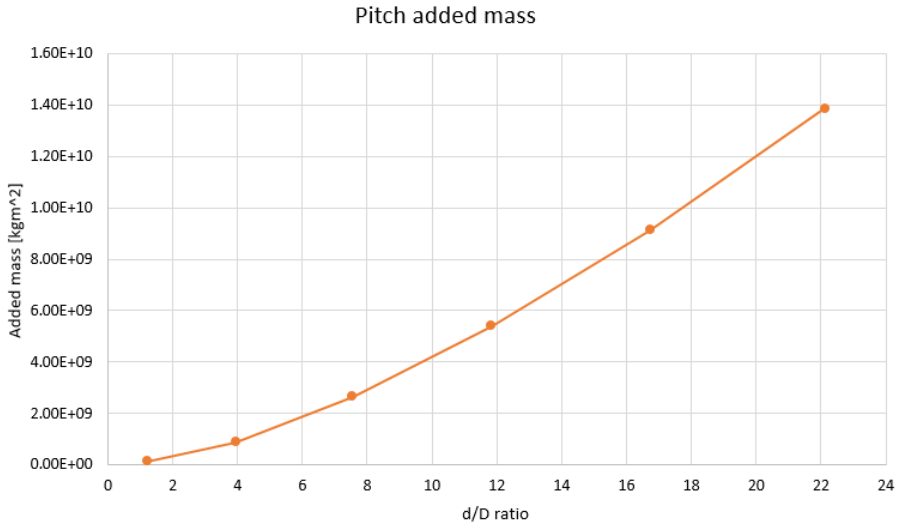

Figure 12-3: Pitch added mass vs d/D ratio for the six studied floaters

A higher draft therefore leads to a higher pitch added mass and larger radius of gyration, which counterbalances some of the imposed reduction from the increased metacentric height associated with these floaters. The natural periods in pitch and roll is therefore above 25 seconds for all studied floaters, meaning that they fulfill the natural period criterion.

The natural period in heave features a simpler relation. As the mass and water plane area are similar between the studied geometries, the only difference in the natural heave period is the added mass. This quantity was calculated in the spreadsheet analysis using a hemisphere with diameter equal to the bottom diameter of the floater. This implies that the geometries comprising of a larger diameter (and shallower draft) obtains a larger natural period in heave. However, all studied floaters featured natural periods in heave over 40 seconds, fulfilling the set criterion.

As a side note, the applicability of calculating the added mass using the strip theory and hemisphere approximations in the spreadsheet calculation may be evaluated by comparing the resulting natural periods in heave, roll and pitch to the results obtained in the HydroD analysis for the three floaters studied in the dynamic simulations. This is done in Table 12-3, where the natural periods obtained in the spreadsheet calculation are presented as percentage deviation from the values obtained in the HydroD analysis.

Table 12-3: Comparison of natural periods obtained from HydroD and spreadsheet calculations

Floater	Period from HydroD			Period from spreadsheet		
	Heave	Roll	Pitch	Heave	Roll	Pitch
7.47-115x4-10	41.48	26.3	26.3	**-0.92%**	**5.17%**	**5.17%**
8.45-90x4-10	41.49	25.5	25.5	**-0.41%**	**4.86%**	**4.86%**
9.94-65x4-10	42.60	25.7	25.7	**-2.14%**	**5.02%**	**5.02%**

As may be observed, the hemisphere approximation have a tendency of underestimating the natural period in heave, while the strip theory leads to a slight overestimation of the natural period in roll and pitch. The deviations are however relatively small, and the use of the approximations to calculate the added mass yields surprisingly accurate results.

12.2 HydroD

The obtained frequency dependent added mass, damping, displacement RAOs and load RAOs for the three floaters studied in the dynamic simulations are compared and evaluated in this section.

12.2.1 Frequency dependent added mass and damping

A comparison of the damping in the selected modes studied in section 10 is presented in Figure 12-4.

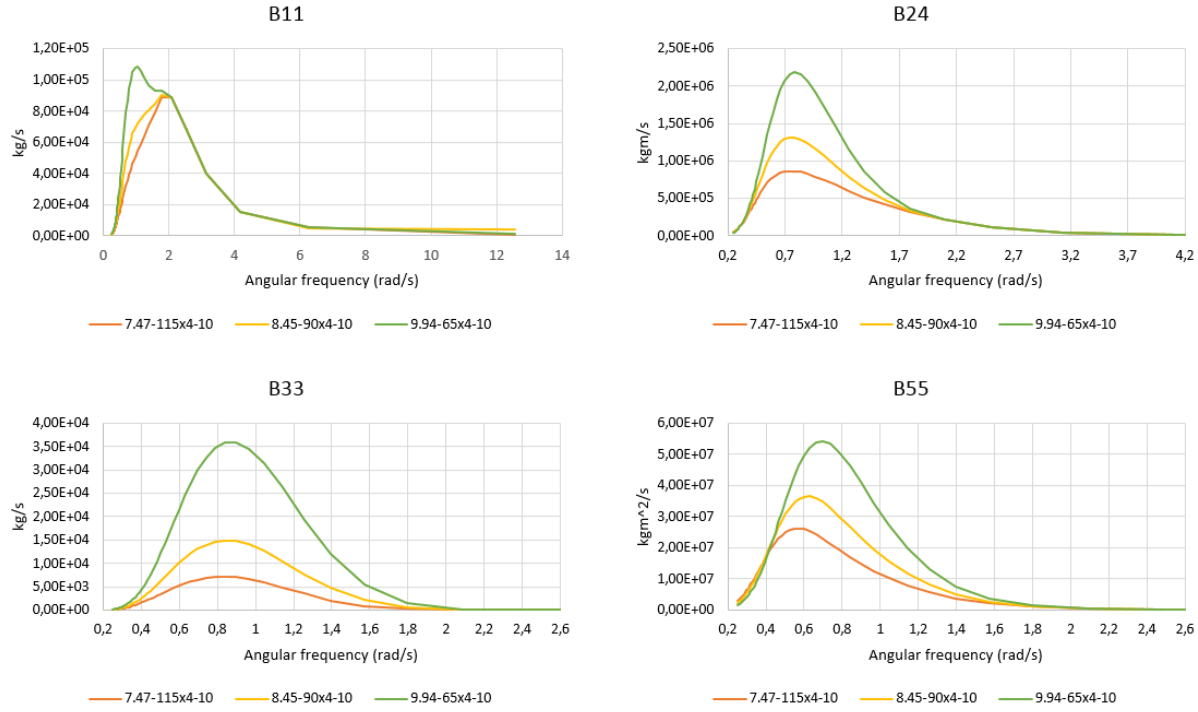

Figure 12-4: Comparison of damping for selected modes for each floater, wave heading of zero degrees

As may be observed, floater 9.94-65x4-10 generally obtains the highest damping values in all modes among the studied geometries, while floater 7.47-115x4-10 features the lowest damping values. There is a general trend where a shorter draft and larger diameter floater obtains more significant damping compared to a higher draft and lower diameter floater. As that the damping values are derived from potential theory, they may be understood as the amount of energy that is withdrawn from the forced oscillations of the structure by the generated outgoing surface waves. A larger diameter therefore seems to generate outgoing waves that is able to transport more of the energy away from the system. Furthermore, it may be noted that all three floaters features relevant damping in similar frequency ranges for each mode.

A comparison for the frequency dependent added mass in the selected modes for the three floaters is presented in Figure 12-5.

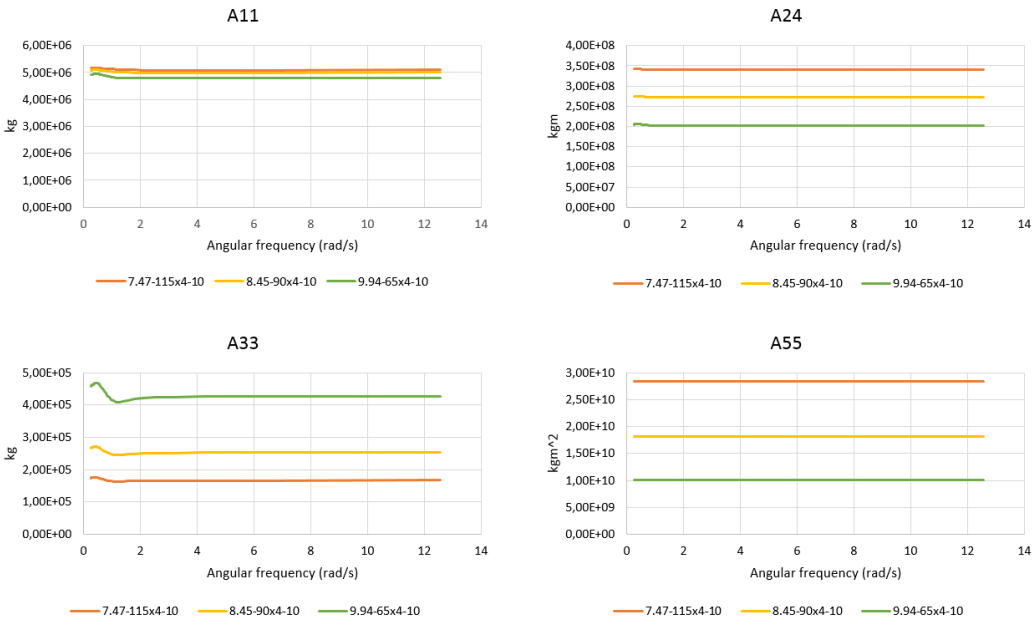

Figure 12-5: Comparison of added mass for selected modes for each floater, wave heading of zero degrees

As may be observed, floater 7.47-115x4-10 obtains the highest added mass values in A24 and A55, while floater 9.94-65x4-10 features the lowest values. This indicates that a deeper draft increases the added mass in these DOFs with a greater significance than the reduction in diameter. The added mass in mode A11 is however similar between the studied geometries, where floater 7.47-115x4-10 features slightly higher values compared to the other floaters. It therefore seems that the increase in diameter more or less counteracts the decrease in draft, and a similar amount of fluid is disturbed by forced oscillations of the studied floaters. The added mass in heave is largest for floater 9.94-65x4-10, as it is highly dependent upon the diameter of the floating geometry.

As stated in section 5.5.3, the added mass and damping forces counteracts some of the imposed first-order wave excitation force, consequently reducing the force giving net motion. This effect is illustrated in Figure 12-6, depicting a time series of the added mass and damping forces (orange) versus the imposed first order hydrodynamic loadings (blue) to give the total force, i.e. force that gives net motion (gray).

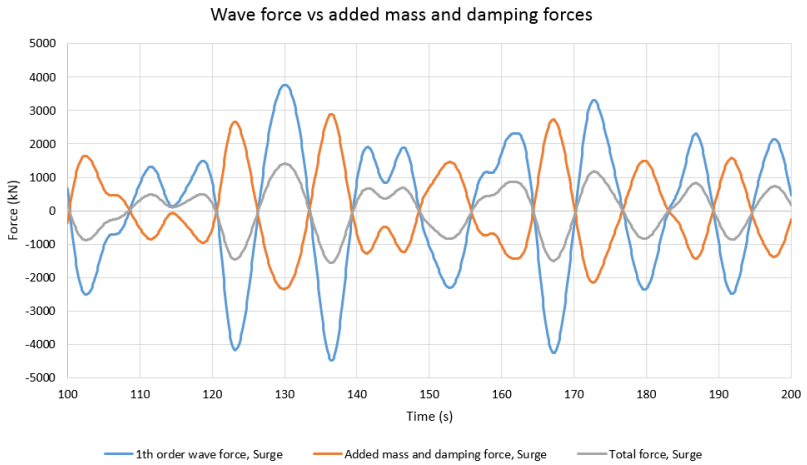

Figure 12-6: Time series of imposed first order wave force vs added mass and damping force in surge

It is therefore of interest to evaluate which floater gains the most resistance against wave excitation forces, i.e. obtains the highest added mass and damping forces throughout the simulations. From the discussion above, it is realized that floater 9.94-65x4-10 generally obtains the highest damping in the evaluated damping modes. It also features the largest added mass in heave, so it is fair to expect that this floater will impose the most resistance in heave motions among the studied geometries. This will also be true for surge, as the floaters featured similar added mass in this DOF. However, floater 9.94-65x4-10 features the lowest added mass values in sway-roll and pitch-pitch among the studied geometries, where floater 7.47-115x4-10 obtained the highest values. It is therefore difficult to evaluate which floater will impose the highest resistance in these modes based on the plots presented in Figure 12-4 and Figure 12-5. The added mass and damping forces will therefore be evaluated in more detail in the OrcaFlex section, where statistical values resulting from the studied environmental condition will be presented.

12.2.2 Displacement RAOs

A comparison of the displacement RAOs in surge, heave and pitch between the three studied floaters is presented in Figure 12-7. Note that the presented frequency range have been narrowed down to 2.0 rad/s, as there was no significant displacement amplitudes beyond this frequency. Furthermore, the depicted RAOs applies to a wave heading of 0 degrees, corresponding to the direction studied in the OrcaFlex simulations. This implies that the surge and pitch RAOs are maximum. This is also true for the heave RAOs, as heave was independent upon the incoming wave direction, as shown in section 10.2.1 through 10.2.3.

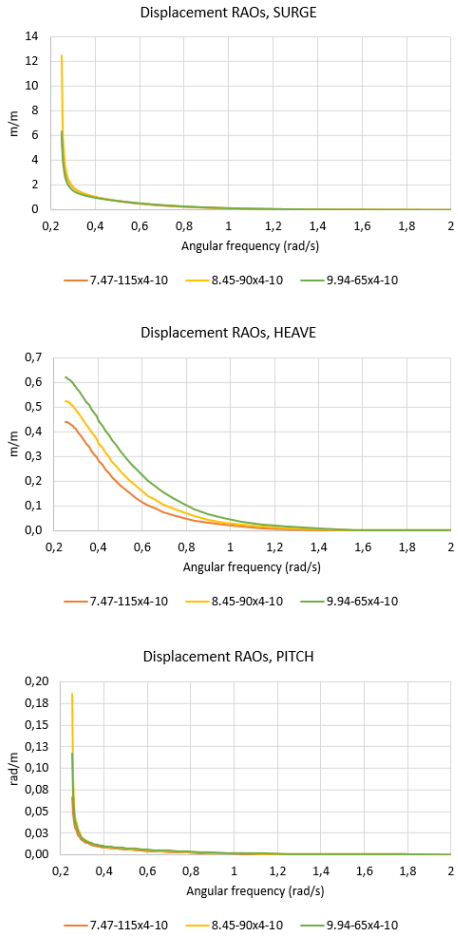

Figure 12-7: Displacement RAOs in surge, heave and pitch for the studied floaters, wave heading of zero degrees

As may be observed, the displacement RAOs in surge is similar between the studied geometries. However, floater 8.45-90x4-10 features a significantly higher maximum amplitude at frequency 0.251 rad/s (25 seconds), compared to the other geometries. Referring to the presented results in section 10.2.1 through 10.2.3, the maximum displacement amplitude for floater 7.47-115x4-10 and 9.45-90x4-10 was 5.90 m/m and 6.37 m/m, respectively, while floater 8.45-90x4-10 comprised of a maximum displacement amplitude of 12.6 m/m. As stated in section 10.2, HydroD recognized an infinite natural period in surge, so resonance motions does not explain the higher displacement amplitudes for floater 8.45-90x4-10. Efforts were made to assess this deviation by generating a new hydrodynamic analysis in HydroD featuring a new constructed Inventor model and FE-model in GeniE. However, the result did not change. As all geometries were analyzed in a similar fashion, it was concluded that the deviation had to be related to some distinctive features with the associated mesh model and geometry of this floater. Nevertheless, this does not have any significance in the OrcaFlex simulation, as the specified sea state modelled by a JONSWAP spectrum with peakedness factor 3.3 only produces waves with periods up to 19.8 seconds in the extreme sea state, corresponding to an angular frequency of 0.317 rad/s. In other words, the large displacement observed at frequency 0.251 rad/s never occurs in the dynamic simulation. The displacement amplitudes for frequencies higher than 0.317 rad/s is relatively similar between the studied floaters, implying that they respond similarly to the generated waves in OrcaFlex.

The displacement RAO in pitch also contains the rapid increase in amplitude value at a frequency of 0.251 rad/s. This may however be explained by resonance motions, as was discussed in section 10.2.1 through 10.2.3. Floater 8.45-90x4-10 obtains the largest displacement amplitudes, as it features the natural period closest to the 25-second wave period among the studied geometries. However, as the OrcaFlex simulations does not comprise of waves with periods over 19.8 seconds, the floaters will not experience the resonance motion. This was of course the intention by setting a design criterion of natural periods over 25 seconds in the spreadsheet analysis. The displacement RAO in pitch are similar among the studied geometries for angular frequencies of 0.317 rad/s and higher, implying that they respond similarly to the incoming waves in OrcaFlex

The differences in heave displacement RAO are however more pronounced, where floater 9.94-65x4-10 obtains a largest displacement amplitude and floater 7.47-115x4-10 features the lowest displacement amplitude. A floater comprising of larger diameter seems to excite the structure more severely in heave than a floater with smaller diameter. It may be noted that the displacements becomes more or less insignificant at the same frequency for all floaters, i.e. around 1.2 – 1.4 rad/s.

12.2.3 Load RAOs

A comparison of the resultant load RAOs in surge, heave and pitch is presented in Figure 12-8. As done for the displacement RAOs, the plots are generated based on a wave heading of 0 degrees, as this is the studied wave direction in OrcaFlex. The load RAOs in surge and pitch will therefore be maximum, along with the heave RAOs due to this DOF independency upon the direction of the incoming waves.

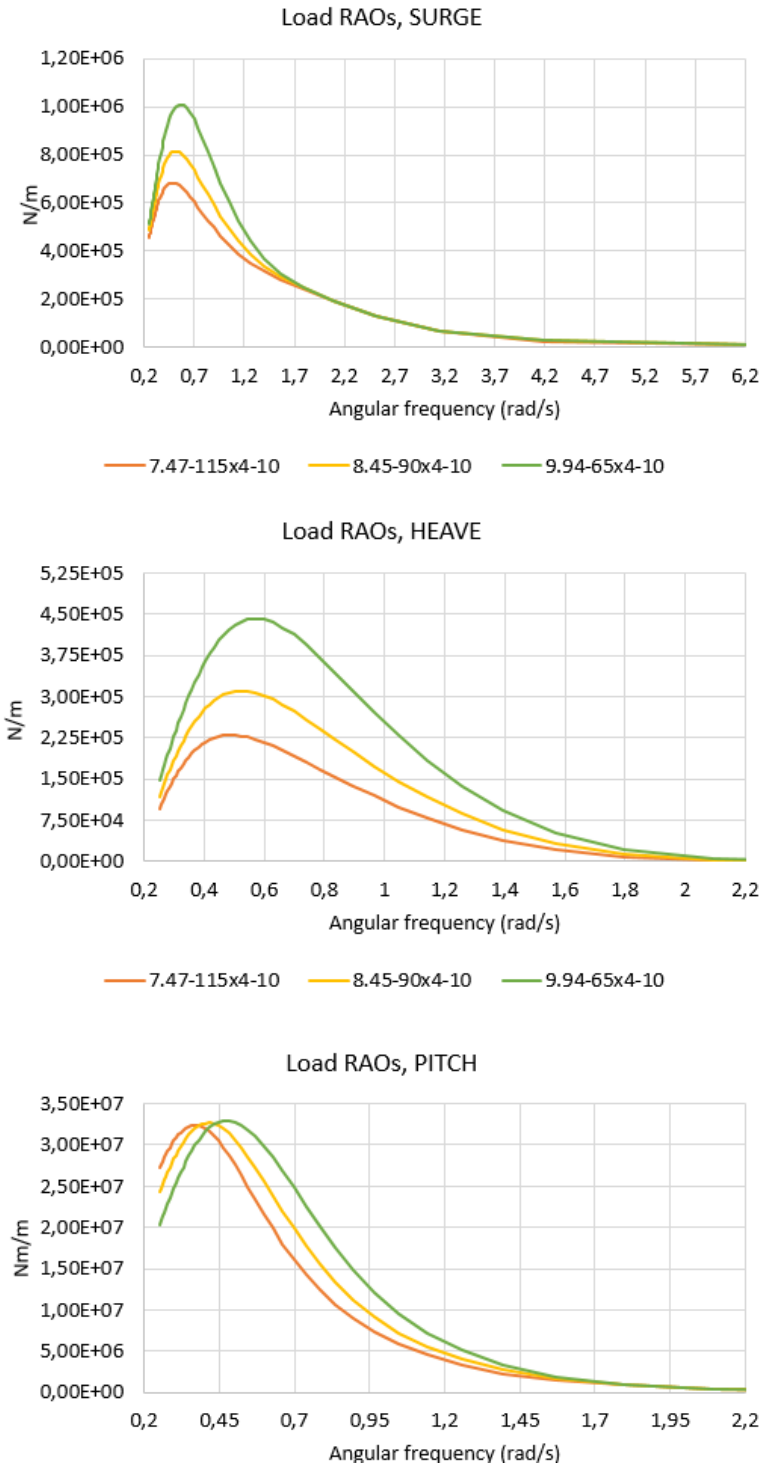

Figure 12-8: Load RAO in surge, heave and pitch for the studied floaters, wave heading of zero degrees

As may be observed, the load RAOs in surge features similar amplitudes at frequency 0.251 rad/s and a general conformity for frequencies 1.7 rad/s and upwards for the studied floaters. However, the load amplitudes differs in between these frequencies, corresponding to a wave periods of 4 to 25 seconds. In this region, floater 9.94-65x4-10 generally obtains the highest load amplitudes while floater 7.47-115x4-10 obtains the lowest amplitudes. The increased diameter and decreased draft therefore gives higher hydrodynamic loadings for periods containing significant wave energy. This is most probably related to an increased surface area is being exposed to relevant wave velocities and acceleration when the diameter increases. As deep-water waves decays with depth, and increase in draft will not give the same effect.

A similar tendency may be observed for the load RAOs in heave, i.e. the amplitudes are similar at an angular frequency of 0.251 rad/s and for frequencies 2.2 rad/s and upwards. Furthermore, floater 9.94-65x4-10 also comprises of the largest load amplitudes in heave, while floater 7.47-115x4-10 obtains the lowest amplitudes. An increase in the floater's diameter therefore seems to increase the load amplitude in heave. There is also a shift in frequency for which the maximum load amplitude occurs between the studied floaters. Observing the results presented in section 10.2.1 through 10.2.3, floater 7.47-115x4-10 gains the maximum load amplitude for wave periods of 13 seconds, while floater 8.45-90x4-10 and 9.94-65x4-10 is most severely exited in wave periods of 12 and 11 seconds, respectively.

The studied geometries features similar maximum load amplitudes in pitch, but for different wave periods. Furthermore, floater 9.94-65x4-10 generally comprises of higher load amplitudes between the frequencies 0.4 rad/s and 1.6 rad/s, corresponding to a wave period interval of 4 to 15 seconds. This is most probably related to diffraction effects becoming increasingly important in lower wave periods. As floater 9.94-65x4-10 features the largest diameter, it disturbs the incoming waves to a higher degree compared to the other floaters, leading to larger diffraction forces and thus the higher load amplitudes observed at this frequency range. However, between the wave periods 15 to 25 seconds, floater 7-47-115x4-10 experiences the highest loads while floater 9.94-65x4-10 feature the lowest load amplitudes. An increased draft therefore seems to give more hydrodynamic loadings in higher wave periods, where the inertia and drag terms dominates.

12.3 OrcaFlex

The results from the dynamic simulations will be compared in the following section to evaluate the effect of varying the Spar buoy's draft and diameter on the system's hydrodynamic performance. As stated in section 11.1, the primary performance parameters studied in the presented work includes surge, heave and pitch, freeboard and airgap, effective tension and the arc-length to touchdown point of the mooring lines.

12.3.1 Comparison of motion characteristics

The motion characteristics will be evaluated first. The mean values in surge, heave and pitch, along with the associated standard deviations for both environmental conditions is presented in Figure 12-9. As indicated in section 11.3.2 the mean values are indications of the studied floaters ability to absorb the constant applied wind load, i.e. which motions is imposed by the wind load, while the standard deviations gives indications of the magnitude of the oscillatory motions induced from the waves.

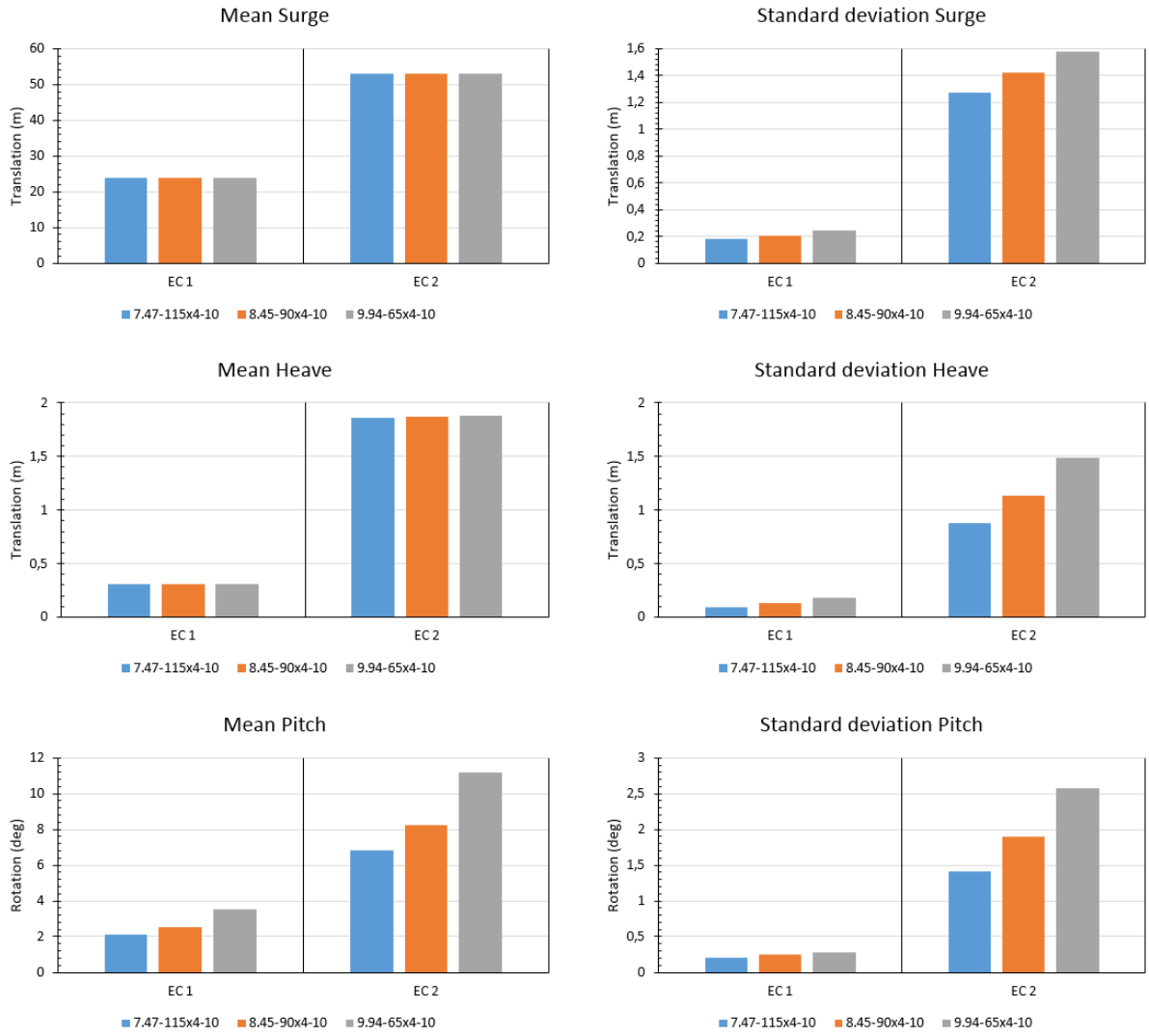

Figure 12-9: Comparison of mean position and associated standard deviation in surge, heave and pitch

As may be observed, the mean surge position are nearly identical between the studied geometries. The force that opposes the translational motion in surge due to the applied wind load is the horizontal force component from the mooring lines. This force is equal among the studied floaters, as the mooring line configurations were constructed to be identical to make the dynamic results comparable, resulting in the similar mean surge positions. This also gives similar mean heave positions between the studied geometries, as an equal amount of mooring line is being suspended in the mean surge positions. The mean pitch rotations does however vary between the studied geometries, where floater 7.47-115x4-10 features the most favorable characteristics, i.e. lowest mean pitch rotation. The analysis of the mean pitch positions in the dynamic simulations are similar to the static heeling analysis performed in relation with the spreadsheet calculation, as it evaluates the rotation induced from a static point load. The observable differences may therefore be explained by the difference in metacentric height, where a larger $\overline{GM}$ imposes a higher moment arm and consequently a greater up-righting moment, as discussed in section 12.1. This is in line with the results presented in Figure 12-9, as floater 8.45-90x4-10 features the second largest metacentric height and floater 9.94-65x4-10 features the lowest metacentric height. The differences are more pronounced in environmental condition 2, where a wind load of 1200 kN is applied at the center of the rotor blades.

Unlike the mean positions, the standard deviations are indications of the floater's hydrodynamic performance, i.e. how they interact with the waves. As may be observed, the standard deviations are

largest for floater 9.94-65x4-10, second largest for floater 8.45-90x4-10 and smallest for floater 7.47-115x4-10 in all of the studied DOFs. This is true in both environmental conditions, but the tendencies are more pronounced in EC 2. There is thus a tendency of a shallower draft and larger diameter floater experiences higher oscillatory motions induced from the waves in the studied DOFs compared to a floater comprising of a high draft and small diameter. This was observed in the comparison plot for the displacement RAOs in heave, where floater 9.94-65x4-10 obtained the highest displacement amplitudes in the frequency range containing significant wave energy, while floater 7.47-115x4-10 obtained the lowest displacement amplitudes. However, the displacement RAOs in surge and pitch were similar between the studied geometries for the wave periods included in the dynamic simulations. In order to evaluate the trend further, the total hydrodynamic loads in surge, heave and pitch, along with the associated standard deviations, are presented in Figure 12-10. Note that the total load represents the force or moment that gives net motion in the studied DOF, i.e. the wave excitation forces or moment subtracted with the hydromechanical forces or moment.

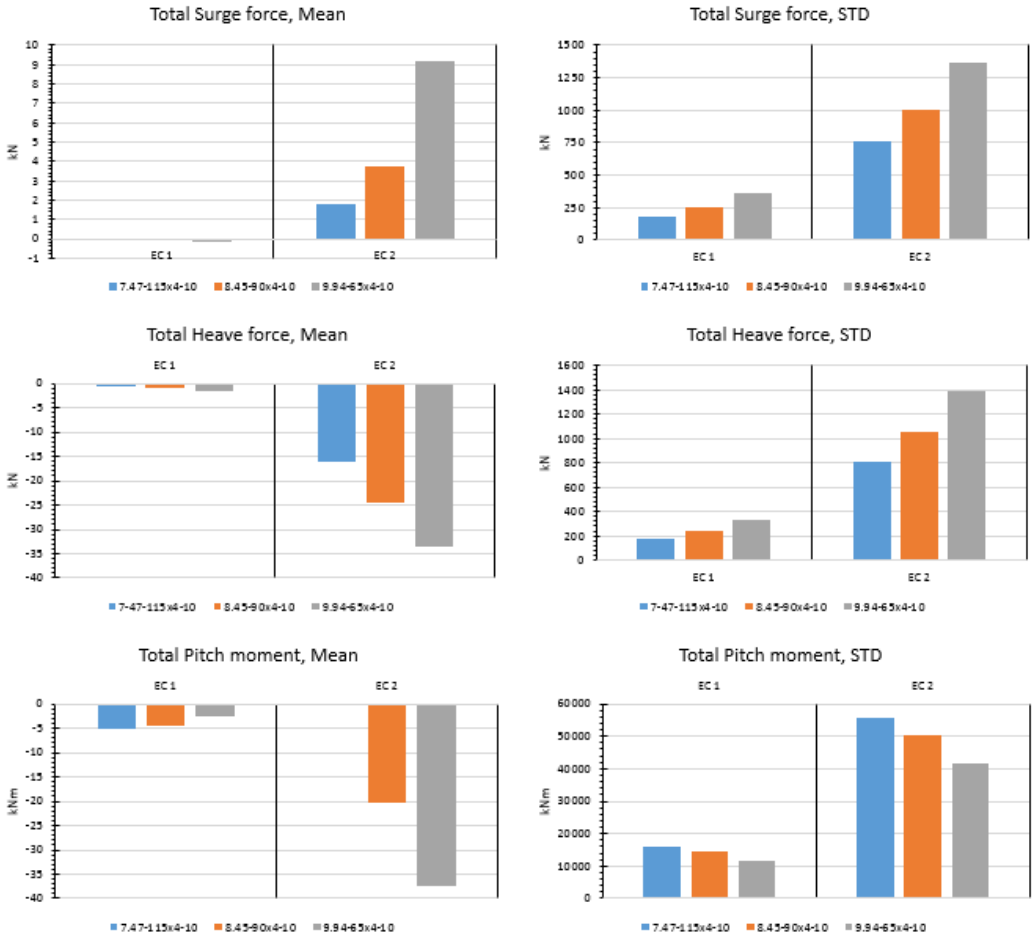

Figure 12-10: Total hydrodynamic mean forces and moments along with associated standard deviations

It may be noted that the mean total force are not perfectly zero in any of the studied DOF, as would be expected from the oscillatory nature of the waves. This is most probably related to the simulation time of one hour being insufficient to give an average total force of zero. However, the mean values are generally small when compared to the standard deviations, and may be regarded as zero for the purpose of this discussion.

By first evaluating the total force in surge, it may be realized that floater 9.94-65x4-10 obtains the highest standard deviation among the studied geometries, implying that this floater experiences

oscillatory forces with higher amplitudes compared to the two other geometries. As floater 8.45-90x4-10 features the second largest standard deviation and floater 7.47-115x4-10 obtains the lowest standard deviation, the results indicate that a floater comprising of a shorter draft and larger diameter experiences increased total forces in surge. The comparison plot of the load RAO in this DOF (ref. Figure 12-8) also indicated similar tendencies, where the load amplitude was generally largest for floater 9.94-65x4-10 and smallest for floater 7.47-115x4-10 in the frequency range containing significant wave energy. In order to evaluate the force characteristics in greater depth, the resultant added mass force, damping force and the imposed wave excitation force in the x-direction (surge direction) is presented in Figure 12-11. It is reminded that the hydromechanical loadings opposes some of the excitation forces.

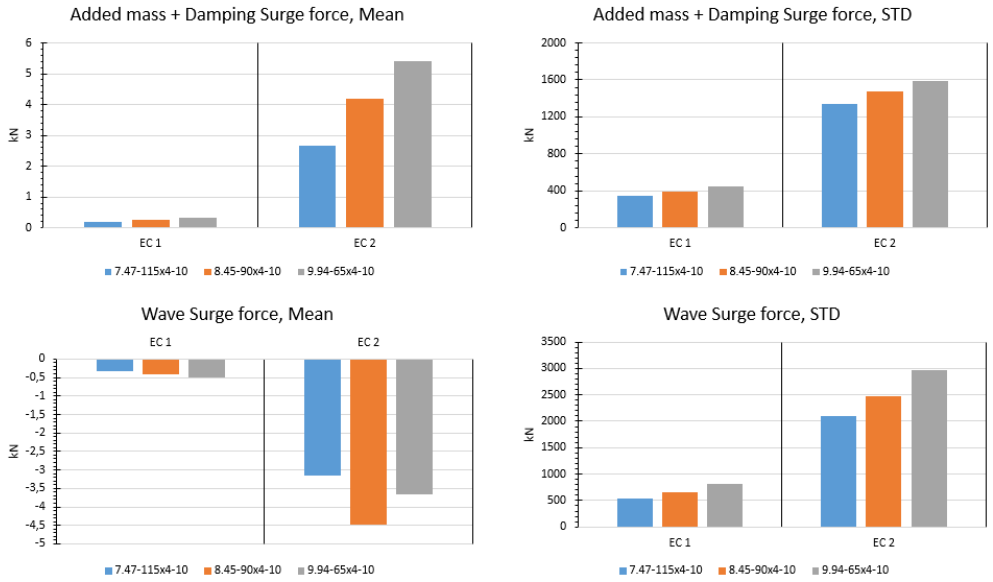

Figure 12-11: Mean added mass + damping and wave excitation force in surge, along with associated standard deviations

As may be observed, the mean values are small compared to the associated standard deviation and may be regarded as zero for the sake of this discussion. The standard deviation will therefore be a direct indication of the magnitude of the added mass + damping forces and the wave excitation forces. As may be observed, floater 9.94-65x4-10 obtains the highest standard deviation of added mass and damping force in the surge direction, while floater 7.47-115x4-10 obtains the lowest standard deviations. The results therefore indicates that a floater comprising of a shallower draft and higher diameter will generate more resistance against a translation in surge compared to a floater comprising of a higher draft and lower diameter. This tendency matches the observations made in section 12.2.1, where the added mass were similar between the studied geometries, but floater 9.94-65x4-10 obtained significantly higher damping values in the interval 0.25 to 2 rad/s. However, the standard deviation of the wave excitation force in surge is also largest for floater 9.94-65x4-10 and smallest for floater 7.47-115x4-10. As the total force, i.e. force that gives net motion, followed a similar tendency, the results indicates that a floater comprising of a shallow draft and high diameter leads to a greater increase in wave excitation force compared to the beneficial increase in added mass and damping forces. This is most probably the reason for floater 9.94-65x4-10 obtaining the worst surge characteristics and floater 7.47-115x4-10 the best surge characteristics.

Referring back to Figure 12-10, it may be observed that the standard deviation of the total force in heave is highest for floater 9.94-65x4-10, second highest for floater 8.45-90x4-10 and lowest for floater 7.47-115x4-10. This indicates that a floater comprising of a shallower draft and larger diameter experiences higher hydrodynamic loadings that gives net motion in heave compared to a floater comprising of a high

draft and smaller diameter. This tendency was also observed in the comparison plot of the load RAOs in heave, depicted in Figure 12-8, where floater 9.94-65x4-10 obtained the highest load amplitudes in the frequency range of 0.251 rad/s to 2 rad/s, and floater 7-47-115x4-10 the lowest. In order to evaluate the force characteristics in more depth, the mean and standard deviations of the added mass and damping force, along with the wave excitation force, is presented in Figure 12-12. Similar to what was observed for the plot in surge, the mean values are generally low and can be regarded as zero for the sake of this discussion. The magnitude of these forces will therefore be related to the standard deviation.

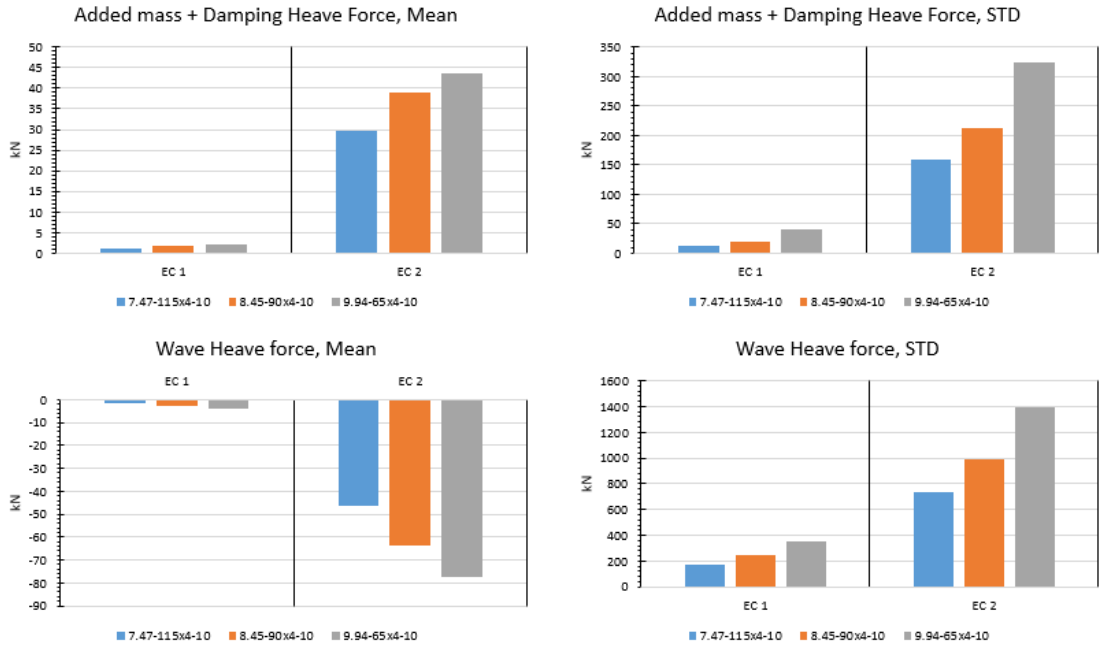

Figure 12-12: Mean added mass + damping and wave excitation force in heave, along with associated standard deviations

The added mass and damping forces are largest for floater 9.94-65x4-10 and lowest for floater 7.47-115x4-10, as indicated by the standard deviations. There is therefore a tendency of shallower drafts and larger diameters floaters generates more resistance to motions in heave. This was also seen in section 12.2.1, where floater 9.94-65x4-10 obtained the greatest added mass and damping values in the frequency range containing significant wave energy. However, the wave excitation forces imposed on the structure are also largest for floater 9.94-65x4-10 and lowest for floater 7-47-115x4-10. The increase in wave excitation force on a floater comprising of a shallower draft and larger diameter therefore seems to be greater than the beneficial increase in added mass and damping forces associated with such a floater, leading to the observed increase in total force, i.e. force that gives net heave motion. This, along with the fact that the displacement RAO in heave also illustrated larger displacements amplitudes for floater 9.94-65x4-10 and 8.45-90x4-10, explains the increased heave motion with the increase in diameter and reduction in draft.

Lastly, the pitch force characteristics are evaluated. From Figure 12-10, it is realized that the total pitch moment, i.e. moment that gives resultant motions, is smallest for floater 9.94-65x4-10 and largest for floater 7.47-115x4-10. This is probably related to the difference in metacenter position relative to the sea surface for each individual geometry. As already stated, the floaters pitches around their respective metacenters. As floater 7.47-115x4-10 features a longer distance to the metacenter from the sea-surface compared to floater 9.94-65x4-10 due to the increased draft, the resultant moment arm from the imposed wave excitation forces is larger, thus leading to an increased inclination moment. The load RAOs in pitch also revealed that floater 7.47-115x4-10 featured higher load amplitudes in the higher

period range, i.e. between 13 seconds and 25 seconds, where floater 9.94-65x4-10 obtained the lowest amplitudes. Wind generated waves generally becomes more energetic in the longer period range, which may also explain some of the observed tendencies in total hydrodynamic pitch moment. To assess this trend further, mean values of the wave excitation moment and added mass and damping moment in pitch, along with the associated standard deviations, are presented in Figure 12-13. As for the previous plots, the mean values are generally small when compared to the standard deviations, and may be regarded as zero.

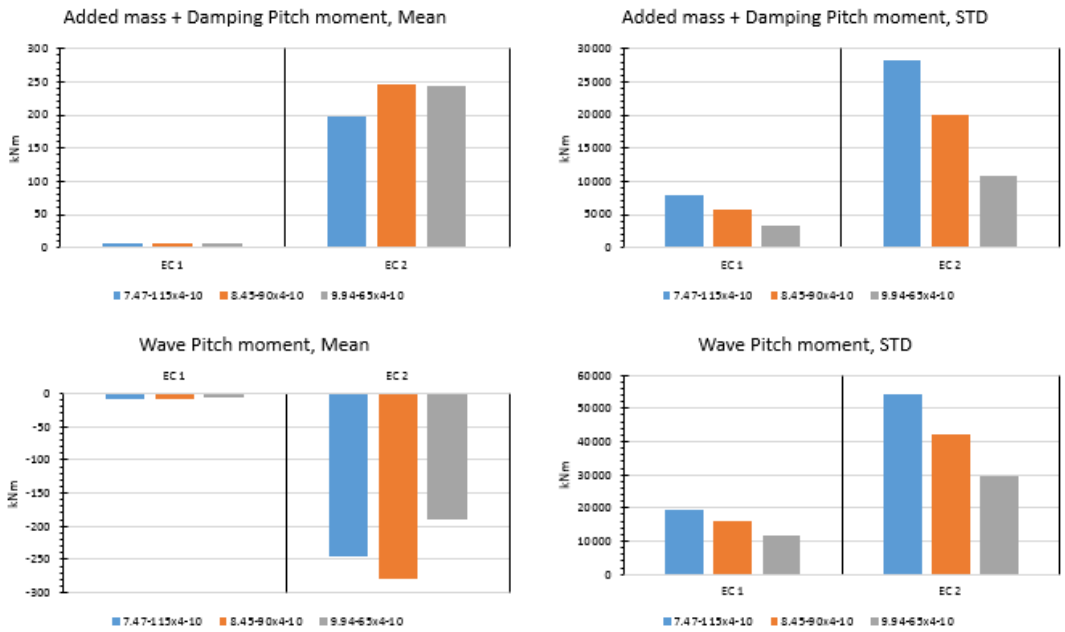

Figure 12-13: Mean added mass + damping and wave excitation force in pitch, along with associated standard deviations

As may be observed, the added mass and damping moment is largest for floater 7.47-115x4-10 and smallest for floater 9.94-65x4-10. Observing these quantities in the comparison plots presented in Figure 12-4 and Figure 12-5, respectively, it may be realized that floater 7.47-115x4-10 featured the highest added mass in pitch, but the lowest damping values in the frequency range containing significant wave energy. This indicates that the increase in added mass force is more significant than the decrease in damping force for a floater comprising of a high draft and low diameter, leading to an overall increase in resistance force against pitch rotations. However, the standard deviation of the wave excitation moment is largest for floater 7.47-115x4-10. As the total moment, i.e. moment that gives net motion, was also greatest for the aforementioned floater, it may be stated that the increase in excitation moment for a floater comprising of a high draft and low diameter is greater than the beneficial increase in added mass and damping moment. Nevertheless, floater 7.47-115x4-10 obtained the most favorable motion characteristics in pitch, even though it experiences the highest total force. This indicates that a higher metacentric height increases the up-righting moment more significantly than the increase in total moment associated with a lower position of the metacenter relative to the sea surface. This is in-line with the observed results, as floater 7.47-115x4-10 features the most favorable pitch characteristics while still experiencing the largest inclination moment and floater 9.94-65x4-10 features the worst pitch characteristics even though it experiences the lowest induced inclination moment.

To summarize:

- A higher draft and lower diameter floater seems to experience less surge motions due to the decrease in total force, i.e. net force that induces a surge translation. This reduction is most probably related to the reduced surface area at depths where significant wave velocity and acceleration interacts with the structure.
- A higher draft and lower diameter floater gives reduced heave motions, which was observable in the displacement RAO. A larger diameter also seems to increase the wave induced excitation forces more significantly compared to the beneficial increase in added mass and damping forces associated with such a geometry, ultimately leading to higher loads that induces heave motions.
- A higher draft and lower diameter floater features more favorable pitch characteristics relative to the constant applied wind load and the oscillatory motions imposed from the waves. The high draft increase the wave excitation moment as the position of the metacenter relative to the sea surface increases. However, the associated up-righting moment also increases for such a geometry due to a higher metacentric height. As the motion characteristics are more favorable for a floater comprising of a high draft and low diameter, the increase in up-righting moment seems to be more significant than the increase in inclination moment.

12.3.2 Sea surface clearance

As stated in section 6.1.1, all floaters were constructed to feature an equal freeboard and air-gap of 10 and 23 meters, respectively. These values were set in accordance with similar floating offshore wind turbine concepts, like Statoil's Hywind Pilot project [9] and the OC3 phase IV project [29]. Furthermore, as indicated in section 11, the sea surface clearance parameters are dependent upon the heave and pitch motions of the floaters. The air-gap and freeboard are therefore not independent performance parameters, but illustrates the resultant heave and pitch motions in a different form. However, these are important parameters to consider, as severe hydrodynamic loadings on the rotor-column and rotor blades are not acceptable. The minimum freeboard and air-gap obtained during the simulations are presented in Figure 12-14 for each studied floater. Note that only the results from environmental condition 2 is presented, as this is the critical condition to consider. It is also reminded that it is applicable to compare the minimum values obtained in the simulations due to the characteristics of the pseudo-random wave generation process, i.e. identical wave trains are generated between the simulations as long as the input seed is kept constant.

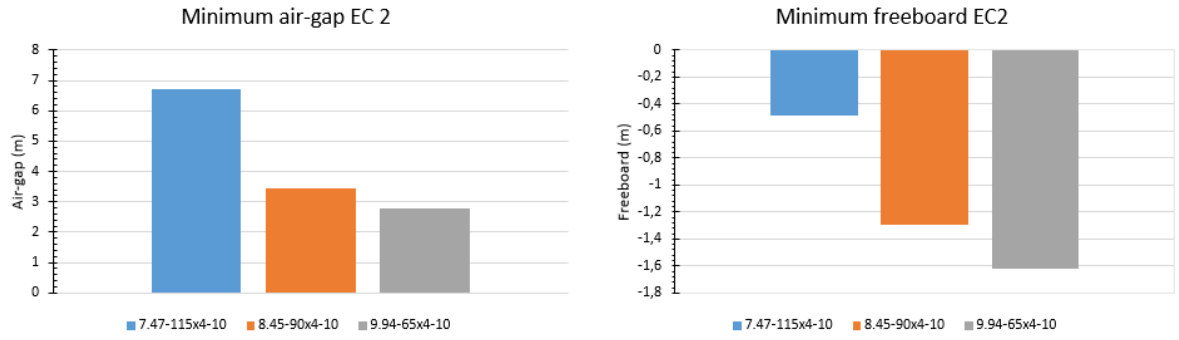

Figure 12-14: Minimum freeboard and air-gap obtained in the hydrodynamic simulations

As may be observed, the minimum clearance between the rotor blades and the sea elevation process is highest for floater 7.47-115x4-10. This is as expected as it possesses the most favorable pitch and heave motion characteristics. The minimum air-gap is lowest for floater 9.94-65x4-10, as this geometry features the most unfavorable motion characteristics. However, the minimum air-gap observed

between the studied geometries is 2.78 meters, which still contains some additional safety margins before hydrodynamic loadings are exerted onto the rotor blades. The air-gap of 23 meters is therefore deemed sufficient to fulfill its purpose during the studied extreme environmental condition.

However, none of the studied floaters features sufficient freeboard to avoid hydrodynamic forces being exerted onto the rotor column at some point during the one-hour storm. The negative freeboard is lowest for floater 7.47-115x4-10, as this geometry features the best heave and pitch characteristics. The extent of negative freeboard increases for floater 9.94-65x4-10, which exhibited the worst motion characteristics. Nevertheless, a negative freeboard is not acceptable and the freeboard needs to be increased for all floater in order to achieve acceptable designs.

As previously stated, the freeboard in the presented work was set in accordance with the OC3 Hywind floater. This is a proven concept developed by the national renewable energy laboratory (NREL) with the main intention of supporting offshore wind turbine concept studies [29]. It was therefore believed that the set freeboard would be sufficient, but this was not the case in the simulations performed in the presented work.

12.3.3 Effective tension and arc-length to touchdown point for the mooring system

As indicated in section 11, the effective tension in the mooring lines and the arc-length to touchdown point are highly dependent upon the induced surge and heave motions. These parameters are less dependent upon the pitch motions, as the mooring lines are connected to the pitch center, i.e. metacenter, of each individual floater. Also note that this discussion will base itself on results from mooring line 1 in environmental condition 2, as this is most critical to study.

The resulting maximum arc-length to touchdown point and maximum tension in mooring line 1, along with the associated standard deviations are presented in Figure 12-15.

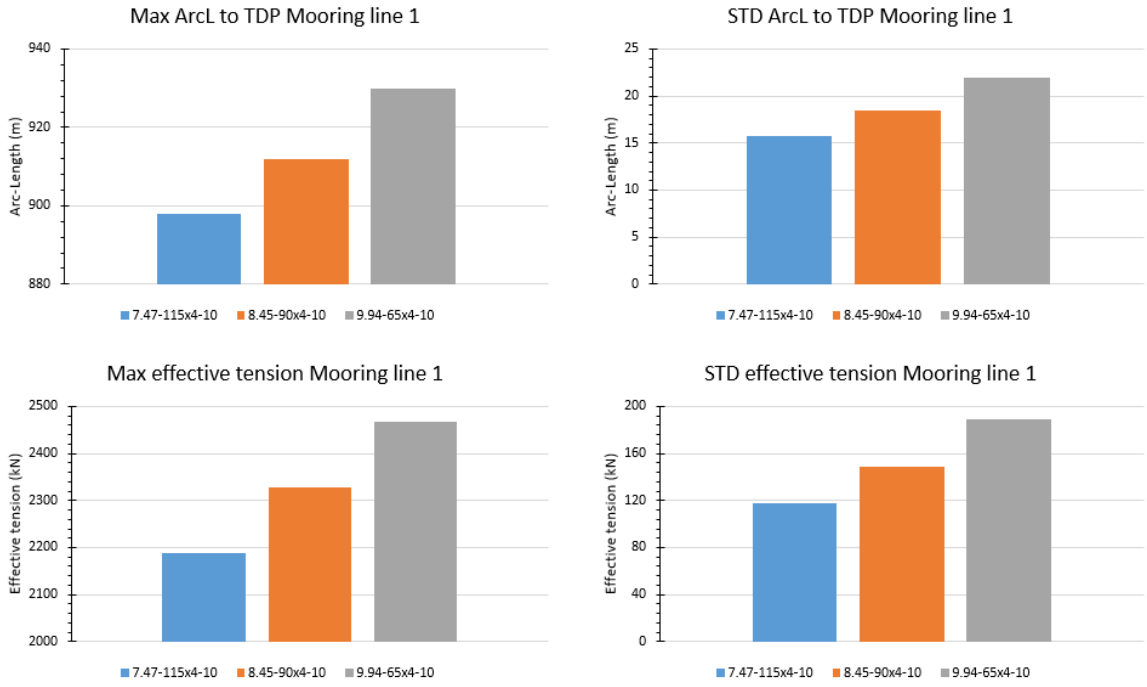

Figure 12-15: Maximum arc-length to touchdown point and effective tension with associated standard deviations

As may be observed, the arc-length to touchdown point during the one-hour storm is largest for floater 9.94-65x4-10. This indicates that the maximum surge and heave motions are more severe for this geometry, which was also observed in section 12.3.1. The maximum effective tension is therefore also highest for floater 9.94-65x4-10, as more mooring line length is suspended in the instantaneous point in time where the arc-length is maximum. The maximum values decreases for floater 8.45-90x4-10 and 7.47-115x4-10 as these geometries generally features more favorable heave and surge motion characteristics.

The generally higher oscillatory surge and heave motions that was observed of floater 9.94-65x4-10 also leads the largest variations arc-length to touchdown point among the studied geometries, as may be observed from the standard deviations in Figure 12-15. The variation in effective tension will consequently also be highest in relation to floater 9.94-65x4-10. This may be important for the fatigue characteristics of the lines, but is not evaluated in the presented work. The variations, i.e. standard deviation, becomes smaller for floater 8.45-90x4-10 and 7.47-115x4-10 due to the generally lower oscillatory motions in surge and heave that was observed in section 12.3.1.

It may therefore be stated that a floater comprising of a high draft and low diameter will obtain lower maximum arc-lengths to touchdown point and maximum effective tensions due to smaller maximum motions. The variations in these parameters are also lower for such a floater, as the oscillatory motions in surge and heave are generally smaller.

As a side note, the established mooring line configuration's suitability may be evaluated by studying the vertical loads in the anchors and the line's structural integrity. As already discussed in the result section, each analysis yielded some additional mooring line resting on the seabed, ensuring no vertical pull-up load at the anchor. This is also illustrated through the maximum arc-length to touchdown point in Figure 12-15, where the numerical values are presented in Table 12-4, along with the minimum additional line length resting on the seabed.

Table 12-4: Summary of max arc-length to TDP and minimum additional line resting on seabed

Floater	Max arc-length to touchdown point	Min additional line resting on the seabed
7.47-115x4-10	898 m	62 m
8.45-90x4-10	912 m	48 m
9.94-65x4-10	930 m	30 m

As may be observed there are relatively large length of additional mooring line resting on the seabed, especially for floater 7.47-115x4-10. As discussed in section 11.2, it was intended to establishing a common mooring line configuration that gave some additional line resting on the seabed by studying floater 9.94-65x4-10. However, at the time of performing the trials to establish the needed line mass density, it was not known how the other two floaters would fare in the dynamic simulations. The relatively conservative 30 meters of line-length resting on the seabed was at the time believed to be suitable to ensure that all simulations resulted in no vertical loadings at the anchor, in case floater 8.45-90x4-10 and 7.47-115x4-10 would fare worse than floater 9.94-65x4-10. However, as it turned out that floater 7.47-115x4-10 and 8.45-90x4-10 featured more favorable surge and heave motions; the resulting line length resting on the seabed is higher for these geometries. A lighter mooring line, i.e. a reduced line mass density, could consequently have been utilized and still fulfill the requirement of no vertical pull-up load in the anchor. An analysis of floater 9.94-65x4-10 comprising of a line mass density of 120 kg/m in environmental condition 2 resulted in an additional minimum line length resting on the seabed of 10 meters, and would be more suitable in the presented work. However, new analysis with

this line mass density was not performed due to time limitations. It is also of course possible to optimize the mooring line configuration further for floater 8.45-90x4-10 and 7.47-115x4-10 by either reducing the un-stretched line length or line mass density, while still ensuring no vertical pull-up load in the anchor point. This would however lead to a different mooring system between the studied floaters and would therefore not be in line with the problem description of evaluating the floater's hydrodynamic performance due to variations of the diameter and draft.

The structural integrity of the mooring lines may be evaluated by comparing the maximum tension in the lines to a commercially available mooring chain used for offshore applications. As stated in DNV-OS-J103, if the wind and waves are directed collinearly, i.e. wind and wave aligned, and acts in the direction that is most unfavorable for the mooring lines, conservatism is ensured and the estimated tension can be set as the design tension with no load factors applied. The obtained maximum effective tension during the one-hour storm may therefore be used as the design tension. Studying for example the datasheet presented in [51], a stud mooring chain with a mass density of 126 kg/m is observed, which is the closest to the 125 kg/m value studied in the presented work. This chain features a break load of 4196 kN with an R3 quality, which has an ultimate strength of 690 MPa and a yield strength of 410 MPa [51]. Table 12-5 presents the total used capacity of the specified chain when compared to the maximum effective tension obtained in each analysis.

Table 12-5: Comparison of maximum effective tension and break load of commercial available mooring chain

Floater	Max effective tension [kN]	Total usage [%]	Safety factor (SF)
7.47-115x4-10	2187.75	52.14	1.92
8.45-90x4-10	2327.67	55.47	1.80
9.94-65x4-10	2468.23	58.82	1.70

As may be observed, the mooring chain's strength is somewhat underused in the presented work. A lighter chain could therefore have been embedded while still satisfying the ULS criterion. The somewhat over-dimensioned mooring chain capacity is a direct result of the belief that a line mass density of 125 kg/m was needed to achieve some conservativism with respect to additional mooring line resting on the seabed, as previously explained.

There is thus room for optimization of the mooring line configuration. As stated in section 11.2, it was initially intended to perform this optimization, but this had to be abandoned due to time limitations. The mooring lines was therefore constructed to be equal between the studied floaters to make the results comparable, and this is the reason for the mooring system being somewhat over-conservative in the presented work.

12.4 Cost evaluation of studied floaters

From the discussion above, it may be realized that floater 7.47-115x4-10 features the most favorable motion characteristics in the studied DOFs (surge, heave and pitch). Consequently, the aforementioned floater also gives lower tension in the mooring lines with less variation, shorter arc-length to touchdown point, a higher minimum freeboard (even though negative) and a higher minimum air-gap. However, as stated in the introduction to this thesis, one of the main challenges with offshore wind power production is to construct cost effective systems. Cost estimates should therefore be included in the evaluation of the floating system in order to assess this challenge. However, establishing realistic cost estimate is not included in the scope of work, but some intuitive relations will discussed regarding the cost of the studied geometries.

There are numerous of cost polls related to an offshore turbine system. Some are for example cost of material, construction/manufacturing cost, transportation cost, installation cost and operation and maintenance cost. However, the material and construction cost will be the basis for the presented discussion, as it is believed that transportation cost, installation cost and operation and maintenance cost will be somewhat similar between the studied geometries. In order to obtain an estimate of the material cost, the resulting steel mass of each of the studied floater are presented in Table 12-7. The values are obtained from the respective inventor models by evaluating the shell of the floater geometry and assuming a steel density of 7850 kg/m^3. It may also be noted that these values are also presented in section 9.3, but are restated here for ease of reference.

Table 12-6: Steel mass per studied floater

Floater	Steel mass [tons]
7.47-115x4-10	593.85
8.45-90x4-10	538.26
9.94-65x4-10	476.51

As may be observed, the steel mass is highest for floater 7.47-115x4-10 and lowest for floater 9.94-65x4-10. A higher draft therefore increases the floater's total steel mass, even though the diameter is reduced to achieve the required displacement of 5300 tons used in the presented work. It is also fair to assume that the steel mass will somehow be proportional to the amount of manufacturing needed to construct the vessel. A high draft-low diameter floater therefore leads to an increased manufacturing cost, as more steel needs some sort of industrial processing. It may be noted that floater 9.94-65x4-10 can accommodate more ballast mass, as less of the available displacement is used on the steel mass of the floater. The cost of ballast material will therefore be highest for floater 9.94-65x4-10. However, ballast material is deemed cheaper than the cost of steel and associated manufacturing. An increase in the draft is therefore believed to increase the overall cost of the floater, even though the diameter is reduced to achieve the 5300 tons target displacement used in the presented work.

Furthermore, a high draft may impose some challenges in the installation and tow out operation, which should also be evaluated. As stated in the introduction to this these, the use of a floating support structure enables for installation in a shelter in-shore site. However, the site needs to feature a suitable water depth to accommodate for the draft. Statoil's Hywind pilot project was, for example, installed in Åmøyfjorden outside of Dusavika, featuring a total water depth of 110-120 meters [52]. The floater was ballasted down to a total draft of 107 meters in order to ease the lifting operations associated with the rotor assembly, leading a total distance to the seabed of 9 meters relative to the bottom of the structure. The transportation route to site also needs to feature sufficient depth to accommodate the floaters draft. By again taking example in the Hywind project, the assembled turbine was towed to site with a total draft of 95 meters [52]. The installation sites and tow out routes may therefore be a limiting factor on the floater's draft. Similar relations may be made for the operation sites, which must feature a depth sufficient to accommodate the floater's draft and the additional mooring lines used for station keeping purposes.

In conclusion, even though a long and slender floater seems to obtain the best motion characteristics, it is most probably also a more expensive solution compared to a shorter floater with a larger diameter. A high draft may also limit the applicable installation sites and tow out routes, along with the number of applicable operation sites. The discussion above reveals that there will be a compromise between

suitable floating characteristics and cost, where applicable installation and operation sites may also be a deciding factor on the floater's geometry.

12.5 Limitation and sources of error

There are some limitations and sources of error present in the presented work, which will be discussed in more detail in the following section.

12.5.1 Limitations

Most of the limitations in the presented work are related to the dynamic analysis. Some simplifications were also made in the spreadsheet calculations, mainly related to the estimate of added mass. However, the spreadsheet was intended to feature some engineering simplifications to evaluate a number of floating geometries efficiently at an early stage in the analysis procedure. These simplifications are covered in section 8.1, and will not be restated here. The presented limitations are therefore mainly related to the dynamic analysis.

The wind climate is modelled in a relatively simplified manner in the OrcaFlex simulations. Only the mean wind component is considered, modelled as a point load acting in the middle of the rotor blades. This implies that the wind and wave environment is completely decoupled. The highly irregular and random turbulence component is also neglected in the presented work. This simplification was necessary, as time was rather spent performing detailed analysis in HydroD to model the hydrodynamics accurately. Turbulence is important when evaluating the instantaneous maximum response of the turbine system, i.e. load and motions. The maximum motions and loads gained in the presented work will therefore be smaller compared to a real case scenario, as turbulence is an inseparable part of the wind climate.

The torque induced from the turbine in the operational condition (EC 1) was excluded in the hydrodynamic simulations due to difficulties of modelling sufficient yaw stiffness. It was therefore not possible to assess the adequacy of utilizing a Spar buoy with a crowfoot connection to accommodate a VAWT in the MW-class. This is an important and interesting aspect to consider, as the generated torque from a VAWT is transferred to the floating structure about the yaw axis, whereas a HAWT generates the torque about the surge or roll axis.

It was also planned to evaluate the performance of each floater in the respective environmental condition, i.e. operational and storm condition, with respect to power generation abilities and survivability characteristics with respect to the induced motions. Some survivability characteristics have been evaluated through the freeboard and air-gap in EC 2. However, guidelines for allowed maximum motions to ensure suitable operations in a wind park containing VAWT was not obtained, as this is a relatively new concept. It was therefore difficult to assess the suitability of the motions resulting from environmental condition 1, and both environmental condition were therefore used to assess the effect of varying the principal hull parameters on the evaluated hydrodynamic performance parameters.

The second order load terms, i.e. slow-drift motions, was not evaluated in the presented dynamic simulations due to time limitations. As stated in section 5.5.5, modeling of the slow-drift effects demands estimates of quadratic transfer function. HydroD is able to obtain the QTFs, but this demands more modelling work. As the author had limited experience with HydroD, much time was invested in researching how to operate the software. It was therefore decided to exclude the second order load terms in the analysis, and obtain the needed input to model wave-frequency responses, i.e. first order effects, accurately. As stated in section 5.5.5, a moored system is prone to experience slow-drift motions

in surge, sway and yaw, implying that there could be additional motions in these DOFs if the vessel comes into resonance with the higher order load terms. It may also be noted that modelling the slow-drift demands more detailed dynamic simulation than performed in the presented work. As slow-drift motions are damped insignificantly by the radiation of the free surface waves, effects like viscous loads on the hull, drag force on the mooring lines and variation of the wind loads with the velocity of the structure needs to be properly represented to model the damping of the slow-drift motions accurately.

An offshore wind turbine also comprises of a power cable system that allows the generated electricity to be transported to mainland. The power cable system was however not included in the OrcaFlex simulations. Due to the compliant motions in all DOFs for the Spar buoy studied in the presented work, this power cable will most probably be a flexible umbilical. The umbilical will add additional weight to the system, depending on the depth at the studied site.

12.5.2 Sources of error

Some sources of error occurred during the analysis procedure, most related to the hydrodynamic analysis, i.e. HydroD and OrcaFlex.

The spreadsheet analysis evaluated a floating system without mooring lines attached, and the entirety of the spare displacement was used as ballast mass to obtain a freeboard of 10 meters. Due to the nature of the design procedure, hydrodynamic coefficients had to be obtained before being able to run realistic simulations in OrcaFlex. This implies that the HydroD analysis had to be performed before being able to establish the mooring line configuration in OrcaFlex through the trials presented in section 11.2. The mass model in HydroD was consequently based on the results from the spreadsheet analysis, with the mooring lines excluded. Implementing the mooring system into OrcaFlex model led to an increased in the system's total mass of 175.95 tons, which had to be reduced from the vessel's mass to obtain the intended freeboard. This reduction was achieved by reducing the amount of ballast mass, which yielded a different center of gravity and moment of inertia properties. There is consequently a difference in the mass model used in the HydroD analysis and the OrcaFlex simulation. This may impose some deviations in the system studied in OrcaFlex and the frequency dependent added mass, damping, load RAO and displacement RAOs obtained in HydroD. In order to obtain a better understand of the differences, the structural properties with, and without mooring lines included are compared in Table 12-7.

Table 12-7: Comparison of mass model used in HydroD and OrcaFlex

Floater	Δmass [%]	ΔI_{xx} [%]	ΔI_{yy} [%]	ΔI_{zz} [%]	$\Delta\overline{GM}$ [%]
7.47-115x4-10	3.323	0.054	0.054	0.884	3.576
8.45-90x4-10	3.318	0.061	0.061	1.058	3.566
9.94-65x4-10	3.321	0.081	0.081	1.314	3.617

As may be observed there are some differences in the vessel's mass and mass moment of inertia around the z-axis between the two analyses. The differences in moment of inertia around the x and y-axis are insignificant, and should not impose any significant errors. It was assumed that the entire mooring line mass acts at the connection point, i.e. at the respective metacenter of each individual floaters. The implementation of the mooring lines therefore increases $\overline{KG}$ for each geometry, as the ballast mass is reduced and the mooring line mass is being added at a larger distance from the keel. This consequently reduces the metacentric height in the OrcaFlex model compared to the HydroD model, as observed in Table 12-7. The difference in $\overline{GM}$ between the two analysis is around 3.6%.

The frequency dependent added mass and damping matrices, displacement RAOs and load RAOs are therefore established based on a mass model featuring slightly more favorable inertial properties and metacentric height compared to the system studied in the OrcaFlex simulations. The significance of this is somewhat unclear from the current perspective, but it is believed to have only a small impact on the obtained results, as the differences are generally low. Furthermore, the tendencies in the results are still valid, as the difference in mass models are present for all floaters, making it a systematic error. The results are therefore still in line with the problem description, and the error should not have a significance on the conclusion of the presented work.

There were also some difficulties making damping mode B33 converge in the convergence study performed in relation to the HydroD analysis. The analyses were relatively time consuming for the finer mesh models and the simulation time seemed to increase disproportionately to the number of panels. The finest mesh model evaluated for each floater was therefore deemed to sufficiently converge the solution due to time limitations. There were however relatively significant deviations between the deemed converged mesh model and the prior mesh model (about 5% to 10%), and the solution may not be sufficiently converged for damping mode B33.

In order to make the mooring line configurations equal for each studied floater, the water-depth was increased in the OrcaFlex analysis corresponding to the difference in position of the metacenter between floater 9.94-65x4-10 and the geometry in question. The HydroD analysis was however performed for a water-depth of 320 meters for all floaters, as it was not known at the time of performing these calculations that the depth had to be altered to generate equal mooring configurations. This implies that only floater 9.94-65x4-10 features the same water depth between the HydroD analysis and OrcaFlex simulation. This shall however not to impose any significant errors, as the wave induced velocities and accelerations are generally insignificant at these depths due to the decaying nature of deep-water waves.

13 Conclusion

The results from the spreadsheet calculations gave strong indications that a floater comprising of a higher draft and lower diameter obtains a higher metacentric height. By studying the results, it was realized that an increased draft led to a larger increase in $(\overline{KB})$ than an increase in $(\overline{KG})$, ultimately resulting in a higher $\overline{GM}$. Since the studied floaters featured similar displacements, i.e. similar buoyancy force, the high draft and low diameter floaters also gave more favorable static inclination angles in both environmental conditions, as the increased $\overline{GM}$ leads to a greater moment arm in the up-righting moment. There were some initial concerns regarding the natural period in pitch and roll for the long and slender floaters, as the metacenter is inversely proportional to these parameters. However, it was observed that a higher draft led to an increase in radius of gyration and added mass in pitch/roll, approximated by strip theory. This counterbalanced some of the reduction in pitch/roll natural period imposed from a higher $\overline{GM}$, and all floaters consequently featured a pitch/roll natural period over 25 seconds. The natural period in heave featured simplerer relations. The water-plane area and mass were almost idendical between the studeid floaters, implying that the difference in heave natural period is soley related to the difference in added mass. This quantity was approximated using the volume of hemisphere with a diameter equal to the bottom of the floater, meaning that a geometry with larger diameter and shorter draft obtaines more favorable natural periods in heave. However, all studied floaters featured heave natural periods higher than 40 seconds, which is sufficient to avoid resonance motions with first-order waves. It may be noted that the natural periods obtained in the spreadsheet calculations were compared to the results from the HydroD analysis, where deviations of around 1-2% and 5% were observed for natural periods in heave and pitch, respectively. The approximated methods for calculating added mass was therefore surprisingly accurate. Based on the results, floaters 7.47-115x4-10, 8.45-90x4-10 and 9.94-65x4-10 were selected for further evaluation in the hydrodynamic simulation.

The hydrodynamic simulation included both a mean wind force and first order waves modelled through a JONSWAP spectrum with peakedness factor 3.3. The results were mainly presented as mean values and associated standard deviations, where the mean illustrated the floater's ability to absorb the constant applied wind load, and the standard deviation gave indications of the floater's response induced from the first order irregular waves.

The mean surge position imposed by the applied wind load were similar between the studied geometries, due to the horizontal force component from the mooring lines being identical in all three cases. This also led to a similar average heave position among the studied floaters, as an equal length of mooring line was suspended in the mean surge position, adding a similar additional downwards weight to the structures. Some differences were however observed in the mean pitch angle, where floater 7.47-115x4-10 obtained the lowest average rotation and floater 9.94-65x4-10 the highest average rotation. As the mean position obtained in the datasets were indications of the wind induced motions, the evaluation of mean pitch angle in the dynamic simulations is equal to the static pitch study performed in the spreadsheet calculation. Similar explanations may therefore be given, i.e. the lower average pitch angle for floater 7.47-115x4-10 is related to its higher metacentric height and thus increased up-righting moment. This is in line with the observed results as floater 8.45-90x4-10 obtained the second highest mean pitch angle while floater 9.94-65x4-10 featured the highest.

The standard deviations related to the studied motions revealed that floater 7.47-115x4-10 features the most favorable motion characteristics and floater 9.94-65x4-10 the least favorable motion characteristics. The results from the hydrodynamic simulations therefore indicates that a floater comprising of a higher draft and lower diameter experiences lower oscillatory motions imposed from

the waves compared to a floater comprising of a shallower draft and larger diameter. This were observed in the comparison plot of heave displacement RAOs. However, the displacement RAOs in surge and pitch were similar between the studied geometries, and the differences in motion characteristics in these DOFs is therefore related to the imposed wave loadings. The standard deviations for the total load, i.e. force/moment that gives net motions, illustrated that floater 9.94-65x4-10 obtained the highest oscillatory hydrodynamic loadings in surge and heave, while floater 8.45-90x4-10 obtained the second highest loadings. This tendency was also observed in the comparison plot of the load RAOs, and explains the higher oscillatory surge motions observed for a shallower draft and larger diameter floater. Furthermore, the standard deviation for total pitch moment was largest for floater 7.47-115x4-10, even though this geometry featured the smallest oscillatory motions induced from the first order waves. The increase in up-righting moment due to the higher metacentric height therefore seems to be more significant than the increase in inclination moment from the waves, reducing the overall pitch motions for a high draft and low diameter floater.

Due to its favorable motions in heave and pitch, floater 7.47-115x4-10 also gained the best freeboard and air-gap characteristics. However, the freeboard was negative for all studied floaters, indicating that hydrodynamic forces are exerted onto the rotor-column, which is not acceptable. The freeboard must therefore be increased for all studied geometries in order to obtain suitable floater designs. The air-gap was however found to be suitable for all studied floaters, where additional clearance was observed even for floater 9.94-65x4-10.

The tension in the mooring lines and arc-length to touchdown point is dependent upon the induced surge and heave motions. Floater 7.47-115x4-10 therefore obtained the lowest maximum arc-length to touchdown point and maximum effective tension in the lines troughout the simulations, while floater 9.94-65x4-10 obtained the highest values. Furthermore, as floater 9.94-65x4-10 oscillates in surge and heave with higher amplitudes, the variation in effective tension and arc-length to touchdown point of the lines also varies the most when analyzed in relation to the afromentioned flotaer. This might have significance of the fatuigue life of the mooring system.

To summarize, the results obtained in the presented work indicates:

- A floater comprising of a higher draft and smaller diameter obtains a higher metacentric height due to a greater increase in $\overline{KB}$ compared to $\overline{KG}$.
- A floater comprising of a higher draft and smaller diameter features more favorable static inclination angles due to the increased metacentric height
- A floater comprising of a higher draft and smaller diameter still features suitable natural periods in pitch/roll due to an increased radius of gyration and added mass associated with the increase in draft.
- A floater comprising of a higher draft and smaller diameter obtains more favorable motion characteristics in surge, sway, heave, roll and pitch due to a reduced total force, i.e. force that gives net motions, and an increased up-righting moment imposed from an increase in metacentric height.
- A floater comprising of a higher draft and smaller diameter features more favorable freeboard and air-gap due to the reduced motions associated with such a floater.
- A floater comprising of a higher draft and smaller diameter gives less overall tension in the mooring lines, while also reducing the arc-length to touchdown point due to the favorable motion characteristics. The reduced motions also gives less variation in the effective tension and arc-length to touchdown point, which may provide a more favorable fatigue life.

However, some cost considerations based on intuitive relations revealed that a higher draft would most probably lead to a more expensive floater than a lower draft. Furthermore, a high draft may limit the number of sites the turbine system is able to operate, as the site needs to feature sufficient water depth to accommodate the draft and the mooring lines used for station keeping purposes. It is therefore believed that the optimum principal hull parameters combination will be a compromise of sufficient stability, cost and depth at the location where the turbine shall operate.

Note that the obtained results features a mooring line configuration comprising of a line mass density of 125 kg/m, an un-stretched mooring line length of 960 meters, an arc-length to touchdown of 491 meters in a static state and connected at the level of the metacenter of each respective floater. This mooring line configuration is identical between the studied geometries to obtain comparable results, and is therefore not optimized for each particular floater. An optimized mooring configuration per floater may give other results with a different conclusion. Furthermore, theoretical hydrodynamic models often contain some uncertainties, and the analysis in the presented work is no exception. The results should therefore be checked against small-scale model testing in order to validate the tendencies observed in the presented work.

14 Proposed further work

As the presented study analyzed a floating turbine system established from initial designs, there are opportunities for further work. The following are some recommended extensions to the presented study.

- Optimization of the mooring line configuration:

The mooring line configuration was found to be somewhat over dimensioned in the presented work, and is suceptable for optimalization. This may be achieved by constructuring a line featuring different sections of chain and wire, and by possibly adding clump weights. The mooring system utilized in this thesis was also of a fictive nature, and it is recommended to use data for commerically availible offshore mooring chains and wires.

- Perform HydroD analysis with correct mass model:

As stated in the sources of error, there are deviations in the mass model embedded in the HydroD analysis and OrcaFlex analysis. It is recommended to establish an optimized mooring line configuration and performing the HydroD analysis for the mass model resulting from this configuraiton. It is also recommended to perform the HydroD analysis using a quarter model and specify symmetry around the xz- and yz-planes. This makes it possible to study finer mesh models in shorter computation time.

- Improve wind environment:

The turbulent wind component was not assessed in the presented work. Turbulence is important with respect to maximum responses and fatigue considerations. It is also recommended to conduct an coupled wind-wave time domain analysis. This may be done in Simo/Riflex and Fast.

- Implement yaw stiffness to the models:

Implementing a realistic yaw stiffness was not achieved in the presented work. VAWT impares the generated torque around the structure's yaw axis, and it is recommended to study the needed yaw stiffness to ensure suitable operation of the presented turbine system.

- Add non-linear effects:

Model the slow drift resonance motions in order to evaluate the significance of these on the concept evaluated in the presented work. This includes obtaining QTFs and accurately model effects like viscous loads on the hull, drag force on the mooring lines and variation of the wind loads with the velocity of the structure.

- Conduct strength analysis on the rotor and floater:

The structural integrity of the turbine system was not assessed in the presented work. A strength analysis should be performed in order to obtain a functional system able to withstand relevant environmental loadings.

15 References

[1] Global Wind Energy Council (GWEC), «Global Wind Report - Annual Market Update,» GWEC, Brussel, 2014.

[2] F. G. Nielsen, «An introduction to offshore wind energy,» *Norwegian Center for Offshore Wind Energy - Annual report,* pp. 7-9, 2011.

[3] European Wind Energy Association , «Deep Water - the next step for offshore wind energy,» EWEA, Brussel, 2013.

[4] DNV GL, *DNV-OS-J103: Design of Floating Wind Turbine Structures,* DNV GL, 2013.

[5] M. Barone & J. Paquette, «Vertical-Axis Wind Turbines Revisited: A Sandia Perspective,» Sandia National Laboratories, 2012.

[6] D. A. Spera, Wind Turbine Technology: Fundamental Concepts in Wind Turbine Engineering, New York: ASME Press, 2009.

[7] Statoil, «Hywind Scotland Pilot Park,» 01 06 2015. [Internet]. Available: http://www.statoil.com/en/TechnologyInnovation/NewEnergy/RenewablePowerProduction/Offshore/HywindScotland/Downloads/Public%20Event%20-%20Hywind%20Scotland%20Pilot%20Park%2020jan2016.pdf. [Found 09 02 2016].

[8] Simens, «Simens Wind Turbine SWT-2.3-82 VS,» 2009. [Internet]. Available: http://www.energy.siemens.com/us/pool/hq/power-generation/wind-power/E50001-W310-A123-X-4A00_WS_SWT-2.3-82%20VS_US.pdf. [Found 26 03 2016].

[9] Statoil, «Hywind Demo,» 11 2012. [Internet]. Available: http://www.statoil.com/no/TechnologyInnovation/NewEnergy/RenewablePowerProduction/Offshore/Hywind/Downloads/Hywind_nov_2012.pdf. [Found 09 02 2016].

[10] U. S. Paulsen, Author, *Prospects of Large Floating Vertical Axis Wind Turbines.* [Performance]. Risø DTU, 2011.

[11] Nenuphar, Author, *Vertiwind: making floating wind turbine technology competitive for offshore.* [Performance]. 2012.

[12] J. Dodd, «First 2MW Vertiwind vertical-axis prototype built,» 28 July 2014. [Internet]. Available: http://www.windpowermonthly.com/article/1305428/first-2mw-vertiwind-vertical-axis-prototype-built. [Found 05 05 2016].

[13] J. Quilter, «Technology,» Wind Power Offshore, 26 08 2012. [Internet]. Available: http://www.windpoweroffshore.com/article/1208793/analysis-aerogenerator-x-going-anywhere. [Found 27 03 2016].

[14] Gwind, «Flytende vind,» [Internet]. Available: http://www.gwind.no/?page_id=369. [Found 2016 05 05].

[15] Norwegian Centre for Offshore Wind Energy, «Annual Report 2013,» NORCOWE, 2013.

[16] MODEC, «Floating Production Solutions: Offshore Power: Floating Wind & Current Hybrid Power Generation,» [Internet]. Available: http://www.modec.com/fps/skwid/. [Found 27 03 2016].

[17] Brian Publicover, «Wind,» Recharge, 19 December 2014. [Internet]. Available: http://www.rechargenews.com/wind/1387148/Modecs-Skwid-windtidal-offshore-turbine-sinks-again-off-western-Japan. [Found 27 03 2016].

[18] T. Burton, Wind Energy Handbook, West Sussex: John Wiley & Sons, Ltd, 2011.

[19] DNV GL, *DNV-RP-C205: Environmental Conditions and Environmental Loads,* April: DNV GL, 2014.

[20] E. Hau, Wind Turbines: Fundamentals, Technologies, Application, Economics, Berlin Heidelberg: Springer-Verlag, 2013.

[21] T. Hansen & Ø. Torvanger, «Design of an Offshore Vertical Axis Wind Turbine,» Norwegian Centre for Offshore Wind Energy, 2012.

[22] J. M. Journée & W. W. Massie, Offshore hydromechanics, First edition, Delft, The Netherlands: Delft University of Technology, 2001.

[23] O. T. Gudmestad, Marine Technology and Operations - Theory & Practice, Southampton, Boston: Witpress, 2015.

[24] DNV GL, *DNV-OS-J101: Design of Offshore Wind Turbine Structures,* DNV GL, 2014.

[25] S. Haver, *Description of Metocean Characteritics for Planning of Marine Operations,* Stavanger: Lucture note in OFF600 - Marine Operations, 2015.

[26] O. M. Faltinsen, Sea Loads on Ships and Offshore Structures, Cambridge: Cambridge University Press, 1998.

[27] DNV GL, *DNV-RP-F205: Global Performance Analysis of Deepwater Floating Structures,* DNV GL, 2010.

[28] M. B. Sumer & J. Fredsøe, Hydrodynamics Around Cylindrical Structures, Singapore: World Scientific Publishing Co. Pte. Ltd, 2006.

[29] J. Jonkman, «Definition of the Floating System of Phase IV of OC3,» National Renewable Energy Laboratory, Colorado, 2010.

[30] DNV GL, *DNV-RP-H103: Modelling and Analysis of Marine Operations,* DNV GL, 2014.

[31] V. Luca, «Offshore Vertical Axis Wind Turbine with Floating and Rotating Foundation,» Technical University of Denmark (DTU), Lyngby, Denmark, 2011.

[32] Wärtsilä , «Materials: Glass Reinforced Epoxy Resin Composite,» Wärtsilä , [Internet]. Available: http://www.shipham-valves.com/en/materials/glass-reinforced-epoxy-resin-composite-gre. [Found 27 03 2016].

[33] Airfoiltools, «Airfoil Tools,» 2016. [Internet]. Available: http://airfoiltools.com/airfoil/details?airfoil=naca0021-il. [Found 22 04 2016].

[34] K. Wang, «PhD thesis: Modelling and dynamic analysis of a semi-submercible floating vertical axis wind turbine,» Norwegian University of Science and Technology, Trondheim, 2015.

[35] DNVGL, «Sesam User Manual: HydroD,» DNVGL, 2013.

[36] DNVGL, «Sesam User Manual: Wadam,» 2010.

[37] Orcina Ltd., «OrcaFlex user manual - Dynamic analysis: Calculation Method,» 2014.

[38] Orcina Ltd., «OrcaFlex user manual - General Data: Implicit Integration,» 2014.

[39] Orcina Ltd., «OrcaFlex user manual - Environment: Data for Random Waves,» 2014.

[40] Orcina Ltd., «OrcaFlex user manual - Importing Hydrodynamic data,» 2014.

[41] Orcina Ltd., «OrcaFlex user manual - Lines,» 2014.

[42] Orcina Ltd., «OrcaFlex user manual - Environment: Seabed data,» 2014.

[43] Orcina Ltd., «OrcaFlex user manual - Line types: Data,» 2014.

[44] Orcina Ltd., «OrcaFlex user manual - Limits data,» 2014.

[45] Orcina Ltd., «OrcaFlex user manual - Line Data: Connections,» 2014.

[46] Orcina Ltd., «OrcaFlex user manual - Rayleigh Damping: Guidance,» 2014.

[47] Orcina Ltd., «OrcaFlex user manual - Vessel theory: Impulse Response and Convolution,» 2014.

[48] Orcina Ltd., «OrcaFlex user manual - Vessel Theory: Stiffness, added mass and damping,» 2014.

[49] S. Quallen, «CFD Simulation of a Floating Offshore Wind Turbine System Using a Quasi-static Crowfoot Mooring-Line Model,» *Journal of Ocean and Wind Energy,* pp. 143-152, August 2014.

[50] M. Borg & M. Collu, «A comparison on the dynamics of a floating vertical axis wind turbine on three different floating support structures,» *EERA Deep Wind 2014. 11th Deep Sea Offshore Wind R&D Conference ,* pp. 268-279, 2014.

[51] Vicinay Cadenas S.A, «Brochure,» Vicinay Cadenas S.A, 2015. [Internet]. Available: http://www.vicinaycadenas.net/brochure/#p=56. [Found 21 05 2016].

[52] J. S. Thygeson, Author, *Hywind Demo Construction and Installation.* [Performance]. Technip, 2010.

16 List of figures

17 List of tables

18 Table of appendices

The appendices associated to the presented work are listed below. Appendix A is enclosed on the CD attached to the report.

Appendix number	Description	File format
A	Full results of static analysis	.xlsx
B	Turbine's inertia properties, unmoored state	.pdf
C	Turbine's inertia properties, moored state	.pdf

Appendix B

Inertia properties for the evaluated floater geometries for use in HydroD, retrieved from Inventor

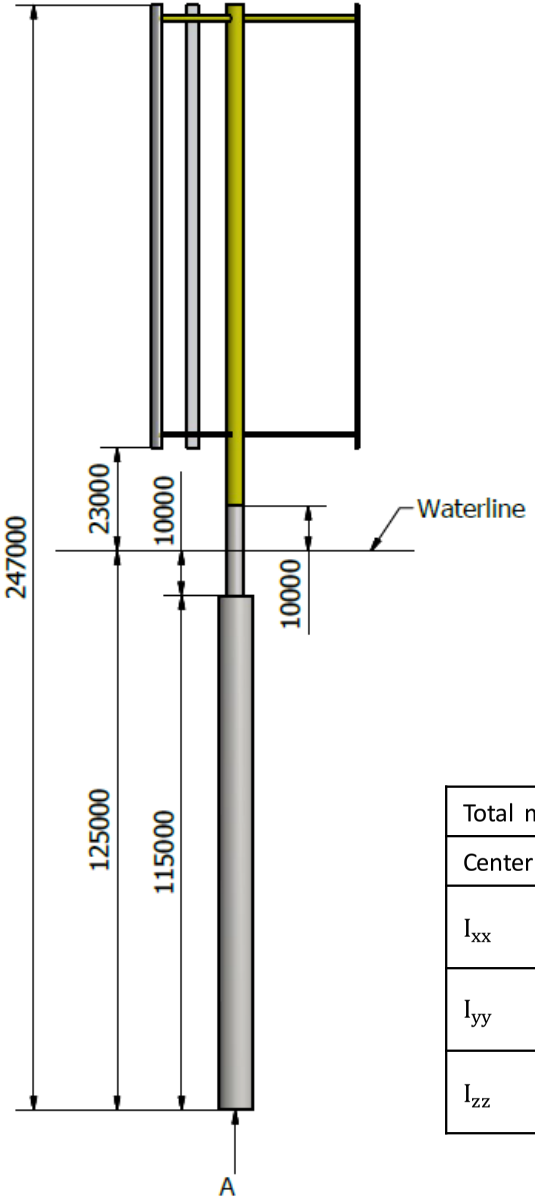

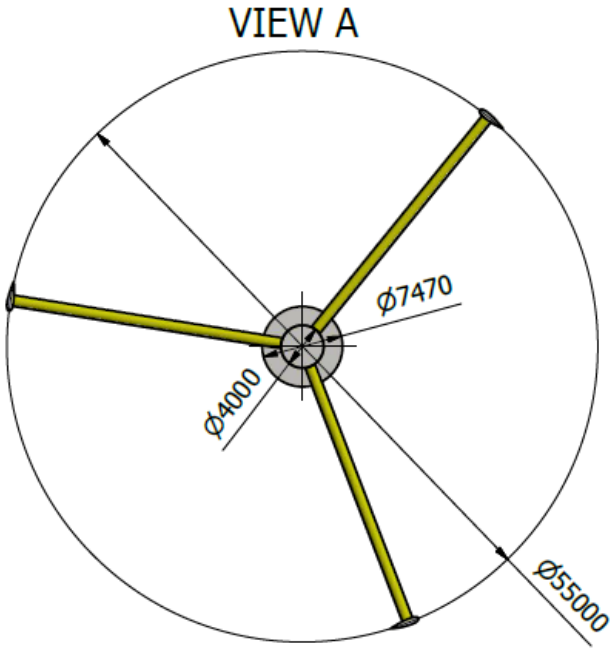

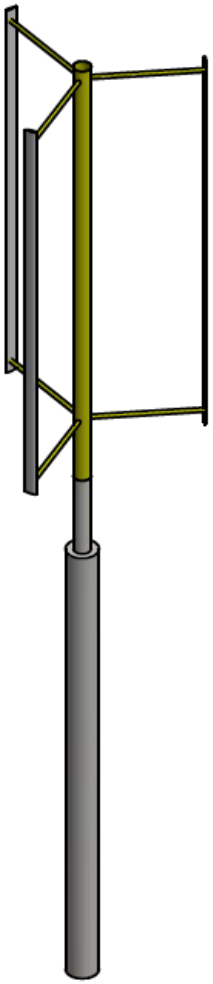

Total mass	5294786,128 kg (Relative Error = 0,003840%)
Center of gravity (x, y, z)	(0, 0, 35268,580 mm) (Relative Error = 0,003840%)
I_{xx}	1,448657103673646800 0E+016 kg mm^2 (Relative Error = 0,003840%)
I_{yy}	1,448657103673646800 0E+016 kg mm^2 (Relative Error = 0,003840%)
I_{zz}	1,369392537677408 00E+014 kg mm^2 (Relative Error = 0,003840%)

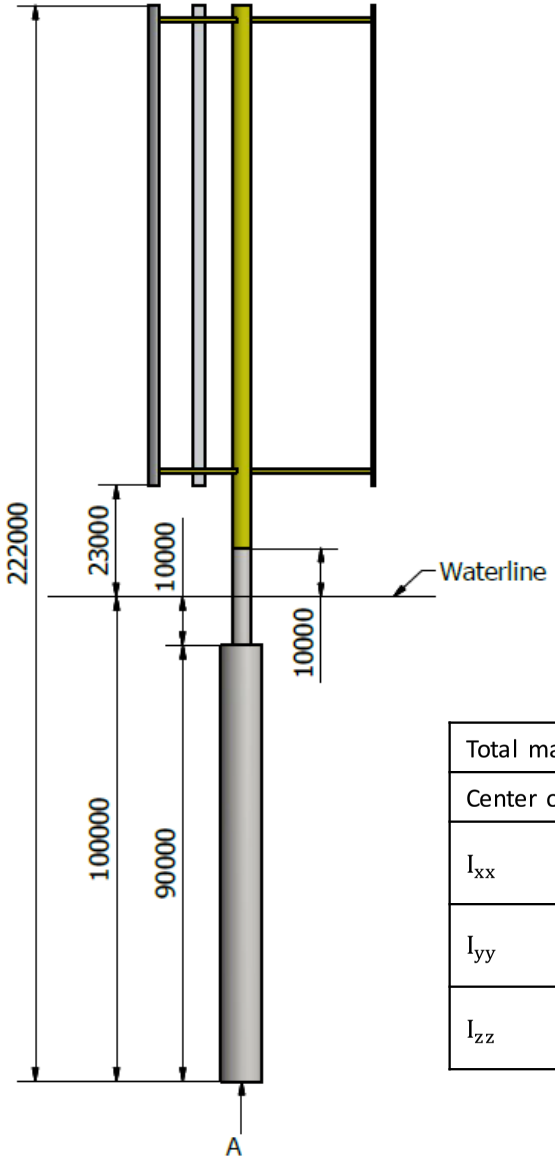

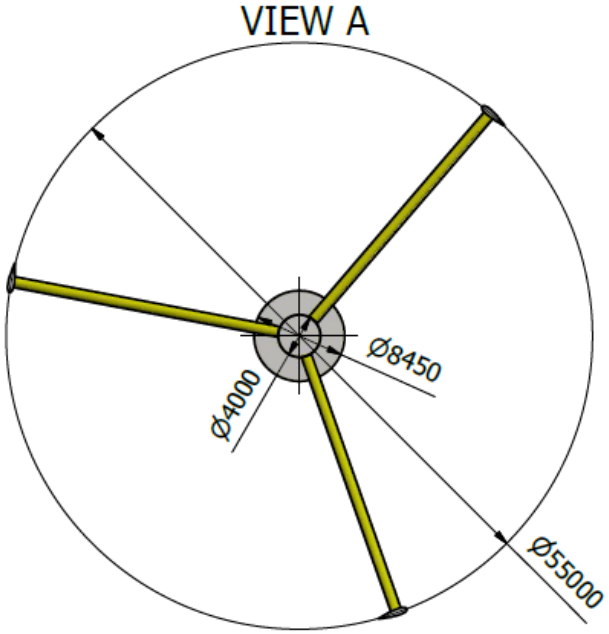

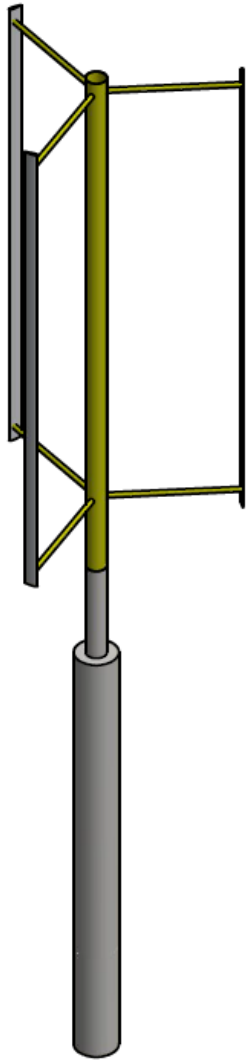

Total mass	5302130,054 kg (Relative Error = 0,003828%)
Center of gravity (x, y, z)	(0, 0, 28656.271 mm) (Relative Error = 0,003828%)
I_{xx}	1,08728430920546420 00E+016 kg mm^2 (Relative Error = 0,003828%)
I_{yy}	1,08728430920546400 00E+016 kg mm^2 (Relative Error = 0,003828%)
I_{zz}	1,46729294018819060E+014 kg mm^2 (Relative Error = 0,003828%)

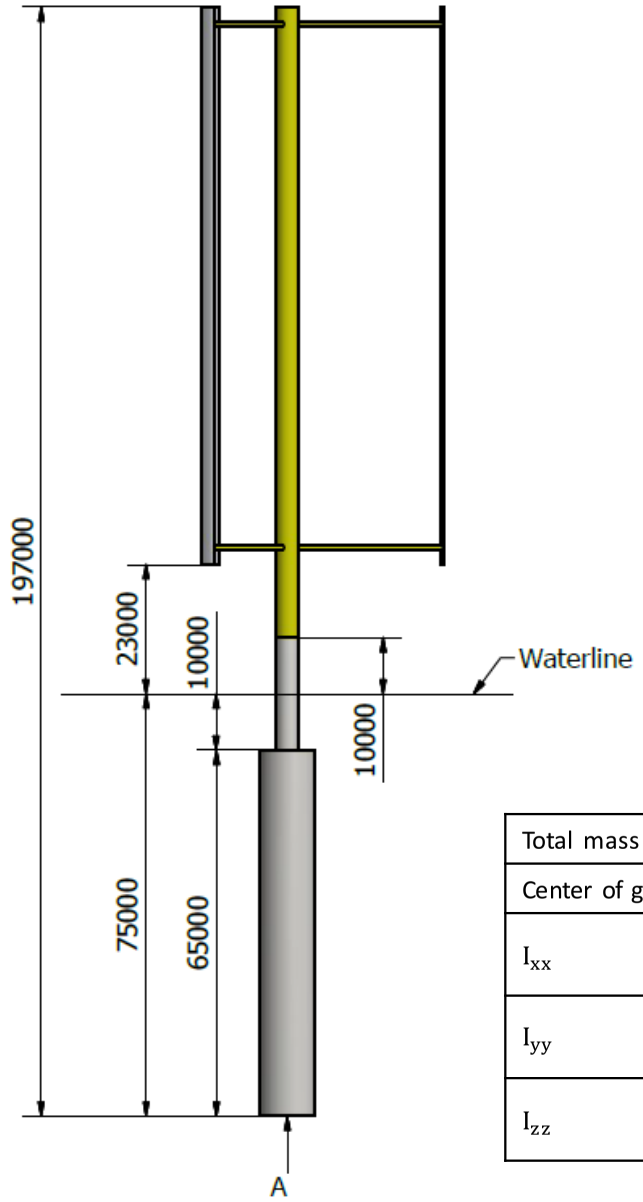

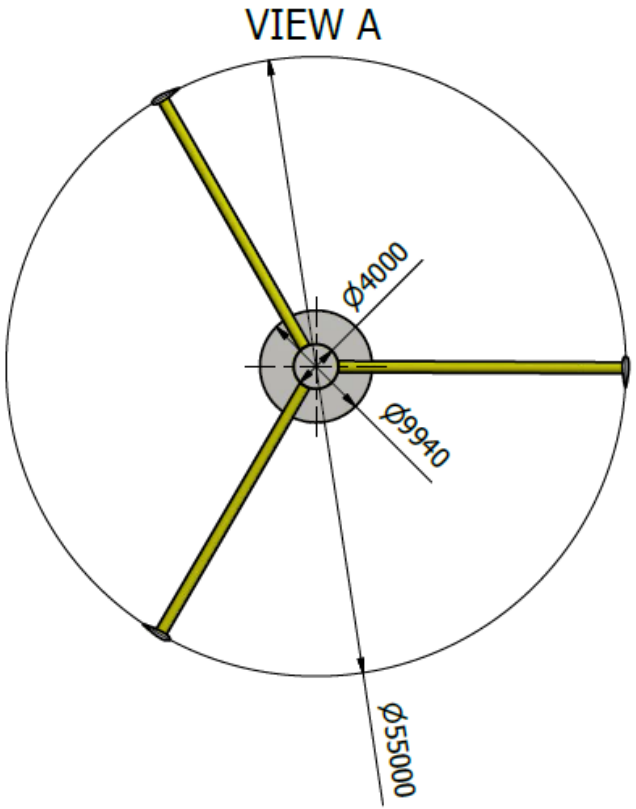

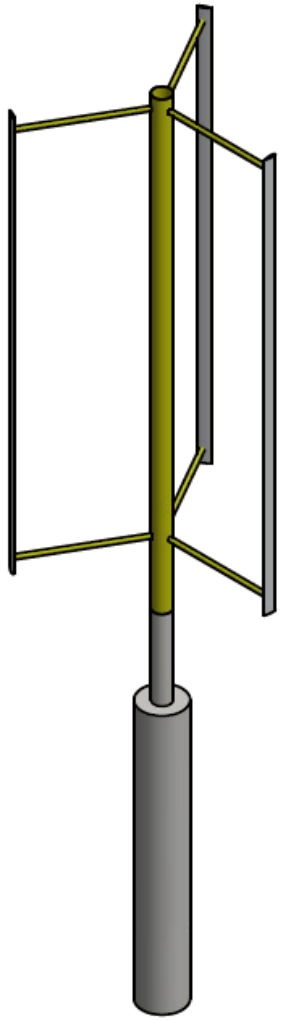

Total mass	5298926,373 kg (Relative Error = 0,003811%)
Center of gravity (x, y, z)	(0, 0, 22192.938 mm) (Relative Error = 0,003811%)
I_{xx}	7,887307442495786000E+015 kg mm^2 (Relative Error = 0,003811%)
I_{yy}	7,887307442495786000E+015 kg mm^2 (Relative Error = 0,003811%)
I_{zz}	1,636826726528643400E+014 kg mm^2 (Relative Error = 0,003811%)

Appendix C

Inertia properties for the evaluated floater geometries for use in OrcaFlex, retrieved from Inventor

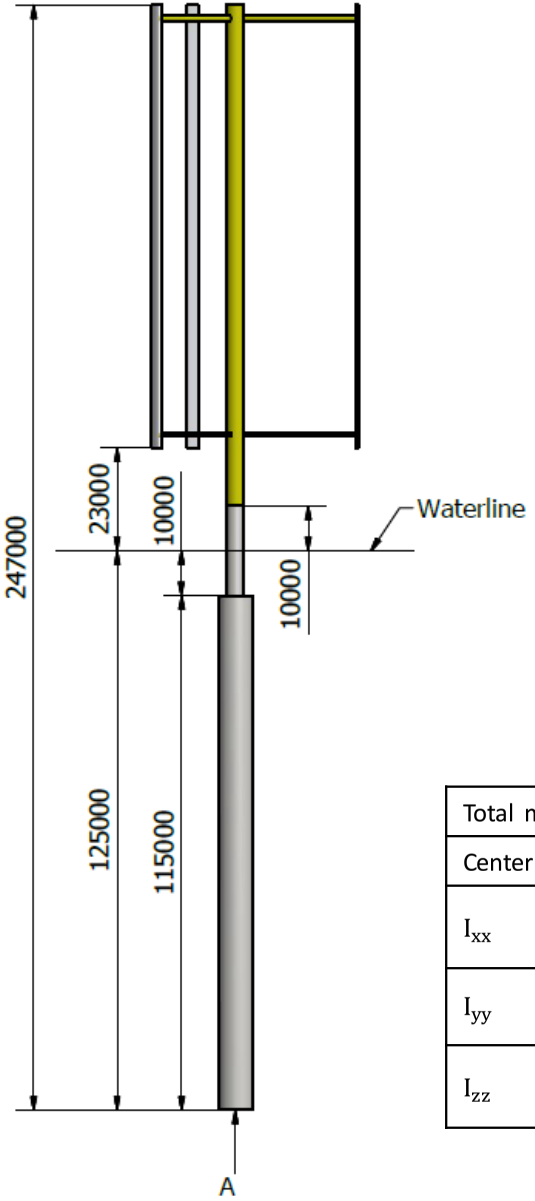

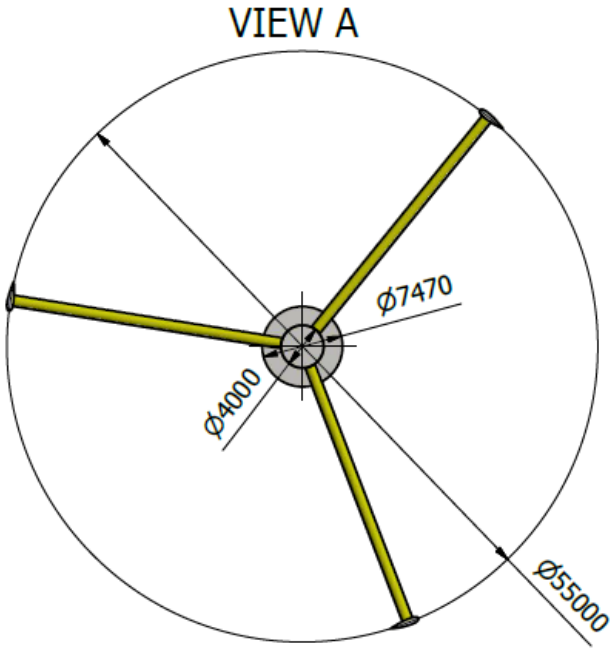

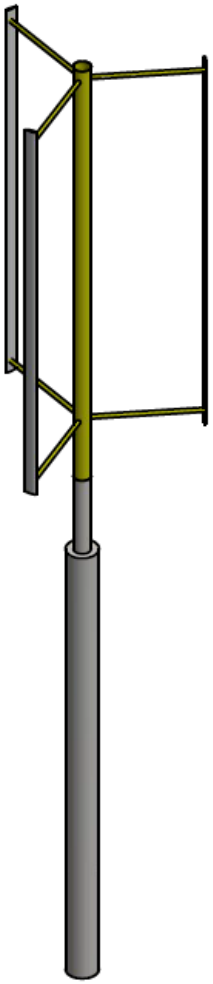

Total mass	5118835,796 kg (Relative Error = 0,003950%)
Center of gravity (x, y, z)	(0, 0, 35484,591 mm) (Relative Error = 0,003950%)
I_{xx}	1,44787557419327100000E+016 kg mm^2 (Relative Error = 0,003950%)
I_{yy}	1,44787557419327100000E+016 kg mm^2 (Relative Error = 0,003950%)
I_{zz}	1,35728354787664020E+014 kg mm^2 (Relative Error = 0,003950%)

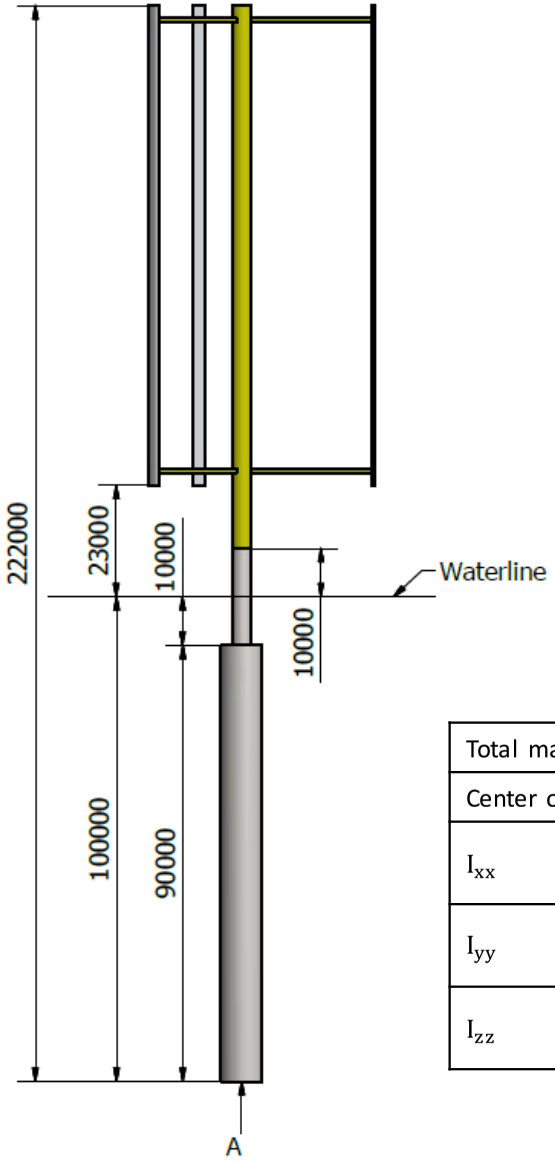

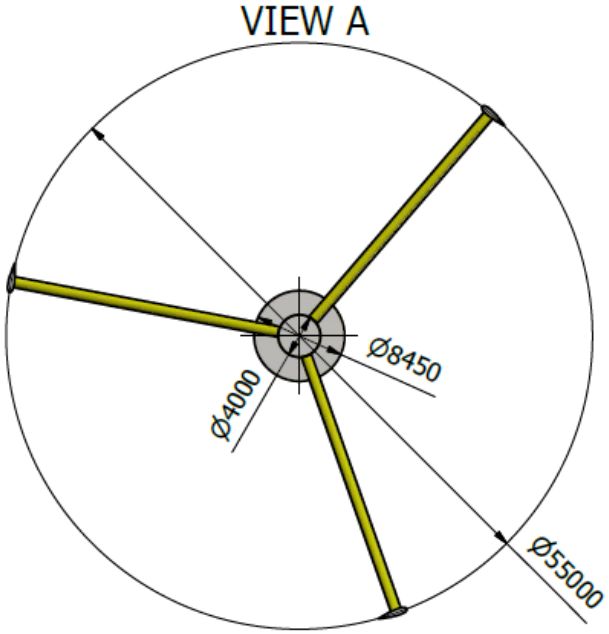

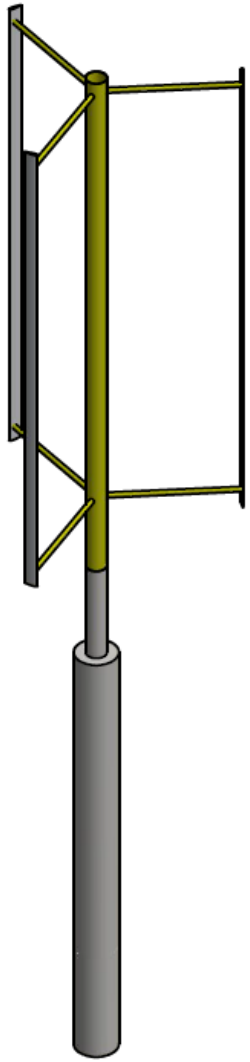

Total mass	5126178,896 kg (Relative Error = 0,003937%)
Center of gravity (x, y, z)	(0, 0, 28851,603 mm (Relative Error = 0,003937%)
I_{xx}	1,08661597091605860 00E+016 kg mm^2 (Relative Error = 0,003937%)
I_{yy}	1,08661597091605820 00E+016 kg mm^2 (Relative Error = 0,003937%)
I_{zz}	1,45177404810407590E+014 kg mm^2 (Relative Error = 0,003937%)

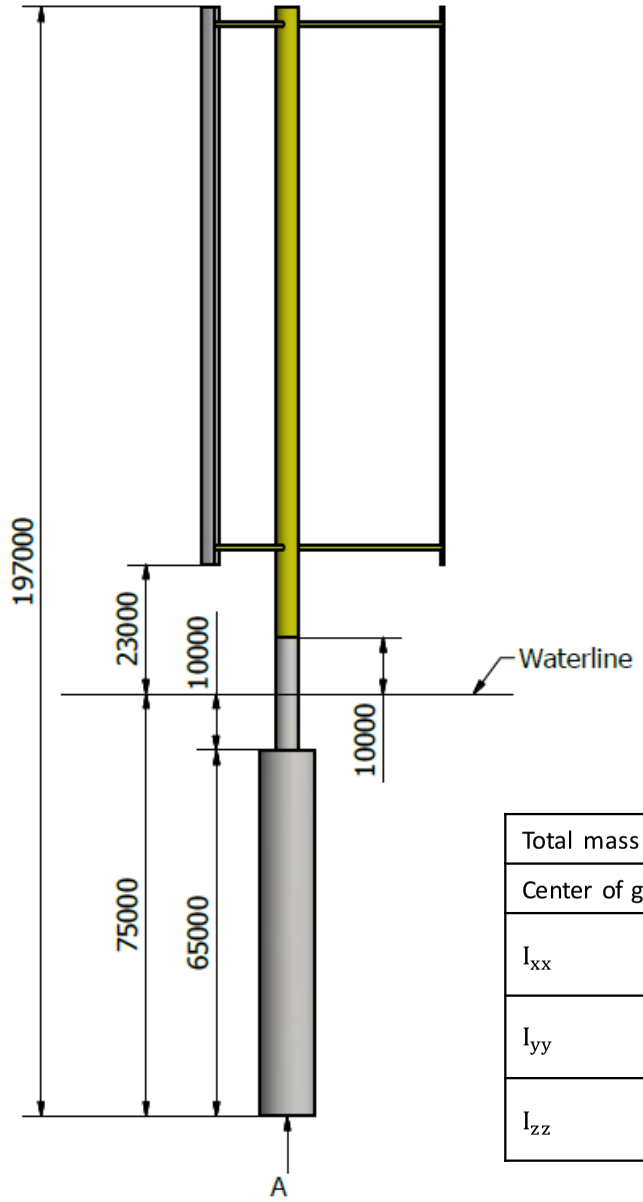

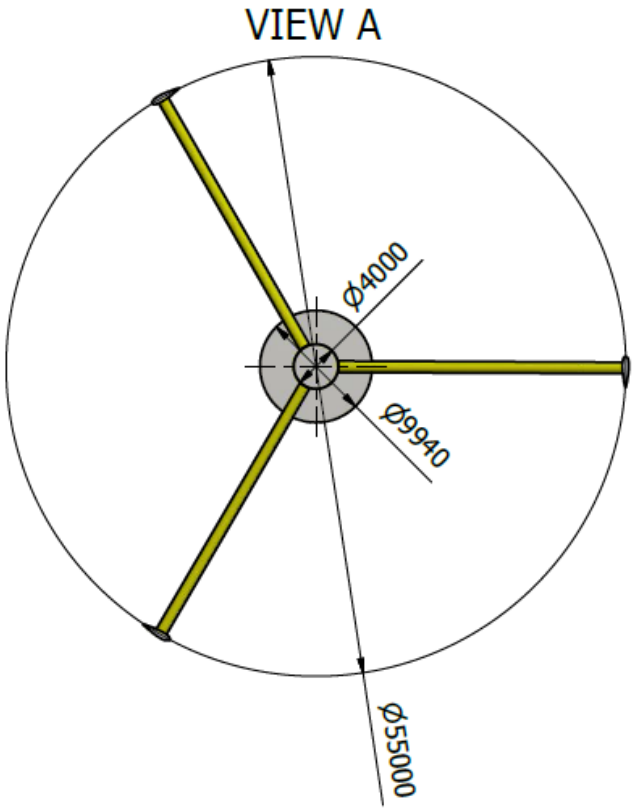

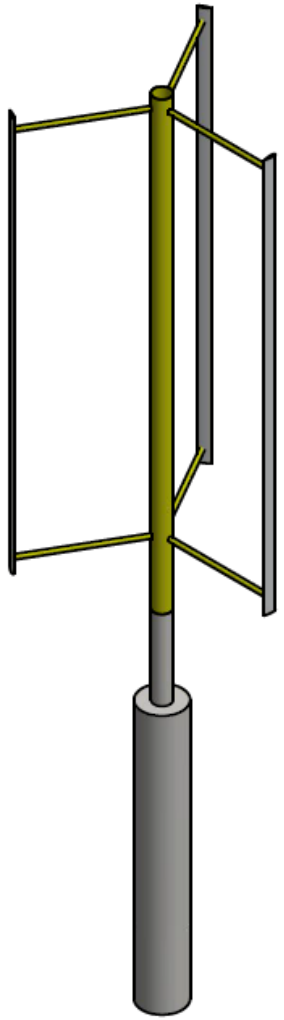

Total mass	5122966,547 kg (Relative Error = 0,003919%)
Center of gravity (x, y, z)	(0, 0, 22378,007 mm) (Relative Error = 0,003919%)
I_{xx}	7,880940667908842000E+015 kg mm^2 (Relative Error = 0,003919%)
I_{yy}	7,880940667908842000E+015 kg mm^2 (Relative Error = 0,003919%)
I_{zz}	1,615312976370610000E+014 kg mm^2 (Relative Error = 0,003919%)